University of Sussex

Passive Casing Treatments for Stall Margin Improvement in Axial Compressors

Ahmad Fikri Bin Mustaffa

A thesis submitted for the degree of Doctor of Philosophy

University of Sussex

School of Engineering & Informatics

September 2020

Declaration

I hereby declare that I am responsible for the work submitted in this thesis and the original work is my own otherwise specified in the acknowledgements. This thesis has not been and will not be, submitted in whole or in part to another university for the award of any other degree.

Ahmad Fikri Bin Mustaffa

Acknowledgements

All praise be to God for giving me the strength, wisdom, health and perseverance to complete this thesis.

First and foremost, I would like to express my sincerest gratitude to my supervisor, Dr Vasudevan Kanjirakkad, for his advice, guidance and relentless support throughout the years I spent to complete this thesis. Vasu has been a great mentor and he is always willing to go the extra mile for his students. I would also like to thank Dr Esra Sorguven for the invaluable discussions regarding to CFD. I am grateful to Mr Simon Davies for helping me build the test rig. Special thanks to Thomas Irps who helped me with the tensile test setup. Once again, I would like to say thank you to Vasu for providing me with the preliminary results of the test rig. I would also like to extend my thanks to all my colleagues at the TFMRC for their support and friendship.

It would be impossible for me to come to the University of Sussex without the financial support from the Ministry of Education, Malaysia and Universiti Sains Malaysia. I must also thank the University of Sussex for providing some financial support for attending conferences. This opportunity provided valuable feedback to the quality of my thesis.

I am deeply indebted to my beautiful wife, Attiya, and my lovely daughter, Huda, for the never-ending support and companionship throughout our wonderful time in Brighton. I would like to thank my parents, and my family for their continuous support in any way. Finally, I must say thanks to the Malaysian friends in Brighton for their friendship and amazing food.

Summary

Axial flow compressors are mainly used in the power generation and aerospace industry. Axial compressors are prone to instability issues since it is the nature of compressors to impart work on a fluid across an adverse pressure gradient. Instability in the compressor will instigate rotating stall and ultimately surge within the compression system. For tip-critical compressor, rotating stall can be delayed using passive casing treatments such as circumferential grooves. The design of circumferential grooves for improving the stability limit of axial compressors is the main theme of this thesis.

A transonic isolated axial compressor rotor is selected as the testbed for the application of the circumferential casing grooves. Prior to applying the casing grooves, the near-casing flow aerodynamics of that compressor rotor is numerically studied and validated using experimental test data. The shock-tip leakage vortex interaction is found to be responsible for the accumulation of the near casing blockage. The near casing blockage is quantified using a mass flow overshoot criteria. As the compressor approaches stall, the location of the peak blockage is found to move upstream towards the leading edge.

Based on the findings from the numerical study of the smooth casing, a design optimisation procedure is developed for identifying an optimised groove design. This procedure is based on a surrogate-based optimisation method. The magnitude of the peak blockage location and adiabatic efficiency at conditions close to stall are used for finding the optimised groove design. This method is different from the ‘black-box’ approach used by many researchers as found in the literature. The stall margin improvement gained by the optimised groove is about 1%. Further studies are conducted by changing the optimised groove axial location and simulating the grooved casing at part-speed conditions. No detrimental effects to the stall margin improvement are found at part-speed conditions.

The design optimisation method is numerically validated on a low-speed version of the testbed transonic compressor test rig. For this, the low speed blades are rescaled and designed using an inverse design method. The aim of the design is to mimic the same stalling criteria as the high speed version. Using the same design optimisation approach applied

on the testbed compressor, a single casing groove design is obtained. The effect of the optimised casing groove on the stall margin improvement is studied using numerical simulation. The optimal groove design is found to improve the stall margin of the low-speed compressor by about 5.4%.

Publications

Selected parts of this thesis have been presented and published as the following:

Mustaffa, Ahmad Fikri and Kanjirakkad, Vasudevan (2019), *Design optimisation of circumferential casing groove for stall margin improvement in a transonic compressor rotor*, In: 54th 3AF International Conference on Applied Aerodynamics AERO2019, 25-27 March 2019, Paris.

Mustaffa, A.F. and Kanjirakkad, V. (2020), *Casing-groove optimisation for stall margin in a transonic compressor rotor*, International Journal of Numerical Methods for Heat & Fluid Flow, Vol. ahead-of-print No. ahead-of-print.

Mustaffa, A.F. and Kanjirakkad, V. (2020), *Stall margin improvement in a low-speed axial compressor rotor using a blockage-optimised single circumferential casing groove*, In: GPPS Chania 2020, 7-9 September 2020, Online Conference. (Recommended for journal publication)

Mustaffa, A.F. and Kanjirakkad, V. (2020), *Single and multiple circumferential casing groove for stall margin improvement in a transonic axial compressor*, In: ASME TurboExpo 2020, 21-25 September 2020 Virtual Conference. (Recommended for journal publication)

Contents

List of Figures

List of Tables

Nomenclature

A_{int}	Area of groove-passage interface
A_t	Area of tip gap
C_p	Specific heat at constant pressure
c_{ax}	Axial chord
$c_{ax,t}$	Tip axial chord
c_p	Static pressure coefficient
f	Objective function
$f(x)$	Response variable
h_0	Total enthalpy change
H	Normalised groove height
H_n	Normalised helicity
i	i^{th} grid cell
M_{rel}	Relative Mach number
m	Mass flow rate
$\widetilde{m}$	Normalised mass flow rate
N	Total number of cells in an axial plane
P	Static pressure
P_{atm}	Atmospheric pressure
P_{01}	Inlet total pressure
P_{0exit}	Outlet total pressure
$P_{01,rel}$	Relative inlet total pressure
$P_{02,rel}$	Relative total pressure at a specified location
r	Radius
s	Entropy generation, pitch distance
T	Static temperature
T_0	Total temperature
U	Blade speed
V	Velocity
V_z	Axial velocity
V_θ	Pitchwise velocity

V_r	Radial velocity
$V_\perp$	Velocity normal
w'	Normlaised groove width
x	Input value
y	Output value
Y_n	Total pressure loss coefficient
z'	Normalised axial distance between groove front and tip LE
$\tilde{z}_t$	Axial distance normalised by the tip axial chord
α	Groove upper internal angle
β	Blade angle
ρ	Density
π	Total pressure ratio
Π	Total temperature ratio
η	Adiabatic efficiency/ Isentropic efficiency
Ω	Blade RPM
ψ	Binary blockage index
ψ_{ts}	Total to static pressure rise coefficient
Ψ	Non-dimensional blockage parameter
Ψ_{m}	Non-dimensional mass-flow blockage parameter
Ψ'	Stage loading coefficient
φ	Mass flux
ϕ	Flow coefficient
Φ	Tip leakage momentum
Δh_0	Total enthalpy change
ξ	TLV trajectory angle
χ	Shock trajectory angle
$\zeta, \Delta\zeta$	Stall margin, Stall margin improvement
ω	Vorticity
γ	Heat capacity ratio
μ	Split parameter

Subscripts

ax	Axial chord

exit	Outlet
hub	Hub
casing	Casing
t	Tip
mid	Mid-span value of variable
rel	Relative
r	Radial
θ	Pitchwise
z	Axial
0	Total values
1	Inlet
2	Specified location

Operators

$\bar{X}$	Pitchwise mass-averaged
$\bar{\bar{X}}$	Area-averaged/Passage mass averaged

Abbreviations

AMG	Algebraic Multigrid
ANN	Artificial Neural Network
CFD	Computational Fluid Dynamics
CoV	Coefficient of Variation
DF	Diffusion Factor
DoE	Design of Experiments
DT	Decision Tree
Exp	Experimental results
FEA	Finite Element Analysis
GA	Genetic Algorithm
HS	High-speed
ILU	Incomplete Lower Upper
LE	Leading Edge
LHS	Latin Hypercube Square
LS	Low-speed

LSAC	Low Speed Axial Compressor
MOGA	Multi-Objective Genetic Algorithm
MSE	Mean Square Error
ND	Near Design
NS	Near Stall / Navier-Stokes
PS	Pressure side
RANS	Reynolds Averaged Navier-Stokes
RF	Random Forest
RSV	Radial Separation Vortex
RSS	Residual Sum of Squares
SBAO	Surrogate-Based Analysis and Optimisation
SMI	Stall Margin Improvement
SS	Suction side
TE	Trailing Edge
TLF	Tip Leakage Flow
TLV	Tip Leakage Vortex
OOB	Out-of-Bag

Chapter 1

Introduction

Axial compressors are widely used in gas turbines for propulsion and power generation. The role of the axial compressor is to pressurise the working fluid by imparting energy through a stage (or multiple stages) which consist of rotating blades (rotor) and downstream stationary blades (stator). Flow downstream of the compressor has a relatively higher pressure than the upstream which means that within the compressor, the flow travels against an adverse pressure gradient. For this reason, flow in axial compressors is prone to instability problems such as boundary layer flow separation and tip leakage vortex instability. The flow instability problem limits the working range of compressors within a stability margin. Beyond this stability margin, flow within compressor can undergo rotating stall and this could be followed by surge for a compression system.

Rotating stall is a local flow phenomenon at off-design conditions where the compressor tries to adapt to a relatively lower flow rate. At a lower mass flow rate, limited flow is shared unequally leading to some parts (or blades) of the compressor annulus handling relatively less flow than the rest. The flow in the compressor at this point is no longer axisymmetric whereby circumferentially non-uniform flow patterns occur around the annulus. Compressors are no longer able to produce useful pressure rise as it enters rotating stall. On the other hand, surge is a compression system instability which may give rise to flow reversal across the whole compressor. The flow reversal is due to the failure of the compressor to provide positive net axial momentum flow due to the compressor stall. As a result, the flow is pushed in the negative direction (reverse flow) due to the prevailing adverse pressure gradient. Surge results in a drop in overall performance of the gas turbine and is a major safety concern especially in aviation. The failure of compressor to provide pressure rise may cause engine flameout which is catastrophic for propulsion systems. There have been several major incidents and accidents that have been linked to compressor stall or surge. One of them occurred in 2009 when an aircraft was forced to land in

the Hudson River after the engines failed shortly after take-off (Tikkanen, 2020). The compressor of the engines stalled after ingesting a flock of birds. Although no casualties were reported, 5 people were seriously injured. In a different event in 2019, a military instructor pilot was killed during a touch-and-go landing practice (Losey, 2019). The pilots heard a loud noise immediately after touching down which was followed by a loss of most of the engine's thrust. The pilots realised that the compressor was stalling after noticing the yawing and rolling motion of the aircraft. Despite numerous attempts, the pilots failed to recover the aircraft engine to normal operating conditions in which resulted in a crash. One of the pilots managed to safely eject from the aircraft while the other one failed to eject in time before the plane had crashed. Although, the reason for the compressor stalling was inconclusive, this event highlights the importance of improving the stability of compressors. This helps to prevent future accidents and improve the safety of flights.

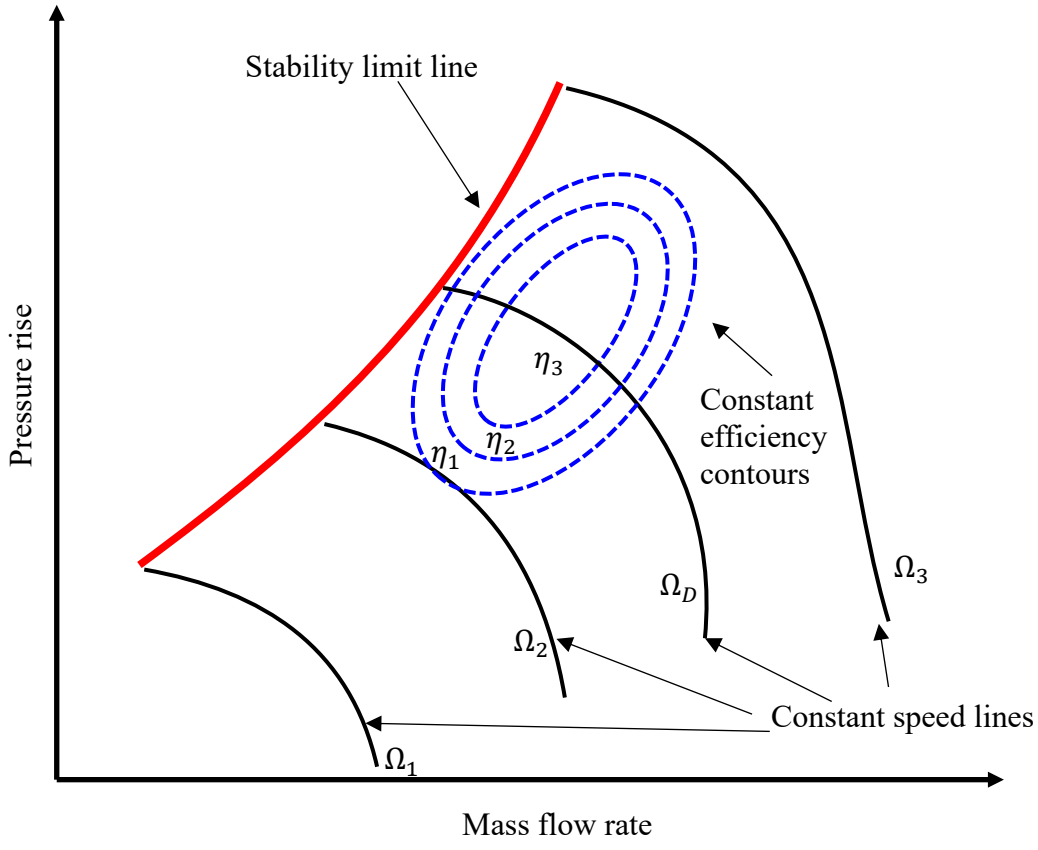

Figure 1-1 A generic axial compressor performance map

Figure 1-1 depicts a generic compressor performance map. The compressor performance map characterises the global performance of the compressor over a range of speeds. The performance map is made up of constant speed lines (shown by smooth black lines), each line represents the operation of the compressor at a fixed rotational speed (Ω). Even

though, the compressor is designed initially to operate at the design speed, Ω_D, a few scenarios require the compressor to run at various operating speeds to match the engine power demand. For instance, the demand for engine power in propulsion systems may vary depending on the various phases of flight. During take-off, the compressor is normally run at full-speed whereas it is run at a relatively lower speed during cruise and landing. In addition, for power generation systems, the compressor speed varies depending on the demand for electricity throughout the day and season.

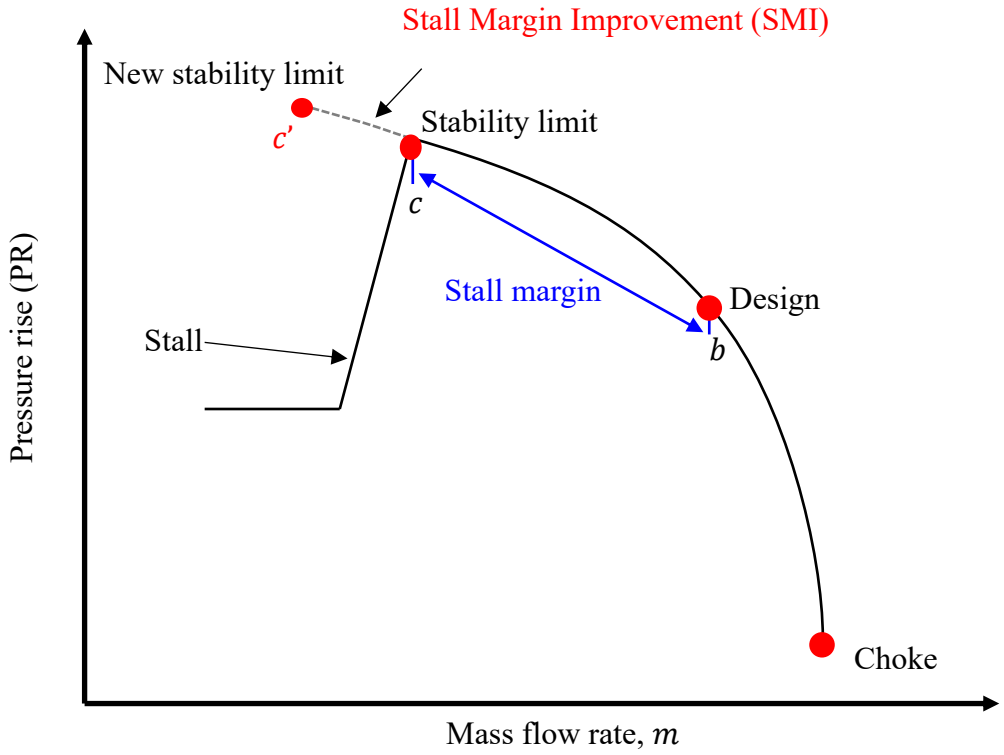

Figure 1-2 Generic compressor characteristic showing the choke, design and stability limit operating point

At a given speed, the performance of the compressor is shown by a performance characteristic as shown in Figure 1-2. Each characteristic is bounded by the rotating stall and 'choke' operating conditions. Rotating stall as explained previously can be triggered at low mass flow rates due to several reasons such as ingestion of foreign objects, high incidence due to misaligned blades, and extreme weather conditions that induce non-uniform inlet flow. Rotating stall can also be initiated by other factors such as blade geometric deformations and manufacturing defects. These factors may cause the compressor to deviate from its design operating point due to (circumferentially) localised reduction in mass flow rate below a critical value as defined by the stability limit. The stall line in Figure 1-1 is the limiting line that cut across the all the stability limit operating point for

each of the speed lines. 'Choke' on the other hand occurs at very high flow rates where some parts of the compressor reach sonic conditions. A choked flow would mean that any changes to the downstream flow conditions will have no effect on the flow upstream because the flow is not travelling faster than the pressure waves. The operating range between the design operating point (operating point b), and the rotating stall point (operating point c) is referred to as the 'stall margin'. A large stall margin would mean that there is a lot of room for the mass flow rate to be reduced before the compressor arrives at the rotating stall operating point. The method of extending the stall margin so that the rotating stall happens at relatively lower mass flow rate is known as 'stall margin improvement (SMI)'. The fictitious new rotating stall point is annotated as operating point c' in Figure 1-2. A common definition used for calculating SMI is described in Equation 1-1.

$$SMI = SM'\text{-}SM$$

$$SMI = \left[1 - \frac{PR_b}{PR_{c'}}\frac{m_{c'}}{m_b}\right]\text{-}\left[1 - \frac{PR_b}{PR_c}\frac{m_c}{m_b}\right] \quad (1\text{-}1)$$

Here, SM' is the stall margin calculated between the design operating point (operating point b) and the fictitious new rotating stall point (operating point c'). SM is the stall margin between the design operating point and the existing rotating stall operating point (operating point c). PR and m are the pressure rise and the mass flow rate, respectively.

SMI can be achieved using 'passive casing treatments' such as 'circumferential grooves'. Circumferential groove is a continuous cavity in the circumferential direction that can be machined over the rotor blade tip into the rotor casing. The design of circumferential casing grooves is currently a subject of active research. Although the concept of using circumferential grooves for SMI is not new, the method of finding the optimal location and size of the grooves is still a topic that needs further attention.

The main aim of the present work is to develop a method of optimally designing a circumferential groove for stall margin improvement using numerical simulations. Chapter 2 presents a background study on rotating stall and inception patterns. This includes experimental and numerical studies performed to understand the physics behind the development of rotating stall. Additionally, a review on the use of casing treatments for SMI

is presented. Chapter 3 presents the numerical methods used in this thesis. Chapter 4 presents the validation of the numerical method using a transonic compressor rotor test case. The results from this validation are used to explain the physical flow mechanisms near the tip that lead to rotor stall. A blockage parameter that quantifies the blockage within the blade passage, especially in the tip region, has been introduced. Chapter 5 describes the method used for obtaining an optimised casing groove design. In this chapter, the theoretical concept and implementation of the optimisation method and the resulting groove are presented. The outcome and performance of the design optimisation method are presented in Chapter 6. The link between SMI and blockage reduction is discussed. A sensitivity study of the groove location and prospects of multiple casing grooves are also studied in this chapter. Chapter 7 presents the design of a low-speed axial compressor for numerically validating the casing groove optimisation strategy as implemented in the thesis. The physics of the near casing flow at low-speed is first explained and the same optimisation strategy is therefore applied to this low speed rotor. Finally, the summary, conclusions and recommended future works are presented in Chapter 8.

Chapter 2

Literature Review and Research Objective

2.1 Overview

The first part of this chapter reviews related studies on rotating stall and its inception patterns in axial compressors. The aerodynamics of the tip region flow for high and low-speed compressors are reviewed next due to its possible link to stall inception. Thirdly, casing treatment methods for stall margin improvement are presented. Finally, the objective of this research is identified and explained based on the reviewed literature.

2.2 Rotating stall inception in axial compressors

Some of the earliest attempts to understand rotating stall in axial compressor can be traced back to the early 1950's. Huppert (1952) conducted experiments on a single and multi-stage axial compressor. Based on the experiments, two types of rotating stall are found. The first type is a 'progressive' type stall where the reduction in pressure ratio is small and less dramatic. 'Progressive' stall is linked to a multiple stalled region or otherwise known as part-span stall as shown in Figure 2-1a). A part-span stall is a high frequency propagating stall that is initiated near the blade tip. The stall regions known as 'cells' are equally spaced around the annulus. The speed of the propagation was observed to be almost 85% of the compressor speed. The second type of stall is known as an 'abrupt' stall where a sharp and dramatic drop of pressure ratio is found. This type of stall is associated with a single-stalled cell known as a full-span stall as shown in Figure 2-1b). A full-span stall is a low frequency propagating stall that rotates at approximately a third of the compressor speed. A part-span stall may develop into a full-span stall if the compressor is throttled even further.

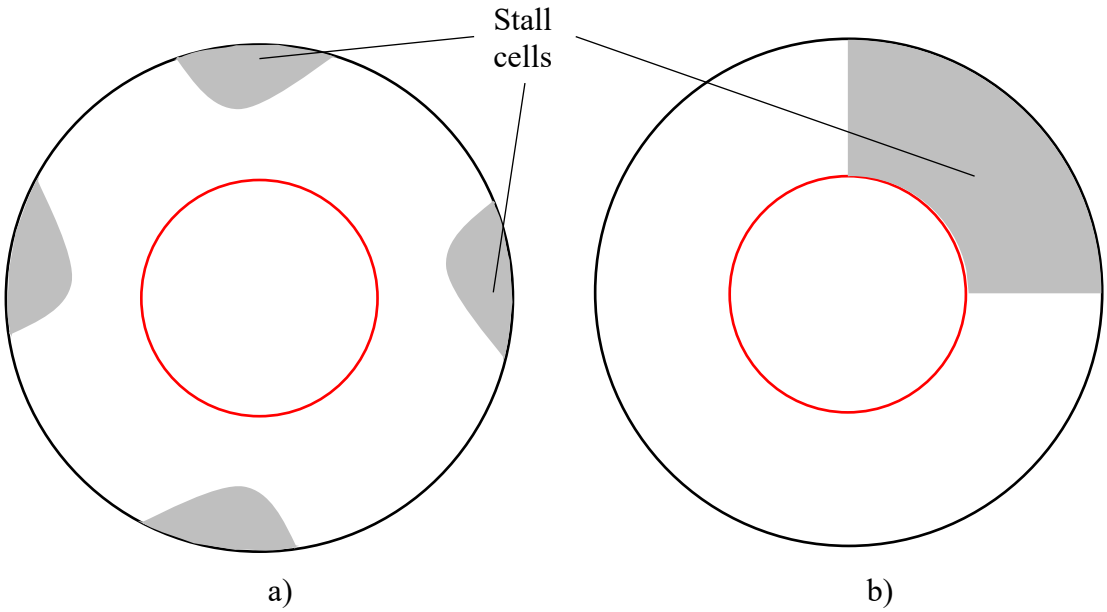

Figure 2-1 Development of stall cells for a) part-span and b) full-span across the annulus

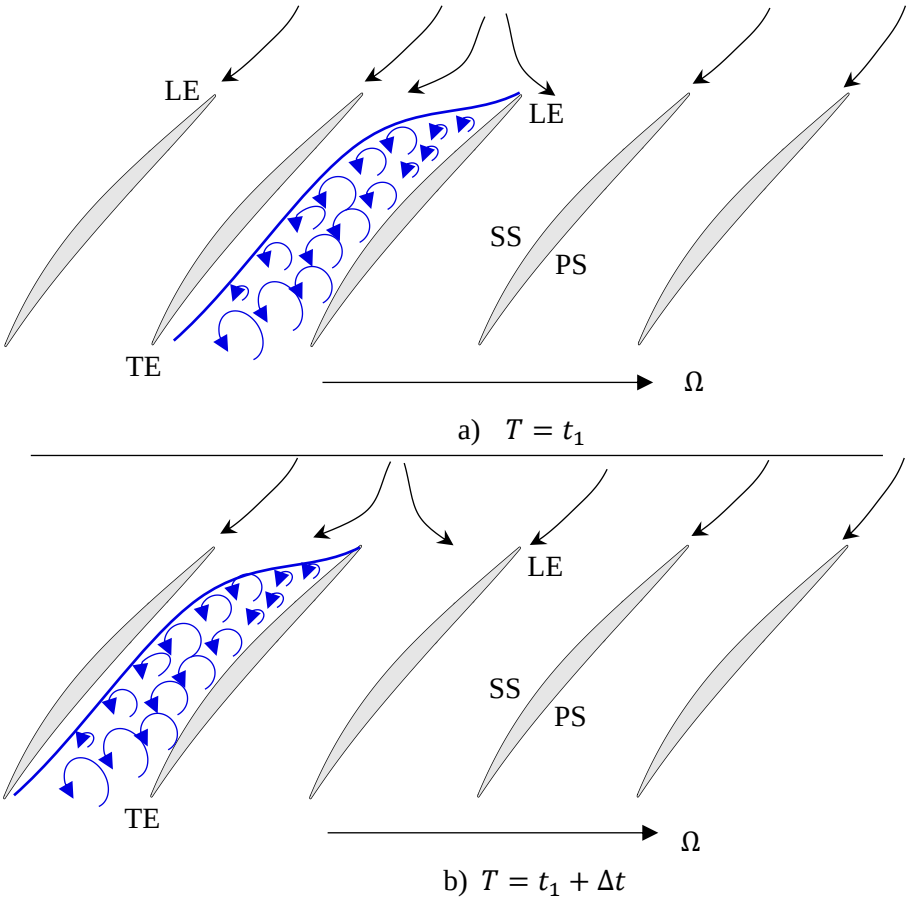

Figure 2-2 Propagation of stall cells explained by Emmons et al. (1955) and adapted from (Day, 1993b). a) Development of stall in one of the blade passages at time, $T = t_1$ and b) subsequent propagation of the stall cell into the adjacent blade passage

The works of Emmons et al. (1955) was among the first to explain the idea of the propagation of stall cells. Figure 2-2 shows a single bladed row of an axial compressor undergoing stall. As the compressor approaches stall, a local velocity deficit causes a change in the flow incidence. The flow at a relatively higher flow incidence is intolerable to the pressure rise across the rotor. This causes the flow to separate from the blade as shown happening to the middle blade. The flow separation acts as a blockage that effectively reduces the through flow. In addition, the blockage caused by the separated flow causes the incoming flow to be spilled to the adjacent blade passage. The spillage causes an increase of the incoming flow angle of the adjacent (left) blade passage and reduction of the incoming flow angle of the right blade passage. Subsequently, the left blade passage will therefore be subjected to stall while the middle blade passage will recover from stall. Hence, in the relative frame of reference, the stall cell propagates to the left passage which is the opposite to the blade rotation. The propagation of the stall cells is commonly known as 'rotating' stall.

Greitzer (1976a, 1976b) showed that rotating stall and surge can both be linked to the compression system instability. It was shown that flow perturbations in a compressor may develop into rotating stall or surge depending on the resonance frequency of the compression system. McDougall et al. (1990) performed experiments on a single stage low speed axial compressor to investigate the link between the flow perturbations and the inception of rotating stall. For a relatively small tip clearance, modal disturbance prior to rotating stall was observed near the hub region and the hub blockage is larger than the near casing blockage. As for relatively larger tip clearances, the casing blockage is larger than at the hub and the modal perturbations are observed near the casing prior to stall. From these findings, it was concluded that the modal perturbations prior to stall are dependent on the endwall blockage.

The link between modal perturbations and stall inception was further investigated by Day (1993b). Experiments conducted on two low speed axial compressors suggest that modal perturbations and the formation of stall cells are two separate events. Modal perturbations are associated with a long wavelength circumferential disturbance within an otherwise axisymmetric flow field. The formation of stall cells on the other hand represents the breakdown of flow symmetry which may not be preceded by signs of modal perturbations. A rapid breakdown of flow symmetry, without any warning, occurs if the formation of stall cells is not preceded by modal perturbations. Data from both compressors suggest

that this event is linked to a short-length type disturbance that originates from the near casing region. This type of disturbance is later known as a 'spike'-type stall because of the 'spike'-like pattern that appear in velocity traces prior to rotating stall (Camp and Day, 1998). Up until here, two types of stall inception patterns have been established. The first is the modal-type stall where the breakdown of flow symmetry is preceded by modal perturbations. Secondly, a 'spike'-type stall where an abrupt destruction of flow symmetry is observed without any signs of modal perturbations. Experiments performed by the above authors in a low-speed multi-stage axial show that the spike appears to originate at the tip. Furthermore, it was shown that modal-type stall and spike-type stall can be identified by examining the slope of the total-to-static compressor characteristic near stall as depicted in Figure 2-3. This finding is obtained from a series of tests on the same multi-stage low-speed axial compressor by varying the rotor incidence. The rotor incidence is varied by varying the stagger angle of the inlet guide vanes and stator blade rows. Spike-type stall is found to occur on the negative slope of the characteristic before the peak pressure rise is reached. On the other hand, modal-type stall is found to occur on the positive slope of the characteristic when the characteristic rolls-over the peak pressure rise.

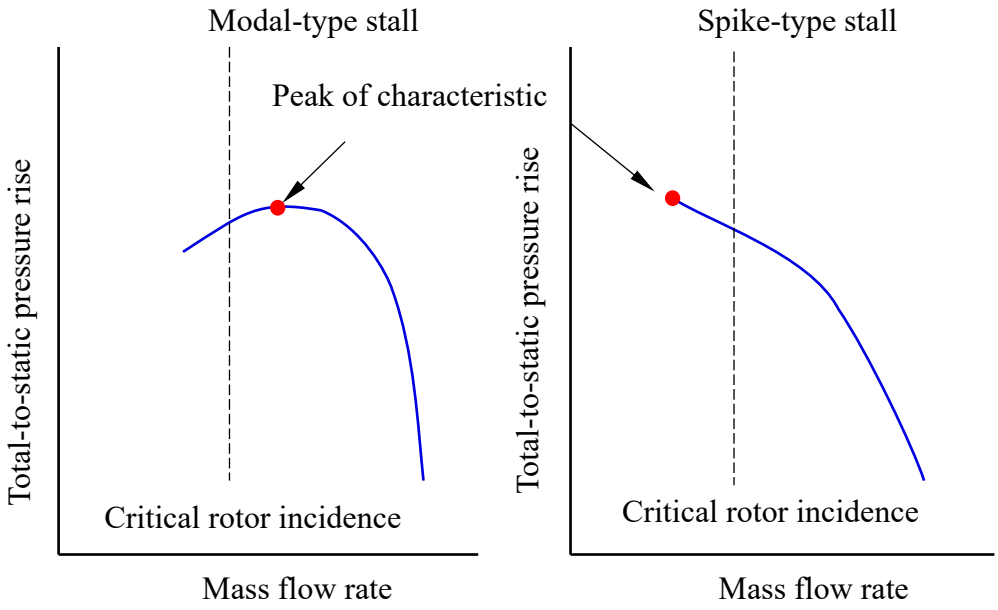

Figure 2-3 Characteristics of a compressor exhibiting modal and spike stall (adapted from Camp and Day (1998))

Two criteria for a spike-type stall were proposed by Vo et al. (2008) through unsteady numerical simulations. The first is the leading edge 'spillage' where the incoming flow

spills into the adjacent blade passage due to increased blockage at the tip region. The spillage is caused by the upstream movement of the interface where the inlet flow interacts with the tip leakage flow. At a relatively lower mass flow rate, the above interface loses its momentum balance and is pushed towards the leading edge of the adjacent blade which results in blockage. The second criterion for spike-type stall is the reversal of the tip clearance flow at the blade trailing edge. This happens as a result of increased tip clearance blockage that displaces the flow around the blade before moving upstream inside the adjacent blade passage. It is stated that both the above criteria which are linked to the tip leakage flow are required to be present for a spike-type stall.

2.3 Aerodynamics of the tip region flow

The previous section has discussed the characteristics of stall where two types of stall inception patterns have been established. So far, the link between tip region flow and the inception of spike-type stall is not yet established although strong evidence shows that spike-type stall originates from the near casing region. Therefore, the current section reviews some studies that have been conducted to link the aerodynamics of the near casing flow with the inception of spike-type stall.

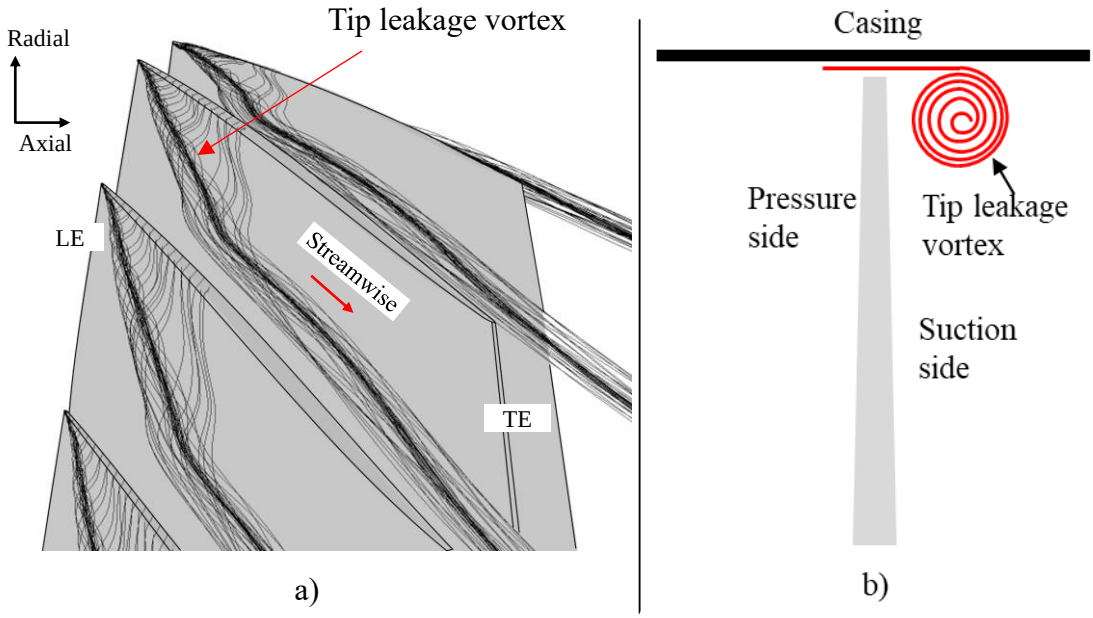

Figure 2-4 a) Illustration of a tip leakage vortex phenomenon in an axial compressor. b) Roll-up of the tip leakage flow into a vortex due to the pressure difference between the pressure and suction side (view from the front looking into the compressor).

Figure 2-4 shows an illustration of a tip leakage vortex in an axial compressor obtained numerically. The tip leakage flow is driven by the pressure difference between the blade surfaces. The relatively higher pressure near the pressure side as compared to the suction side causes the leakage flow to be pushed through the clearance between the blade and casing as the blade rotates. The tip leakage flow rolls up into a tip leakage vortex as it exits the tip clearance.

Furukawa et al. (1999) studied the characteristics of the tip leakage vortex for a low speed compressor. Using numerical simulations, vortex breakdown was shown to occur at a slightly lower mass flow rate than the peak pressure rise operating point. The vortex breakdown is identified as a 'bubble'-like structure near the mid-passage. This breakdown region grows rapidly in size and results in a large blockage effect as the mass flow rate is reduced. A further reduction in mass flow rate show that the breakdown region occupies a relatively larger portion of the blade passage which causes a three dimensional flow separation on the blade suction side. This results in an abrupt drop in the compressor pressure rise. Numerical simulations performed by Hoying et al. (1999) show that the spike-type stall can be linked to the upstream movement of the tip leakage vortex at conditions near stall. At near design conditions, the trajectory of the tip leakage vortex is pushed inside the blade passage by the momentum of the incoming flow. As the compressor is throttled towards stall, the strength of the tip leakage vortex increases due to increased tip loading. This results in an upstream movement of the tip leakage vortex trajectory in order to restore equilibrium. At this point, trajectory of the tip leakage vortex is perpendicular to the axial direction near the blade leading edge. The breakdown of the flow symmetry is observed when the tip leakage vortex 'spills forward' as the mass flow rate is further reduced. Mailach et al. (2000) investigated the link between the tip leakage flow and the near casing aerodynamic instabilities in a multi-stage low speed axial compressor. The above authors found that at near stall conditions, the aerodynamic instability is caused by periodical interactions of the tip leakage flow with the incoming flow of an adjacent blade. The near casing aerodynamic instability is responsible for noise and blade vibrations problems.

The tip leakage flow aerodynamics for low-speed compressors differ from high-speed compressors due to the absence of passage shock. For high-speed compressors, the near casing region is affected by the shock-tip leakage vortex (TLV) interaction as shown in Figure 2-5. The position of the shock varies depending on the operating conditions of the compressor. The change in the structure and location of the shock increases the intensity of the shock-TLV interaction and hence results in the increase in blockage. In Figure 2-5a), the shock is located inside the blade passage and is attached to the blade LE. As the compressor approaches stall, as shown in Figure 2-5b), the shock detaches from the blade LE. This causes the shock to interact more with the TLV. Adamczyk et al. (1993) conducted numerical simulations on a high-speed fan rotor to investigate the flow instability initiated by the tip leakage flow. The height of the tip gap is varied to investigate its effect on the performance of the high-speed fan. It was found that the pressure ratio reduces with a relatively larger clearance and the efficiency is maximum when no gap is present. The interaction between the passage shock and the tip leakage vortex results in a build-up of blockage near the casing region. The size of the blockage region grows and moves upstream when the mass flow rate is further decreased. When no gap is present, the fan exhibits a wider stable operating region due to the absence of the shock-TLV interaction. Suder and Celestina (1996) showed that the shock-TLV interaction is responsible for the near casing blockage inside a transonic isolated rotor compressor. Results from experiments and numerical simulations show that the blockage region increases in the circumferential and radial direction as the compressor is throttled towards stall. The blockage region is thought to be responsible for relatively higher incidence angle at near-stall conditions. Suder (1998) later showed that the near casing blockage is two to three times higher than the core flow region at conditions close to stall. At part-speed conditions where the effect of the shock is weaker, the casing blockage is found to be relatively lower than at design speed conditions. This clearly shows that the shock-TLV is responsible for additional blockage due to stronger interaction at design speed conditions as compared to part-speed conditions. Schlechtriem & Lötzerich (1997) numerically showed that shock-TLV interaction is responsible for a TLV breakdown in transonic axial fan rotor. Numerical simulations on a mixed-flow and centrifugal compressor however show no signs of TLV breakdown. The TLV breakdown is thought to be responsible for significant blockage regions which eventually lead to stall.

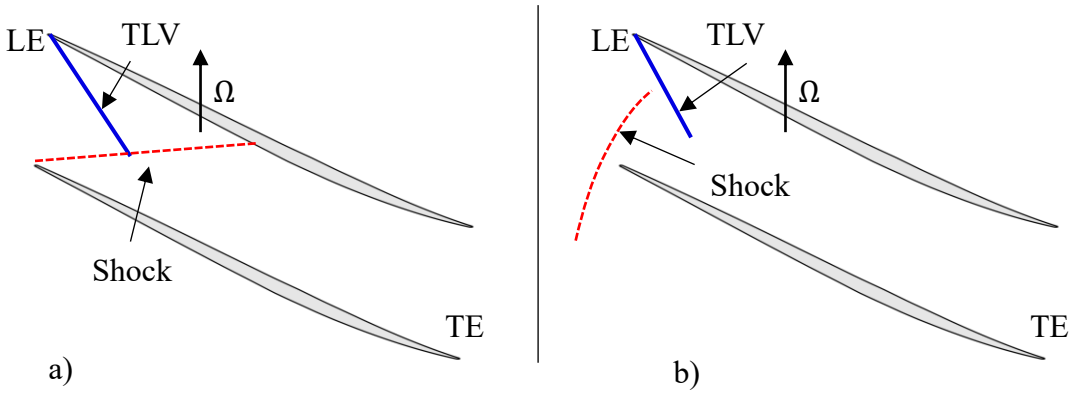

Figure 2-5 Illustration of a passage shock-TLV interaction in a high-speed compressor environment. a) At near choke and b) near stall conditions.

Another aerodynamic phenomenon near the casing region that can be linked to a spike-type stall is the radial separation vortex (RSV) as illustrated in Figure 2-6. The existence of RSV can be linked to the existence of bound vortices on the blade that is responsible for generating lift. As the compressor approaches stall, the flow near the tip leading edge (LE) separates. As a result of the flow separation, the bound vortex is released from the blade surface near the tip. The released vortex resembles a tornado-like structure of predominantly radial vorticity.

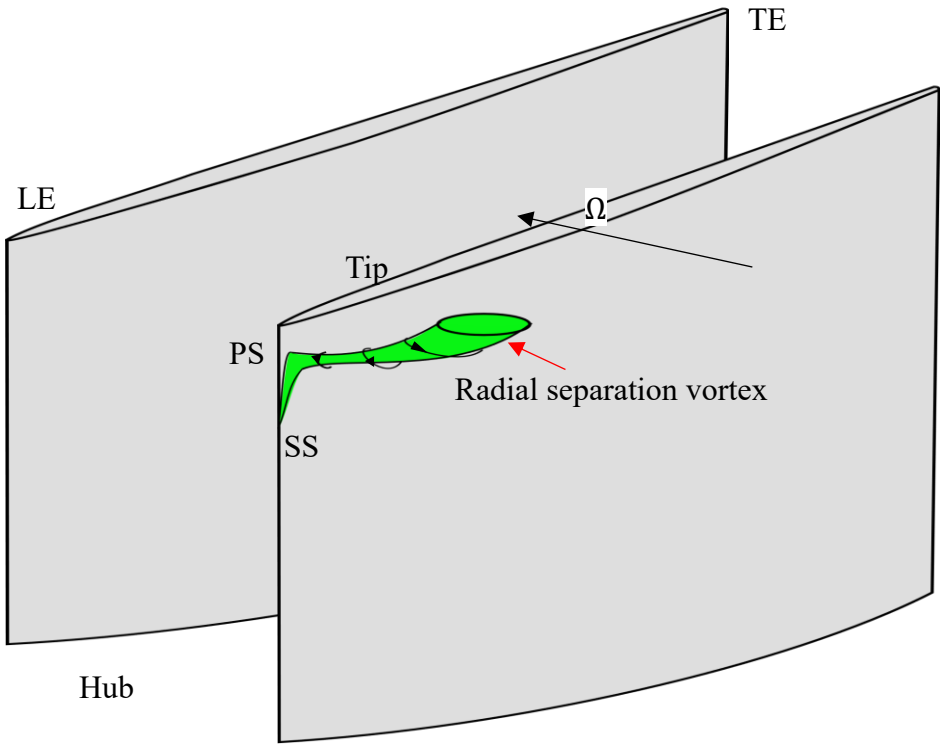

Figure 2-6 Illustration of a radial separation vortex phenomenon occurring near the tip region

Within a low-speed compressor environment, the RSV is said to be responsible for a 'spike' type disturbance near the casing (Inoue et al., 1999; Pullan et al., 2015; Yamada et al., 2012). Inoue et al. (1999) experimentally showed that the RSV created reverse flow regions near the casing downstream of the rotor blade. The rotation of the blade causes the RSV to stretch and break away from the blade and subsequently propagate into the adjacent blade passage. Numerical simulations performed by Yamada et al. (2012) showed that the circumferential propagation of the RSV as it breaks away generates a LE separation on the adjacent blade. The LE separation is propagated into the rotor passage and eventually develops into stall cells. Pullan et al. (2015) showed that the RSV can also exists in a low-speed axial compressor with no tip gap. This shows that the tip leakage flow is not a requirement for RSV to exist. The RSV has also been shown to exist in a high-speed environment as shown by Brandstetter et al. (2018). At near stall conditions, optical measurements near the casing show that a large blockage region exist due to the breakdown of the TLV. The blockage region causes a 'spill forward' effect which causes the flow at the LE to separate. This LE separation develops into a RSV and is shed into the blade passage.

2.4 Stall margin improvement methods

The understanding of the flow mechanism that is responsible for stall has sparked interest for finding ways to delay stall. The idea for delaying stall can be traced back to the early 1950's. After nearly 70 years of research, stall margin improvement technologies are yet to be fully utilised in production engines. This is because, apart from performance benefits, some other aspects are required to be considered before employing casing treatment technology in production engines. These include the cost, manufacturability, aeromechanical and acoustics impact. Some of these challenges are discussed as the methods for delaying stall are reviewed in this thesis.

In general, studies related to stall margin improvement can be categorized into active and passive treatment methods. Paduano et al. (1993) used an active feedback control technique to suppress modal waves that occur prior to rotating stall in a low-speed axial compressor. The technique involves using variable inlet guide vanes (IGV) that obtained feedback from hot wire measurements. The stagger of the IGV are individually controlled to create a disturbance in order to damp the modal waves that appear prior to stall. This work

has shown that actively suppressing the velocity perturbations may increase the stability range up to 20%. Day (1993a) tested active stall control techniques using air injection valves on a low speed multi-stage compressor. Two types of injection were used in this work. In the first method, air injection was used to suppress the development of modal perturbation prior to the formation of rotating stall. Twelve air injection valves were placed around the annulus near the tip of the first rotor. Hot wire measurements provided feedback to the valve control system. The modal waves were damped by opening all injection valves simultaneously. The stall margin improvement by applying this technique was 4%. The second method involves air injection at a local disturbance to remove blockage caused by the development of stall cells. This method differs from the first method as only one valve opens when a disturbance region is detected. A stall margin improvement of 6% was obtained using this technique. Day et al. (1999) investigated the prospects of applying active stall control techniques to four high-speed compressors. Each compressor was supplied by different industrial companies. At first, tests were conducted to characterize the stalling process of each compressor. Parameters such as compressor speed, IGV setting, and Reynolds number were varied to investigate the effect of these parameters on the stall inception pattern. From these tests, several observations were made. Modal and spike stall occurred in most of the compressors tested. One compressor experienced abrupt stalling in which was difficult for application of any active stall control measures. Other forms of instabilities such as shaft order disturbances and inlet distortion were also identified. Shaft order disturbances can be easily identified and ignored by the active control system since the frequency associated with the disturbance is well defined. Inlet flow distortion such as from nacelle separation and ingestion of hot fumes were found to generate spikes and modes in some regions inside the compressor. Based on these observations, it was concluded that the major challenge for active stall control is the ability to identify and classify all the disturbances that may exist in a compressor. The feasibility of active stall control technology was tested on real engine by Freeman et al. (1998). Active control bleed valves were used on a Rolls-Royce Viper turbojet engine. Stall was artificially induced using several methods such as combustor air in-bleed, hot gas ingestion and fuel spiking. Flow perturbation across the compressor were detected using high-frequency response pressure transducers. Stall cells were eliminated through controlled recirculation of pressurised bleed air. It was shown that the active stall suppression method was able to extend the surge margin of the compressor at different operating speeds and stall inducing methods. However, although it has been demonstrated that

the active stall suppression method is promising on a real engine testbed, there is still a lot of work required for making this method flightworthy.

As opposed to active treatments, passive treatments do not involve the usage of a feedback control system. Passive treatments are often applied on endwalls especially on the casing owing to the reasons explained in the previous section. This method also applies to tip-critical compressors that are highly like to exhibit spike-stall. Passive casing treatments are relatively easier to design and cheaper to implement as compared to active treatments. This is because active treatments require extra hardware for the feedback system which may add cost and additional weight to engines. Furthermore, active control methods may not be possible for spike-type stall. Spike-type stall happens so rapid which is reported to be within 3 rotor revolutions after the appearance of the spike in velocity traces (Vo et al., 2008). This requires a feedback system with a high response time to remove the blockage associated with the spike to prevent the compressor from stalling. This is difficult to design, and this explains why passive casing treatments are more attractive for a spike-type stall.

Past attempts in using passive casing treatments for stall margin improvement have been compiled and reviewed in detail by Hathaway (2007). Early passive casing treatment technology were inspired by boundary layer control methods such as blowing and suction. These methods later evolved into more advanced methods such as casing wall recirculation method.

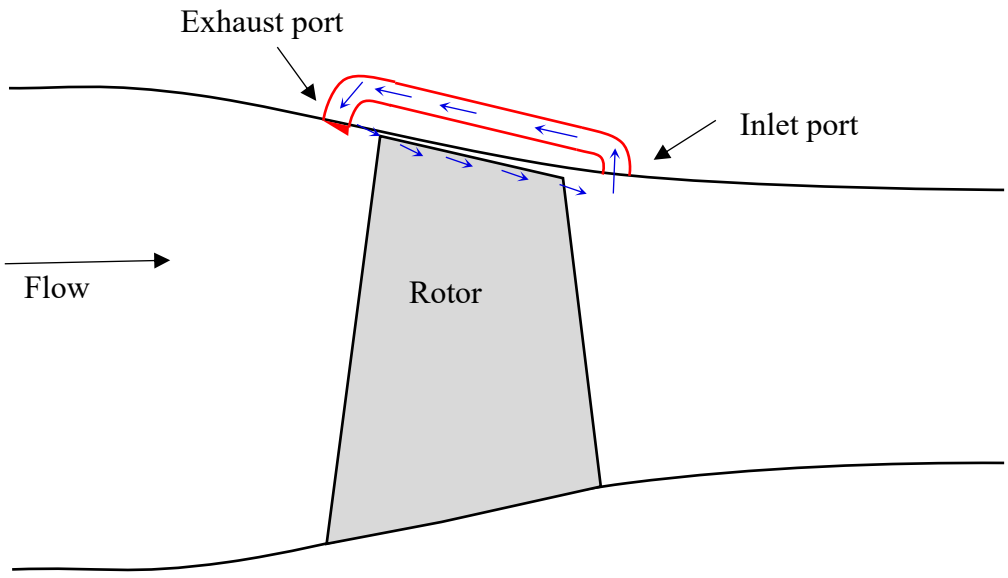

Figure 2-7 Casing wall self-recirculating concept

Hathaway (2002) and Khaleghi (2014) numerically tested casing wall self-recirculating concepts in high-speed compressors. Casing wall self-recirculating concept as shown in Figure 2-7 is a method of re-injecting air into the upstream casing region using the air that is bled from downstream of the compressor. This is done by an external ducting that connects the downstream and upstream region of the compressor rotor. The injected air reenergises the low flow momentum region at the near casing which resulted in a stall margin improvement. However, the real challenge of applying this type of casing treatment is the design of the bleed and injection system. The effectiveness of casing wall self-recirculating concepts relies on factors such as the location of where air is re-injected and the amount of mass flow that is bled. As noted by Strazisar et al (2004), the self-recirculating concept requires a two-to-one pressure ratio between the injector supply pressure and the static pressure upstream of the rotor tip for maximum effectiveness. This pressure ratio requirement may not be available across a single stage that necessitates air to be bled from stages located downstream of a multi-stage compressor. Furthermore, the design of the injector should be such that it is small enough to be placed in the inter-blade row gap, which typically is a fraction of the rotor chord. The injector should also be non-intrusive so that it does not add blockage effects to incoming flow. Therefore, although self-recirculating casing treatments are promising for stall margin improvement, a lot of work is still required for designing the injection system in order to integrate this technology to existing engine designs.

As compared to endwall recirculation treatment methods, axial slots and circumferential grooves can readily be integrated to any engine once the design has been finalised. This is because axial slots and circumferential grooves are considered as non-intrusive and can be engraved onto the casing of existing engines. In addition, axial slots and casing grooves do not require any additional hardware which, in a way, reduces the cost of the casing treatment development. In fact, circumferential grooves have been used in production engines as reported in Hathaway (2007). The difference between axial slots and circumferential grooves are depicted in Figure 2-8. A circumferential groove is a continuous cavity that extends around the whole annulus in the circumferential direction. On the other hand, axial slots are cavities that are discrete in the circumferential direction and also extend axially as compared to grooves. The cavities (groove and slots) allow the flow in the tip region to be transported radially in order to energise the low momentum flow associated to the tip region aerodynamics.

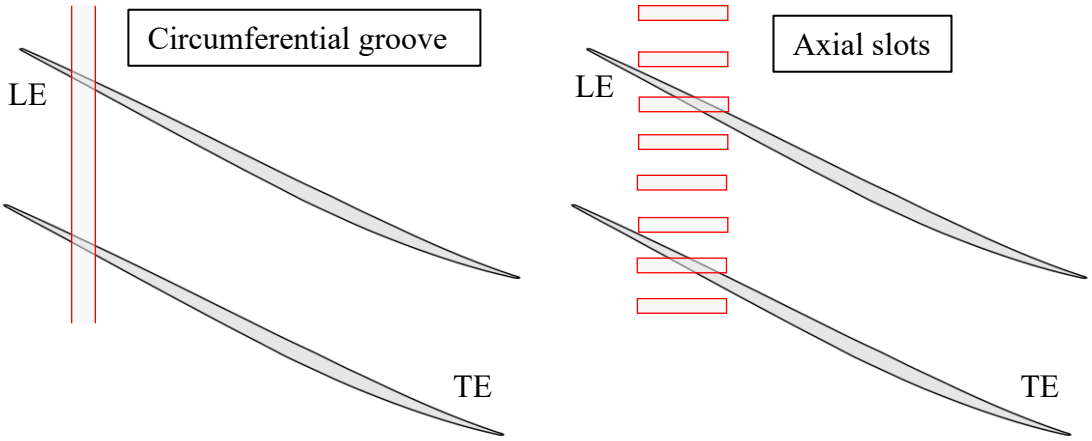

Figure 2-8 Circumferential groove and axial slots casing treatment methods

Osborn et al. (1971) and Moore et al. (1971) tested the performance of several types of casing treatments methods in a high-speed compressor. The casing treatment included circumferential grooves and axial slots. Axial slots were found to perform better than circumferential grooves in terms of stall margin improvement, but the former resulted in a relatively higher loss of efficiency. The same trend was also reported by Prince et al. (1975) and Fujita and Takata (1984) when testing the performance of circumferential grooves and axial slots in a low speed axial compressor. Fujita and Takata (1984) also noted that the selection of casing treatment should not be based on only a single parameter whether it is stall margin improvement or efficiency penalty. Instead, the choice of casing treatment should be judged based on both SMI and efficiency penalty to determine which casing treatment is superior. The findings here clearly show that the selection of the casing treatment should be aimed at the one that balances between SMI and efficiency penalty. Experiments and numerical studies by Houghton (2010) suggest that there can be no superior casing treatment when choosing between axial slots and circumferential grooves. The choice should also put into consideration the type of compressor that needs treatment and also the design requirement. For instance, if the design of the casing treatment permits a relatively high efficiency penalty, then casing with axial slots could be a design consideration. If the casing treatment design permits no efficiency penalty, then circumferential grooves could be a choice. This indicates that a direct comparison cannot be made when comparing between axial slots and circumferential grooves. Nevertheless, the previous discussions did not include other aspects such as manufacturability and acoustic impacts.

If these design conditions are factored in, circumferential grooves can be considered as the best choice. From the manufacturability perspective, circumferential grooves are relatively easier to machine as compared to axial slots. In addition, the discrete nature of axial slots also require acoustic tuning during design as shown in Osborn et al. (1971).

The preceding discussion in this section is only intended to inform the reader of the major types of casing treatment concepts that have been considered in the literature. Comparative study of each of the available casing treatment design is not within the scope of this thesis. Considering that there is a prospect of testing casing treatment designs on a test rig, a circumferential groove casing treatment is selected for this study. This selection is based solely on the aspects of manufacturability since a circumferential groove is relatively easy to manufacture with respect to the other available methods.

2.5 Circumferential groove casing design

Studies related to circumferential grooves has been attempted for both high speed and low speed compressors. Bailey (1972) performed experiments using multiple casing groove configurations on a single stage transonic axial compressor. The number of grooves, location and depth were varied throughout the test. The deepest groove showed the best performance with respect to the relatively shallow ones when tested at design speed. The best SMI was gained when five deep grooves were located at about the tip mid-chord of the rotor blade. Numerical studies by Rabe and Hah (2002) suggest that the depth of the groove do not impact the SMI for a highly loaded compressor. The SMI of five deep equally spaced groove across the rotor tip is similar to when only the first two of the five grooves were used. Muller et al. (2011) tested four casing groove configurations on a single stage transonic axial compressor at different rotor speeds. The depth and coverage region of the rotor tip chord were varied. Steady-state numerical simulations were also performed to help in understanding the physical effect of the grooves on the tip region flow. The best SMI was obtained when deep grooves that covered a relatively larger length of the tip chord were used. In addition, the shallow grooves were found to increase the peak efficiency at design speed as compared to the smooth casing. From the near casing Mach number contour plot, the SMI obtained was explained to be caused by the reduction of blockage region. The blockage region is reduced due to the interaction between the leakage flow and the flow into and out of the grooves. This prevented the ‘spill forward’ effect thus delaying the onset of stall. Chen et al (2013) numerically analysed the effect of multiple casing grooves in a single stage transonic compressor. It was

shown that the SMI due to the groove was linked to the reduction of the negative tip axial flow momentum. Flow into and out of the grooves provide a positive net axial momentum that reduces the backward momentum of the tip leakage flow. The greatest contributions to increase axial momentum were found to be from the first four grooves located aft of the tip leading edge. This positive axial momentum supplied by the grooves in other words, can be interpreted as the reduction of blockage. Sakuma et al. (2013) numerically studied the effect of the location and depth of a single casing groove on a transonic isolated axial compressor rotor. The axial location of the groove was varied over the tip. The best groove in terms of SMI was found when the deep groove was located at 20% of $c_{ax,t}$ aft of the tip leading edge. As compared with other groove axial locations, the groove at this location causes a large reduction of the tip leakage flow momentum. The reduction of the leakage momentum caused a deflection of the TLV trajectory and also resulted in shifting the location of the blockage region. Ross et al. (2017) tested seven casing groove configurations on the same transonic compressor as found in Chen et al. (2013). A linear relationship between SMI and the casing groove location was found by performing an analysis of the tip region smooth casing axial momentum flux density. The individual SMI produced by each groove was found to be additive when combined.

For low-speed subsonic compressors, circumferential grooves have also shown promising results in terms of SMI. Shabbir and Adamczyk (2005) performed a numerical study on a multi-stage low speed axial compressor. Multiple equidistant circumferential grooves were located on the casing around the first rotor. It was shown that removing the last groove from this multi-groove configuration does not affect the SMI. An axial momentum balance analysis shows that the SMI is caused by the radial transport of axial momentum across the groove. Unlike for a smooth casing, casing grooves provide an alternative path for the blocked flow to be transported radially. In the axial momentum balance equation, this provides a positive term that helps to balance the axial pressure force and hence delay the onset of stall. The downstream blockage is also shown to be reduced due to the introduction of the casing grooves. Houghton and Day (2011) performed experiments and numerical simulations to find the best possible circumferential casing groove design. First, a single circumferential groove is varied axially across the rotor tip. The best SMI was obtained when the groove is located at 10% and 50% of the tip axial chord aft of the tip leading edge. The efficiency penalty due the groove, however, was found to be negligible when it was located about the mid-chord. From this analysis, the best case for a single

circumferential groove is determined to be at the mid-chord. Secondly, additional grooves were placed aft of the previously determined single groove to investigate the effect of multiple casing grooves on the SMI and efficiency penalty. Increasing the groove count to three results in a drop of SMI and also increase in efficiency penalty. Experimental testing by Li et al. (2014) also show a similar trend as those obtained in Houghton and Day (2011) in terms of the relationship between SMI and groove axial location. The above authors show that there exist two peaks of the SMI when the groove is varied axially. The two peaks are located near the leading edge and at about mid-chord. However, the highest SMI is obtained when the groove is located about the mid-chord as compared to the near the leading edge.

Based on the literature review of studies related to circumferential casing groove design, several observations can be made as the following:

1. The SMI due to the grooves can be linked to the reduction of near casing blockage. This is finding is consistent for both low-speed and high-speed compressors.
2. There is a discrepancy related to best groove design in terms of location, size and number of grooves. This is partly because different compressors have distinctive blockage features that makes it difficult to expect any similarity between the findings made by the authors. For instance, at high-speed conditions, the presence of the passage shock adds another aerodynamic feature at the tip region such as the shock-TLV interaction that is not present in low-speed subsonic conditions. If the comparison is made at the same speed conditions; for instance, at low-speed conditions, the discrepancy can be expected from the compressor or blade design itself. The tip gap height, solidity, diffusion factor and loading coefficient are among the design factors that may influence the blockage characteristic of a compressor. Therefore, it is difficult to find a circumferential groove design that is a 'one-size-fits-all' to any compressor. This resorts to performing a design optimisation to obtain a circumferential groove design that can be judged to be optimal for a particular compressor.

2.5.1 Optimised casing groove design

There has been a number of studies related to design optimisation of circumferential grooves in the past. Kim et al. (2011) performed a multi-objective optimisation study to

a multiple groove configuration on a transonic compressor rotor. The optimal groove width and depth of five equidistantly distributed grooves were found using SMI and efficiency change as the objective functions. Two optimal multiple groove designs (extremum of the Pareto-optimal solution) were chosen for additional verification through RANS simulations. From the performance characteristics, the calculated SMI due to the first optimised multiple casing groove design was 10.78% whereas the second one was 1.204%. On a same transonic compressor rotor, Qin et al. (2013) performed an optimisation study that optimises the width, gap and also height of a multiple groove configuration. The objective functions used is the change in stalling mass flow rate with respect to the smooth casing. The SMI obtained due to the optimised multiple groove configuration is 0.73%. The SMI reported in Qin et al. (2013) is closer to the SMI obtained due to second optimised multiple groove design of Kim et al. (2011).

Both of the above optimisation studies reported improved stall margin when assessed numerically. However, there are two limitations when the SMI or stalling mass flow rate is used as one of the objective functions for the optimisation study. Firstly, the SMI or stalling mass flow rate of a groove design can only be known from a compressor characteristic. This is to say that for any groove design variation, the full characteristic is required to evaluate the SMI. Constructing the characteristic requires several numerical simulations at different operating points until the stalling mass flow rate is found. This is computationally expensive even with the advent of today's high-performance computers. The attempt of addressing this current problem is shown in Goinis et al. (2013) where the stalling mass flow rate is automatically determined using a PID controller algorithm. Secondly, optimising for SMI can be viewed as a 'black-box' optimisation approach. In a 'black-box' optimisation approach, the optimiser algorithm has no input of the casing groove internal workings. The algorithm decides the optimum casing groove design (output) from the input SMI of each groove design variation. Therefore, it is difficult to explicitly explain the physical significance of the output with respect to other design considerations. This poses a question whether to trust the output of the algorithm, since the physics of optimum groove design cannot be directly linked to SMI.

2.6 Research objectives

Continuing from the preceding discussion, the primary objective of this thesis is therefore to address the second part of the problem in relation to a 'black-box' optimisation approach. In this thesis, a method for developing a physics-based approach for optimising

a single circumferential groove is presented. Although many authors talk about the link between blockage and SMI, there has been hardly any attempt to do this quantitatively. Therefore, in this study, a blockage quantification parameter is defined to quantify blockage in an effort to further understand the physics of stall and SMI. This blockage parameter is then used as one of the objective functions for achieving SMI rather than using SMI itself as the objective function. Additionally, the use of this blockage-based parameter in a way reduces the computational cost required for constructing the optimisation algorithm. This is partly because, the performance of each groove variation can be directly evaluated from a single operating condition near-stall which does not require the construction of a full compressor characteristic each time a candidate geometry is assessed during the optimisation process itself.

Chapter 3

Computational Method

3.1 Overview

This chapter describes the flow modelling process which is predominantly used in this thesis. First, the governing equations, turbulence modelling and numerical discretisation method are presented. This is followed by a description of the numerical domain and the grid. The boundary conditions used for the simulations are presented next. The chapter ends with a description of the convergence criteria that is employed in the present study. The convergence criteria need to enable a consistent way for identifying the stalling mass flow (or flow coefficient) for the various numerical test cases.

3.2 Governing equations

The physical motion of the fluid is governed by the Navier-Stokes (NS) equations. The NS equations are based on the principle of mass, momentum and energy conservation. The generic form of the three dimensional and compressible NS equations are shown in Equations 3.1 to 3.4.

$$\frac{\partial \rho}{\partial t} + \nabla \cdot \left(\rho \vec{V}\right) = 0 \tag{3.1}$$

$$\frac{\partial \rho \vec{V}}{\partial t} + \nabla \cdot \left(\rho \vec{V} \times \vec{V}\right) = -\nabla \mathrm{P} + \nabla \cdot \vec{\tau} + \vec{F} \tag{3.2}$$

Equation 3.1 is the mass continuity equation which governs the mass conservation law. Variable ρ is the fluid density and $\vec{V}$ is the flow velocity. The momentum conservation law is represented by Equation 3.2. The left-hand side (LHS) of Equation 3.2 is the temporal and convective terms of the flow which is balanced by the sum of the external forces exerted on the fluid. ∇P and $\vec{F}$ are the pressure gradient and the sum of body forces across

a defined control volume, respectively. The term $\nabla \cdot \vec{\tau}$ is the viscous stress tensor that can be related to the strain rate as shown in Equation 3.3

$$\tau = \mu(\nabla\vec{V} + (\nabla\vec{V})^T) - \lambda\delta\nabla \cdot \vec{V} \tag{3.3}$$

Variable μ on the first term at the right-hand side (RHS) of Equation 3.3 is the dynamic viscosity of the fluid and can be found from Sutherland's formula. λ is the bulk viscosity coefficient and is set to $-\frac{2}{3}\mu$ according to Stokes's hypothesis. δ is the Kronecker delta function which returns a value of 1 for normal vectors. The conservation of energy can be expressed in the form shown in Equation 3.4.

$$\frac{\partial \rho h_0}{\partial t} - \frac{\partial P}{\partial t} + \nabla \cdot \left(\rho\vec{V}h_0\right) = \nabla \cdot (k\nabla \mathrm{T}) + \nabla \cdot \left(\vec{V} \cdot \vec{\tau}\right) + \vec{V} \cdot \vec{F} + \vec{S} \tag{3.4}$$

Variable h_0 on the LHS of Equation 3.4 is the total enthalpy which can be calculated from the static enthalpy, h, and $\overrightarrow{V}$. The first term on the RHS of equation 3.4 can be associated with the heat diffusion of fluid. k is thermal diffusivity coefficient and ∇T is the temperature gradient across the control volume. The third term represents the internal heating on the fluid due to viscous effects whilst $\vec{S}$ represents the external heating and can be omitted for adiabatic cases.

3.3 Turbulence model

For a turbulent flow, the NS equations are transformed into Reynolds Averaged Navier-Stokes (RANS) equations through the Reynolds decomposition method. The Reynolds decomposition method is an averaging method meant for removing the fluctuating quantities of the flow so that a time-averaged description of the flow can be obtained. This method adds a non-linear Reynolds stress term to the momentum equation. For this reason, the RANS equations are considered underdetermined as there are more unknowns than the available number of equations. This is otherwise known as the turbulence closure problem when solving RANS equations. Closure of the RANS equations requires modelling of the non-linear Reynolds stress term. The Reynolds stress can be modelled by drawing a relationship between the mean velocity gradients and the Eddy viscosity, μ_t, based on the Boussinesq hypothesis. In this study, μ_t of the flow is calculated from a standard two equation k-ε turbulence model (Launder & Spalding, 1974). This model relates the

turbulent viscosity μ_t to the turbulence kinetic energy, k, and the turbulence energy dissipation, ε as shown in Equation 3.5.

$$\mu_t = C_\mu \rho \frac{k}{\epsilon} \tag{3.5}$$

Here, C_μ and ρ are the correction coefficient and fluid density, respectively. Although not shown here, the transport equations of k and ϵ also consist of some adjustable coefficients, $\sigma_k, \sigma_\epsilon, C_{1\epsilon,}$ and $C_{2\epsilon}$ that are empirical values. Table 3-1 lists the default values of the coefficients used in this thesis.

Table 3-1 Correction coefficients of the standard $k-\epsilon$ model

C_μ	σ_k	σ_ϵ	$C_{1\epsilon,}$	$C_{2\epsilon}$
0.09	1.0	1.3	1.44	1.92

The standard k-ε model is only valid for fully turbulent flows so a wall function is required for solving the equations in the laminar sublayer region up until the buffer region. The buffer region is the region between the laminar sublayer region and the law of the wall region. The buffer region is located at non-dimensional grid spacing, y^+ = 11.225. A scalable wall function is used so that the k-ε model can be applied to if the y^+ is less than 11.225 (ANSYS CFX 17.1 Documentation). The selection of k-ε model is discussed later in Chapter 5.

3.4 Numerical discretisation method

The governing equations are solved using commercial code ANSYS CFX 17.1. The code uses a finite volume method on an unstructured grid system for obtaining the solutions. The convective and diffusive terms across the control volume are converted to fluxes according to the divergence theorem. Since the solution variables are stored at the cell-centred grid nodes, φ_{cell}, flux values at the cell volume faces, φ_f, are evaluated using a high-resolution upwind scheme. The high-resolution upwind scheme as shown in Equation 3.6 is a blend between the first and second order upwind scheme.

$$\varphi_f = \varphi_{cell} + \beta \nabla \varphi \cdot \vec{r} \tag{3.6}$$

Quantity β is the blending factor which has a value between 0 to 1. A value of $\beta = 0$ results in a first-order upwind scheme whilst $\beta = 1$ results in a second order accurate scheme. The blending is performed to address the shortcomings of the first and second-order upwind schemes (ANSYS CFX 17.1 Documentation). Although a second order upwind scheme is more accurate than a first-order scheme, the second-order scheme has problems related to unboundedness for regions with a rapid solution variation. In order to avoid the unboundedness problem, β is kept closer to 1 thus resulting in a quasi-second order accurate scheme. $\nabla\varphi$ and $\vec{r}$ are the upstream cell face value gradient and the displacement vector from the upwind cell-centered nodal location to the evaluated cell face location, respectively.

The discretised system of linear equations are solved iteratively using an Incomplete Lower Upper (ILU) factorization technique. The convergence rate of the iterative ILU technique is enhanced using an Algebraic Multigrid (AMG) method (ANSYS CFX 17.1 Documentation). For the ILU scheme, the error in the order of the size of the domain appears as low frequency error (Moukalled et al. 2015). Low frequency error takes more iterations to be removed than high frequency error. This causes a slower convergence rate. The AMG method enhances the convergence rate by solving the system of equations on a hierarchy of virtual grid with different sizes. The convergence rate is enhanced by transforming the low frequency error to a high frequency error by solving the solution on a relatively coarser grid than the original grid size.

3.5 Description of geometry

3.5.1 Rotor 37

The numerical study is performed on an isolated axial transonic compressor rotor, NASA Rotor 37. The aerodynamic properties of Rotor 37 are representative of an inlet rotor of an 8-stage advance core compressor with a 20:1 pressure ratio (Suder, 1996). The Rotor 37 test compressor was originally designed for NASA's research program to study the flow features of a single blade-row without any interactions arising from the upstream vane or downstream stator. The availability of extensive measurement data from the experimental research program made Rotor 37 ideal for validating in-house CFD codes as

shown by Ameri (2009) and Li (2014). Rotor 37 was also chosen as the numerical testbed for a 'blind' test to compare the performance of multiple CFD codes (Denton, 1997). Rotor 37 is known to exhibit a spike-type stall since the stall initiation mechanism is associated with the near casing flow. Together with the availability of experimental data for validation, this makes it an ideal test case for numerically testing casing treatment concepts using Rotor 37 (Kim et al., 2011; Qin et al., 2013; Sakuma et al., 2013).

Table 3-2 Aerodynamic design parameters of Rotor 37 and the low-speed axial compressor (LSAC)

	Rotor 37	LSAC
Blade count	36	27
Aspect ratio	1.19	1.23
Tip solidity	1.3	1.34
Total pressure ratio	2.106	1.015
Rotational speed	17188.7 rpm	3000 rpm
Tip speed	454.14 m/s	71.94 m/s
Tip clearance	0.356 mm	1 mm
Tip radius at LE	253.7 mm	229 mm
Hub to tip ratio at LE	0.7	0.7
Stage loading coefficient	0.37	0.37

The second column of Table 3-2 summarises the aerodynamic design specifications of Rotor 37. The blade row has 36 multiple circular arc blades. The tip solidity has a value of 1.29. The design speed is 17188.7 rpm which results in a tip speed of 454.14 m/s. The design pressure ratio of 2.106 corresponds to a corrected mass flow rate of 20.19 kg/s. The choking mass flow rate found numerically by Suder (1996) is 20.93 kg/s. Further details regarding Rotor 37 test case geometry can be found from Reid and Moore (1978). The numerical domain of Rotor 37 as shown in Figure 3-1 consist of a single blade passage. A single blade passage simulation is thought to be appropriate since all the simulations are conducted for operating points in the stability limit where periodic flow assumptions is reasonably valid. Furthermore, Rotor 37 is simulated in isolation (no upstream or downstream blade rows) so that the flow can be considered as steady in the relative frame of reference (Denton, 1997). The fillet at hub is removed for simplifying the meshing

process. The hub and shroud are divided into sections to mimic the relative motion between stationary and rotating walls. In this thesis work, the Rotor 37 geometry is used to study the stall development process within a transonic compressor rotor environment and to numerically design an optimised circumferential groove that improves the stall margin of the rotor. Discussion of the numerical study into the Rotor 37 performance with a smooth casing and for a casing with an optimised groove can be found in Chapter 4 and Chapter 5 respectively.

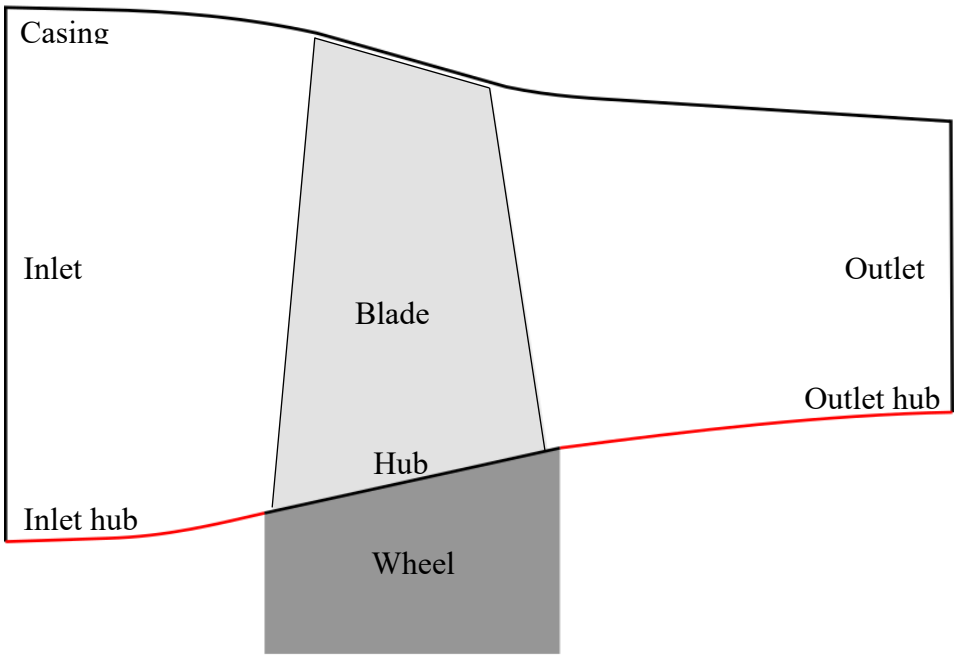

Figure 3-1 A meridional depiction of the Rotor 37 domain (not to scale).

3.5.2 Low-Speed Axial Compressor (LSAC)

The LSAC as shown in Figure 3-2 is designed to test the effectiveness of the groove optimisation methodology in a low speed environment that is devoid of compressibility effects. The LSAC is designed to mimic the stalling behaviour of Rotor 37 at part-speed conditions, where the passage shock is absent using an inverse-design method. Table 3-2 presents the aerodynamic properties of the LSAC. These values are obtained through high-to-low speed aerodynamic scaling exercise. The details regarding the design methodology and specifications of the LSAC is explained later in Chapter 6.

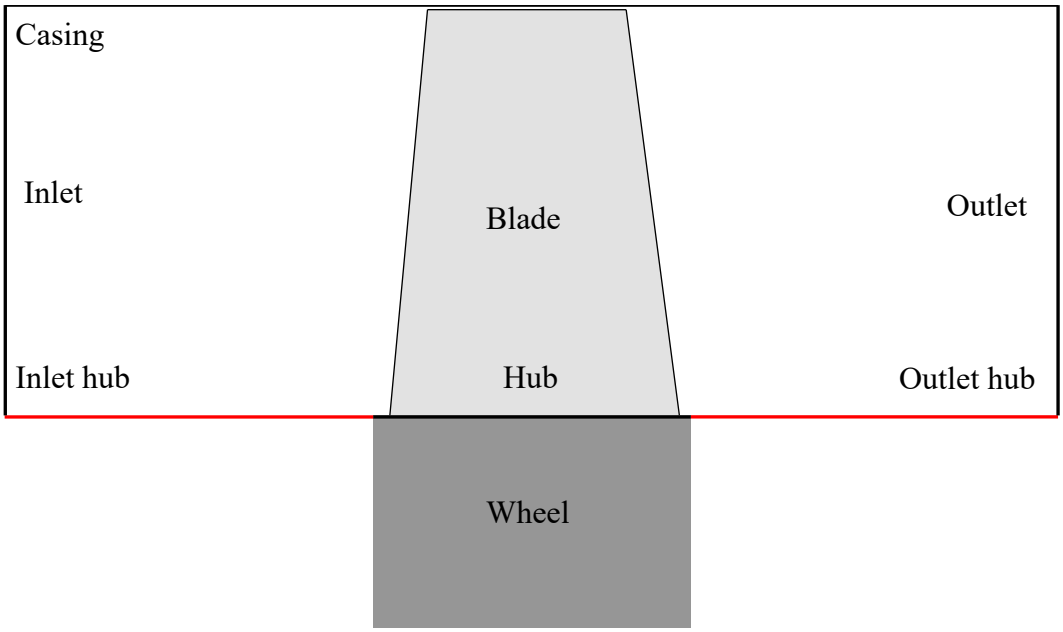

Figure 3-2 Meridional cut-view of the LSAC (not to scale).

3.6 Mesh generation

3.6.1 Rotor 37

The numerical domain of Rotor 37 is imported into ANSYS meshing package ICEM 17.1 for generating the grid. The unstructured grid for the numerical domain is generated using a combination of hexahedral (H) and O-grids as shown in Figure 3-3. The total number of grids generated is about 4 million. The H-grid that covers the entire computation domain has 248 × 86 × 148 grid points in the axial, pitch and radial direction, respectively. As for the rotor blade, there are 125 streamwise grid points along the blade surfaces and 115 radial grid points from hub to tip. The tip gap has 30 grid points radially. An O-grid is generated along the periphery of the blade to allow grid refinements closer to the blade surface. The O-grid has 35 grid points along the direction normal to blade surface. Grid refinements are also performed near the endwalls to resolve the turbulent boundary layer. The y^+ near solid walls are less than 2.

The grid resolution is chosen based on the outcome of a grid independence study. This grid independent study is performed at the near design operating point using three different grid densities. The sizes of the three grids and a comparison of the resulting numerical mass flow rates are shown in Table 3-3. The difference between the inlet mass flow rate value for Grid B and C with respect to Grid A are 0.48% and 0.47%, respectively. The

effect of grid density on the blade surface static pressure distribution, c_p, is shown in Figure 3-4. The c_p is calculated using Equation 3.7.

$$c_p = \frac{P - \bar{\bar{P}}_1}{\bar{\bar{P}}_{01} - \bar{\bar{P}}_1} \tag{3.7}$$

Here, P is the blade static pressure extracted at 98% span. $\bar{\bar{P}}_{01}$ and $\bar{\bar{P}}_1$ are the mass-averaged inlet total pressure and area-averaged inlet static-pressure, respectively. The effect of grid density on c_p at 98% span is small even when the number of grids in the tip gap is increased by a factor of 2 from Grid A to Grid C. Therefore, the Grid B is chosen for the all the Rotor 37 simulations as a compromise between simulation run time and the accuracy of the simulation. The grid resolution chosen is also benchmarked against other steady RANS numerical studies in the literature using Rotor 37. For comparison, the number of grid points used by Hah and Loellbach (1999) and Sakuma et al. (2013) was 0.5 million and 1.5 million grid points, respectively.

Table 3-3 Grids used for the grid independence study and comparison of the inlet mass flow rate for Rotor 37

Grid	Total grid	Grid inside tip gap	Inlet mass flow rate [kg/s]	Change [%]
Grid A	2 million	20	20.508	0.00
Grid B	4 million	30	20.607	0.48
Grid C	6 million	45	20.604	0.47

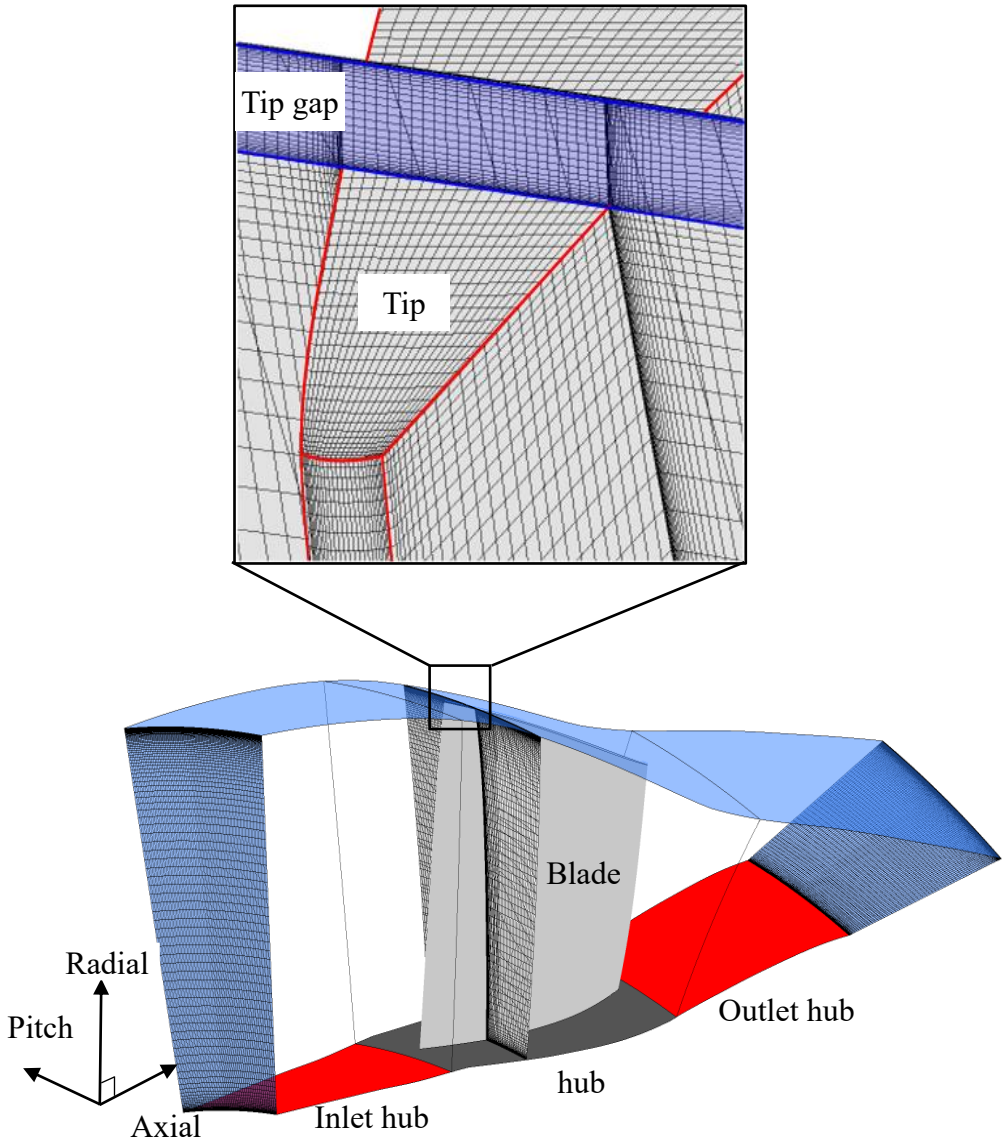

Figure 3-3 ICEM generated grid (Grid B) for the Rotor 37 calculations

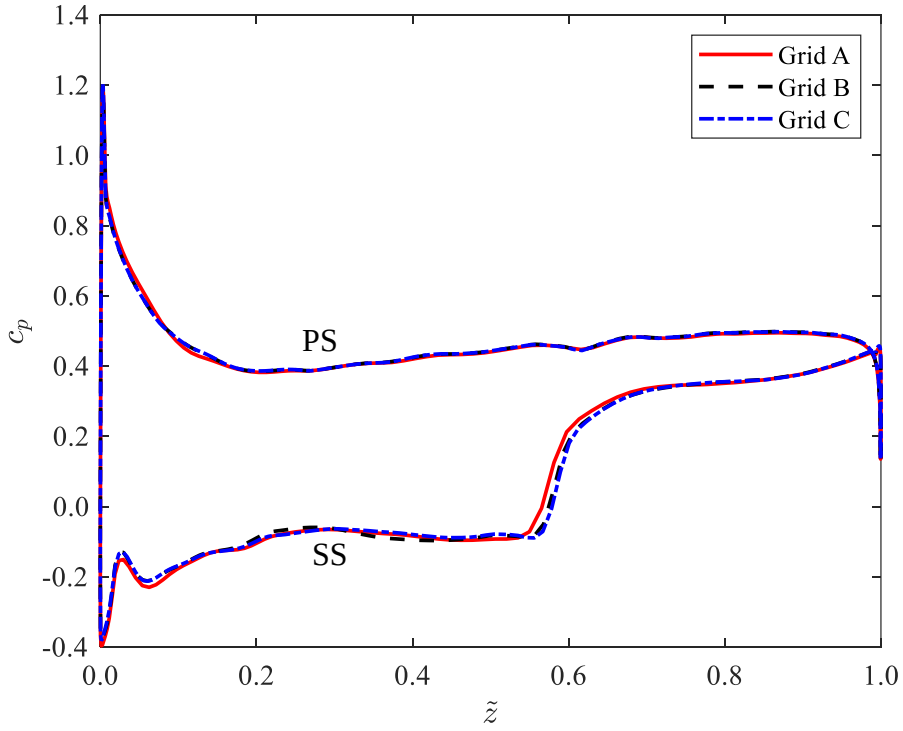

Figure 3-4 Comparison of the blade surface static pressure distribution for Grid A, B and C for Rotor 37

3.6.2 LSAC

The grids for the LSAC domain are generated using ANSYS Turbogrid 17.1. First, 2-D blade profiles at seven span heights are imported together with the hub and casing profiles. The grids are generated automatically by specifying the target grid node count and y^+ requirements near the wall. As shown in Table 3-4, three grid sizes are generated based on the target grid node count with the maximum y^+ requirement is set to 2. In addition, the number of radial grid point in the tip gap is increased as the number of total grid nodes are increased. The change of the inlet mass flow rate between Grid A and B is 0.32% whereas it is 0.36% between Grid A and Grid C. The c_p calculated at 98%, shown in Figure 3-5, also show negligible changes except for at the leading edge near the pressure side. Therefore, as a compromise between accuracy and computational resources, Grid B is selected for the LSAC numerical domain as shown in Figure 3-6.

Table 3-4 Grids used for the grid independence study and comparison of the inlet mass flow rate for the LSAC

Grid	Total grid node count	Grid inside tip gap	Inlet mass flow rate [kg/s]	Change [%]
Grid A	1.7 million	20	3.412	0.00
Grid B	3.2 million	30	3.423	0.32
Grid C	4.5 million	40	3.424	0.36

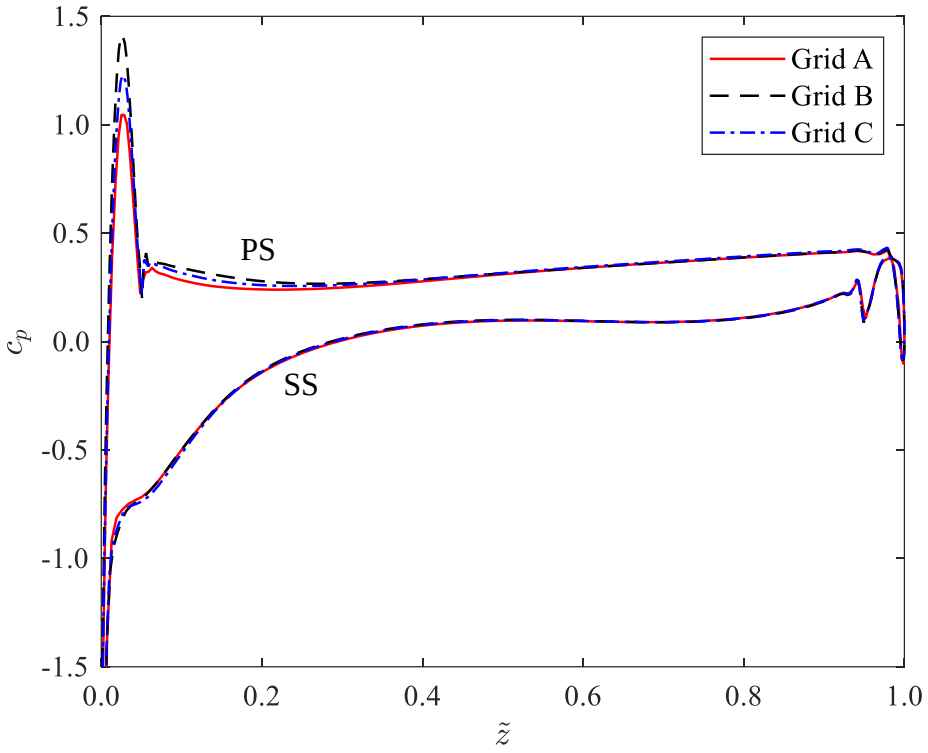

Figure 3-5 Comparison of the blade surface static pressure distribution for Grid A, B and C for LSAC

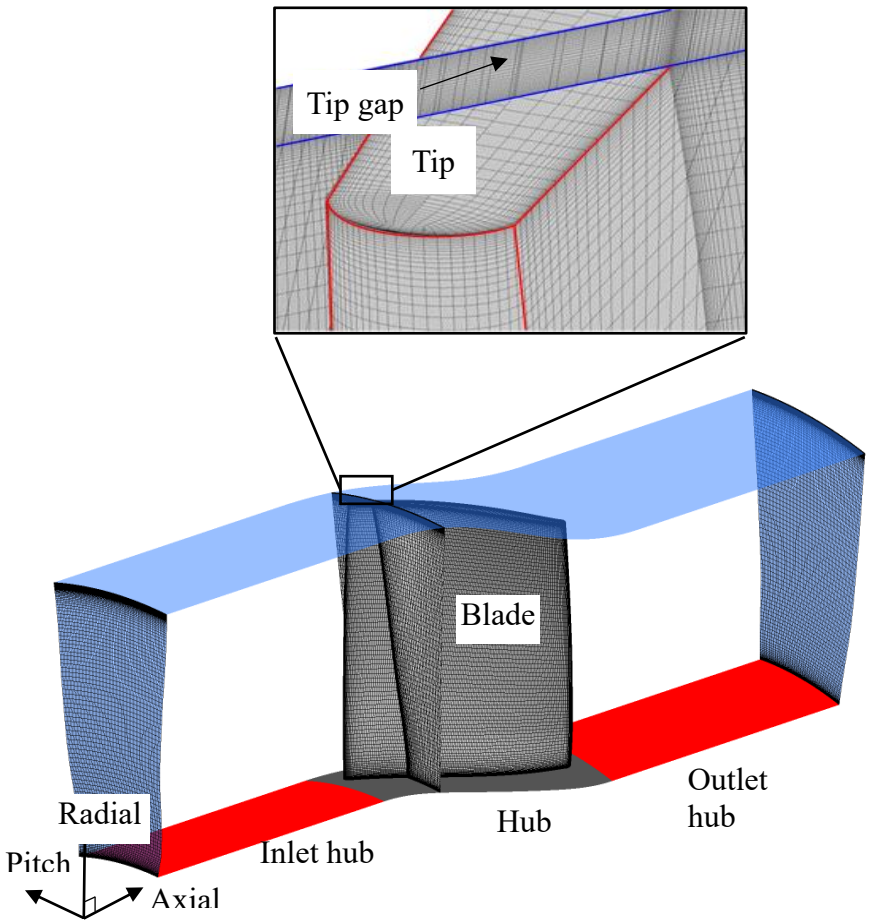

Figure 3-6 Turbogrid generated grid (Grid B) for the LSAC calculations

3.7 Boundary conditions for Rotor 37 and LSAC

3.7.1 Rotor 37

A total pressure and total temperature profile are prescribed at the inlet as shown in Figure 3-7. The inlet profile is obtained from the measurements as reported in Dunham (1998). The inlet turbulence intensity is 1% with an eddy viscosity ratio of 1. At the outlet, a simple radial equilibrium static pressure is assumed. Rotor 37 is 'throttled' by gradually increasing the outlet hub static pressure ratio, P_{exit}/P_{atm} from the choking point. The choking point for Rotor 37 is determined iteratively and corresponds to a value of $P_{exit}/P_{atm} = 1.05$. The hub static increment is 0.5% of P_{atm} and gradually reduced to find the numerical stall operating point. Numerical stall is determined iteratively using a 'bisection method' until the increment size of ΔP_{exit} reaches 5 Pa. The last stable operating point is the last solution that satisfies the convergence criteria. The entire domain is solved in the rotating frame hence stationary walls are set to counter-rotating. All walls are treated to be no slip, impermeable and adiabatic.

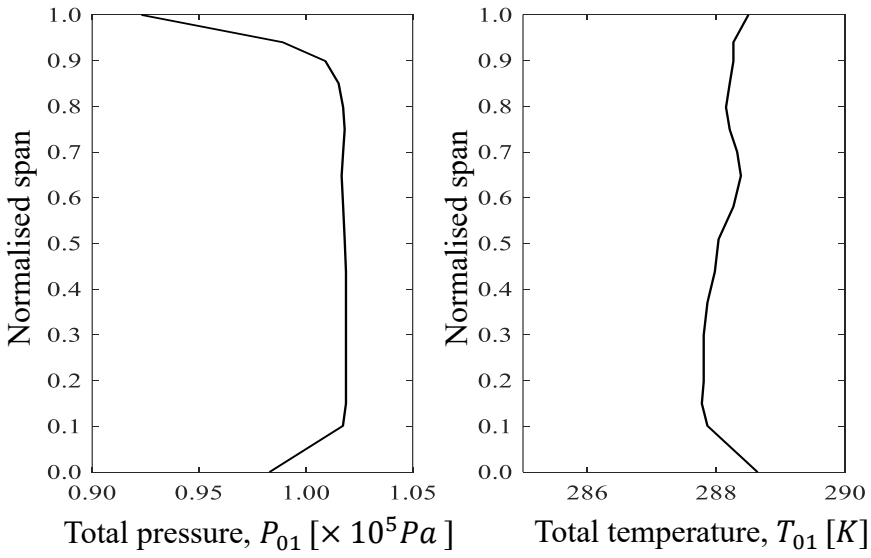

Figure 3-7 Total pressure and total temperature profile prescribed at inlet of Rotor 37

3.7.2 LSAC

The selection of the inlet conditions used for the LSAC simulations is guided by those used for the Rotor 37 simulations. A total pressure and total temperature velocity profile was used as shown in Figure 3-8. The inlet profiles are artificially generated based on the inlet conditions of Rotor 37 shown in Figure 3-7. This is to simulate a similar level of blockage as in the high-speed case. The inlet turbulence intensity is 1% with an eddy viscosity ratio of 1. At the outlet, a simple radial equilibrium static pressure is assumed. The LSAC is 'throttled' by gradually increasing the outlet hub static pressure from a value of $P_{exit,hub} = 101350\ Pa$. The backpressure increment is between a value of 50-100 Pa and is gradually reduced to find the numerical stall operating point. As in the case of Rotor 37 test cases, the numerical stall is determined iteratively using a 'bisection method' until the increment size of ΔP_{exit} reaches 5 Pa. The last stable operating point is the last solution that satisfies the convergence criteria. The entire domain is solved in the rotating frame hence stationary walls are set as counter-rotating. All walls are treated to be non-slip, impermeable and adiabatic.

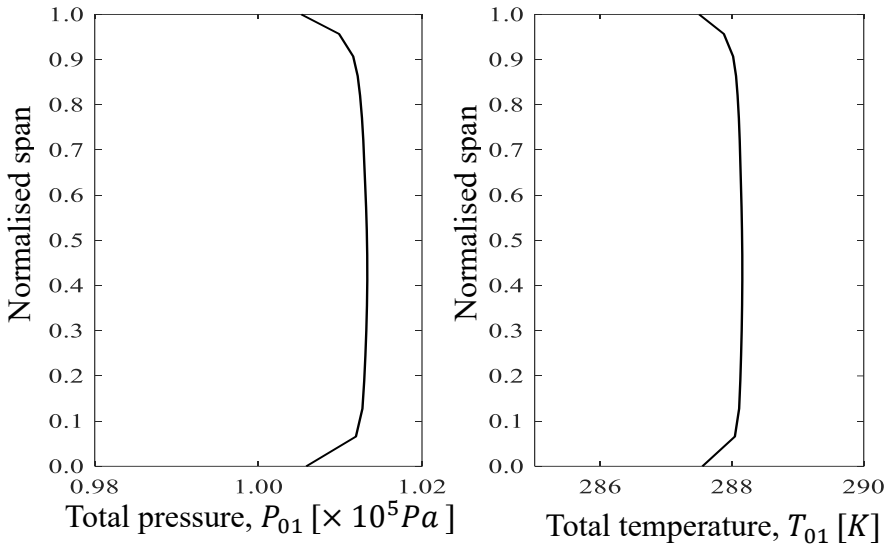

Figure 3-8 Total pressure and total temperature profile prescribed at inlet of LSAC

3.8 Convergence criteria

In the numerical study described in this thesis, a steady RANS code is used to predict the pressure rise characteristics of the isolated compressor rotor with smooth and grooved casing geometry conditions. The physical flow conditions could largely be considered 'steady' over much of this characteristic line. However, for off-design conditions near stall it is less clear if such an assumption is strictly true (Vekinis & Longley, 2018). The approach taken in this thesis is that until stall has occurred the flow within the rotor blade passage could be treated as steady and periodic. The low mass flow condition where the code fails to converge is treated as the onset of 'numerical' stall. It is therefore important that the criteria of convergence used to compare the stalling mass flow (or flow coefficient) across the test cases is reasonably robust and consistent. A convergence criterion based on merely monitoring the residuals may not be sufficient. Therefore, a Coefficient of Variation (CoV) based convergence criteria is employed. The CoV of a monitoring parameter is defined as the ratio between the standard deviation and the mean value of the parameter. The CoV is used to measure the fluctuations of the monitored variable. A relatively low CoV means that change in the monitored variable is minimum. The inlet mass flow rate is chosen as the value being monitored. By using a moving average, the CoV of the inlet mass flow rate is updated for each iteration. A steady-state solution is accepted to be 'converged' if the following criteria are met:

1. The calculations are run for a minimum of 2000 iterations using an implicit scheme.
2. The CoV of the inlet mass flow rate value must not exceed 10^{-3} for the last 200 iterations.
3. Residuals for mass, momentum and energy for the last 1000 iterations behave normally (fall below a nominal value of typically 10^{-4}).

Figure 3-9 shows the comparison of the residuals and CoV between a converged and non-converged solution. The mass residuals show a periodic fluctuating trend. For a diverging solution as shown in Figure 3-9), the CoV will overshoot the specified threshold value of 10^{-3} although the mass flow rate residual falls to a relatively low value.

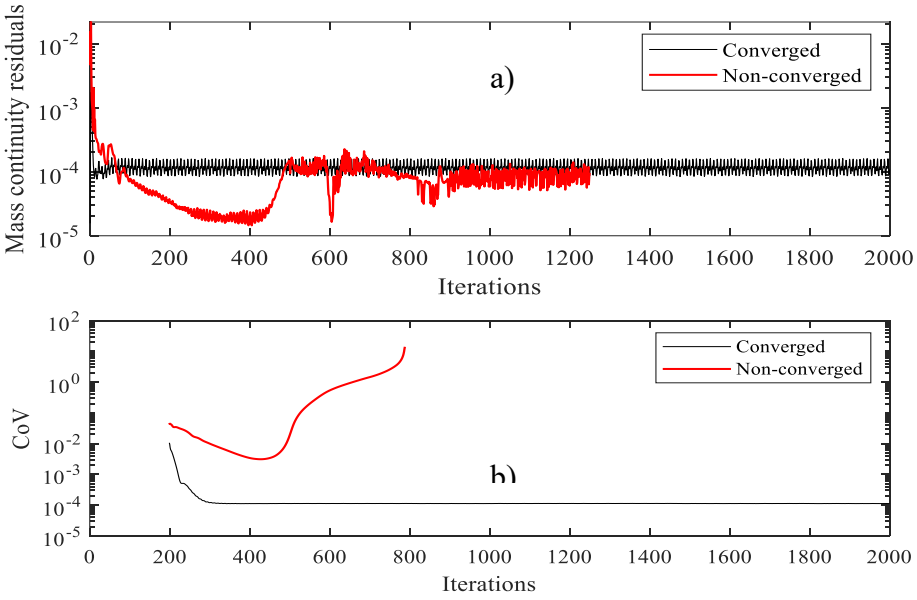

Figure 3-9 Mass residuals and b) CoV history plot for a converged and non-converged case

3.9 Summary

The theoretical aspects of a three-dimensional, compressible and adiabatic RANS simulation are briefly presented in this study. For this study, a $k-\epsilon$ model has been chosen for turbulence closure. A mesh independence study was performed for the Rotor 37 and LSAC numerical domains by comparing the change in the inlet mass flow rate and the near tip blade static pressure distribution for three different mesh sizes. The numerical setup, boundary conditions and convergence criteria are also presented. The coefficient of variation (CoV) of the inlet mass flow rate is used as one of the convergence criteria for steady state simulations.

Chapter 4

Validation and Discussion of Rotor 37 Numerical Simulation Results with Smooth Casing

4.1 Overview

The first part of this chapter aims to validate the numerical simulation of the Rotor 37 test case with a smooth casing against the available experimental data. In addition, the general flow phenomena in a transonic compressor rotor environment is discussed. The second part of this chapter addresses the tip region aerodynamics that has been linked to the onset of rotation stall. In the final part of the chapter, a method of evaluating and quantifying blockage is presented.

4.2 Validation with measured test data and discussion

4.2.1 Performance characteristics

The overall accuracy of the simulation is validated by comparing the pressure ratio and the efficiency performance characteristics of the simulation against the results from the Rotor 37 tests found in Suder (1996) as shown in Figure 4-1. The solid symbols show the experimental result while the open symbols show the simulation result. The total pressure ratio, π, and adiabatic efficiency, η, are calculated using Equation 4-1 and Equation 4-2, respectively.

$$\bar{\bar{\pi}} = \frac{\bar{\bar{P}}_{0out}}{\bar{\bar{P}}_{01}}$$

$$\text{where : } \frac{\bar{\bar{P}}_0}{P_{ref}} = \left[\frac{\sum_{r=1}^{j} \left(\frac{\bar{P}_{0,r}}{P_{ref}} \right)^{\frac{\gamma-1}{\gamma}} \bar{\rho}_r (\bar{V}_z \Delta A_r)}{\sum_{r=1}^{j} \bar{\rho}_r (\bar{V}_z \Delta A_r)} \right]^{\frac{\gamma}{\gamma-1}} \tag{4-1}$$

$$\bar{\bar{\eta}} = \frac{\bar{\bar{\pi}}^{\frac{\gamma-1}{\gamma}} - 1}{\Pi - 1} \text{ where } \Pi = \frac{\bar{\bar{T}}_{0out}}{\bar{\bar{T}}_{01}} \tag{4-2}$$

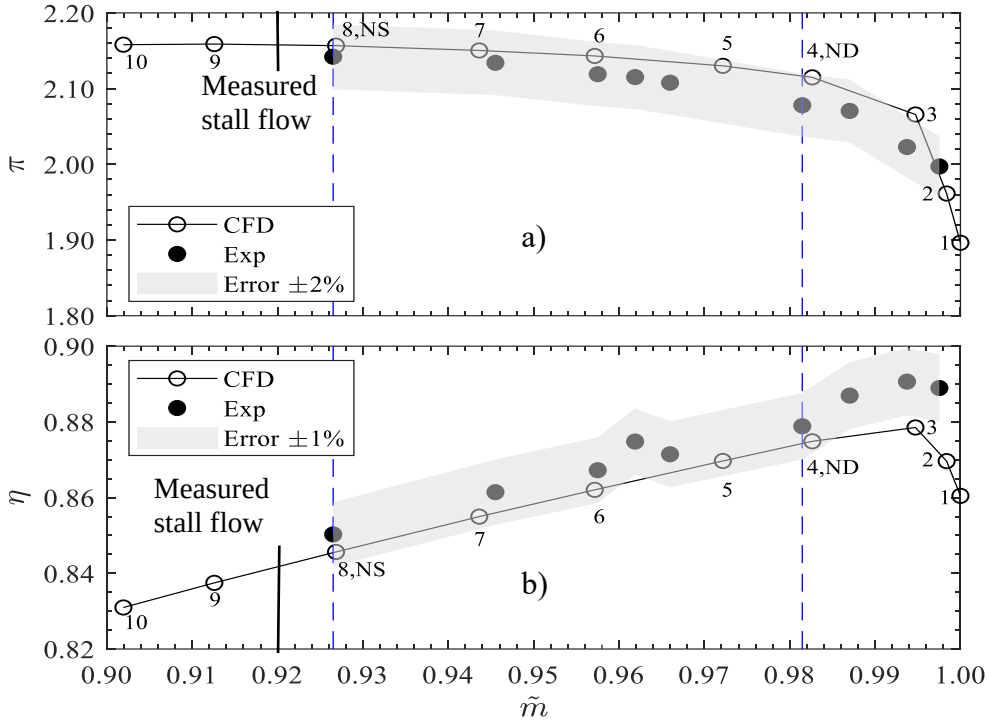

Figure 4-1 Performance characteristics of the simulation compared against the experiment result. a) total pressure ratio, π and b) adiabatic efficiency, η

$\bar{\bar{P}}_{0\text{out}}$ and $\bar{\bar{P}}_{01}$ are obtained by first converting the respective radial distributions of total pressures, $\bar{P}_{0,r}$, into their enthalpy equivalents and then mass averaging across the annulus. Quantities $\bar{\rho}_r$, and $\bar{V}_z$ are the pitch-wise mass average of density and the axial velocity at the corresponding spanwise position, respectively. A_r is the annulus area at the calculated $\bar{\rho}_r$ and $\bar{V}_z$ locations. P_{ref} is the atmospheric pressure and this remains a constant throughout the simulations, unlike in the case of experiments where it may vary with time. Converting the radial distributions of total pressure first, into their enthalpy equivalent is also known as the energy-averaged method. This averaging method is the same method found in Suder (1996). The expression Π in Equation 4-2 is the total temperature ratio calculated from the mass-averaged total temperature at the outlet ($\bar{\bar{T}}_{0out}$) and inlet ($\bar{\bar{T}}_{0in}$) plane. The specific heat ratio of air, γ is taken to be 1.4. The mass flow rate is normalised by the choking point (operating point 1) mass flow rate in order to obtain the normalised mass flow rate, $\tilde{m}$, as shown in the abscissa of Figure 4-1. The numerically obtained mass

flow rate at operating point 1 is 20.94 kg/s which is close to what has been found in Suder (1996). In the experiment, it was reported that choking did not happen in the rotor but occurred in the facility diffuser. The maximum mass flow rate at which the diffuser is choking was reported to be 20.9 kg/s. The calculated π and η show a good overall agreement with the experiments where the error of most of the selected simulated operating points as shown in Table 4-1 are of the order of $\pm 2\%$ and $\pm 1\%$, respectively.

Table 4-1 Comparison of the numerically obtained π and η quantities with respect to the measurements for selected operating points.

Operating point	π		ϵ [%]	η [%]		ϵ [%]
	Exp	CFD		Exp	CFD	
3	2.02	2.07	2.48	89.06	87.85	1.21
4 (ND)	2.08	2.12	1.92	87.88	87.49	0.39
6	2.12	2.14	0.94	86.72	86.20	0.52
8 (NS)	2.14	2.16	0.93	85.03	84.56	0.47

As for the stall point, the simulation under-predicted the stalling mass flow rate of the experiment. The measured stall point occurred at about $\widetilde{m} = 0.92$ whereas the numerical stall point occurred at about $\widetilde{m} = 0.90$. The discrepancy between numerical stall point and measured stall point can be attributed to the weakness of RANS modelling in predicting stall. The predictive performance of RANS simulations is sensitive to several factors such as the mesh size, turbulence modelling and also the imposition of a steady state flow condition. As discussed by Cornelius et al. (2013), the sensitivity of the simulations due to the above-mentioned factors are more apparent as the compressor approaches stall. For instance, at design speed, the numerical domain with a relatively finer mesh stalled at a 2.5% lower mass flow rate than the domain with a medium density mesh. Steady-state and periodic flow assumptions at off-design conditions when the compressor is approaching stall may also contribute to the under-prediction of the stalling mass flow rate of the experiment. This is mainly because of the unsteadiness that is associated with flow separation and the tip leakage flow at near stall conditions. Thus, while acknowledging the limitations of steady RANS modelling in predicting stall, the approach taken in this thesis is to use steady simulations to capture the flow as measured and presented by Suder (1996) with the least error possible. Some of this has already been discussed in Chapter 3 where a mesh sensitivity analysis is shown and also the introduction of a convergence

criteria to consistently define the numerical stall point. Other aspects such as the turbulence model selection will be discussed further as the results of the simulation are compared against the measured data. Nevertheless, the discrepancy in predicting the exact stall point mass flow due may be less relevant since the two major aims of the study are; first, to understand the physical mechanisms that lead to stall and second, to compare the stalling mass flows of selected casing geometries in relation to one another rather than in an absolute sense.

4.2.2 Outlet radial distribution

Figure 4-2 shows the outlet radial distribution of $\bar{\pi}$ and $\bar{\eta}$ for near-design (ND) and near-stall (NS) operating point ND and ND are annotated as operating points 4 and 8, respectively in Figure 4-1. The plot is obtained by mass-averaging π and η across the rotor pitch at the domain outlet. At the hub, a pressure deficit region can be seen for both point 4 and 8. The flow trend at hub region is suspected to be caused by a hub corner separation. Initially, it was thought that the selection of turbulence model affected the ability of the code to predict the hub corner separation. This is due to the fact that in the blind test result (Denton, 1997), only one code managed to correctly predict the hub pressure trend. It was suggested that the code might have modelled the correct boundary layer condition for a hub corner separation. However, numerical studies by Shabbir et al. (1997) show that the selection of turbulence modelling is not the reason why CFD codes are not able to predict the hub corner separation. The above authors found that the hub pressure deficit can only be predicted when the hub leakage flow is introduced regardless of turbulence model chosen. It was found that the hub corner separation is caused by accumulation of hub leakage flow on the blade suction side of the blade that provoked a flow separation. Unfortunately, experimental confirmation on Rotor 37 test rig was not possible due the fact that the blades were damaged. The above authors, however, ran an experiment on a similar test rig to confirm the effect of hub leakage on the hub pressure deficit.

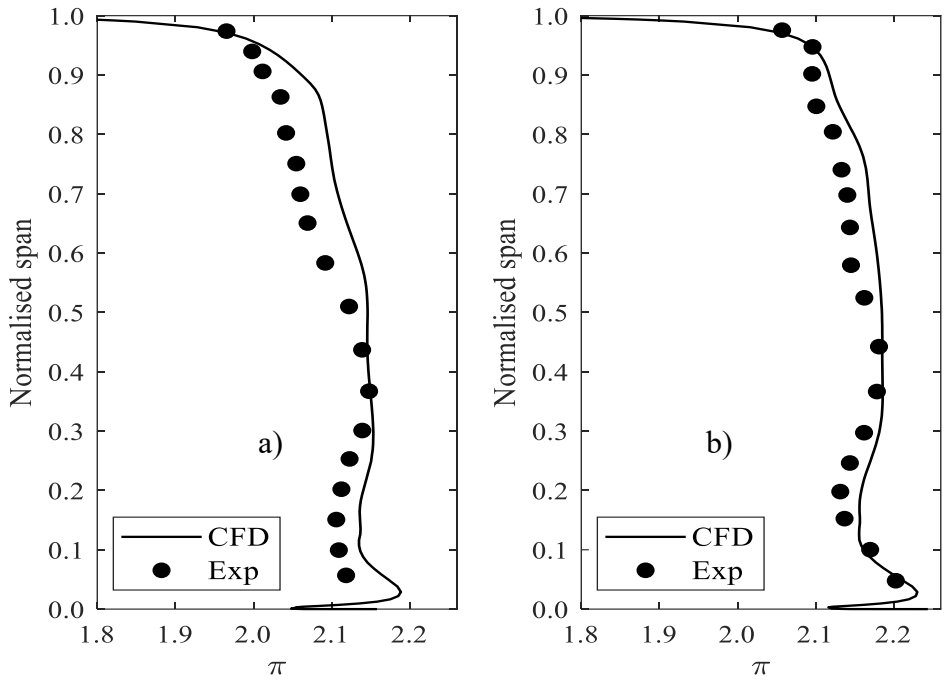

Figure 4-2 Outlet radial distribution of π of the simulation compared against the experiment result at a) ND (operating point 4) and b) NS (operating point 8).

Due to the absence of the test data, modelling the hub leakage would not be a straightforward process as shown by Seshadri et al. (2014). The leakage mass flow, radial angle and whirl velocity are among the properties that are unknown to re-create the same effect of the leakage on the hub pressure deficit. Therefore, another method is attempted to mimic the effect of hub leakage in the current simulation. One of the ways to re-create the hub corner separation without the existence of hub leakage is through the removal of the inlet boundary layer skew.

The inlet boundary layer skew is the effect of relative motion between adjacent endwalls. As the endwall flow from the inlet stationary duct moves into the rotating rotor hub, a pitch-wise velocity component is introduced. The pitch-wise velocity in the relative frame varies from zero at the wall until it reaches the freestream velocity outside the boundary layer. This creates the 'skew' effect on the shape of the inlet boundary layer velocity profile if viewed together with the axial velocity profile. For compressors, the inlet boundary layer skew is found to have an effect on the development of the hub corner separation (Lei et al., 2008). The inlet boundary layer skew creates additional turning to the flow that reduces the strength of the cross-flow. The cross-flow is the transport of flow towards

the blade suction side due to the pitch-wise pressure gradient. With less flow transported towards the blade suction side, there is a less chance for a hub corner separation.

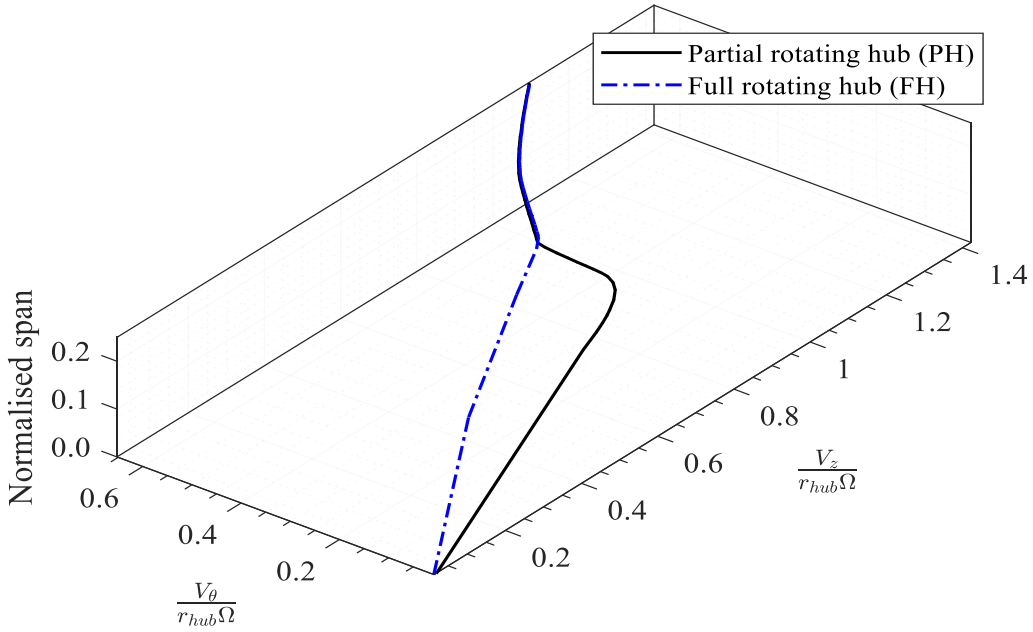

Figure 4-3 The effect of relative motion on the shape of the hub inlet boundary layer at operating point 4 (ND)

In order to remove the of inlet boundary layer skew, another case is simulated where the hub of the inlet and outlet stationary duct (Figure 3-1) are set to rotating. This case is known as a full rotating hub (FH). The other case which represents the true condition of the experiment with no gap between the rotor wheel disk and stationary duct is abbreviated as partial rotating hub (PH). Figure 4-3 shows the comparison of the velocity profiles near the hub region for cases PH and FH at ND conditions. The velocity data is extracted at an axial plane located about 2.5% of the hub axial chord, $c_{ax,h}$, upstream of the hub leading edge. The axial velocity, V_z, and the relative pitch-wise velocity, $V_{\theta,rel}$, are normalised by the blade speed at the hub. Only the bottom 20% span data is shown for clarity. As explained previously, the shape of the velocity profile for PH is 'skewed' due to the relative motion between the stationary inlet hub and rotating rotor hub. This is not the case when no relative motion between the inlet and rotor hub is present.

Flow separation results in pressure loss due to the formation of eddies and vortices. The effect of inlet boundary layer skew on the rotor downstream total pressure loss coefficient, Y_n, is shown in Figure 4-4. The pressure loss is calculated from Equation 4-3.

$$Y_n = \frac{\bar{\bar{P}}_{01,rel} - P_{02,rel}}{\bar{\bar{P}}_{01,rel} - \bar{\bar{P}}_1} \tag{4-3}$$

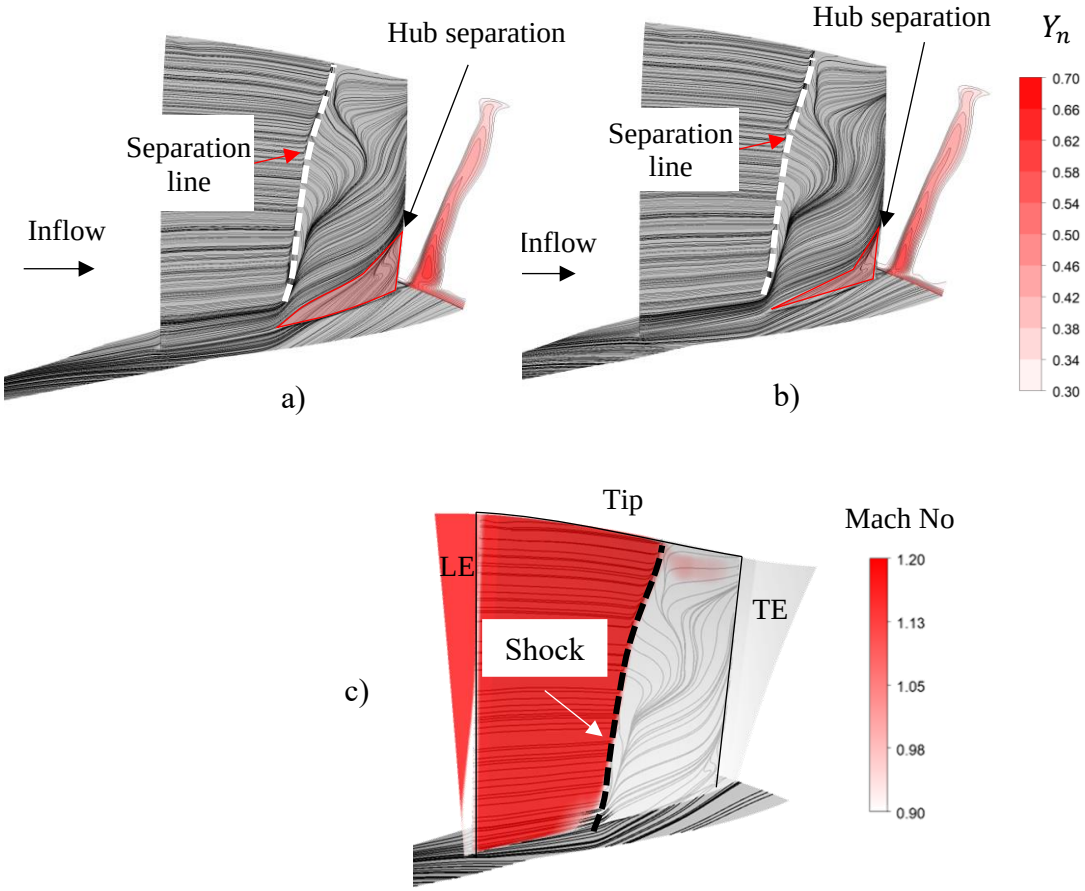

Figure 4-4 Effect of the inlet boundary layer skew on the downstream total pressure loss coefficient, Y_n at ND and surface streamlines for a) FH and b) PH case. c) Mach number contour on a meridional plane near the blade surface to show the location of the shock.

Here, $P_{01,rel}$ and P_1 are the mass-averaged relative total pressure and the area-averaged static pressure at the inlet. $P_{02,rel}$ is the relative total pressure at about 5% of $c_{ax,h}$ downstream of the rotor trailing edge. Surface streamlines are also plotted on the blade suction side (SS) and hub wall to compare the flow field of cases PH and FH. For case FH where no skew is present as shown in Figure 4-4a), a separated flow region is observed and results in a large loss core aft of the blade. For the case PH where boundary layer skew is

present as shown in Figure 4-4b), the size of loss core and separated region is relatively smaller than FH. A white dotted line indicates flow separation on the SS which occurs about halfway through the blade chord. The SS separation is not related to the effect of boundary layer skew but can be linked to the shock-boundary layer interaction as shown in Figure 4-4c). The Mach number contour is plotted at a meridional plane close to the blade SS. The dotted line is the shock that coincides with the separation line shown in Figure 4-4a) and b).

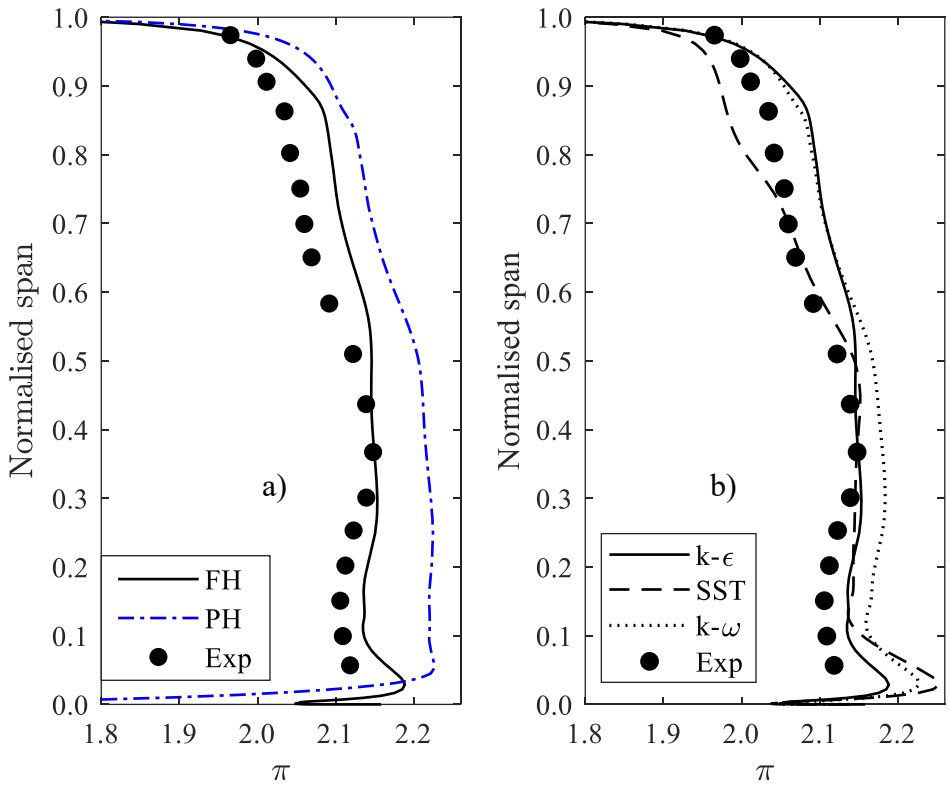

Figure 4-5 Effect of a) inlet boundary layer skew and b) turbulence model selection on radial distribution of π at ND

The effect of the flow separation on the outlet total pressure ratio, π is shown in Figure 4-5. Figure 4-5a) compares the outlet π for cases PH and FH. Near the hub, a pressure deficit region can be seen for case FH as opposed to case PH. The hub corner separation results in mixing loss which causes a hub pressure deficit. This is not seen for case PH where the hub separation is smaller. Figure 4-5b) compares the ability of three different commonly employed turbulence models in predicting the amount of pressure deficit due to the hub corner separation. Since separation is a viscous phenomenon, it is important to

choose the best turbulence model that can predict the best match to the experiment data. Three most common turbulence, namely; $k-\epsilon$, $k-\omega$ and SST models are compared for the selection. The SST models agrees with the experiment data points more as compared to $k-\epsilon$ and $k-\omega$ between 0.3 to 0.7 of the normalised span. However, near the tip region between 0.8 to 0.98 of the normalised span, π is under-predicted with a mismatch in terms of the trend as compared to the experiment data. Models $k-\epsilon$ and $k-\omega$ show a better agreement in the trend despite over-predicting π near the tip region. Near the hub, $k-\omega$ and SST over-predicted π more as compared to $k-\epsilon$. Overall, $k-\epsilon$ model is the best match to the experiment as compared to $k-\omega$ and SST model. Therefore, the $k-\epsilon$ model is chosen for this study. Other researchers such as Hah and Loellbach (1999) and Shabbir et al. (1997) have also successfully used the $k-\epsilon$ model for the Rotor 37 test case.

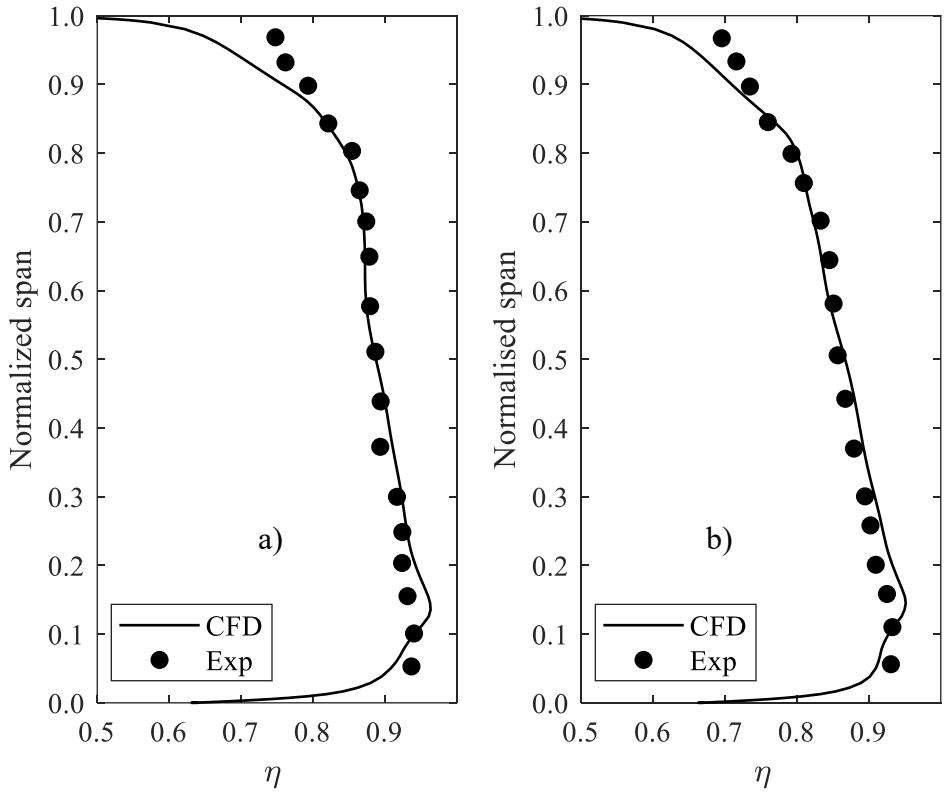

Figure 4-6 Outlet radial distribution of η of the simulation compared against the experiment result at a) ND and b) NS.

The outlet radial distribution of η for both ND and NS conditions in Figure 4-6 show a good overall trend in the free-stream region as compared to the endwalls. The discrepancy of η between the measured and the simulation is due the assumption of adiabatic wall.

Bruna and Turner (2013) showed that the η near the endwall is better matched when the casing temperature is prescribed. The actual endwall temperature was not known so it was assumed to be the same as the inlet total temperature. The above authors have shown that the endwall η difference between isothermal and adiabatic condition is about 1%. Although the real casing temperature is not known, it is suffice to show that η can be better predicted when simulated with heat transfer effects.

4.2.3 Pitch-wise Mach number distribution

As discussed in Suder (1998), the development of blockage in Rotor 37 is attributed to the shock interaction. It is found that the shock-tip leakage flow interaction generates blockage in the tip region that is 2-3 times more than the blockage in the core flow. In addition, the shock-boundary layer interaction causes flow separation on blade suction side (SS). Therefore, the ability to predict blockage relies on the ability of the simulation to correctly predict the shock location.

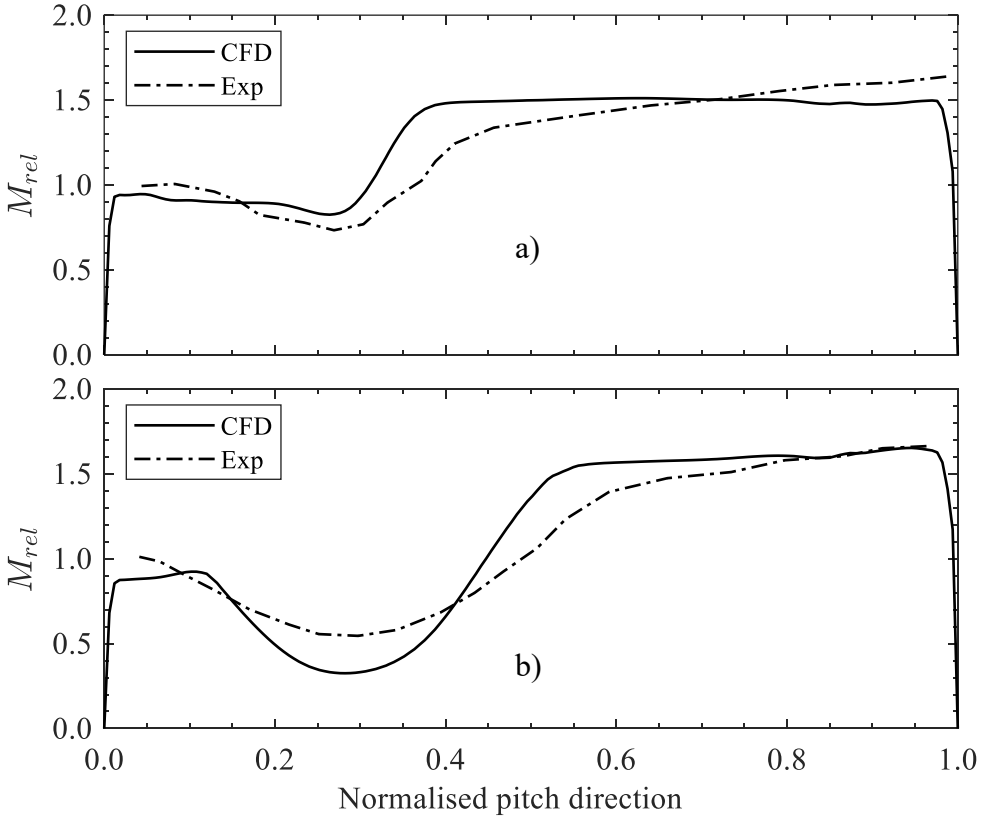

Figure 4-7 Pitchwise distribution of Relative Mach number at 95% span and 20% c_{ax} aft of the blade LE at a) ND and b) NS.

Figure 4-7 shows the pitch-wise distribution of relative Mach number at 95% span and 20% of c_{ax} of the respective span at ND and NS conditions. The simulation shows a relatively good agreement with the trend of the measured data. Despite under and over-predicting the Mach number values, the simulation manages to predict the location of the 'trough' reasonably well. The 'trough' which is located at about 0.3 normalised pitch distance from the pressure side (PS) represents a deficit in Mach number which is due to the deceleration of flow behind the shock. The depth of the 'trough' increases from operating point 4 to operating point 8 which suggest a change in the strength and structure of the shock and also its interaction with the tip leakage flow. In order to understand more about the change in the trough pattern further, the relative Mach number contour at 95% span height at ND and NS conditions as shown in Figure 4-8. The dashed line indicates the location where the data is extracted to plot Figure 4-7. The shock can be identified by the bunching of contour lines which is due to sudden decrease in Mach number across the shock. By comparing the Mach number contour for NS and NS, it can be seen that the shock at NS conditions is no longer attached to the blade leading edge but is rather a detached bow shock. In addition, a relatively large region of low Mach number can be seen aft of the shock at NS conditions. In Figure 4-8b), the dashed line is seen to cross this low Mach number region which explains the change in the 'trough' depth at compressor approaches stall. This low Mach number region is not as pronounced at ND conditions as shown in Figure 4-8a).

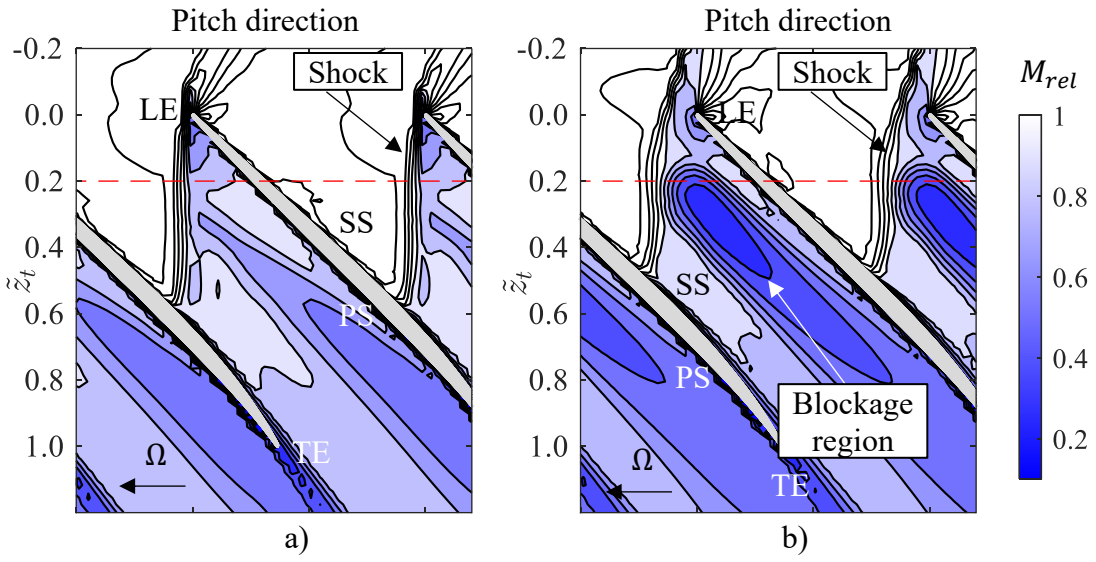

Figure 4-8 Contour of Mach number at 95% span at operating point a) 4 (ND) and b) 8 (NS)

4.2.4 Shock-tip leakage vortex interaction

The occurrence of a low Mach number region at near stall (NS) conditions can be explained by the shock-tip leakage vortex (TLV) interaction as shown in Figure 4-9. The TLV can be identified by the roll-up of the tip leakage flow originating from the tip leading edge. The shock-TLV interaction causes a disintegration of the TLV streamlines which may suggest a possible vortex breakdown although a bubble'-like TLV breakdown as observed by Furukawa et al. (1999) is not seen. The TLV breakdown is caused by the sudden deceleration of the TLV core which in the present case is caused by its interaction with the passage leg of the bow shock. The TLV breakdown results in a slow recirculating region that explains the origin of the low Mach number region. The location of the low Mach number region is slightly downstream of the location where the TLV begins to disintegrate. This clearly links the shock-TLV interaction to the low Mach number region observed at NS conditions as shown in Figure 4-8b).

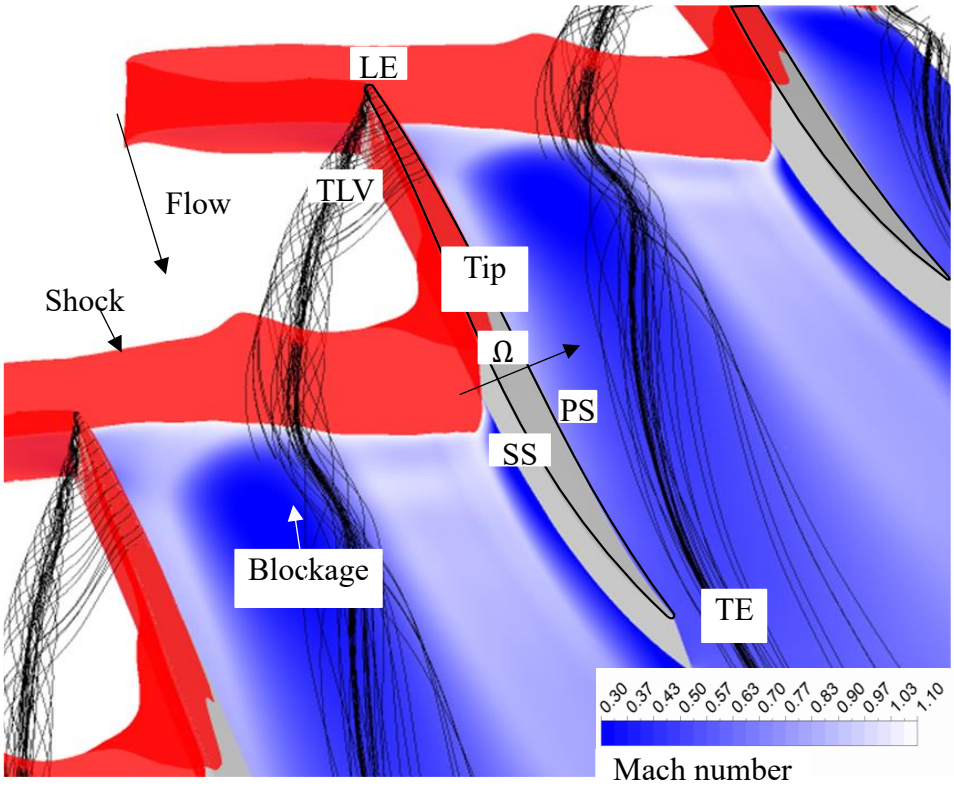

Figure 4-9 Relative Mach number contour at 95% span and tip leakage vortex streamlines at NS conditions. An isosurface of Mach number = 1 is plotted to show the shock plane.

4.2.5 Shock-suction surface boundary layer interaction

As mentioned earlier, the shock-suction surface boundary layer interaction is responsible for the blade SS flow separation as shown in Figure 4-4. The pressure rise across a shock

introduces an adverse pressure gradient in the SS boundary layer which causes flow separation. The effect of change in shock structure on the SS separation can be observed by comparing the thickness of the boundary layer at ND and NS conditions. In the original NASA experiment, it was difficult to obtain measurements close to the blade surface due to laser light reflections and optical blockage of the laser path (Suder et al., 1995b). Therefore, the boundary layer growth was predicted using numerical simulation. An isoline of entropy near the blade surface was extracted to compare the thickness of the boundary layer. This is possible because entropy is high inside the boundary layer and relatively low far from the blade. Hence, the smallest entropy isoline level that encompasses the blade can be thought as a reasonable representation of the boundary layer edge.

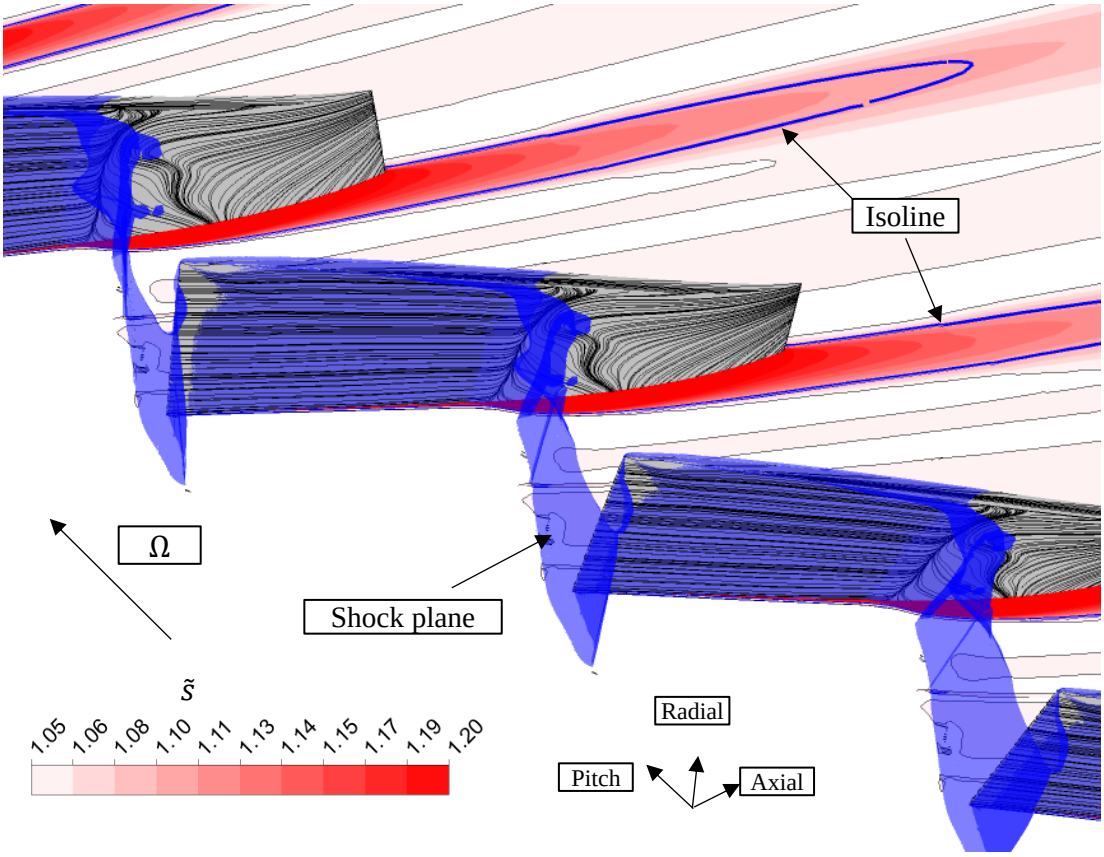

Figure 4-10 Entropy ratio contour at 70% span and shock plane at NS conditions

Figure 4-10 shows the entropy ratio, $\tilde{s}$ contour at 70% height at NS conditions. $\tilde{s}$ is the ratio of entropy, s, to the mass-averaged inlet entropy, $\bar{\bar{s}}_1$ as defined in Equation 4-4. The entropy, s, is not entropy itself but is a measure of entropy change obtained from isentropic ideal gas relations.

$$\tilde{s} = \frac{s}{\bar{s}_1} \text{ where } s = \frac{P}{\rho^{\gamma}} \tag{4-4}$$

The data is presented at 70% height to negate the effects of tip leakage flow so that the SS separation is much clearer. If isentropic compression is assumed across the rotor then the entropy everywhere would be the same as that at the inlet (s_1). If the $\tilde{s}$ value is more than 1, it means that the entropy has increased and can be represented as loss. The shock plane is an isosurface of Mach number equal to 1. It can be seen that the location of the shock plane is consistent to the SS separation line. The SS separation results in an increase of $\tilde{s}$ due to mixing losses. Using the same method as mentioned in Suder (1995), an isoline is drawn to represent the edge of the boundary layer. The isoline is drawn for a value of $\tilde{s} = 1.1$.

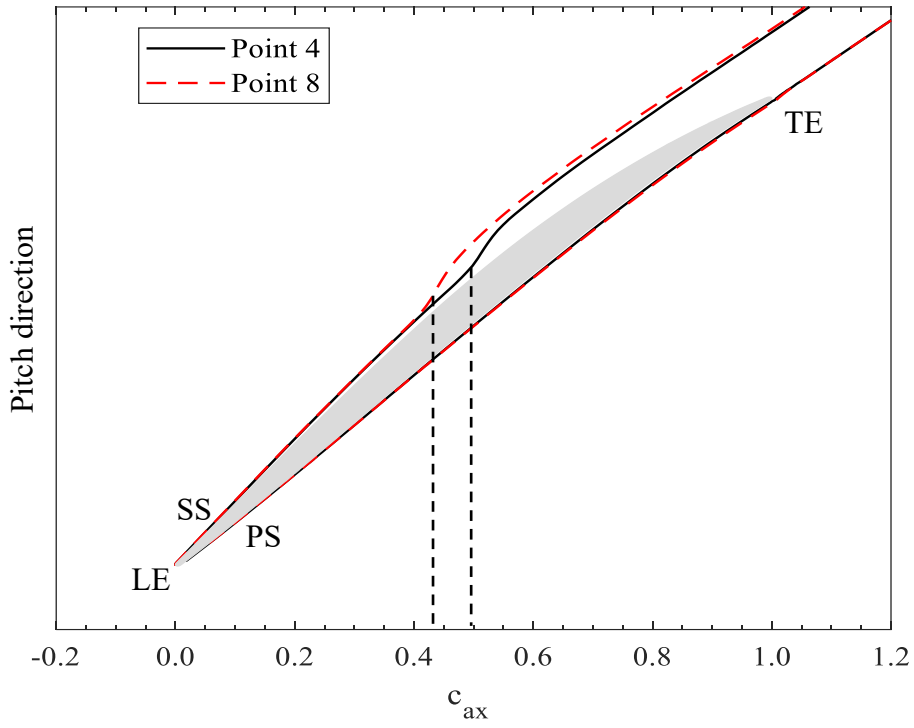

Figure 4-11 Entropy isolines at 70% span at operating point 4(ND) and 8(NS). Dotted lines show the location of the SS flow separation onset

Figure 4-11 shows entropy isolines at 70% span at ND and NS conditions. The dotted lines represent the location of the SS separation onset. It can be seen that the SS boundary layer at ND conditions separates at about 50% of c_{ax} aft of the blade leading edge. At NS conditions, the location of the separation onset occurs at about 42% of c_{ax} aft of the blade leading edge. The upstream movement of the separation onset location can be explained

by the upstream movement of the shock plane at conditions closer to stall. Nevertheless, the thickness of the separated region at NS is similar to ND conditions. This may suggest that the separation is triggered by an inviscid mechanism, namely the shock, which is affected by the back pressure. However, the viscous process that ensues within the separated region seems to be largely unchanged due to the similar thicknesses observed in Figure 4-11 and also as seen in the largely similar surface streamline patterns (Figure 4-4 and Figure 4-10).

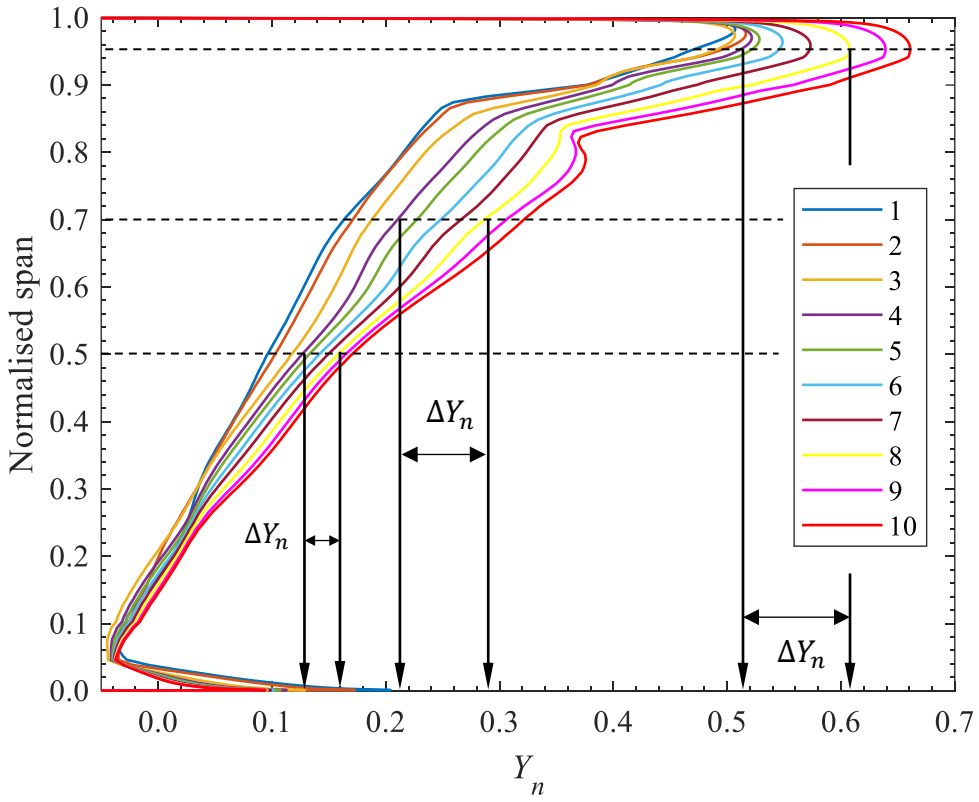

Figure 4-12 Radial distribution of Y_n for all operating points calculated at 30% of $c_{ax,t}$ aft of the rotor tip TE.

4.2.6 Downstream total pressure loss

Figure 4-12 shows the radial distribution of Y_n calculated for all operating points at 30% of $c_{ax,t}$ aft of the rotor tip TE. Y_n is calculated using the same method as described in Equation 4-3. Across all operating points, Y_n, which is calculated using mass-averaged quantities, is larger at the tip region compared to the hub. The increase in loss from hub to tip is also reflected as a reduction in the spanwise distribution of efficiency downstream

of the rotor as seen in Figure 4-6 that was presented earlier. This shows that the loss generated by the hub corner separation is relatively smaller compared with the near-tip aerodynamic features such as tip leakage flow and shock-TLV interaction. Additionally, the effect of shock-TLV interaction and shock-SSBL interaction can be compared by calculating the change of total pressure loss coefficient, ΔY_n at 50%, 70% and 95% span, respectively.

$$\Delta Y_n = Y_{n,8} - Y_{n,4}\ [\%] \tag{4-5}$$

ΔY_n as shown in Equation 4-5 is the change of Y_n between ND and NS conditions. At 95% span, where the shock-TLV interaction is strong, the ΔY_n is about 10% points. At 50% and 70% span which are further away from the casing, ΔY_n are about 3% and 7% points, respectively. This clearly shows that the overall loss in Rotor 37 is dominated by the events of the tip leakage flow at the outer span (casing) than the inner span where the hub corner separation is present.

4.3 Tip region aerodynamics

4.3.1 Revisiting the shock-TLV interaction

The aerodynamics at the tip region has so far been shown to be the main source of loss as the compressor approaches stall. In Rotor 37, the shock-TLV interaction as briefly discussed earlier is known to be one of the sources of the loss. The change of the shock structure and orientation at conditions close to stall is responsible for the generation of a low Mach number region near the casing. This low Mach number region is the result of a TLV breakdown as the intensity of shock-TLV interaction becomes stronger at conditions close to stall. Yamada et al. (2007) explained about the conditions for a vortex breakdown due to shock-TLV interaction in Rotor 37. One of the conditions for TLV breakdown is the angle formed between TLV trajectory and the shock plane. It was suggested that at conditions closer to stall, the orientations of the shock and the TLV would gradually increase and become at right angles to one another. This together with the increase of the TLV swirl intensity due to increased loading at a relatively lower mass flow rate were the conditions reported to have caused TLV breakdown.

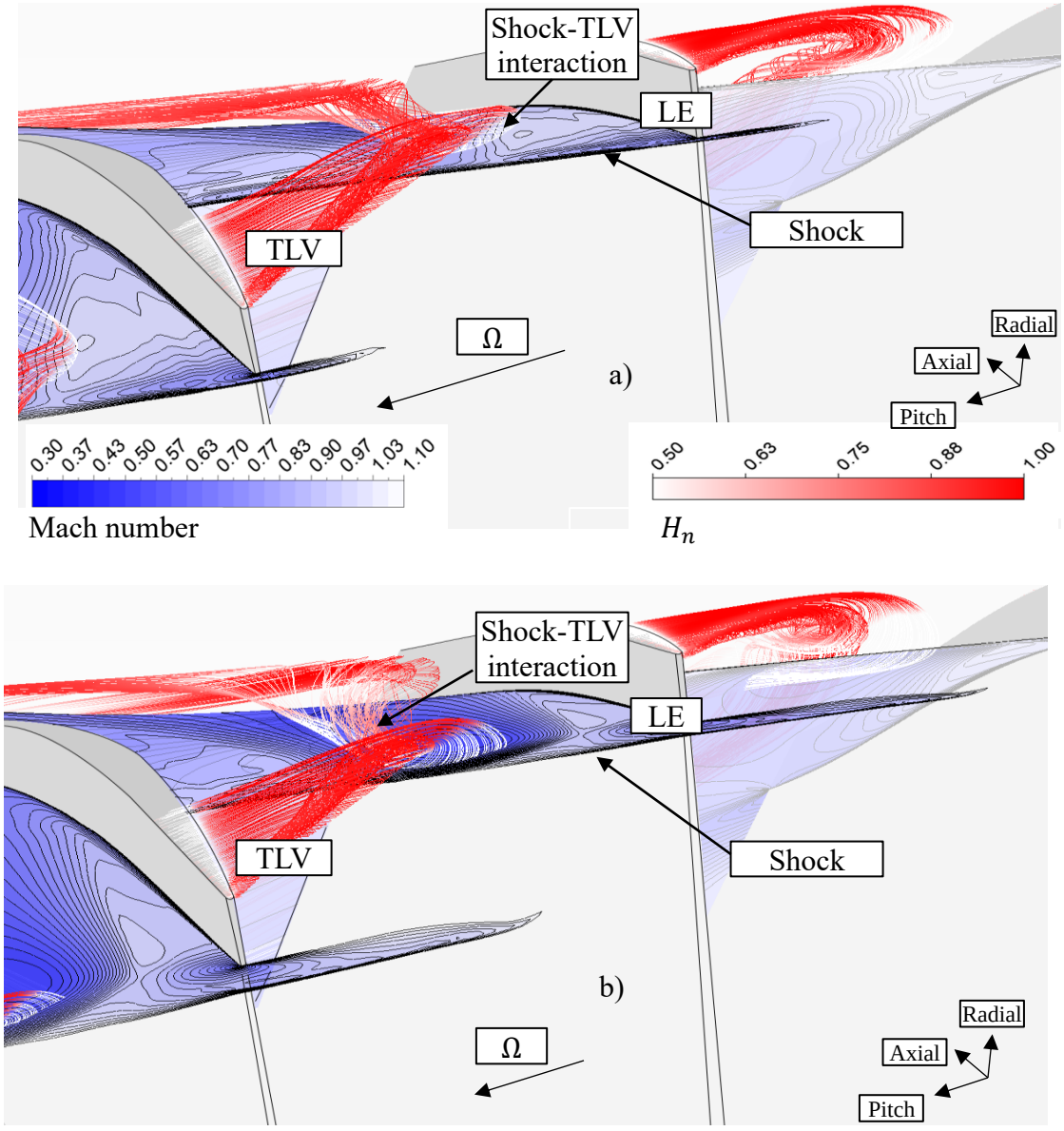

Figure 4-13 TLV streamlines coloured with normalised helicity, H_n and Mach number contour at 95% span at a) ND and b) NS conditions.

Figure 4-13 shows the TLV streamlines coloured with normalised helicity, H_n as defined in Equation 4-6 at ND and NS conditions.

$$H_n = \left| \frac{\vec{\xi} \cdot \vec{v}}{|\vec{\xi}||\vec{v}|} \right| \tag{4-6}$$

Here, $\vec{\xi}$ and $\vec{v}$ are the absolute vorticity vector and relative velocity vectors, respectively. Hence, H_n represents the absolute cosine angle between the $\vec{\xi}$ and $\vec{v}$. The magnitude of H_n is equal to unity within the core of streamwise vortices if $\vec{\xi}$ and $\vec{v}$ are perfectly aligned. H_n can therefore be used to identify the strength of the vortex core as in this case that of

the TLV. The strength of the vortex core may show the effect of vortex breakdown due to the shock-TLV interaction. At near design conditions as shown in Figure 4-13a), the shock-TLV interaction results in a reduction of H_n on the TLV streamlines. Prior to interacting with the shock, the magnitude of H_n on the TLV streamlines is closer to 1 which shows a strong vortex. The pressure rise across a shock causes a deceleration in the TLV which results in a weaker vortex. This effect is more pronounced at conditions closer to stall as shown in Figure 4-13b). The shock-TLV interaction causes a larger reduction in H_n as compared to ND conditions. The relatively stronger shock-TLV interaction at NS conditions results in a low Mach number region as shown in Figure 4-8 which is not present at ND conditions.

The effect of change in the orientation and position of the shock on the strength of the shock-TLV interaction can be investigated by locating the trajectory of the shock and TLV. Figure 4-14 shows the casing static pressure at ND and NS conditions. The bunching of contour lines represents the shock due to sudden change of pressure.

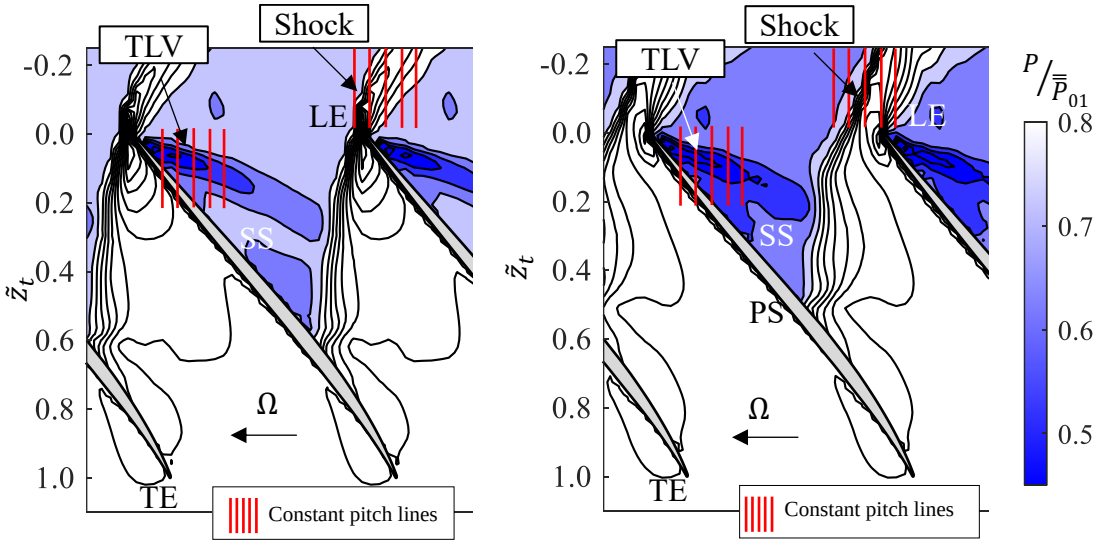

Figure 4-14 Casing static pressure at a) ND and b) NS conditions.

The TLV can be identified by a low pressure region originating from the tip LE. The trajectory of the shock and TLV are obtained by extracting pressure profiles along several constant pitch lines that are drawn across the shock and TLV region. The TLV trajectory is obtained by locating the axial location of the minimum pressure for all the extracted pressure profiles. Since the pitch location along the pressure profile is known, the axial location of the minimum pressure can be found from interpolation. The trajectory of the

shock is obtained through a similar method. Instead of finding the axial location of the minimum pressure region, the axial location of half the pressure rise across the shock is found. From the obtained coordinates, the trajectory of the shock and TLV are found through linear fitting.

Figure 4-15 shows the approximated shock and TLV trajectory drawn for all operating points. The intersection point between the shock and TLV trajectory represents the location of the shock-TLV interaction. Across all operating points, the change in trajectory of the TLV is relatively small as compared to that of the shock trajectory. The change in the shock and TLV trajectory can be quantified by calculating the slope of each trajectory. The slope of the shock and TLV trajectory are represented by angles, χ and ζ, respectively.

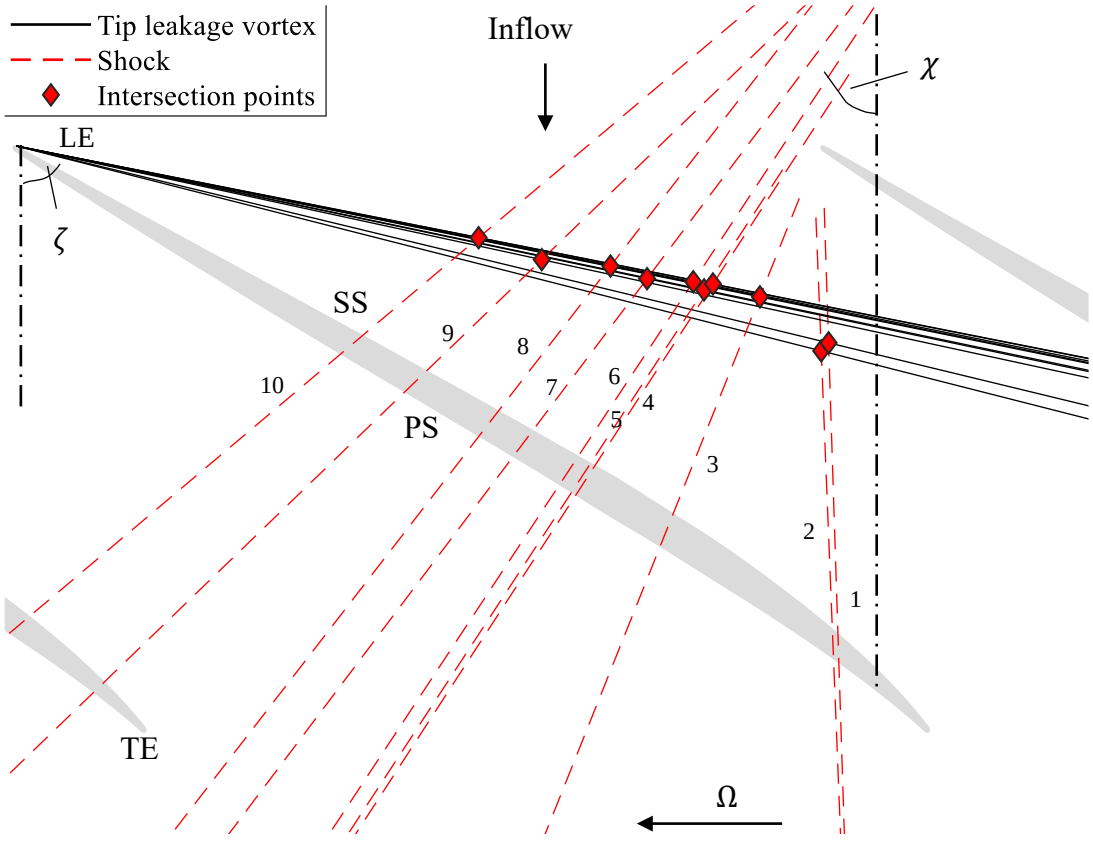

Figure 4-15 Shock and TLV trajectory for all operating points

Figure 4-16a) shows the variations of angles, χ and ζ across all operating points. Both angles are measured from the axial direction and are taken to be positive in the direction of rotation. The TLV angle almost remains unchanged from operating point 1 to operating point 10 where the angle is about -80°. The slope of the shock trajectory shows an increase

of about 20° from ND conditions to operating point 10. The upstream movement of the shock as it detaches from the blade can be measured by finding the change in the axial location of shock-TLV interaction as shown in Figure 4-16b). The axial distance measured aft of the blade LE of the location of the shock-TLV interaction, $\tilde{z}_t$, is normalised by tip axial chord length, $c_{ax,t}$. From ND to operating point 10 (last stable operating point), the shock moves about 10% of the $c_{ax,t}$.upstream of the tip LE.

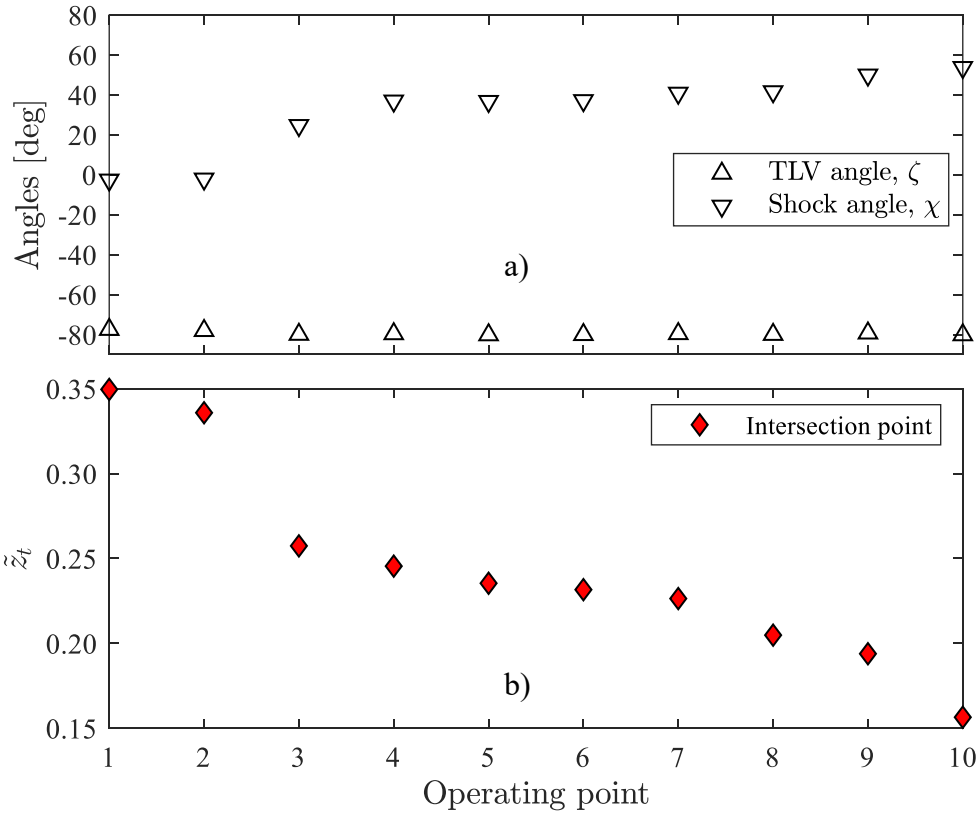

Figure 4-16 a) Shock and TLV angles and b) axial location of the shock-TLV interaction

4.3.2 Radial separation vortex (RSV)

Another flow phenomenon in the tip region that may be linked to rotating stall is the radial separation vortex (RSV). The link between RSV and spike-type rotating stall has so far been proved experimentally and numerically in low speed axial compressors (Inoue et al., 1999; Yamada et al., 2012; Pullan et al., 2012). In a high-speed compressor, the existence of a RSV has been found recently by Brandstetter et al. (2018) through optical measurements. The RSV has a tornado-like shape that originates from a two dimensional LE separation. As the compressor approaches stall the LE separation line detaches from the blade and interacts with the tip leakage flow which results in a tornado-like structure. In Rotor

37, to the author's best knowledge, the existence of RSV has never been discussed although numerous studies have been performed in relation to tip aerodynamics of Rotor 37.

Coherent structures such as the RSV can be detected using a `lambda-2' criterion method. The location of a vortex can be identified by finding a minimum pressure region. This can be done by finding the eigenvalues of a Hessian pressure matrix (Jeong & Hussain 1995). The values of the eigenvalues determine the concavity of the Hessian matrix. A local minimum point can be found if all the eigenvalues are positive and vice versa. Figure 4-17 shows the 'lambda-2' isosurfaces near the casing region and the contour of normalised radial vorticity contour, $\frac{\omega_r}{\Omega}$. A positive ω_r indicate radially outward rotation. The location of a positive ω_r is consistent with a tornado-like shape structure which may suggest a part of a RSV that has been shed into the blade passage.

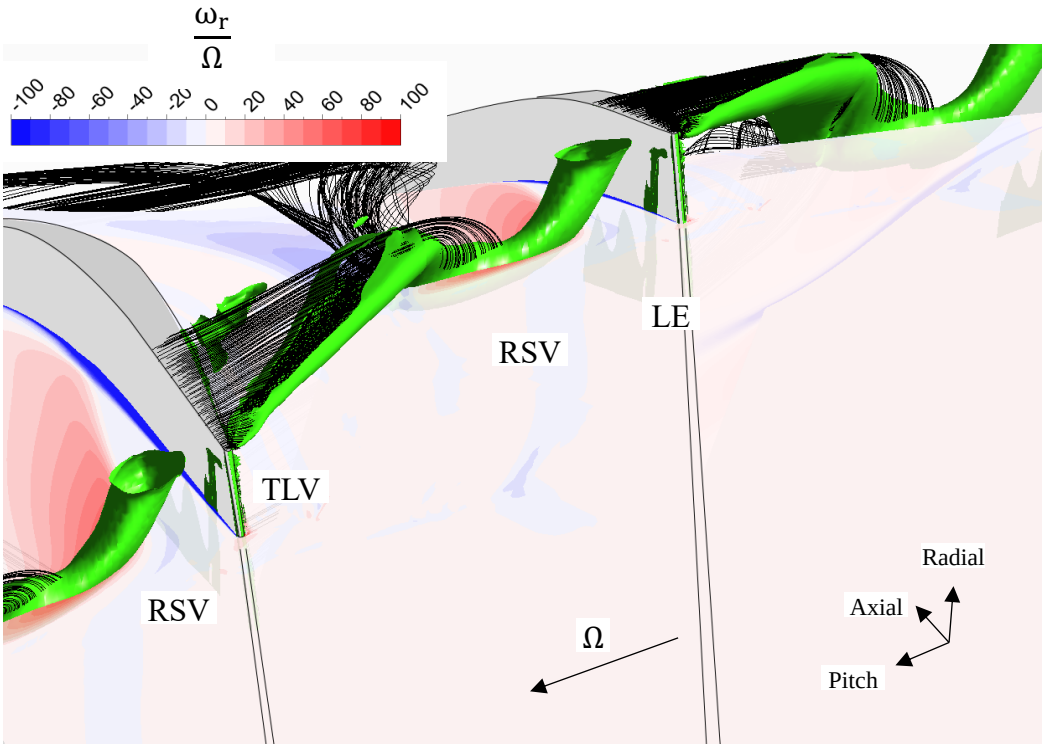

Figure 4-17 'Lambda-2' iso-surfaces near the casing at operating point 8 and normalised radial vorticity contour at 98% span.

In a high-speed compressor, the LE separation that leads to the formation of an RSV is due to the existence of a blockage region near casing (Brandstetter et al., 2018). The blockage region causes a deflection of the incoming flow towards the adjacent blade pas-

sage. The deflection of the incoming flow into the adjacent passage invokes the LE separation. At conditions closer to stall, the blockage region grows circumferentially causing more deflection which results in a larger separation. At this point, the LE separation evolves into an RSV.

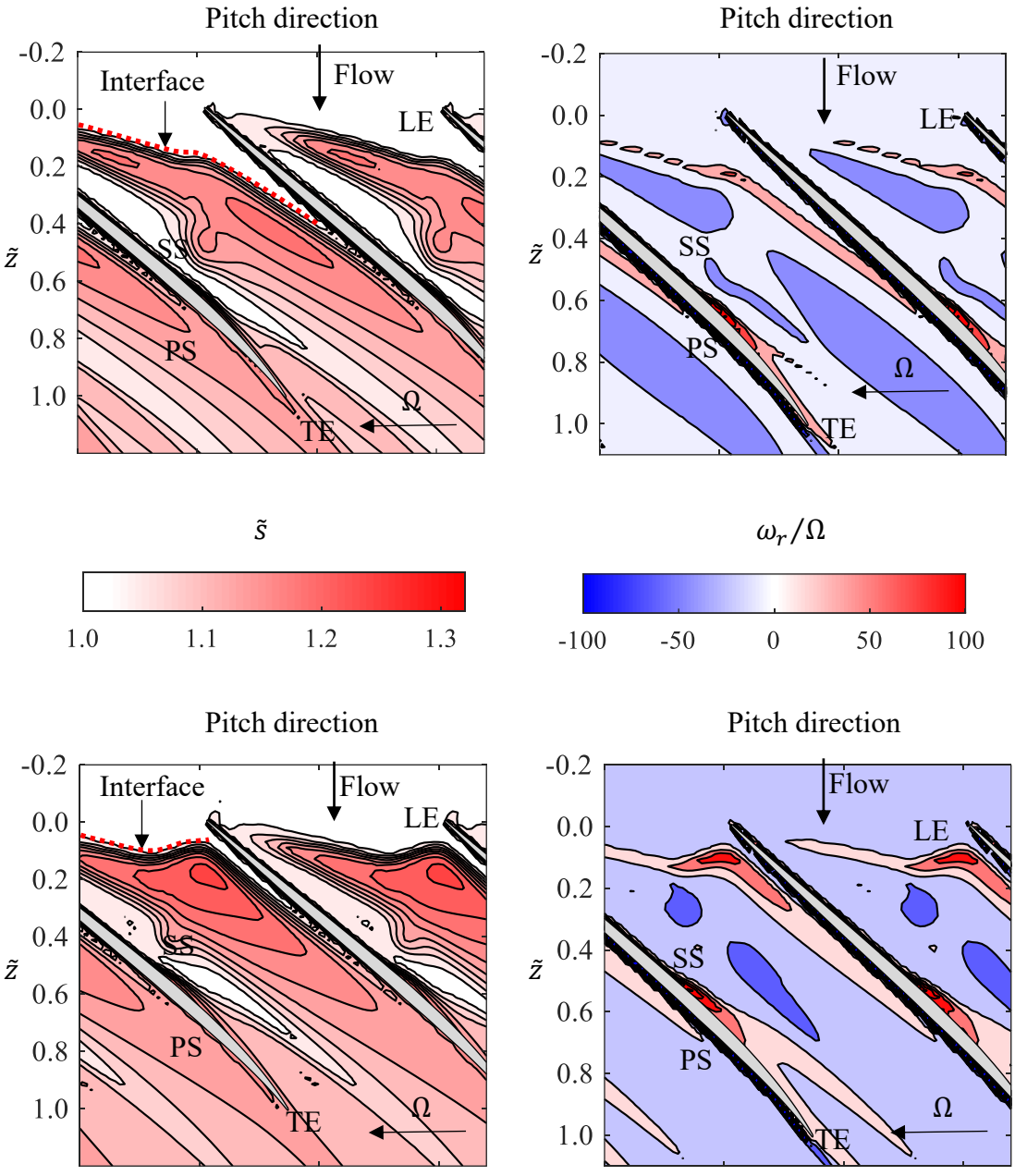

Figure 4-18 Contour of $\tilde{s}$ and ω_r at 98% span at operating point 4(a and c) and 8(b and d)

Figure 4-18 shows the comparison of the $\bar{s}$ contour compared side-by-side with the ω_r contour. The contour plots are drawn at ND and NS conditions to see the change in the

blockage region growth and its effect to the RSV as the compressor approaches stall. The blockage region can be identified by high $\bar{s}$ values as shown darker shades or red in Figure 4-18a) and c). An interface which is represented by a dotted line, is the boundary between the incoming flow and the blockage region. At operating point 8, the growth of the blockage region in the circumferential direction results in the occurrence of positive ω_r region just along the interface. This positive ω_r region is relatively larger than the positive ω_r region at ND conditions. The positive ω_r region as shown earlier in Figure 4-17 is consistent with the location of the tornado-like structure.

4.4 Blockage

The reduction of effective primary flow area due to low axial velocity regions can be referred to as blockage. From the literature discussed in Chapter 2, it is evident that the reason why casing treatment such as casing grooves improve the stability margin of compressor is due to the removal or reduction of blockage. Understanding the development, growth and also location of blockage is thus key for designing casing grooves.

Suder (1998) calculated the blockage downstream of the rotor by identifying the wake velocity defect region. This method, however, does not reveal the blockage development within the blade passage that is responsible for the stall development. A different approach is therefore required for evaluating the blockage inside the blade passage. Sakuma et al. (2013) showed that blockage regions inside the blade passage can be identified using a mass flow overshoot method. The mass flow rate at any given axial plane inside the domain is equal to the inlet mass flow rate to satisfy continuity. In order to identify the blockage cells, the mass flow rate of each cell in that plane is sorted in a descending order. Summation of all the sorted mass flow rate of each cell will equal the inlet mass flow rate. If a cell with negative axial velocity exists, the summation of all grid cells with positive mass flow will initially overshoot the inlet mass flow rate value before being balanced by the cells with negative axial velocity. At a given axial plane, the summation is therefore stopped as the inlet mass flow value has been initially reached. From here, all the summed cells that do not overshoot the inlet mass flow rate value are considered as non-‘blocked’ cells and are assigned a blockage index, ψ=0. The remaining cells whose mass flow rate values are yet to be summed are considered as `blocked' cells and are assigned a value ψ=1. An example of the blockage cell identification method is shown in Figure 4-19.

Figure 4-19a) shows the contour of normalised mass flux, $\tilde{\varphi}$ at an axial plane location of 20% of $c_{ax,t}$ aft of the tip LE. The definition of $\tilde{\varphi}$ can be found in Equation 4-7.

$$\tilde{\varphi} = \frac{\varphi}{\bar{\varphi}} \text{ where } \varphi = \rho V_z \tag{4-7}$$

$\bar{\varphi}$ is the mass-average φ across that plane. For clarity, only the top 20% span region is shown. It can be seen that the near casing region (> 0.95 normalised span) is dominated by low $\tilde{\varphi}$ value which indicate blockage. The mass flow overshoot method is than applied on the same plane as shown in Figure 4-19b). Cells that are blocked (ψ=1) are marked with dots. By comparing both plots, it can be seen that the region with low $\tilde{\varphi}$ is correctly identified using the mass flow overshoot method.

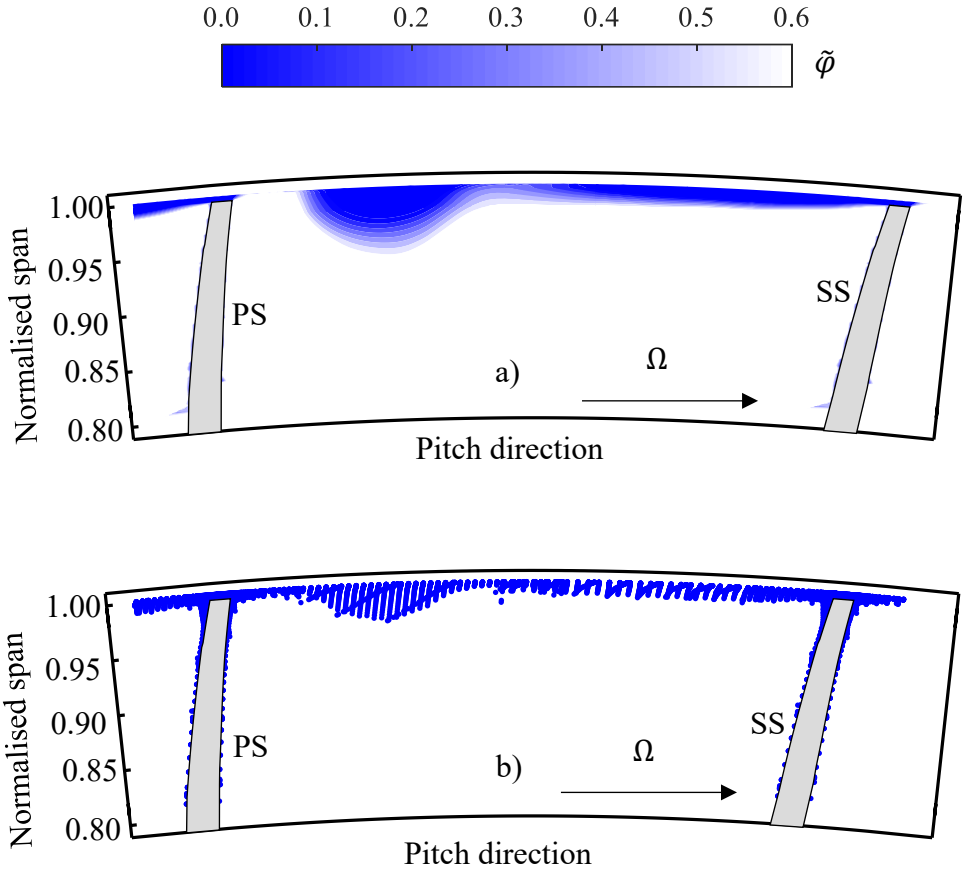

Figure 4-19 $\tilde{\varphi}$ and ψ contour at 20% of $c_{ax,t}$ aft of the LE at operating point 8 (NS)

The mass flow overshoot method can be adapted to obtain a method for quantifying the blockage across any given axial plane. Two new quantification parameters; non-dimensional blockage cell count, Ψ, and non-dimensional blockage mass flowrate , Ψ_m, as in Equation 4-8 and Equation 4-9 respectively are obtained by extending the previous work of Sakuma et al. (2013).

$$\Psi = \frac{1}{N}\sum_{i=1}^{N} \psi(i) \tag{4-8}$$

$$\Psi_m = \frac{\sum_{i=1}^{N} |\psi(i)\, m(i)|}{\sum_{i=1}^{N} m(i)} \tag{4-9}$$

Here, N is the total number of cells in the axial plane. , $\psi(i)$ and $m(i)$ are the blockage index of the i^{th} cell and the mass flow associated with the i^{th} cell, respectively. The physical meaning of each quantification parameter is that Ψ is the normalised number of blocked cells whilst Ψ_m is the normalised absolute sum of the 'blocked' cell mass flow rate. The direction of flow through a blocked cell is therefore discounted in this evaluation as long as it has been identified to be 'blocked'.

Figure 4-20 shows the distribution of Ψ and Ψ_m for all operating points on the compressor map as shown in Figure 4-1. The distribution Ψ and Ψ_m are obtained from 230 axial planes across the rotor. The location of peak blockage is seen to move upstream as the compressor is 'throttled' towards stall. The difference between the location of the peak blockage at operating point 4 and operating point 10 is about 20% of $c_{ax,t}$. This upstream movement of the peak blockage location is consistent with the upstream movement of the shock-TLV interaction location as shown in Figure 4-16. In order to quantify the blockage due to the shock-TLV interaction in an isolated manner, only the top 20% span of the Ψ and Ψ_m distribution are shown as in Figure 4-21. The trend of the top 20% span distribution is similar to when the distribution is shown for the whole span. The location of the peak blockage at operating point 10 is about 20% of $c_{ax,t}$. The discrepancy between the axial location of the shock-TLV interaction and the peak blockage suggests that the blockage is gradually built up downstream of the shock-TLV interaction location before it peaks. The increase of the peak blockage from operating point 4 (ND) to operating point 10 (last stable operating point) shows a stronger shock-TLV interaction as the compressor

approaches stall. At conditions close to stall, the shock detaches from the blade and forms a larger angle which causes the shock to interact more with upstream part of the TLV.

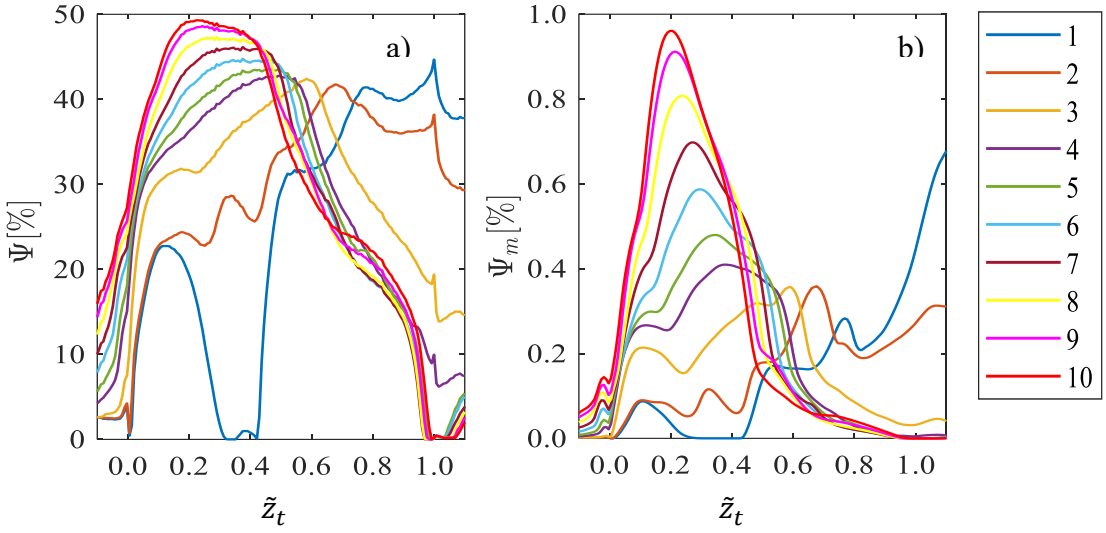

Figure 4-20 Distribution of a) Ψ and b) Ψ_m for all operating points

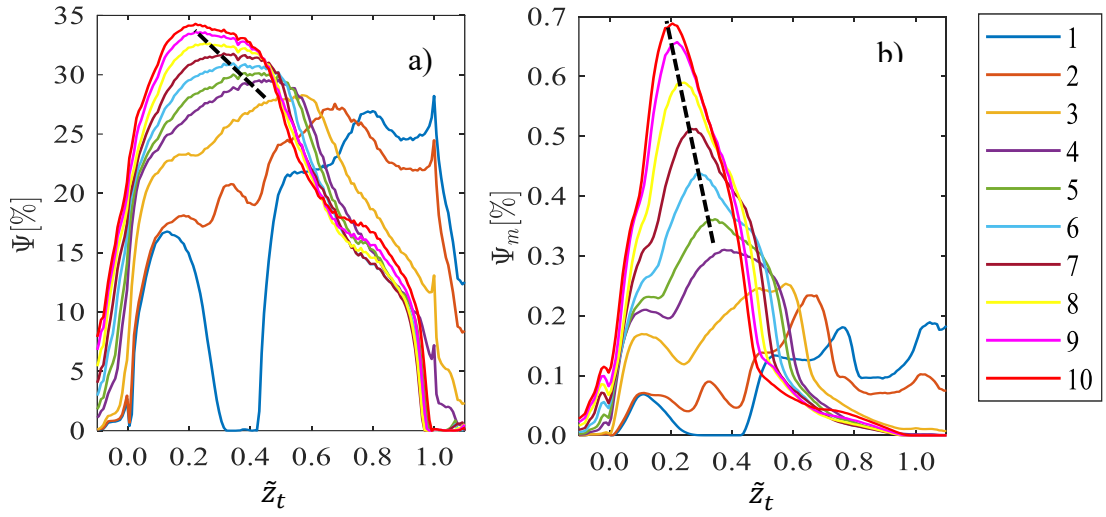

Figure 4-21 Top 20% span distribution of a) Ψ and b) Ψ_m for all operating points

4.5 Summary

The summary of this chapter is as the following:

1. Key results from the numerical simulation have been compared against experimental data for validation. The error of π and η from the numerically obtained performance map at ND (operating point 4) and NS (operating point 8) conditions are within $\pm$2% and $\pm$1%, respectively. The hub pressure trend due the hub leakage flow has been successfully recreated numerically by removal of the boundary

layer skew. The passage shock location at near design and near stall conditions has been correctly captured although the Mach number values are over/under predicted.

2. The radial distribution of total pressure loss coefficient, Y_n for all the operating points show that the biggest changes in loss occurs at the tip region as the compressor approaches stall. This suggest that the flow near the casing is responsible for the development of rotating stall. At near stall conditions, it is found that the shock-TLV interaction generates a low Mach number region the near casing. The shock-TLV interaction at near stall conditions is found to cause a reduction in TLV normalised helicity, H_n, suggesting a TLV breakdown although a 'bubble'-like structure is not successfully captured.
3. The location of the shock-TLV interaction is found from the trajectories of the shock and TLV at all operating points. It is found that the change in the structure of the shock at near stall conditions results in the upstream movement of the shock-TLV interaction location. The change in TLV trajectory across all operating points is relatively small as compared to that of the shock trajectory. From operating point 4 to operating point 10, the shock moves about 10% of the $c_{ax,t}$.upstream of the tip LE.
4. The radial separation vortex which has not been discussed previously in Rotor 37 by other researches has been shown to exist by plotting the 'lambda2' isosurface. The evidence for the RSV existence is further strengthened by comparing the location of the RSV with the radial vorticity contour. The location of the coherent structure that is believed to be RSV is consistent with the location of the positive radial vorticity contour.
5. The near casing blockage is quantified by extending the usage of a blockage cell identification method introduced by Sakuma et al. (2013). The axial distribution of the non-dimensional blockage count (Ψ) shows that at conditions close to stall, the peak of the distribution moves upstream. The non-dimensional blockage mass flow (Ψ_m) shows that the blocked mass flow rate for the last converged point peaks at about 20% of the $c_{ax,t}$ aft of the tip LE. The upstream movement of the peak blockage location can be linked to the upstream movement of the shock at conditions near stall.

Chapter 5

Design Optimisation and Surrogate Modelling

5.1 Overview

An introduction to some of the relevant concepts and models used in the optimisation methodology adopted is provided in this chapter. First the background and methods of solving optimisation problems are discussed. The second part details the implementation of a surrogate-based optimisation to find an optimised casing groove design.

5.2 Optimisation problem

Optimisation in mathematics is a process of finding the best solution from a set of possible solutions whilst satisfying a number of constraints. Optimisation can be applied to engineering design problems in order to find the best possible design from an array of feasible designs. The optimal design can be found by minimising the desired objective function, $f_i(x)$. The subscript integer $i > 1$ denotes a multi-objective optimisation problem where the best compromise solution between competing objective functions is sought. The general statement of a constrained optimisation problem can be expressed as the following:

Minimise	$f_i(\boldsymbol{x_m});\ \boldsymbol{x_m} = [x^1\ x^2\ ..\ x^j]$
such that	$g_i(\boldsymbol{x_m}) \leq c_i$
for	$\boldsymbol{x}_l \leq \boldsymbol{x_m} \leq \boldsymbol{x}_u$

where $g_i(x) \leq c_i$ is the inequality constraint that must be satisfied when solving the optimisation problem. There can be multiple constraints for any optimization problem so

the integer i represents the number of constraints. The solution for the optimisation problem, $\boldsymbol{x_m}$, is written in boldface to indicate that the solution may exist as a vector. The solution of the optimisation problem is sought between the upper bounds, $\boldsymbol{x_u}$, and lower bounds $\boldsymbol{x_l}$ of the design space. In multi-objective optimization problems, there may exist multiple optimal solutions due to the compromise between objective functions. Subscript m in $\boldsymbol{x_m}$, represents the number of solutions that exist in the design space. The optimal solutions are determined based on the dominance test as explained in the following section.

5.3 Dominance and Pareto optimal solution

Consider the multi-objective optimization problem as depicted in Figure 5-1. The 'goodness' of each solution, $\boldsymbol{x_m}$, shown as full circles labelled 1 to 5, are evaluated using the concept of dominance (Yang, 2014). A solution is said to be dominant if that solution is superior to the other solution. For instance, consider the dominance test of solution for m=1 to 3 as shown in Table 5-1.

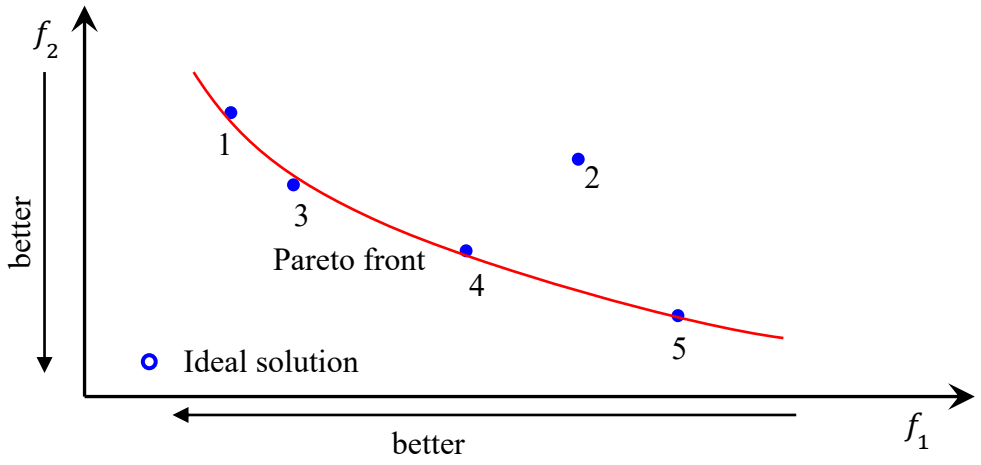

Figure 5-1 Pareto-optimal solution for a multi-objective optimisation problem

When comparing solutions 1 and 2, no solution is found to be dominant as each solution is dominant in the respective objective functions. The same result is obtained when solutions 1 and 3 are compared. However, it is found that solution 3 is dominant than solution 2 as solution 3 is superior when both objective functions are compared together. If the dominance test is extended to solution 4 and 5, it can be seen that both solutions are considered as non-dominant. The set of all the non-dominant solutions are known as the

Pareto-optimal solution. In the example explained in this section, all the solutions except $\boldsymbol{x_2}$ are the Pareto-optimal solution. The Pareto front is an imaginary boundary line that can be drawn across all the optimal solutions. Ideally, the Pareto front will collapse into a single solution if the objective functions do not conflict each other.

Table 5-1 Example of a dominance test based on solutions in Figure 5-1

	$f_1(\boldsymbol{x_m})$	$f_2(\boldsymbol{x_m})$	Dominance test
$\boldsymbol{x_1}$ and $\boldsymbol{x_2}$	$f_1(\boldsymbol{x_1}) < f_1(\boldsymbol{x_2})$	$f_2(\boldsymbol{x_2}) < f_2(\boldsymbol{x_1})$	Non-dominant
$\boldsymbol{x_1}$ and $\boldsymbol{x_3}$	$f_1(\boldsymbol{x_1}) < f_1(\boldsymbol{x_2})$	$f_2(\boldsymbol{x_3}) < f_2(\boldsymbol{x_1})$	Non-dominant
$\boldsymbol{x_2}$ and $\boldsymbol{x_3}$	$f_1(\boldsymbol{x_3}) < f_1(\boldsymbol{x_2})$	$f_2(\boldsymbol{x_3}) < f_2(\boldsymbol{x_2})$	$\boldsymbol{x_3}$ is dominant than $\boldsymbol{x_2}$

5.4 Genetic algorithm

The Pareto-optimal solution is found using a Genetic Algorithm. A Genetic Algorithm (GA) is a nature-inspired random search method in optimisation (Goldberg, 1989). Random search methods are useful when dealing with discrete data. Unlike random search methods, gradient-based methods operate by finding the steepest gradient to determine the optimum value. This may be difficult, as this requires the objective function to be smooth with a well-defined slope value.

The architecture of GA is depicted in Figure 5-2. The main principle of GA is based on the process of biological evolution. Each solution in the design space is represented by binary coded chromosomes. At timestep, $t = t_i$, a set of chromosomes are randomly generated across the design space to create a population of candidate solutions. Based on three evolutionary operators, a new set of population is generated from the current one. The fitness or goodness of each solution (chromosome) is evaluated using a fitness function. The fitness function here is merely the desired objective function of the optimisation problem. The 'fittest' chromosome is guaranteed to exist in the next set of population and is regarded as the 'elitist' in the new population. Next, chromosomes are randomly selected for reproducing a new generation of chromosome. One of the methods to find parents for the generating offspring is through the tournament selection. The tournament method randomly selects a specified number of chromosomes and the 'fitness' of each chromosome is ranked. The 'fittest' chromosome which is the winner of the tournament is chosen as a parent for the cross-over method. In the cross-over method, a trait of each

parent chromosome is paired randomly with another parent candidate to create a new chromosome or offspring. This is possible since the genetic information of each chromosome is binary coded. A determined number of chromosomes are generated through mutation. Mutation is done by permuting a trait of the newly generated chromosome. Mutation prevents over-bias to any parent thus allows for the algorithm to continue exploring the design space. Without exploration, the solution may be heading towards a local minimum. The algorithm continues generating a new population until the average change in the population fitness reaches a specified target value.

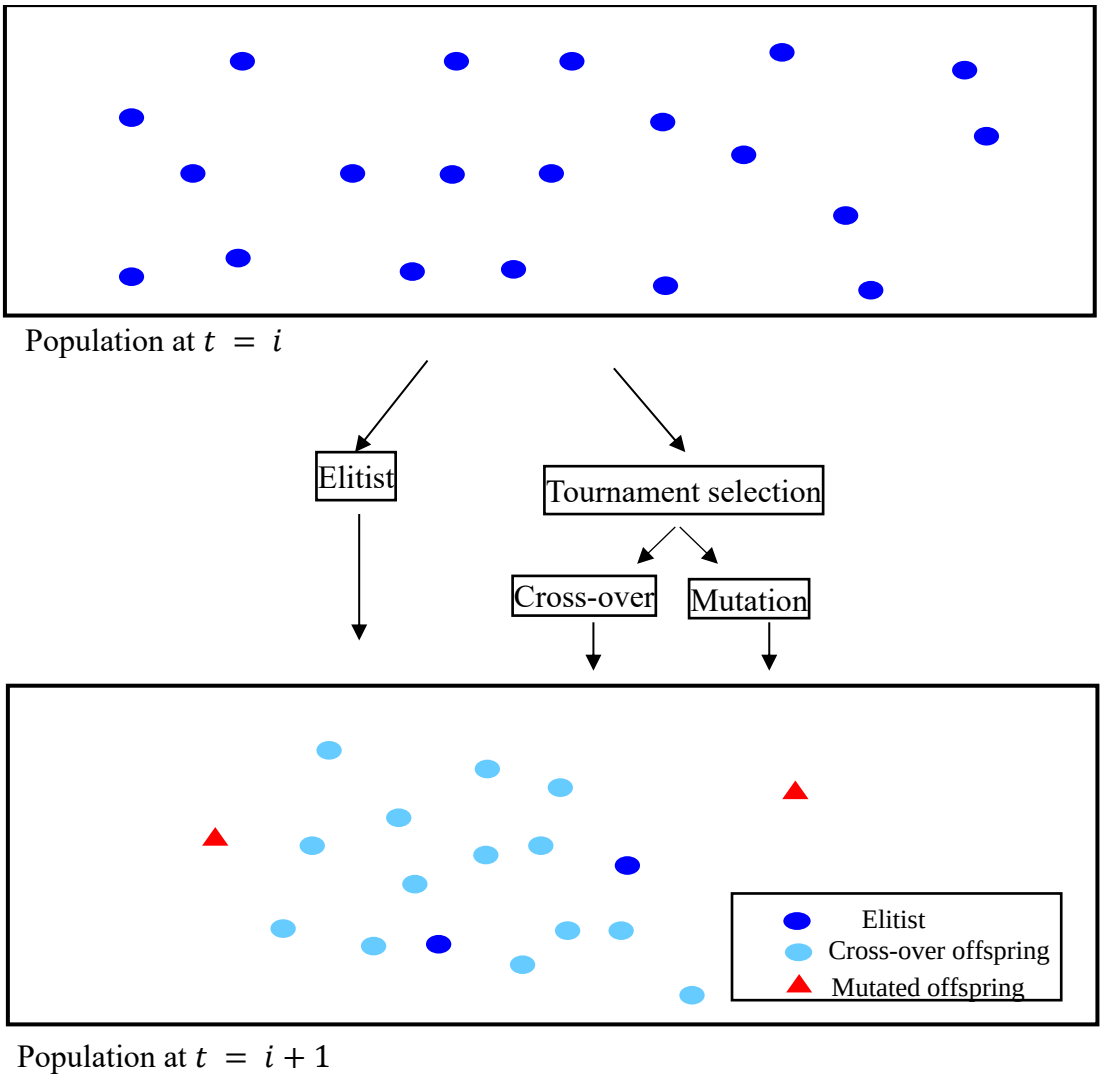

Figure 5-2 Genetic algorithm optimisation architecture

The GA was initially intended for single-objective optimisation problems. For a multi-objective optimisation problem, Fonseca and Fleming (1993) introduced a rank-based

method in assigning the fitness of the population. All non-dominating chromosomes are ranked 1 so that a Pareto-optimal solution can found from the implementation of GA. Some previous studies of implementing GA for solving multi-objective turbomachinery design optimisation problems can be found in Öksüz and Akmandor (2010) and Pierret et al. (2007).

5.5 Surrogate-based analysis and optimisation (SBAO)

Among the challenges for design optimisation problem is the associated computational cost. For design engineering problems, expensive high fidelity computer simulations such as the CFD simulations in this study are required to evaluate the goodness of a design. As explained earlier, the GA requires this information to rank the 'fitness' of each design so that a Pareto-optimal solution can be sought. This will mean that hundreds, if not thousands, of expensive CFD simulations are required before the GA can search for the Pareto-optimal solution. This is not computationally feasible thus an alternative method is required. One such method that can be used is the surrogate-based analysis and optimisation (SBAO) technique. The term 'surrogate' refers to the method of surrogate modelling where expensive high-fidelity computer simulations are replaced with low-fidelity approximations. SBAO aims to speed up the optimisation process and has been shown to be effective for multi-objective optimisation problems (Queipo et al., 2005). The general principle of surrogate modelling is to model a smooth function from a discrete data set. Consider a smooth function representing a response variable, y, which may be obtained from measurements or computer simulations. The relationship between y and the input variable, x, can be written as in Equation 5-1.

$$y = f(x) + \epsilon \tag{5-1}$$

$f(x)$ and ϵ represents the expected response of the model and error, respectively. The aim now is to find a relationship between $f(x)$ and x so that the expensive computer simulation can be replaced by a low-fidelity model.

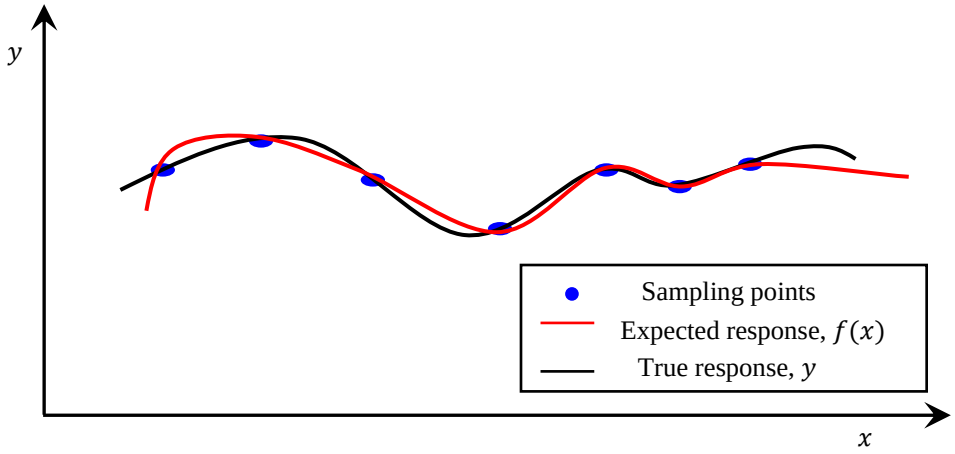

Figure 5-3 Prediction of a true response function from sampling points

5.5.1 Design of Experiments (DoE)

As depicted in Figure 5-3, if several high-fidelity data points are available, a model can be constructed to predict the outcome of y. The number of data to be sampled can be determined through a Design of Experiments (DoE) technique. The aim of the DoE is to minimise the number of experiments so that enough information can be obtained to find the relationship between y and x. By doing this, the time cost of the experiments can be reduced because only selected experiments are required to be conducted. The classical DoE technique is based on three basic principles which are; randomisation, replication and blocking (Montgomery, 2006). These basic principles are used for controlling and minimising the noise and bias in the data set when conducting physical experiments. However, for computer simulations such as performed in this study, the noise and random error in the data set no longer exist. This is because the output values obtained from computer simulations are deterministic in which no randomness is involved. In other words, the computer simulation will always output the same y value from a given set of input values (x). Therefore, applying the above-mentioned basic principles of DoE to computer simulations is not valid.

For deterministic computer experiments, the DoE technique is no longer used to find the relationship between y and x. Instead, the aim now is to predict the true response of y at any given set of x. Hence, the experiments or in this case the simulations performed should cover the entire region of the design space. Running the simulation across the design space can be costly, so a space-filling design technique is often preferred. The space-filling design spreads out the design points uniformly across the design space so

that a large region of the design space can be evaluated with relatively less computing resources. This allows for a high-order model to be used to approximate the response over the entire design space. An example of a space-filling design sampling method is a Latin Hypercube Sampling (LHS) method (Mckay et al., 1979). LHS is a stratified sampling technique intended for ensuring that each region of the design space is represented evenly. This is achieved by dividing x into N strata (intervals) and random samples are taken for each stratum. An example of an LHS sampling outcome for problems with two factors (x) is shown in Figure 5-4 where each x is divided into 10 strata. The blue circles represent the sampling points generated for x_1 and x_2. It can be seen that the sampling method ensures that each interval of x is represented by a data point and hence, this replaces the need to simulate each point in the stratum. The response of the sampled input data is then obtained through computer simulations for constructing the model.

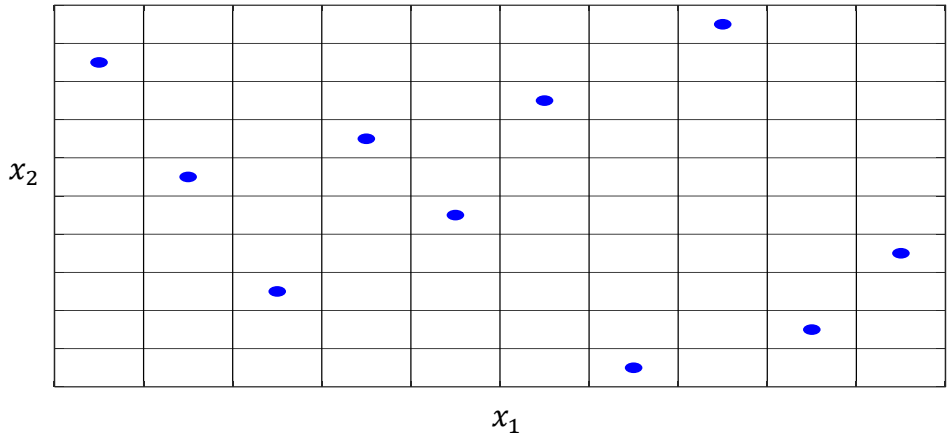

Figure 5-4 Example of LHS method for generating distributed sampling points across the design space

5.5.2 Surrogate model selection

The selection of the model depends on the dimensionality of the optimisation problem. The term dimensionality here refers to the number of input variables that are considered for the optimisation problem. Design optimisation problems often deal with high-dimensionality where three or more design features are considered as input variables. In addition, the correlation between input variables cannot be ignored when constructing the model. This is one of the reason why polynomial models are not reliable for modelling problems in high dimensions (Bishop, 2006). Polynomial models are limited by the increase of the number of independent coefficients that grows proportionally to number of

input variables (dimensions) raised to the order of the polynomial model. Simple polynomial models include quadratic and cubic equations.

The complexity of modelling high dimensionality data can be overcome by using supervised-learning algorithms. Supervised-learning algorithm is a computational process of predicting 'unseen' data from a 'seen' dataset. In other words, the algorithm is 'trained' using available dataset in order to predict the response variable. The training dataset can be obtained from the sampling method discussed earlier. Some examples of supervised learning algorithms are Artificial Neural Networks (ANN) and Random Forest (RF).

ANN is an algorithm that is based on the functionality of a human brain. ANN may consist of single or multiple layers of neurons that can be trained to map input data to the output. With enough training data, the algorithm can be used for predicting the response of the input data. The ANN algorithm has been applied for design optimisation problems such as those reported by Pierret and Braembussche (1999) and Mengistu and Ghaly (2008). RF is an algorithm that makes predictions based on an ensemble of Decision Trees (DT). RF was developed by Breiman (2001) and can be considered as a relatively newer method when compared to ANN. RF has been applied to various fields and has shown to be on par when compared to other predictive models (Verikas et al., 2011). Ahmad et al. (2017) compared the performance of RF against ANN in predicting building energy consumption. It was found that ANN slightly outperforms RF in terms of accuracy but RF is found to be more effective when handing missing data. Han et al. (2018) compared the performance of RF against two other models; ANN and support vector machines (SVM) for turbomachinery component fault diagnosis. From the comparative study, it was shown that RF has a better diagnostic performance even with a relatively small training data set. Williams and Cremaschi (2019) evaluated the performance of various models for design space exploration and also surrogate-based optimisation problems. RF is found to perform poorly when predicting the actual output values when compared to ANN. Despite failing to accurately predict the actual output values, RF managed to capture the overall trend of the test function. RF was able to accurately locate the minima of the function in comparison to other models. For this reason, it was concluded that RF is more suitable for surrogate-based optimisation problems rather than for design space exploration.

5.5.3 Random Forest (RF)

As mentioned earlier, RF is adapted from a Decision Tree (DT) model. DT makes prediction by splitting the input design space to create multiple sub-regions. The splitting is stopped once the number of data points in each sub-region reaches a certain number. The predicted output value is the mean value of the region it belongs to. An example of a DT is depicted in Figure 5-5.

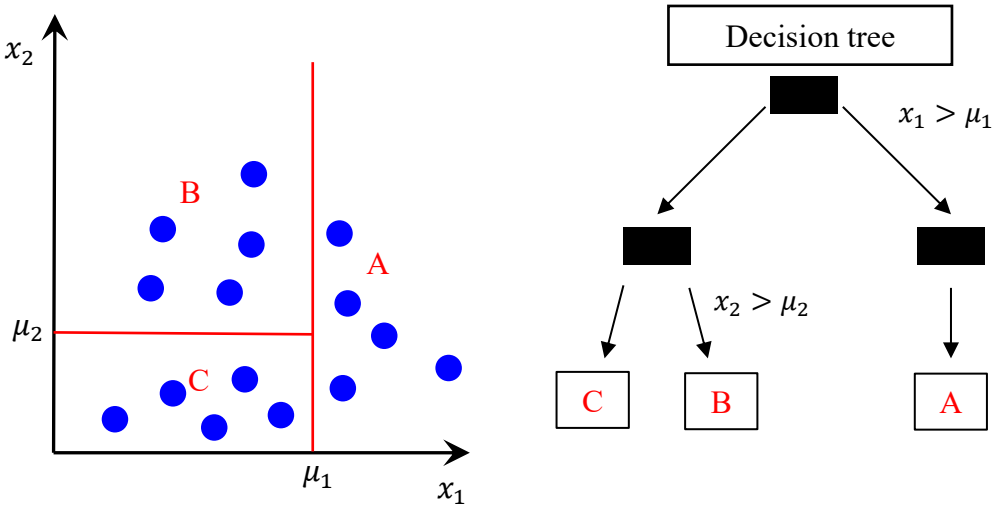

Figure 5-5 Decision Tree approach for predicting an output value

In the illustration, x_1 and x_2 are the input design variables or also known as predictors, p. The design space is subdivided based on parameters μ_1 and μ_2. μ_1 and μ_2 that are obtained by finding the split with the least residual sum of squares (RSS) as shown in Equation 5-2. Further explanation regarding the method to obtain the best split can be found in (Cutler et al., 2011)

$$RSS = \sum_{i=1}^{n} (f(x)_i - \hat{f}(x))^2 \tag{5-2}$$

Here, n is the number of data points in the design space, $f(x)_i$ is the i^{th} output variable and $\hat{f}(x)$ is the mean of the output variables. The splitting is stopped until the number of data points in each subdivided region reaches a certain value. In this example, all sub-regions A, B and C contain 5 data points. The routine for subdividing the design space can be represented as a structure that resembles a tree hence the name DT. The output can

be predicted by following the 'branch' that satisfies the decision criteria. For instance, if the input variable has a value of $x_1 > \mu_1$, then the predicted value falls within region A. The mean of all data points in region A is the predicted output value.

One of the disadvantages of DT is that the model tends to 'overfit' the training data. 'Overfit' means that the model has captured all the noise in the training data and this will cause the model to only be able to predict the output values based on the data that it was trained on. This is not desirable since the goal of the model is to predict 'unseen' data from a set of training data. In order to overcome this problem, Breiman (2001) proposed a model that combines multiple DT hence the name Random Forest. The method of generating multiple DT is referred to as 'bootsrap aggregating (bagging)' (Breiman, 1996). `Bagging' helps to overcome overfitting by reducing the bias of the DT when making a prediction. `Bootstrapping' is a sampling with replacement technique used to create multiple new samples of training data from the original training data set. Each tree will therefore be trained on different subsets of the training input data. In order to guarantee uniqueness of each tree, the predictor used as split candidates are randomly chosen. This is important to make sure that the trees are not correlated. For regression analysis as in the current study, the number of input variables chosen for the split is equal to $^{p}/_{3}$, where p is the number of predictors. The randomness in choosing the input variable for the splitting criteria is the reason why the word 'random' is attached to algorithm name. The output variable is then obtained by taking the average value of predictions of each tree.

5.6 Implementation of SBAO

This section presents the implementation of the SBAO to the casing groove design procedure. Figure 5-6 shows the flowchart of the SBAO routine. The first step of the SBAO routine is to obtain sampling data for constructing the surrogate model.

5.6.1 Sampling of input casing groove designs

The input design parameters required for the LHS method is shown in the inset of Figure 5-6. Design parameters z', w', H and α are the normalised groove axial position, groove upper width, height and the upper internal angle, respectively. All parameters except α are normalised by the $c_{ax,t}$. The upper and lower limit of the design space is shown in Table 5-2. The limits are the boundary used for generating a total of 100 casing groove

designs using the LHS method. The limit of the design boundary is chosen based on the previous parametric groove design studies on Rotor 37 as found in (Sakuma et al., 2013), (Qin et al., 2013) and (Kim et al., 2011). Result of the LHS method is shown in Figure 5-8.

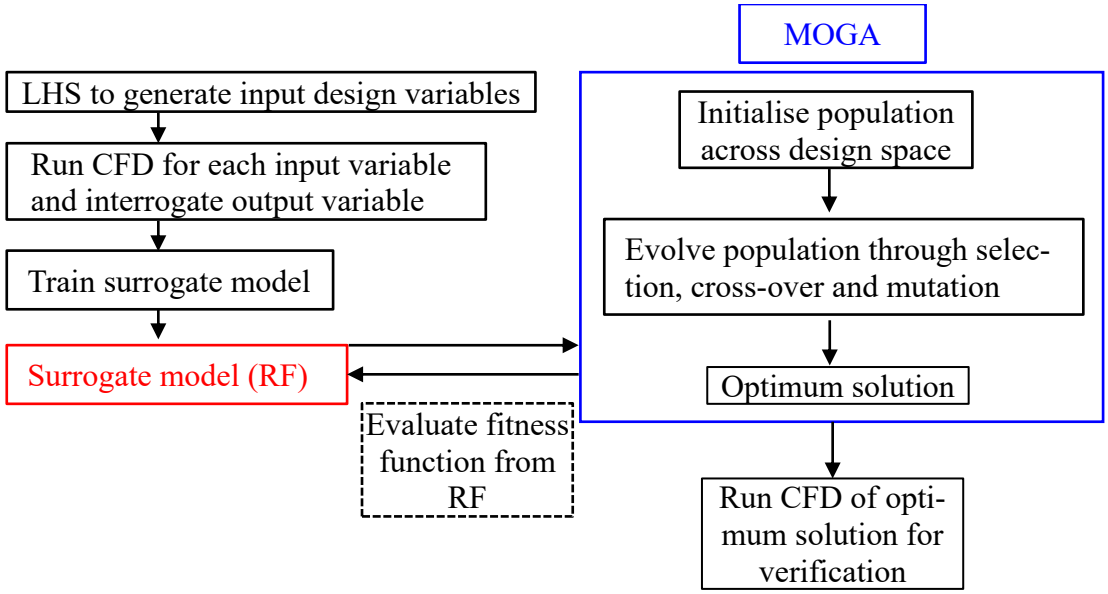

Figure 5-6 SBAO architecture flow chart

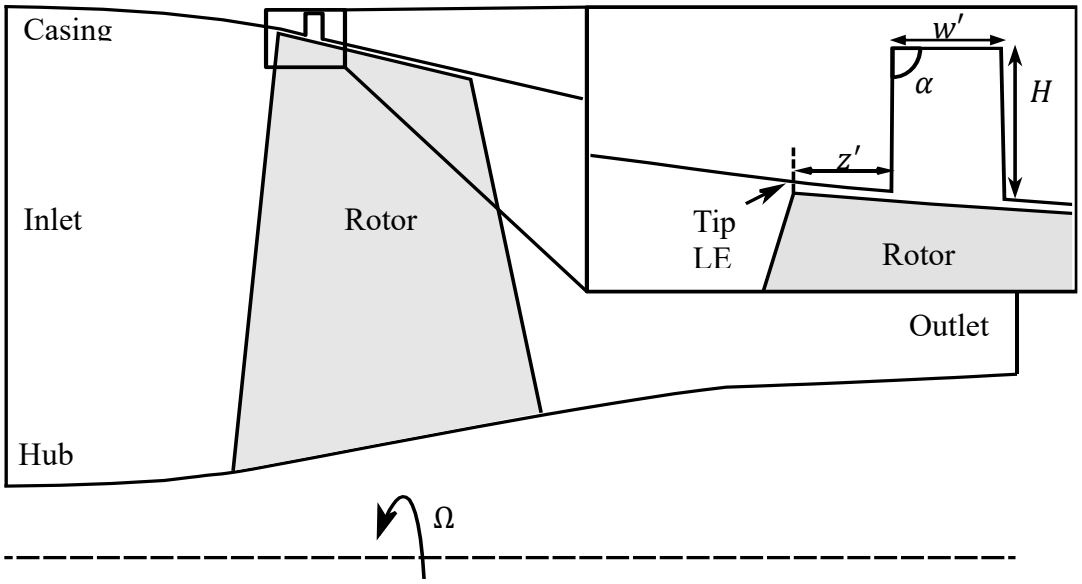

Figure 5-7 Casing groove design parameters

Table 5-2 Design space boundary of the single casing groove design

	z'	w'	H	α^o
Lower	-0.2	0.05	0.1 w'	90
Upper	1.2	0.2	5 w'	115

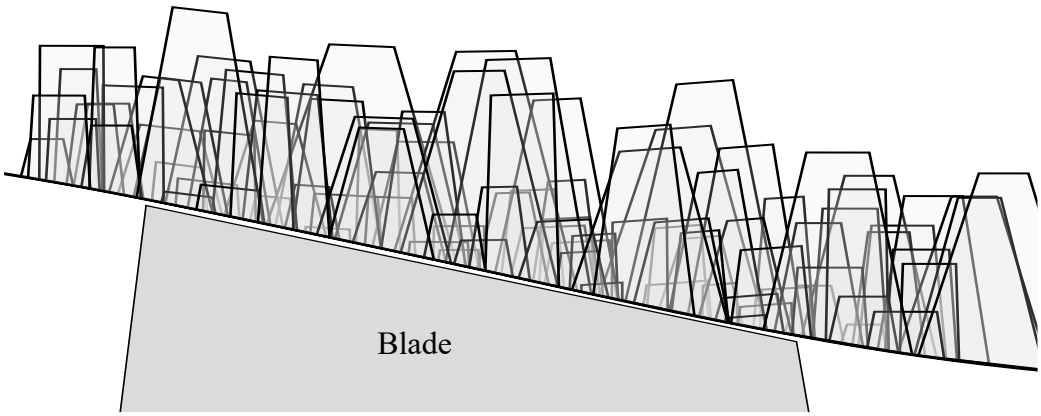

Figure 5-8 Casing grooves generated using LHS method

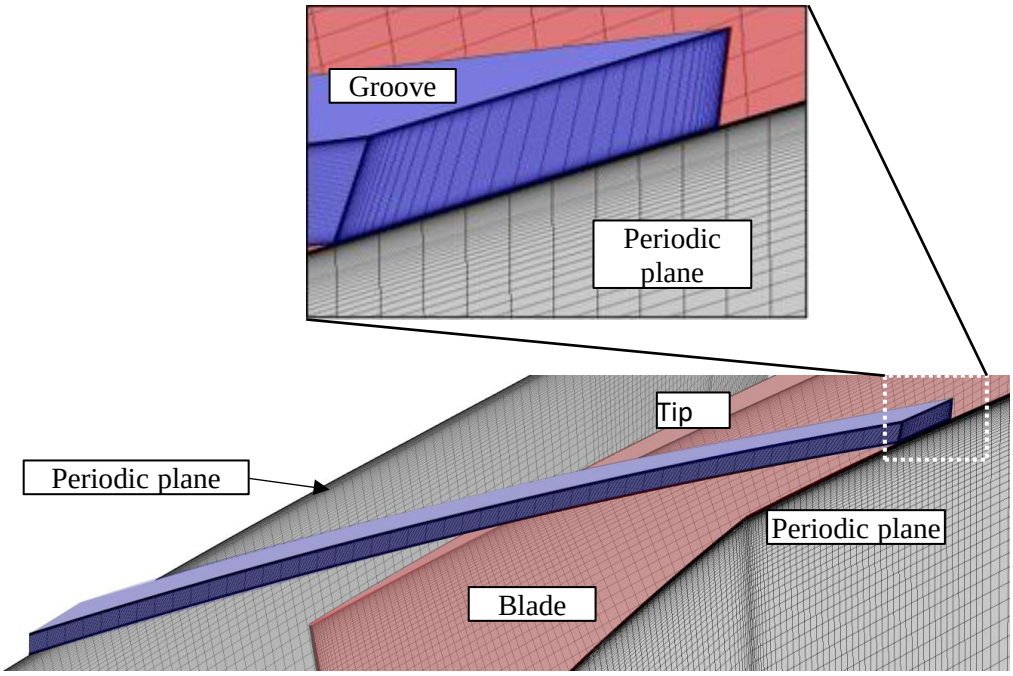

Figure 5-9 Casing groove meshing strategy

All the 100 input groove designs are simulated for obtaining the desired training output values. For the purpose of explaining the meshing strategy for the generated casing grooves, the domain and grid for a selected groove is shown in Figure 5-9. The casing

groove has about 180, 000 grid points. As shown in the inset of Figure 5-9, the ends of the groove domain are aligned with the periodic walls of the blade domain so that a matching interface can be created. Since the groove and rotor domain have a matching interface, the entire domain can be treated as a single body in the rotating frame of reference. This avoids for using multiple frame change models and also mixing plane models which may introduce unwanted numerical error. The groove and rotor domains are connected via a General Grid Interface (GGI) (ANSYS CFX 17.1 Documentation). A GGI connection allows for a non-overlap boundary condition so that the casing regions that do not overlap with the groove are treated as a no-slip, adiabatic and impermeable wall. Hence, any parametric study on the groove will only require modifications to the groove domain without any change to the blade passage grid.

All the input casing groove designs thus generated are then numerically simulated at conditions near stall. The boundary conditions used for simulating the input training data is same as operating point 8 in Figure 4-1. All the simulations performed use the same convergence criteria as explained in Chapter 3.

5.6.2 Objective functions

In a nutshell, the aim of the optimisation is to find the best groove that reduces the peak blockage with the least efficiency penalty. From the literature as discussed in Chapter 2, the SMI gain from casing grooves can be attributed to the reduction of the near casing blockage. The near casing blockage quantification as shown in Figure 4-21 shows that the location of the peak blockage is about 20% of $c_{ax,t}$ aft of the tip LE at point 10. Therefore, the first objective function, f_1, chosen for generating the output training data is the Ψ_m at 20% of $c_{ax,t}$ aft of the tip LE. The peak blockage is chosen because this blockage is related to the shock-TLV interaction which is the responsible for the onset of stall. The second objective function, $1/f_2$, is the η evaluated for the top 20% span. The second objective function f_2 is written as an inverse because, as previously shown in section 5.2, the optimiser aims to minimise the function. Minimising the inverse would therefore mean finding the groove design with the maximum top 20% η.

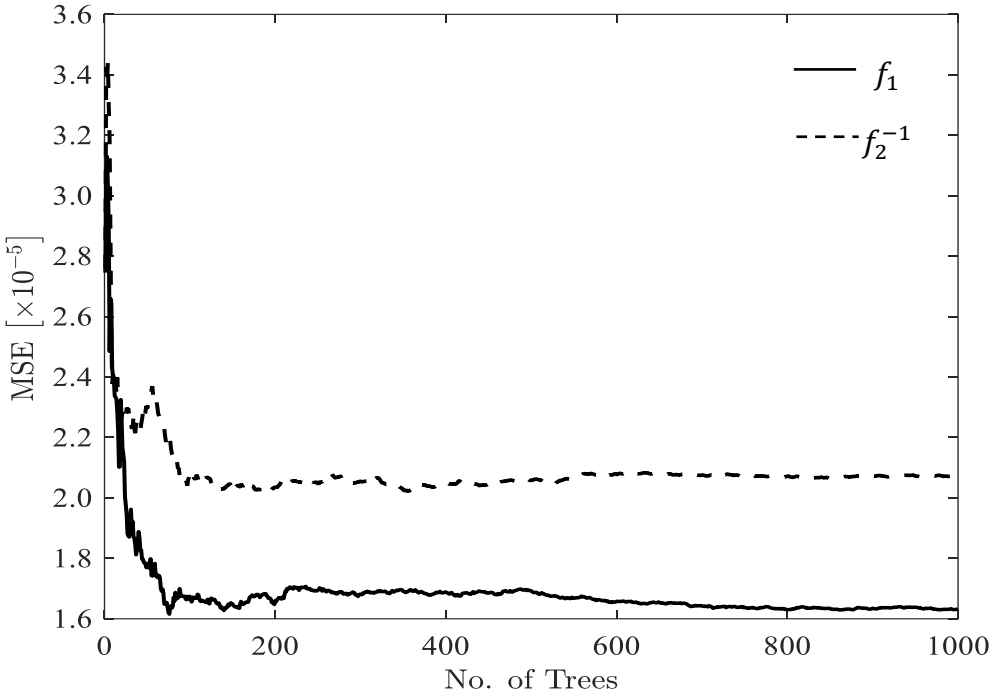

Figure 5-10 Mean squared error of RF model

5.6.3 Training and validation of RF

For building the RF, two hyperparameters are required. The first hyperparameter is the splitting stopping criteria. As explained previously, the data is split into subregions until a certain number of data resides in that region. The terminal number of data point in the subregions is known as the number of 'leaves'. For regression analysis, the number of 'leaves' suggested by Breiman (2001) is 5. The second hyperparameter required is the size of the 'forest' by choosing the number of the trees. The 'bagging' method explained earlier is useful for determining the number of trees. Since a sampling with replacement technique is used for generating each DT, about a third of the training data is left out in the training process. The data left-out is referred to as the 'Out of Bag' (OOB) data (Cutler et al., 2011). The advantages of the OOB data is twofold. First, the OOB data can be used for testing the predictive performance of the RF since these data has not been seen by the trees. Secondly, the size of the forest can be determined from the OOB data. The mean squared error (MSE) as shown in Equation 5-4 can be plotted for each tree as shown in Figure 5-10.

$$MSE = \frac{1}{n}\sum_{i=1}^{n}\left(f(x)_i - \hat{f}(x)_i\right)^2 \tag{5-4}$$

Here, n is the number of OOB data, $f(x)_i$ is the i^{th} output training data and $\hat{f}(x)$ is predicted output value. The MSE for f_1 and f_2 are shown as the size of the RF is increased by increasing the number of trees. The MSE of the RF stabilizes after a few hundred trees which suggest that increasing the size of the forest will not affect the accuracy of the model. Hence, from this exercise, it was the decided that number of trees required for the model is no more than1000 trees.

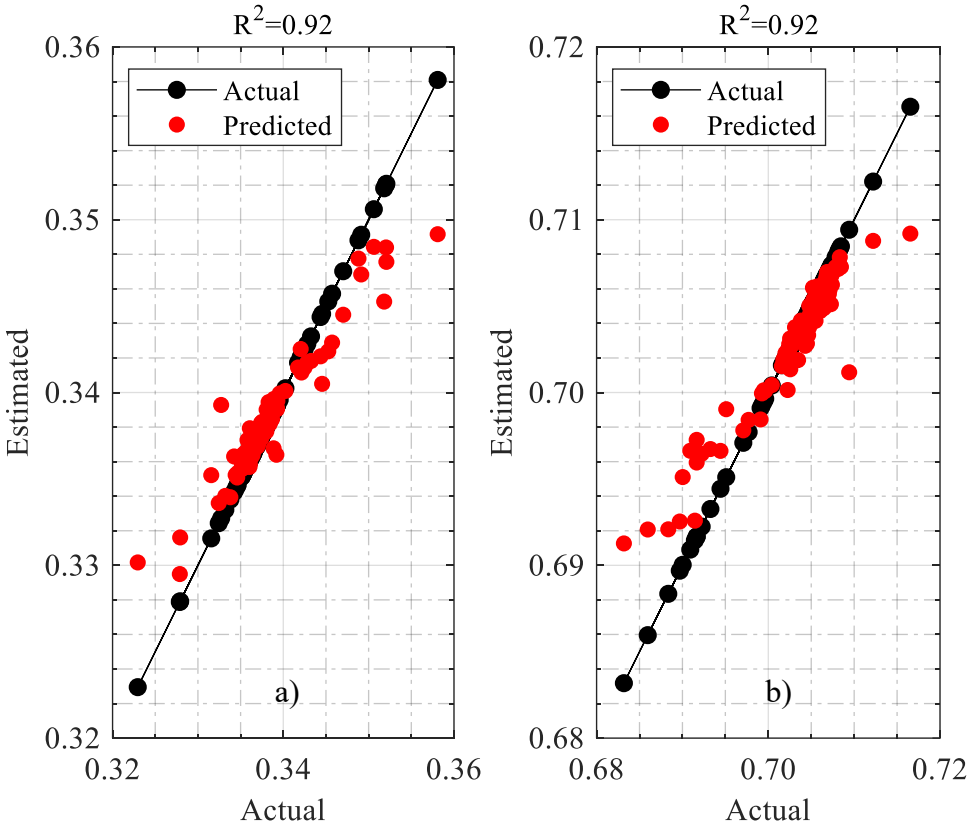

Figure 5-11 R^2 value of the model for f_1 and f_2

Another method of evaluating the predictive performance of the RF is by calculating the coefficient of determination or otherwise known as the R^2 value. Figure 5-11 shows the R^2 value plotted for f_1 and f_2.The R^2 value is used in regression analysis to evaluate the performance of a statistical model. The definition for the R^2 is shown in Equation 5-5.

$$R^2 = 1 - \frac{\sum_i^n (f(x)_i - \hat{f}(x)_i)}{\sum_i^n (f(x)_i - \bar{f}(x))} \tag{5-5}$$

Here, n is the number of training data, $f(x)_i, \hat{f}(x)_i$ and $\bar{f}(x)_i$ are the i^{th} output training data, i^{th} predicted output value and the mean output data. R^2 is a measure of the goodness

of the fit of a model. The term $\sum_i^n (f(x)_i - \hat{f}(x)_i)$ equals to zero for a perfect fit which results in an R^2=1. Thus, an R^2 value closer to unity represents a good model that can approximate the output values. The R^2 value for f_1 and f_2 is 0.92 which suggest that the model is well trained and able to predict the output value with an acceptable level of accuracy.

5.6.4 Multi-objective Genetic Algorithm (MOGA)

The set-up of the MOGA code is based on the default parameters of the MATLAB global optimisation toolbox. Parameters for the MOGA code are specified in Table 5-3.

Table 5-3 Set up of the MOGA code

Initial population	50
Tournament size	4
Mutation	Adaptive feasible which is randomly generated based on the previous population
Cross-over	Randomly chosen from parents to create offspring
Stopping criteria	Algorithm is stopped if one of the following criteria are met first. 1. maximum number of generations 2. Average change in Pareto front spread is below 10^{-4}.

5.6.5 Verification of the Pareto optimal solution

Figure 5-12 shows the Pareto front obtained from the SBAO routine. All the obtained Pareto-optimal solution are run through CFD for verification. The cases are simulated using the same boundary conditions as point 10 in Figure 4-1 which represents the last converged solution of the smooth casing. For each solution, the numerical stall point is found using the same method explained in Chapter 3. Three cases that converged with highest possible backpressure are indicated by the filled circle in Figure 5-12. All the Pareto-optimal casing groove designs are shown in Figure 5-13 where the three best cases are highlighted in red. The design specifications of the Pareto-optimal groove solutions are shown in Table 5-4 where the three best cases are shaded in gray. It can be seen in Figure 5-13 and Table 5-4 that the axial coverage of the three best cases are within the

0.17 and 0.22 z' region. This is the region where the peak of the blockage is located as shown previously in Figure 4-21. Further discussions regarding the effect of the groove and near casing flow are presented in the next chapter.

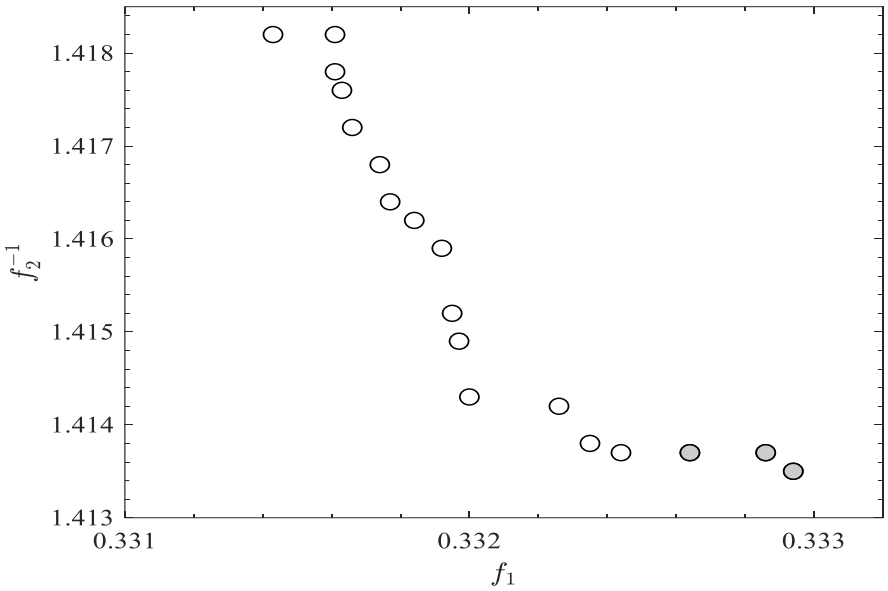

Figure 5-12 Pareto optimal solution of the SBAO routine

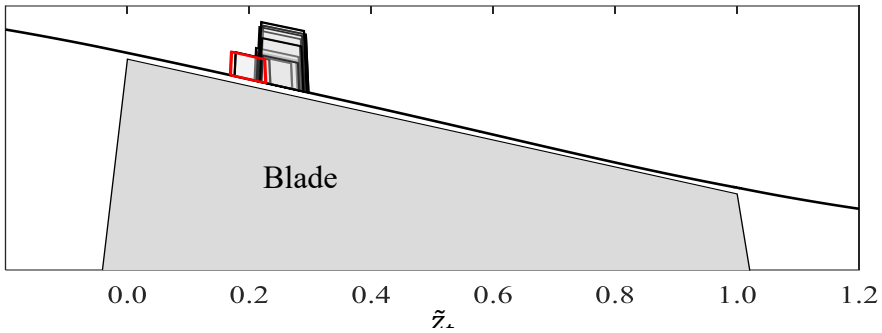

Figure 5-13 Pareto optimal solution of the casing groove design

Table 5-4 Design parameters of the Pareto-optimal groove solutions where the three best cases are shaded

z'	w'	H/w'	$\alpha(°)$
0.218	0.070	1.67	92
0.215	0.070	1.77	92
0.210	0.070	0.86	92
0.215	0.070	0.96	92
0.218	0.070	1.67	92
0.215	0.066	1.60	92

0.212	0.070	1.61	92
0.212	0.055	0.95	92
0.208	0.070	0.97	92
0.214	0.061	0.92	92
0.169	0.054	0.89	92
0.176	0.055	0.91	92
0.215	0.065	1.41	92
0.212	0.055	0.95	92
0.215	0.070	1.76	92
0.176	0.055	0.90	92
0.220	0.058	0.95	92
0.217	0.064	1.41	92

5.7 Summary

In this chapter, the design optimisation process of a single casing groove is discussed. The chapter begins by introducing the optimisation problem and the concept of Pareto-optimal solution. In the following section, the optimisation algorithm, Genetic Algorithm (GA) is introduced. The GA is based on a random search method algorithm which is useful when dealing with discrete data sets. Obtaining the response of input variables from numerical simulations such as in this study is computationally expensive. The computation cost of the optimisation is therefore reduced by using a surrogate-based analysis and optimisation (SBAO) method. The SBAO reduces the computational cost by replacing the high fidelity numerical simulations with a supervised learning algorithm, Random Forest. The accuracy of the RF model is assessed by calculating the MSE and R^2 value of the objective functions. The R^2 calculated for both objective functions are 0.92. In the last part, the implementation of the SBAO method to find the optimised single casing groove design is presented. Using the LHS sampling technique, a total of 100 casing groove designs are generated for the training input data set. The training output data is obtained from steady CFD simulations run at near stall operating conditions. The training data are used for constructing the RF model. The RF model is coupled to the optimiser algorithm to find the Pareto-optimal solution. All the Pareto-optimal groove designs are run through CFD to find the groove design that stalls at the highest back-pressure.

Chapter 6

Numerical Simulation of Rotor 37 with Grooved Casing

6.1 Overview

This chapter discusses the results from numerical simulations carried out on the Rotor 37 geometry with one or more casing grooves. First, the result of the optimised casing groove (as obtained through the procedure discussed in Chapter 5) is discussed by finding the SMI and efficiency change due to its implementation. The physics of the SMI due to the groove is discussed by comparing the near casing flow features with respect to the smooth casing. Next, the performance of the optimised groove at part-speed is investigated. This is to see if the optimised groove has any detrimental effects to the SMI and efficiency at part-speed conditions. The sensitivity of the optimised groove is investigated by axially varying the location of the optimised groove. Finally, the prospect of a multiple groove configuration is explored by combining single grooves.

6.2 Result of the optimised groove

6.2.1 Performance and analysis of the optimised groove

Figure 6-1 shows the three best casing groove designs obtained from CFD simulation of the Pareto optimal solution discussed in the previous chapter. One of the casing groove design as highlighted in red in Figure 6-1 is selected for further verification. Design specification of the optimised casing groove is shown in Table 6-1. This is done by obtaining the performance map of the optimum casing groove design as shown in Figure 6-2.

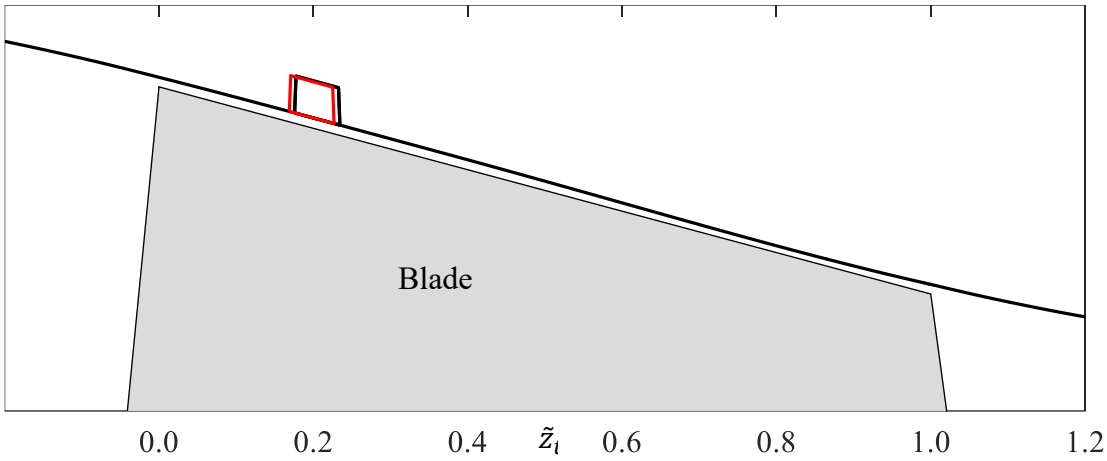

Figure 6-1 The best Pareto-optimal solution verified from CFD simulation

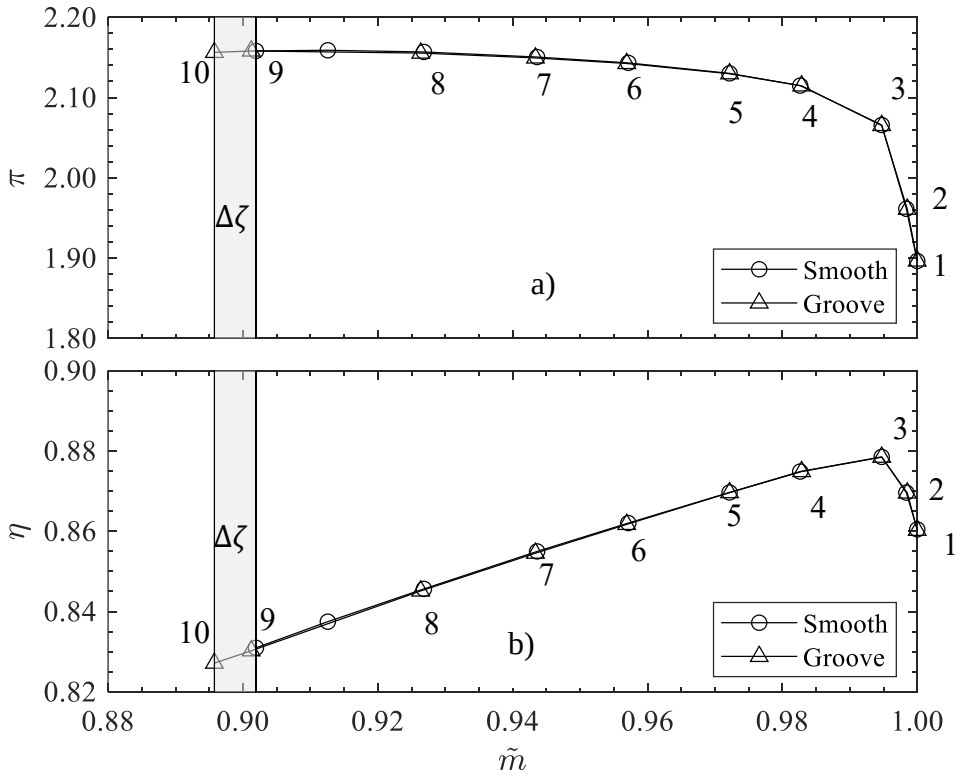

Figure 6-2 Comparison of the performance curve between smooth and the optimised casing groove. a) π and η.

Table 6-1 Design specification of the optimised casing groove

z'	w'	H	$\alpha(°)$
0.169	0.054	0.89 w'	92

The performance of the groove is evaluated by calculating the stall margin improvement, $\Delta\zeta$ as shown in Equation 6-1.

$$\Delta\zeta = \zeta_{GC} - \zeta_{SC}; \quad \zeta = 1 - \frac{\pi_4 m_{10}}{\pi_{10} m_4} \tag{6-1}$$

$\Delta\zeta$ is the percentage change of the stall margin, ζ, due to the casing groove. ζ is calculated from the values obtained at near design conditions (operating point 4) and the last stable operating point (operating point 10). The $\Delta\zeta$ of the optimised groove design is about 0.6%. To put this SMI value as achieved here in context, Qin et al. (2013) reported a stall margin improvement of about 0.7% with a variable depth multi-groove casing arrangement on Rotor 37. The groove configuration was achieved using an optimisation study using the Rolls-Royce proprietary optimisation suite SOPHY (SOFT-PADRAM-HYDRA). The effect of casing groove on η is relatively small ($< 0.1\%$) since it can be seen the η line for smooth and groove are overlapping as shown in Figure 6-2b). Sakuma et al. (2013) suggested that the attenuation of the tip leakage flow due to the casing groove explains why the casing groove has negligible effect on the rotor efficiency. Another plausible reason for this is due to the fact that the loss generation in Rotor 37 is dominated by the shock (Denton, 1997). Although the groove increases the wetted area that increases friction losses, the loss generated by the increased wetted area is probably small in relative to the losses generated by the shock.

6.2.2 Effect of groove on the tip leakage flow momentum

Figure 6-3 shows the c_p distribution at 99% span for the smooth and grooved casing at NS (operating point 8) conditions. At the pressure side (PS) upstream of the groove, the c_p reduces and subsequently increases underneath the groove. The reduction in c_p shows a drop in local static pressure which translates to an increase in local flow velocity as some of the tip flow enters the groove radially. At the suction side (SS) of the blade tip upstream of the groove, there is an increase in c_p before reducing slightly as compared to the smooth casing. The increase in c_p shows an increase in local static pressure which means that the local flow velocity at the SS upstream of the groove has been reduced due to the flow leaving the groove radially.

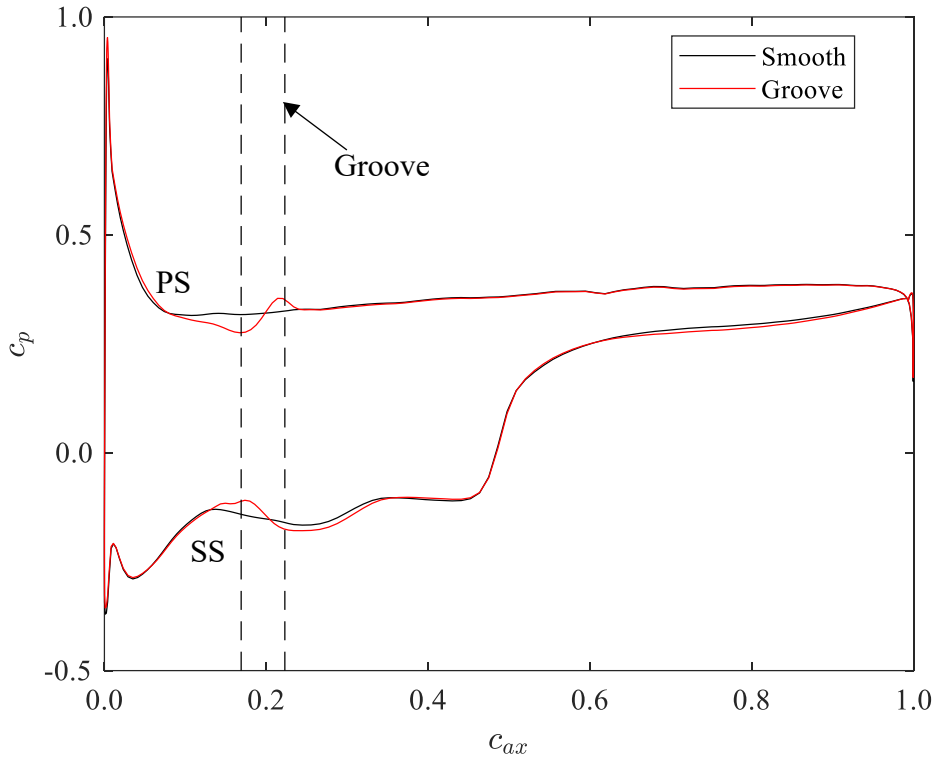

Figure 6-3 Blade static pressure distribution at 99% span at NS conditions for smooth and grooved casing

The variation of c_p profile due to the casing groove is caused by the radial pressure gradient across the groove cavity. Unlike for a smooth casing, the flow is restricted radially and the radial pressure gradient is small. The radial pressure gradient introduced by groove causes a radial transport of the tip leakage flow in and out of the groove cavity. As shown in Figure 6-4, the radial movement of the flow can be observed by plotting the normalised radial velocity, V_r, contour. V_r is normalised by the tip velocity,V_t. Positive V_r regions indicate a radially outward movement of the tip leakage flow into the casing groove. On the other hand, the negative V_r regions indicate a radially inward movement of the flow into the blade main passage. The flow from the passage is leaked into the groove from the PS due to the fact that the static pressure at the PS is higher. The negative region as seen at the SS correspond to an injection of the flow from the groove into the main blade passage. This is further illustrated in Figure 6-5 where the streamlines inside the groove are plotted alongside a cartoon that shows the features of the flow near the groove. In Figure 6-5a), the streamlines are coloured with radial velocity to show radial movement of the flow inside the groove. Arrows are also plotted on the streamlines for showing the direction of the flow. The red-coloured streamlines show a radially outward

movement whilst blue-coloured streamlines indicate a radially inward movement of the flow. The majority of the flow enters the groove near the downstream wall of the groove. At the same time, the flow inside the groove exits at the upstream wall of the groove into the blade passage at the blade SS. The cartoon in Figure 6-5b) illustrates the radial movement of the flow entering and exiting the groove.

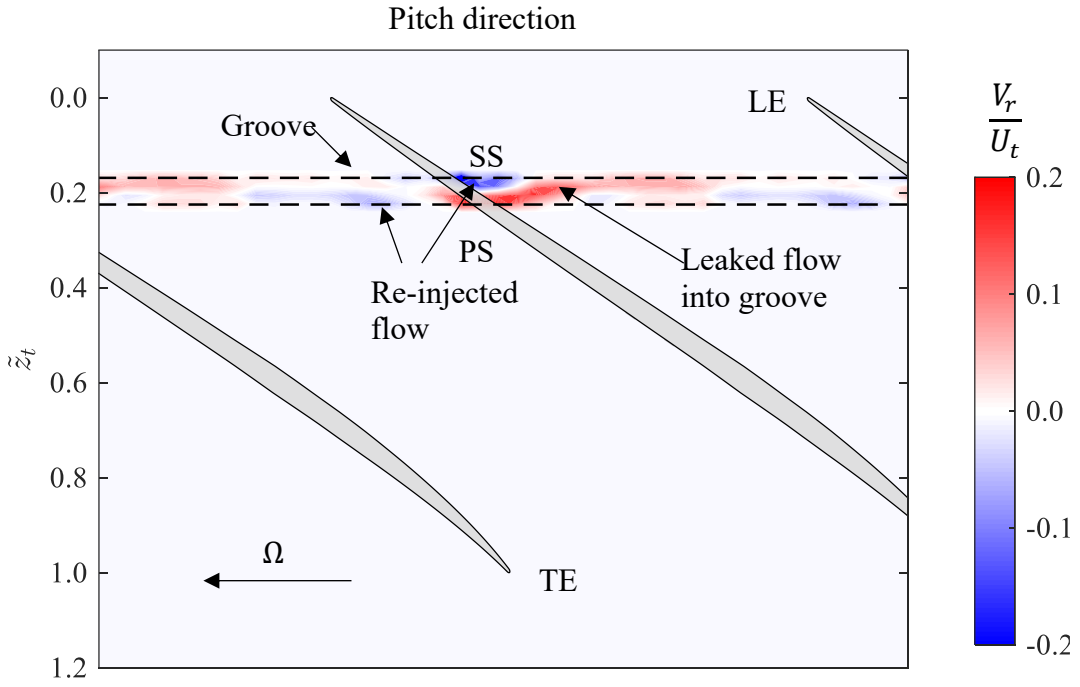

Figure 6-4 Casing normalised radial velocity contour at NS conditions for grooved casing

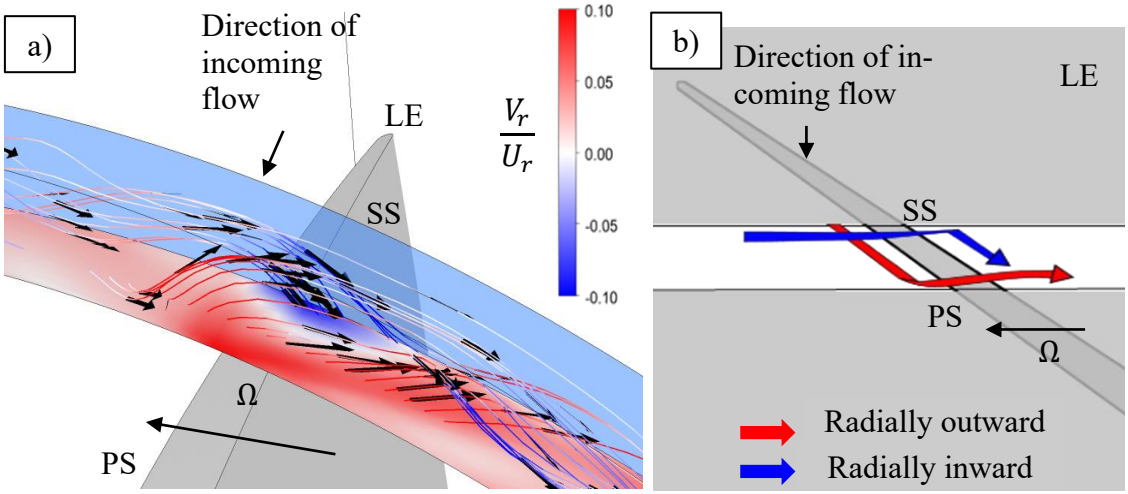

Figure 6-5 a) Streamlines(coloured with radial velocity) inside the groove and b) illustration of the radial transport of flow in and out of the groove.

As reported by Shabbir and Adamczyk (2005), the radial transport of axial momentum across the groove and blade main passage is the flow mechanism that is responsible for SMI. The radial transport of axial momentum which is not present in a smooth casing helps to balance near casing net axial pressure force across the blade. The effect of the groove on the tip leakage flow momentum at NS conditions is shown in Figure 6-6. The tip leakage absolute momentum inside the tip clearance gap and the respective momentum components are calculated using Equation 6-2 to Equation 6-5.

$$\Phi = \frac{\rho V_{\perp} V_{\perp}}{\bar{\rho}_1 (r_t \Omega)^2} \tag{6-2}$$

$$\Phi_z = \frac{\rho V_{\perp} V_z}{\bar{\rho}_1 (r_t \Omega)^2} \tag{6-3}$$

$$\Phi_\theta = \frac{\rho V_{\perp} V_\theta}{\bar{\rho}_1 (r_t \Omega)^2} \tag{6-4}$$

$$\Phi_r = \frac{\rho V_{\perp} V_r}{\bar{\rho}_1 (r_t \Omega)^2} \tag{6-5}$$

Quantities Φ, Φ_z, Φ_θ and Φ_r are the tip leakage absolute, axial, pitchwise and radial momentum respectively. All the quantities are calculated inside the tip gap region only and are normalised by tip momentum which is represented by the denominator of Equation 6-2 to Equation 6-5. $V_\perp$ is the local velocity normal to the tip camber. V_z, V_θ and V_r are the local axial, pitchwise and radial components, respectively. In Figure 6-6a) the absolute tip leakage momentum shows a reduction at the location where the groove is located. The reduction of the absolute momentum means that the strength of the tip leakage flow has been reduced. The Φ_θ as shown in Figure 6-6b) is the strongest compared to Φ_z (Figure 6-6c)) and Φ_r (Figure 6-6d)) because the tip leakage flow is driven by the pitch-wise pressure difference due to the blade rotation. Since momentum is conserved, the reduction of Φ_θ can only be explained by the changes in Φ_z and Φ_r due to effect of casing groove. In Figure 6-6c), it can be seen that the tip leakage axial momentum is negative from the tip LE up until 60% of $\tilde{z}_t$. The negative axial momentum is caused by reverse flow effect of the tip leakage flow. This reversal effect is however reduced for the grooved casing as compared to the smooth casing due to radial exchange of tip leakage flow momentum as previously shown in Figure 6-5. In Figure 6-6d), the reduction in Φ_r in the forward part of the groove is due to the flow exiting

from the groove closer to the upstream side of the groove. Φ_r, however, increases in the aft part of the groove due to the main flow migrating radially into the cavity.

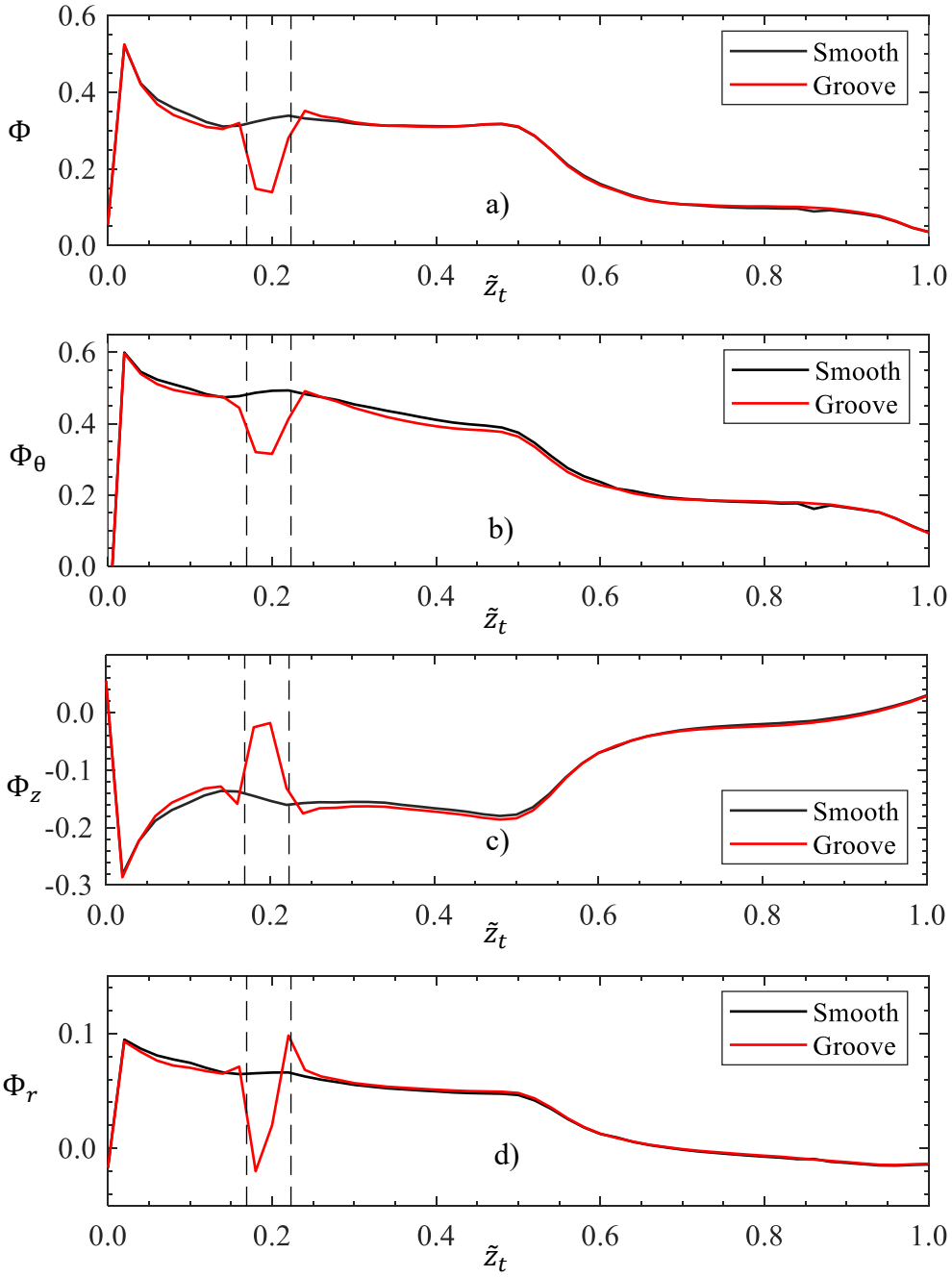

Figure 6-6 Comparison of absolute tip leakage momentum and the respective components for smooth and grooved casing. Tip leakage absolute (a)), pitchwise (b)), axial (c)) and radial (d)) momentum at NS conditions.

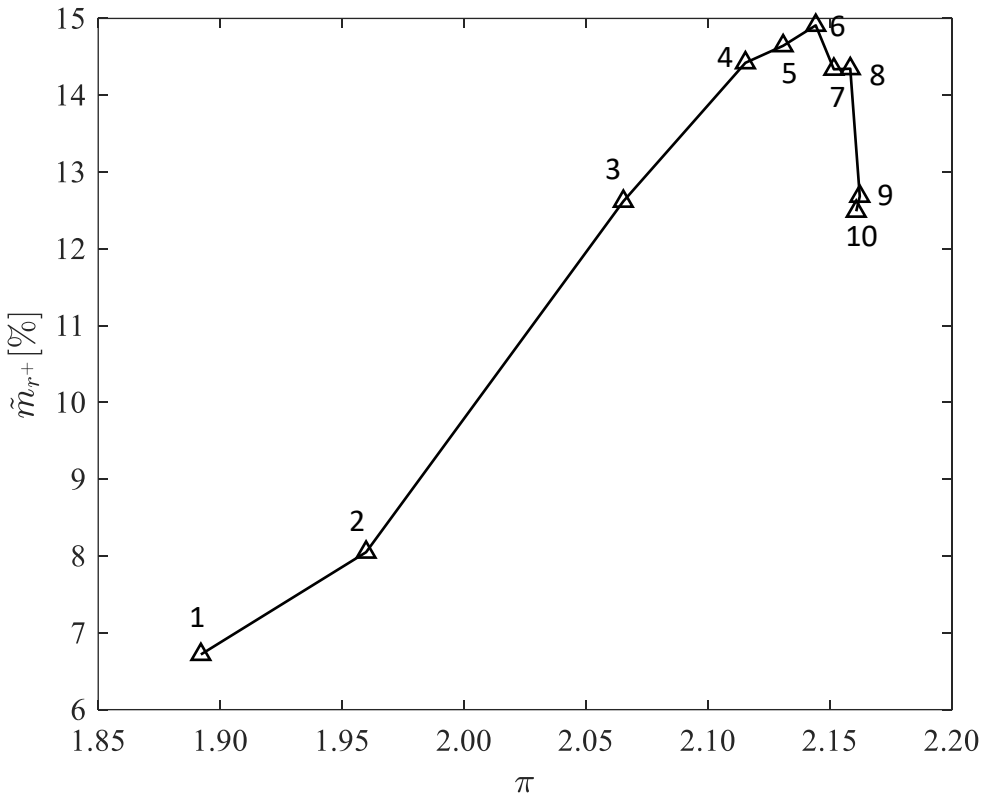

Figure 6-7 Mass flow leaked into the groove as a percentage of tip leakage mass flow plotted against π across all operating points

The amount of mass flow leaked into the casing groove can be calculated by summing the positive mass flow at the groove – main blade passage interface as shown in Equation 6-6. Only the sum of positive mass flow is required since by principle of mass conservation, the sum of mass flow leaked into the groove equals the sum of mass flow injected out into the main blade passage.

$$\tilde{\mathrm{m}}_{r^+} = \frac{\sum \rho V_{r^+} \Delta A_{int}}{\bar{\bar{\rho}} \bar{\bar{V}}_{\perp} A_t} \tag{6-6}$$

Here, V_{r^+} is the cells with positive radial velocity as shown in Figure 6-4. ΔA_{int} is the area of the grid cell with positive V_r at the groove interface. The term in the denominator is the tip leakage mass flow rate. A_t is the surface area of tip gap which is the arc length of the tip camber multiplied by the tip gap height. Figure 6-7 shows the amount of mass flow leaked into the groove, $\tilde{\mathrm{m}}_{r^+}$ as a percentage of the tip leakage mass flow plotted against π for all operating points shown in Figure 6-2. Since $\tilde{\mathrm{m}}_{r^+}$ is driven by the pressure difference, it can be seen that $\tilde{\mathrm{m}}_{r^+}$ increases from operating point 1 to 6. However, from

operating point 7 onwards, $\tilde{m}_{r+}$ shows a decreasing trend. The difference of $\tilde{m}_{r+}$ between operating point 6 and 10 is about 3% although there in a slight increase in π between the two operating points. This is due to the change of the structure of the vortex inside the groove as shown in Figure 6-8. The vortex in Figure 6-8a) is located close to the blade where the TLF is primarily leaked in to the groove. In Figure 6-8b), the vortex is located about the mid-pitch of the blade domain. It is believed that the roll-up of the vortex is caused by the negative axial velocity component of the tip leakage flow. Figure 6-9 compares the structure of the above-mentioned vortices at operating point 4, 6 and 8 using surface streamlines and the pitchwise vorticity contour. Plane P1($\theta \approx 0^{\circ}$) is located over the blade where the TLF is leaked into this groove and Plane P2 ($\theta \approx 5^{\circ}$) is located about near the mid-pitch blade passage. The pitchwise vorticity is positive in the direction of rotation. In P1, the direction of the pitchwise vorticity is counter-clockwise as depicted by Figure 6-8a). The vortex in P1 represents the majority of the flow that enters the groove through the blade PS. This type of vortex forms as the TLF is radially leaked close to aft wall of the groove. The second type of vortex as shown in P2 develops away from the blade near the mid-pitch. From operating point 4 to operating point 6 (low to moderate backpressure conditions) the size of vortex is comparable as shown in Figure 6-9a) and b). As the backpressure increases beyond operating point 6, the tip leakage flow jet strengthens which translates into an increased negative axial velocity component. As shown in Figure 6-9c), this results in a larger vortex that extends axially with respect to operating point 4 and 6. The increase in the size of the vortex disrupts the flow inside the groove that was previously travelling circumferentially. As a result of the reduction in the circumferential momentum within the groove, the mass flow entering the groove reduces. This makes the groove less effective in further removing low momentum fluid from the tip gap region.

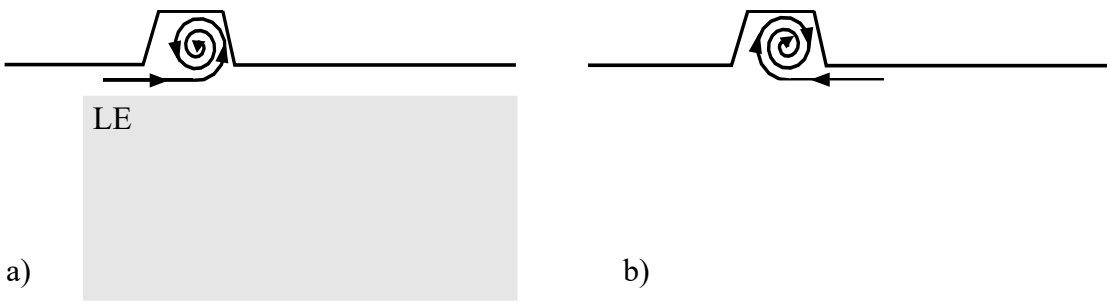

Figure 6-8 Illustration of vortices located inside the casing groove located a) over the blade and b) about the mid-pitch region of the blade passage.

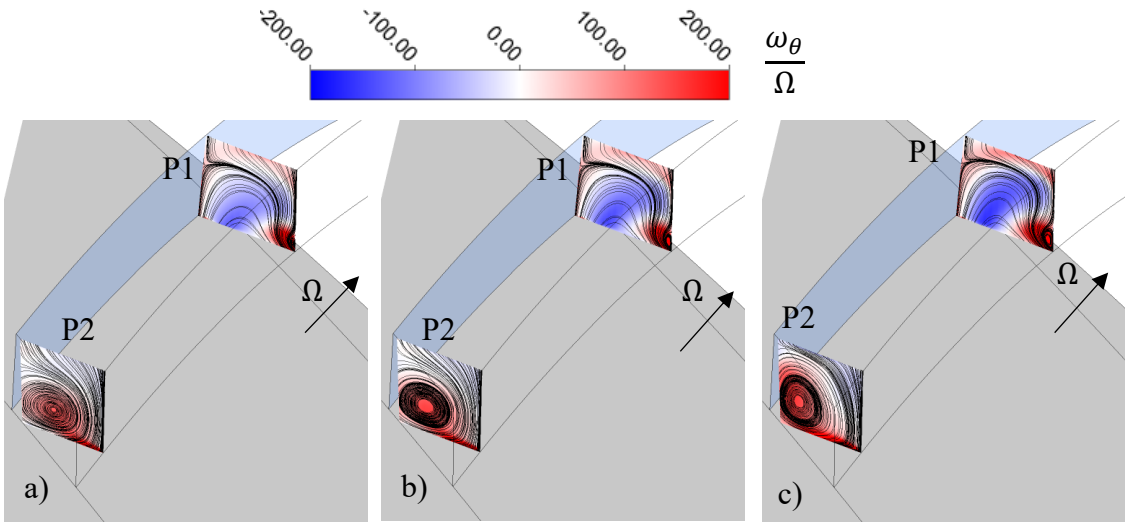

Figure 6-9 Pitchwise vorticity contour and surface streamlines on tow constant pitchwise planes, P1($\theta \approx 0^{\circ}$) and P2($\theta \approx 5^{\circ}$) inside the groove at operating point a) 4, b) 6 and c) 8.

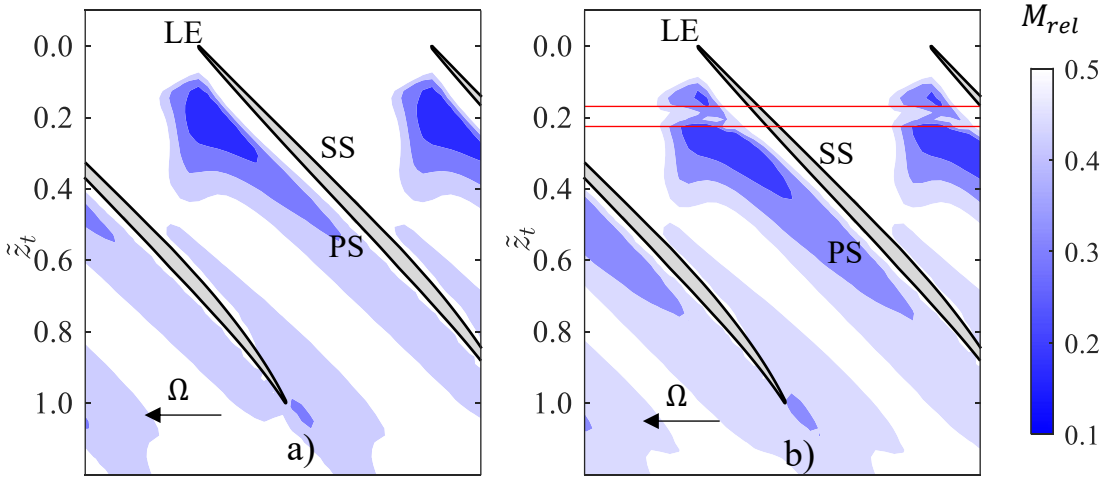

Figure 6-10 Comparison of Mach number contour plot inside the tip gap for a) smooth and b) grooved casing at operating point 8

For a smooth casing, there is no radial movement of mass flow. The effect of radial movement of mass flow on the tip gap blockage can be shown by plotting the Mach number contour inside the tip gap region at NS conditions as shown in Figure 6-10. It can be seen in Figure 6-10b) that the region under the groove has a relatively higher Mach number

region due to the radial movement of flow. As compared to the smooth casing, the blockage region of the grooved casing is split where the bulk of the blockage is located aft of the groove.

The effect of the groove on the blockage at NS conditions is shown in Figure 6-11. The shaded region indicates the effect of the groove on the blockage with respect to the smooth casing. It can be seen that the blockage located upstream of the groove is reduced before increasing and peaking aft of the groove. This is in line with what has been observed in Figure 6-10 where the groove causes the low Mach number region to be split and redistributed aft of the groove. The reduction of blockage as explained earlier is due to radial movement of flow into the groove. The increase of blockage can be attributed to the radial mixing of flow as the flow moves out of the groove. This effective shift in the peak blockage in the presence of the groove is thought to reduce the resistance in admitting flow at the front of the passage and in the process, delays the occurrence of stall.

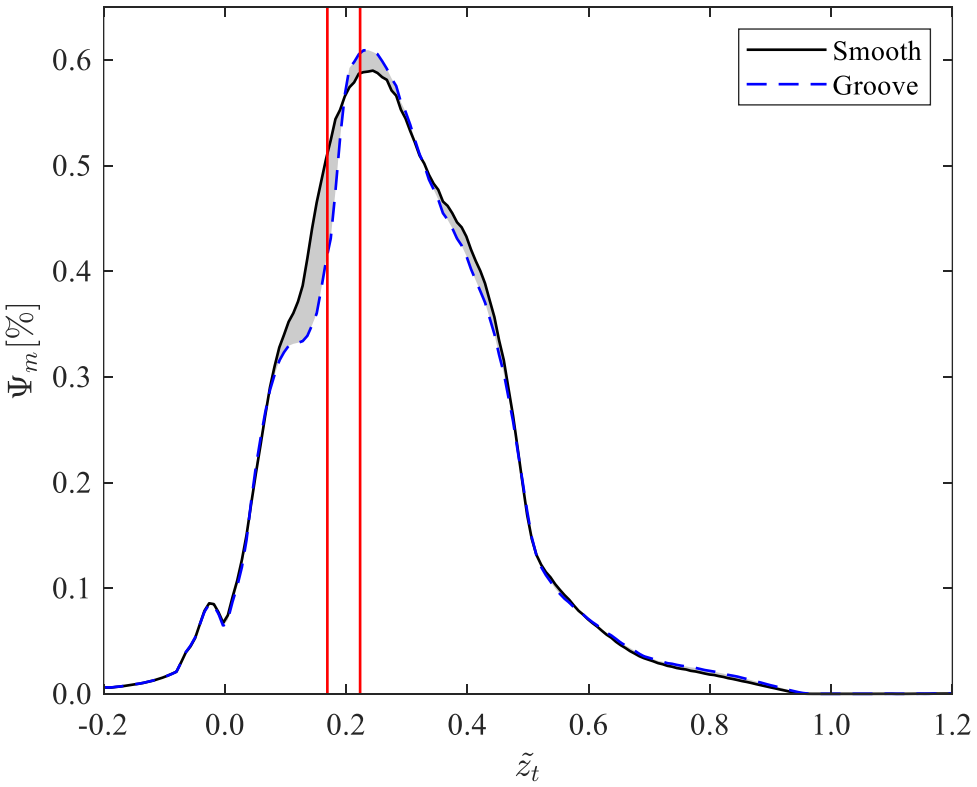

Figure 6-11 Comparison of Ψ_m between smooth and grooved casing at operating point 8

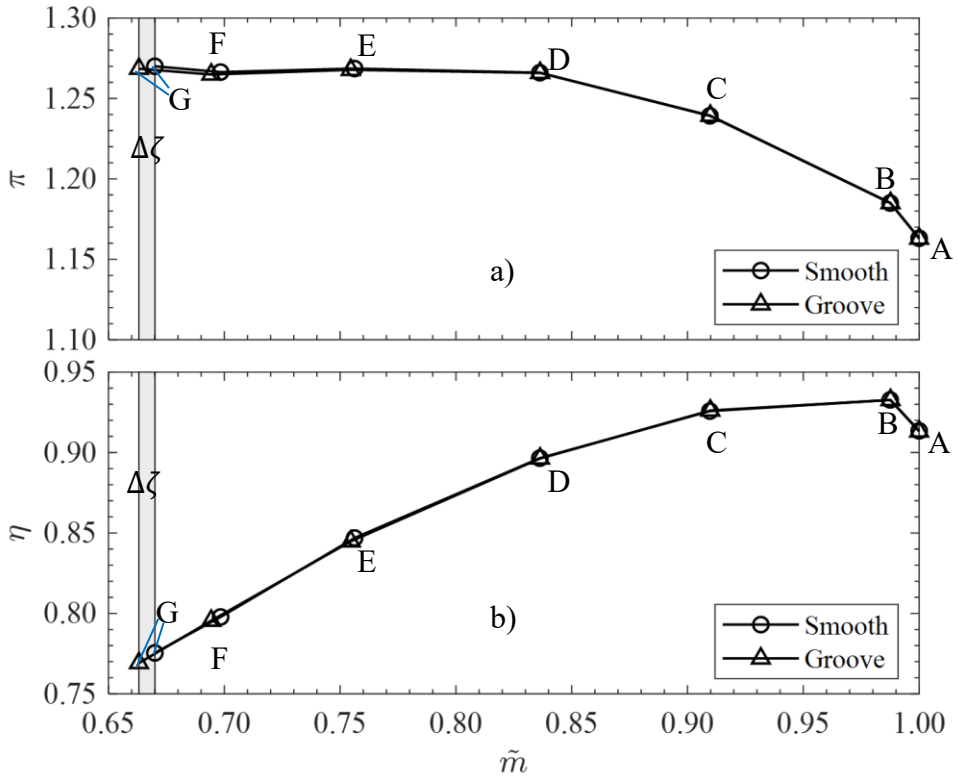

Figure 6-12 Performance characteristics at part-speed a) π and b) η

6.3 Effect of casing groove at part-speed

So far, the SMI of the optimised groove is only evaluated at design speed conditions. There is a possibility that the groove behave differently at part-speed conditions since the groove is optimised for conditions at design speed. For Rotor 37, the flow is reported to be passage shock free when run at 60% of design speed (Suder and Celestina, 1996). This allows for the evaluation of the groove performance with the absence of the shock-TLV interaction. Figure 6-12 shows the performance characteristics of the smooth and grooved casing at part-speed. The calculation here does not account for the changes in blade twist and tip gap height due to reduction in centrifugal force at part speed. Thus, the numerical result presented herein is not comparable to the real conditions measured in the experiment. Furthermore, the inlet conditions at part-speed is not known as is assumed to be the same as the inlet conditions at design speed. Operating point G is the last stable operating point for the smooth and grooved casing. These are found using the same convergence criterion as for the design speed case. The mass flow rate at each operating point is normalised by the mass flow rate at operating point A. The groove is found to give an SMI of 0.6% using the same definition as in Equation 6-1. Here, the operating point C in Figure

6-12 is taken as the reference operating point to calculate $\Delta\zeta$. In addition, the groove do not show any detrimental effect on the η since the η lines for the smooth and grooved casing in Figure 6-12 are found to overlap each other.

The reason for the SMI improvement at part-speed is investigated by comparing the Ψ_m at design and at part-speed conditions for several operating points as shown in Figure 6-13. Ψ_m is plotted for the top 20% span. Without the shock, the upstream movement of the peak blockage location is not as pronounced as compared to the design (high)-speed as shown in Figure 6-13.a). The peak of the blockage at operating point G is closer to the tip LE whereas at high speed the peak blockage location at the last stable operating point is located at 20% of $c_{ax,t}$ aft of the tip LE. In addition, the Ψ_m at part-speed shows a higher and broader peak as compared to the high-speed case. This is due the fact that the blockage is more distributed in the chord direction when the shock is absent. At high speed conditions, the blockage is dominated by the shock-TLV interaction which caused the blockage to be confined to a smaller region hence a relatively narrow peak as compared to the peak at part-speed. Furthermore, the height of the peak blockage is about 2 times higher as compared to design speed which suggest that compressors operating at lower speed can withstand relatively higher blockage than at high-speed.

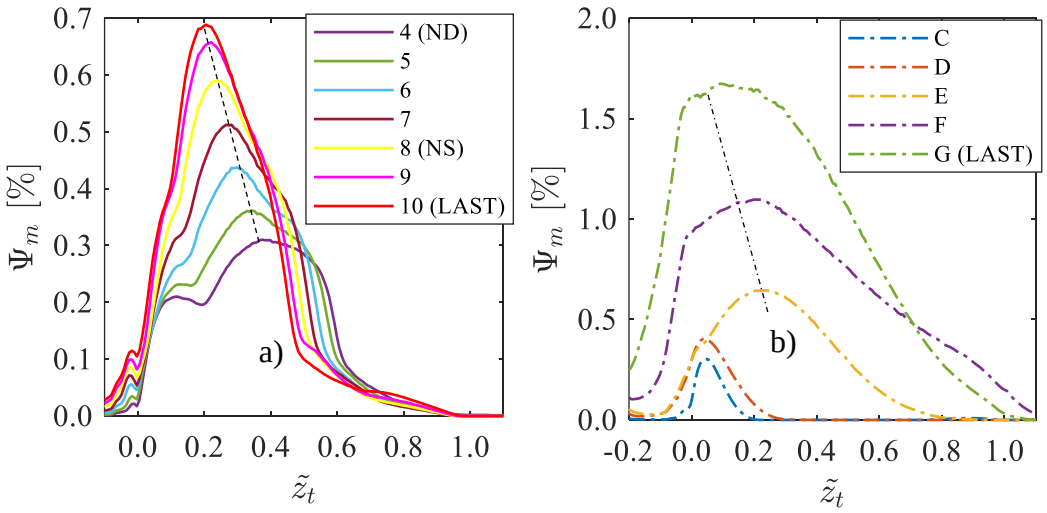

Figure 6-13 Axial distribution of Ψ_m at a) design (100%) speed and b) part (60%)-speed for selected operating points. The dashed line indicates the movement of the peak across the operating points.

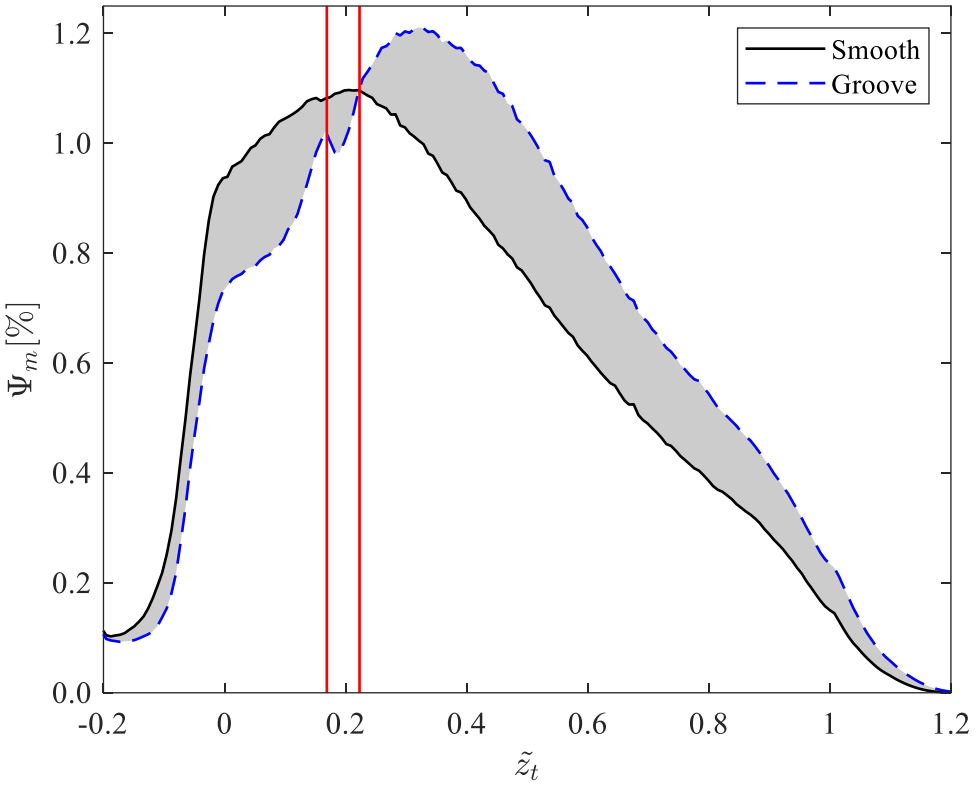

Figure 6-14 Comparison of axial distribution of Ψ_m at operating point F for smooth and grooved casing

Figure 6-14 shows the comparison the distribution of Ψ_m at operating point F from Figure 6-12 for smooth and grooved casing. The shaded region represents the difference of Ψ_m between smooth and grooved casing. A similar trend can be seen as in the high-speed case as shown in Figure 6-11 where the effect of the groove causes the peak blockage location to be shifted aft of the groove. By looking at the trend from Figure 6-11 and Figure 6-14, it seems to suggest that there is a limiting forward location for the peak blockage to exist before undergoing stall. Due to the groove, this peak blockage location is shifted further downstream so that there is more room for the compressor to operate at a reduced mass flow rate as compared to the smooth casing.

6.4 Effect of single groove location and multi-groove configuration

6.4.1 Single groove

In this section, the sensitivity of the single groove axial location is studied by axially varying the location of the optimised groove which henceforth will be referred to as groove S1. Groove S1 is moved upstream and downstream of its original location which results in groove S0 and S2, respectively as shown in Figure 6-15.

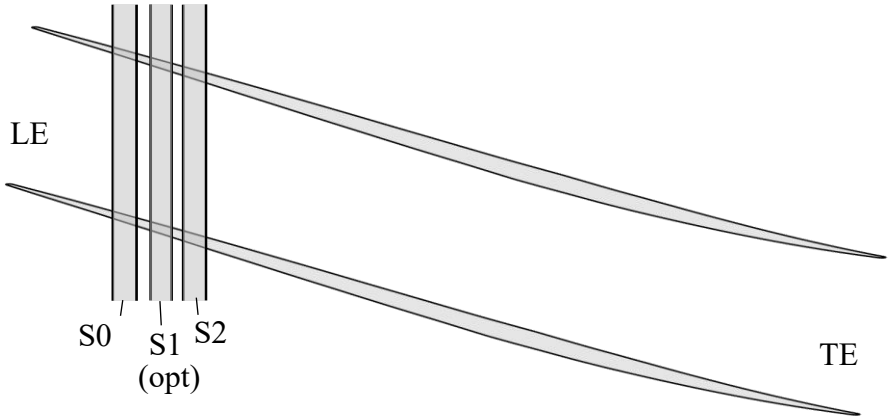

Figure 6-15 Relative position of single casing grooves (not to scale).

Table 6-2 Design specification of the single casing grooves

Groove	z'	w'	H	$\alpha(°)$	$\Delta\zeta$ [%]
S0	0.08	0.054	0.89 w'	92	1.3
S1 (optimised)	0.169	0.054	0.89 w'	92	0.6
S2	0.26	0.054	0.89 w'	92	0.13
M1 (S0+S1)	-	-	-	-	1.2
M2 (S1+S2)	-	-	-	-	0.5

As shown in Table 6-2, the grooves S0 and S2 are obtained by varying the value of z whereas the remaining parameters w', H, and α are kept the same as S1. Figure 6-16 shows the performance curve of the single grooves, S0 and S2 with respect to S1. The $\Delta\zeta$ of S0 and S2 as shown in Table 6-2 are 1.3% and 0.13%, respectively. From this, it can be said that performance of the groove is better when located upstream of the peak blockage location as the $\Delta\zeta$ of S0 is twice that of S1 which is the optimised groove. On the other hand, locating the groove downstream of the peak blockage is worse as S2 only manages to achieve a $\Delta\zeta$ of 0.13% which is less than S1. Despite the changes to $\Delta\zeta$ as the location of the groove is axially varied, it can be seen that there are no significant changes to η. The η curves of S0, S1 and S2 as shown in Figure 6-16b) are overlapping. A similar trend is reported by Sakuma et al. (2013). Using the same compressor as used for this study, it was found that axially varying the location of a single groove results in a negligible effect on the efficiency. It was suggested that this negligible effect of the single groove on η is due to the attenuation of the tip leakage vortex.

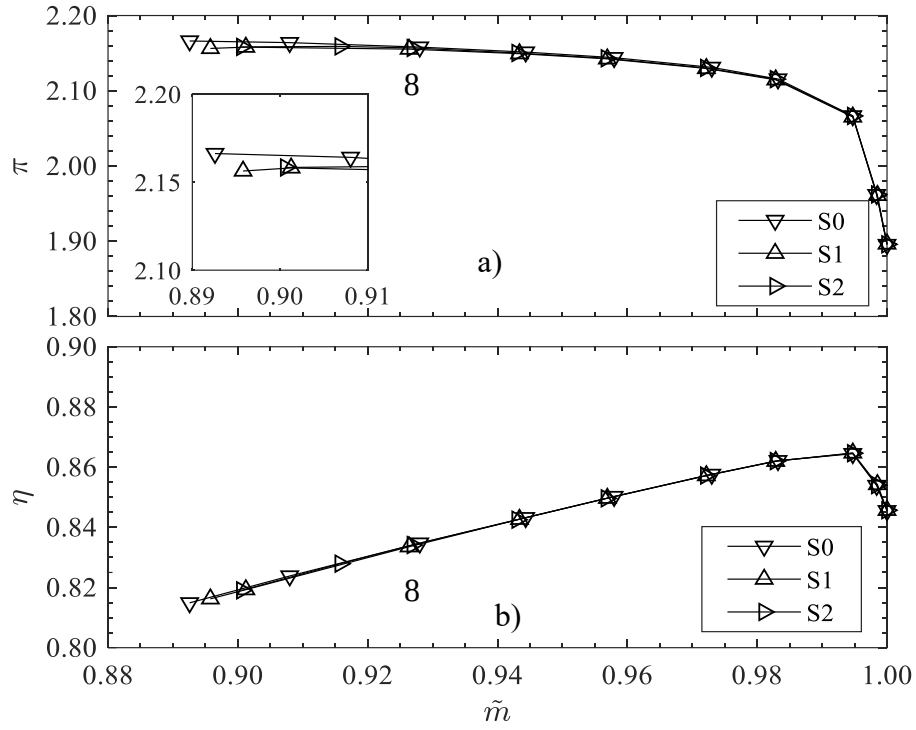

Figure 6-16 Performance map of the single casing grooves. a) π and b) η.

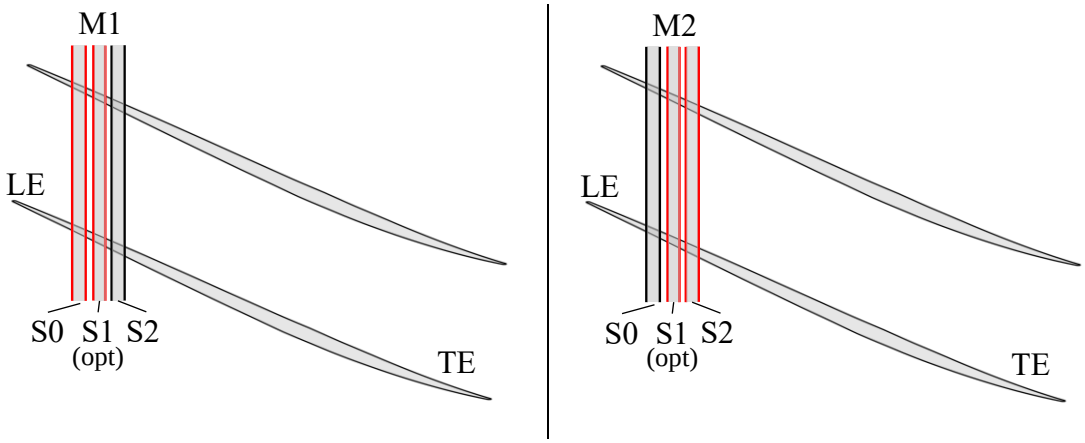

Figure 6-17 Multi-configuration by combining single casing grooves

6.4.2 Multiple grooves

The effect of a multiple groove configuration on the SMI is investigated by combining the individual grooves as shown in Figure 6-18. M1 is the combination of S0 and S1 whilst M2 is the combination of S1 and S2. From the performance curve as shown in Figure 6-17, the $\Delta\zeta$ of M1 and M2 are calculated and shown in Table 6-2. It is found that a multi-groove configuration does not result in a significant effect to $\Delta\zeta$ as compared to the single groove cases. The $\Delta\zeta$ of M1 and M2 are comparable to the $\Delta\zeta$ of the upstream

single groove case in each of multi-groove configuration. For example, the difference between M1 and S0 in terms of $\Delta\zeta$ is 0.1%. This is also the case for M2 where the $\Delta\zeta$ is 0.1% less than the $\Delta\zeta$ of S1. The effect of having a multiple casing groove does not agree with the outcome found in Ross et al. (2017) where it was reported the SMI gain from individual grooves are additive in nature when they are implemented together. However, it is to be noted that different compressors have distinct blockage features such that it is difficult to expect any similarities between these findings.

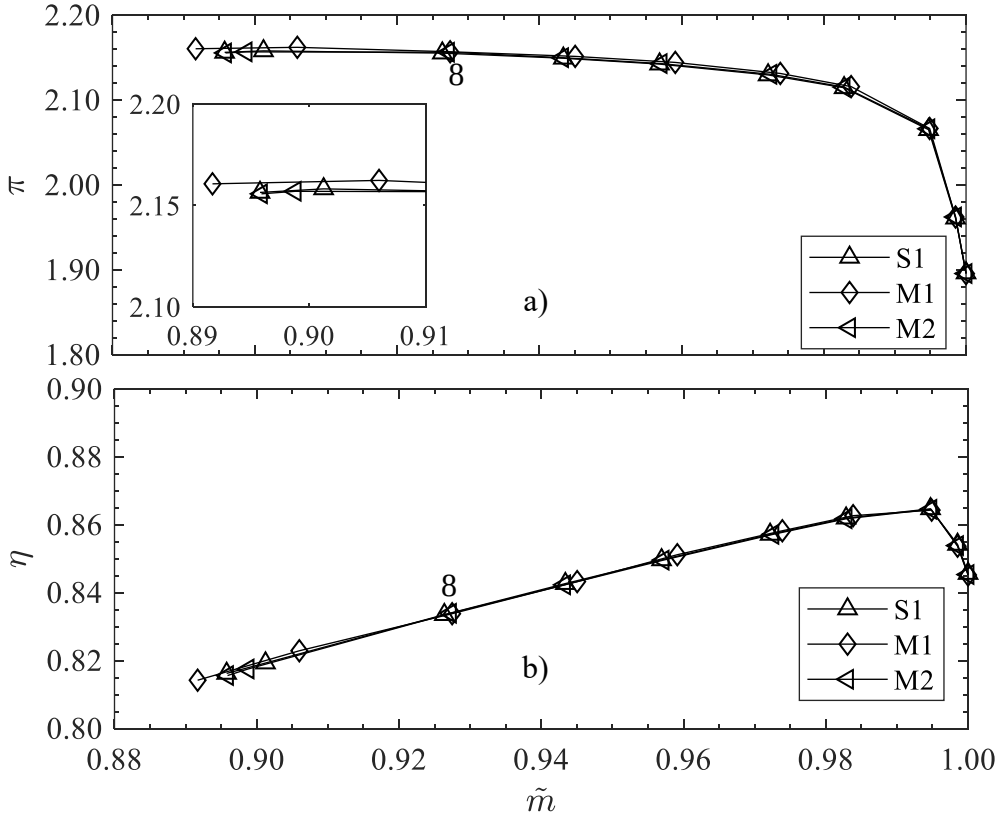

Figure 6-18 Comparison of the performance curve between S1 and multiple grooves. a) π and b) η.

6.4.3 Relationship between blockage reduction and SMI

The effect of the groove on the Ψ_m distribution for the top 20% span at NS conditions is shown in Figure 6-19. It can be seen that the Ψ_m distribution of the grooved casing is modified with respect to the smooth casing. S0 and S1 have relatively lower blockage upstream of the smooth casing peak blockage. On the other hand, S0 and S1 has a relatively higher blockage as compared to the smooth casing. This has been explained previously in sub-section 6.2.2 where the increase of blockage is due to mixing effect caused by radial inward flow from the groove into the main passage. The height of the peak

blockage is the lowest for S2 with respect to the other grooved casing including the smooth casing. However, the blockage within the passage at the front of the groove ($0 < \tilde{z}_t < 0.1$) in not as low as for the other groove cases. The blockage distribution for M1 and M2 shows a similar trend as the single grooves S0 and S2, respectively.

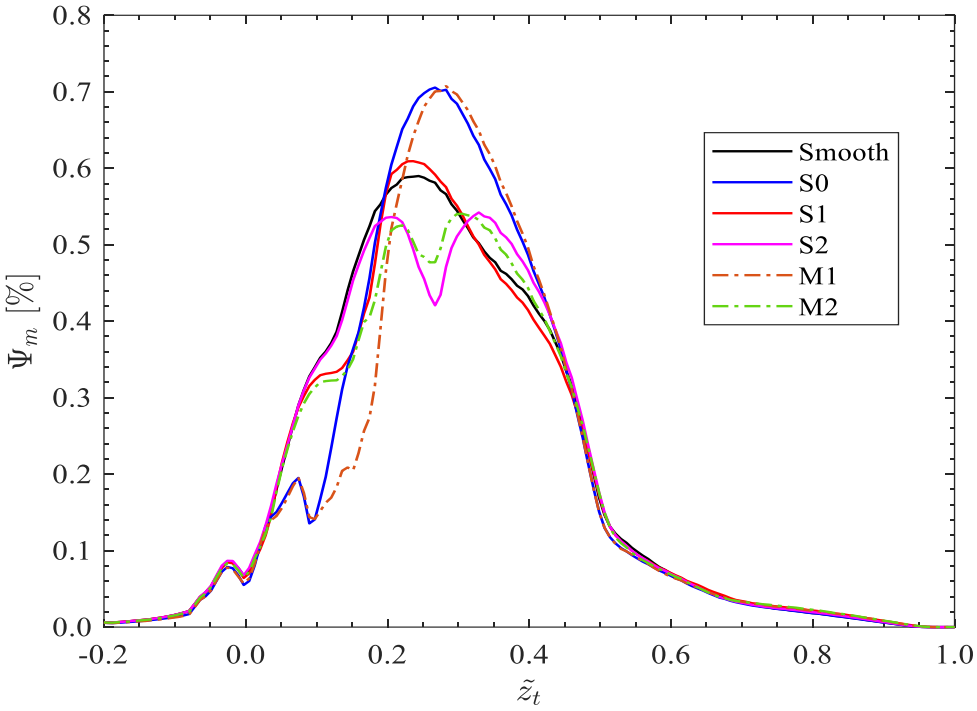

Figure 6-19 Comparison of the Ψ_m axial distribution for all grooved casing cases at operating point 8 for the top 20% span.

The performance of the grooved casings in terms of $\Delta\zeta$ can be explained by linking the effect of the groove on the blockage distribution. Since S0 has the best $\Delta\zeta$ as compared to the other grooved casings, it can be said that removing the upstream part of the peak blockage corresponding to the smooth casing is more beneficial than removal of the peak blockage itself as shown by S2. From Table 6-2, the location of S0 is between 8% and 14% of $c_{ax,t}$ which is upstream than the smooth peak blockage location (about 20% of $c_{ax,t}$) and also the shock-TLV interaction location (about 15% of $c_{ax,t}$) at the last stable operating point as shown in Figure 4-16b). This means that S0 may have affected the origin of the peak blockage itself which from previous discussions in Chapter 4 can be linked to the shock-TLV interaction. For multi-grooved casing, the additional blockage reduction does not seem to translate into better $\Delta\zeta$ as compared to the single grooved

casings. For example, the difference of $\Delta\zeta$ between M1 and S0 is about 0.1% although overall, M1 reduces more blockage than S0.

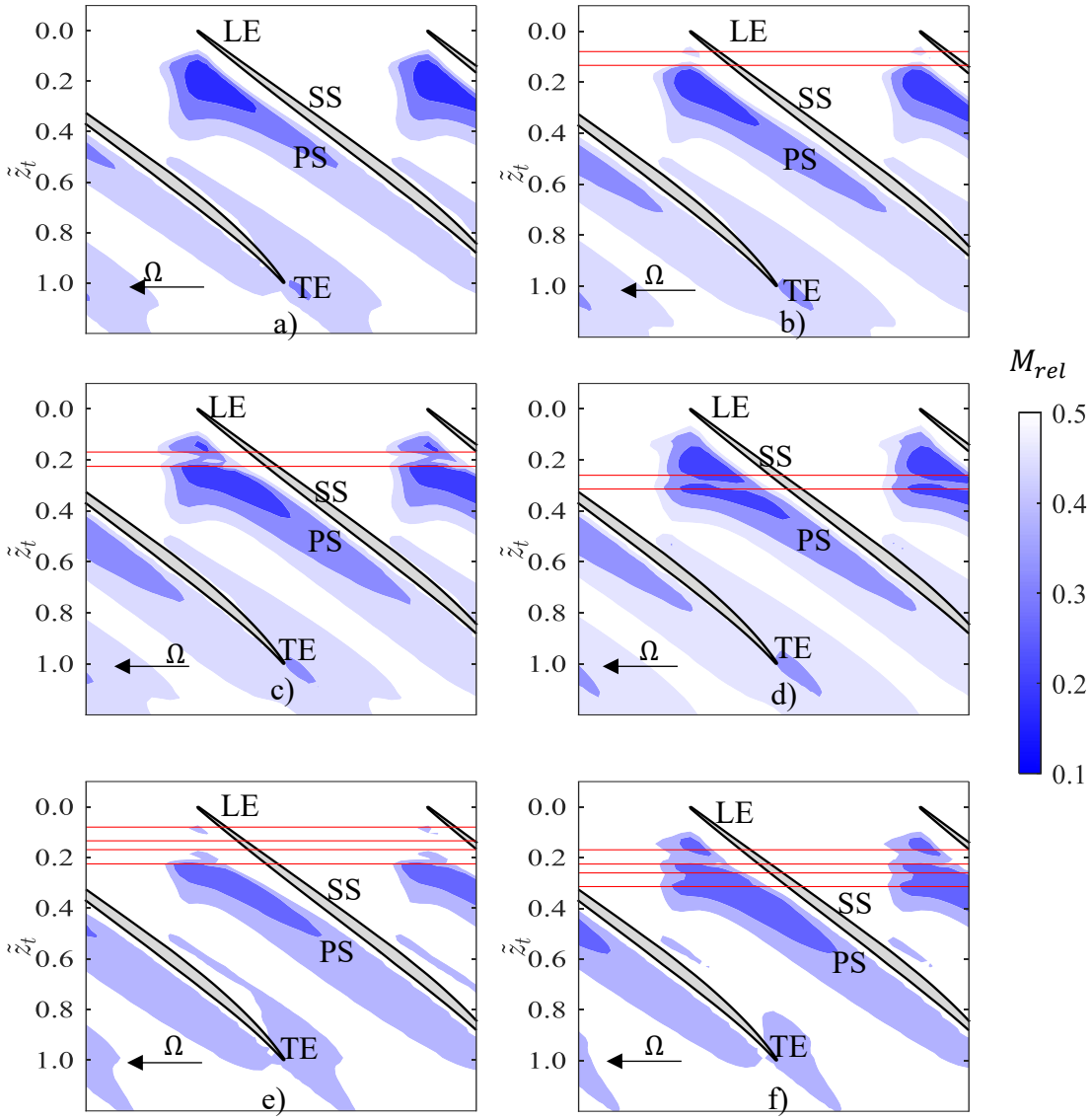

Figure 6-20 Mach number contour plots inside the tip gap region at NS conditions. a) Smooth, b) S0, c) S1, d) S2, e) M1 and f) M

The effect of the blockage reduction due to the groove is further analysed by plotting the Mach number contour at NS conditions at the mid-tip gap region as shown in Figure 6-20. Low Mach number regions in the tip gap region are coloured as darker shades of blue to represent blockage. The reduction of blockage due to the groove as discussed previously, can be seen through the change of the low Mach number regions. This can be seen either as a reduction of the size of the low Mach number region or a decreased intensity of the low Mach number region when the groove is present. S0 and M1 as shown in Figure 6-20)

and e) respectively can be seen to attenuate the front part of the blockage region as compared to the smooth casing (Figure 6-20a)). As shown in Figure 6-20c), d) and e), S1, S2 and M2 only attenuates the aft part of the blockage while the front part of the blockage still exists. It is clear form here that removing or attenuating the front part of the blockage region allows the incoming flow to enter the blade passage with reduced resistance which results in an improvement of ζ. The front part of the blockage prevents incoming flow from entering the blade passage easily. This causes a reduction in any gain in $\Delta\zeta$. Therefore, this shows that $\Delta\zeta$ gained by each grooved casing depends on the location where the blockage is attenuated or reduced.

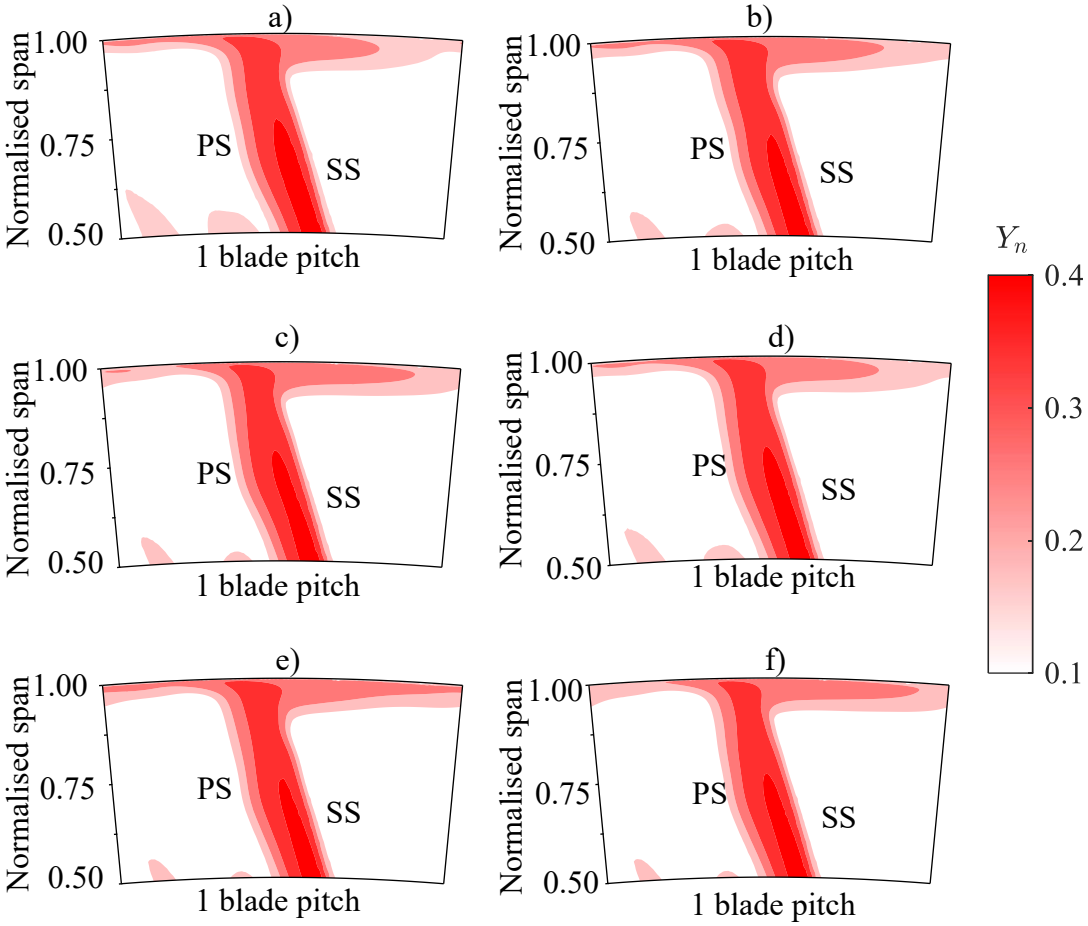

Figure 6-21 Contours of Y_n aft of the blade at 30% of $c_{ax,t}$ downstream of the tip LE at NS conditions. a) Smooth, b) S0, c) S1, d) S2, e) M1, and f) M2.

6.4.4 Near casing downstream losses

Figure 6-21 shows the contours of the total pressure loss coefficient, Y_n, at NS conditions for all the cases. The definition of Y_n is shown in Equation 6-7. Here, $P_{02,rel}$ is the relative

total pressure at 30% of $c_{ax,t}$ downstream of the tip trailing edge (TE). $P_{01,rel}$ and P_1 are the inlet relative total pressure and static pressure, respectively.

$$Y_n = \frac{P_{02,rel} - P_{01,rel}}{P_{01,rel} - P_1} \tag{6-7}$$

The contours are shown for the top 50% span region only for clarity. As compared to the smooth casing as shown in Figure 6-21a), the grooved casings are shown to increase the circumferential extent of the loss region. This is possibly due to the circumferential re-distribution of the tip region fluid within the groove when present. The single grooved casings, S0, S1 and S2 show comparable loss core regions with each other. The multi-grooved casings as shown in Figure 6-21e) and f) respectively show a larger circumferential spread of the loss region with respect to the smooth casing and single grooved casings.

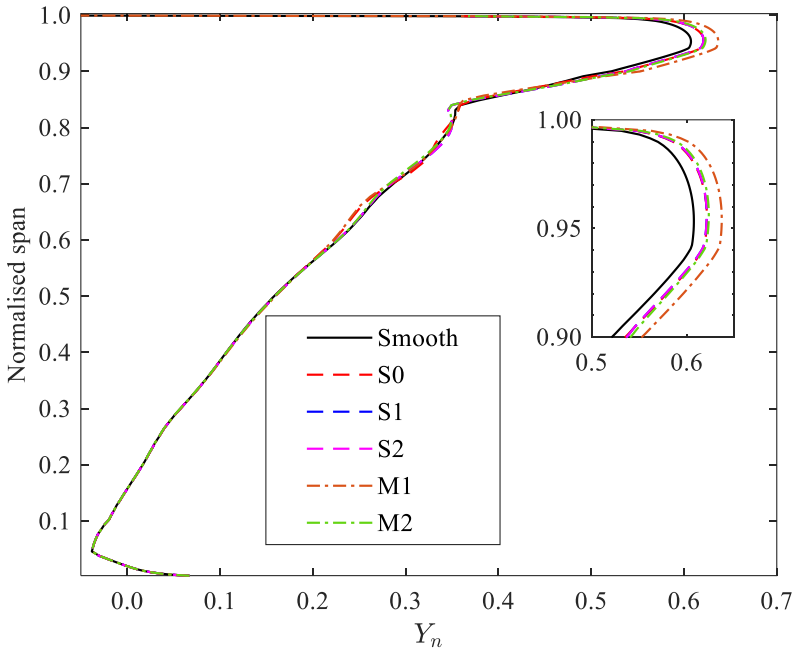

Figure 6-22 Pitch-wise mass-averaged Y_n aft of the blade aft of the blade at NS conditions.

The magnitude of the loss for each case are compared by calculating the pitch-wise mass-averaged Y_n at the same operating point and location where the contours in Figure 6-21 are plotted. The bottom 50% region of the grooved casings show almost no change in Y_n with respect to the smooth casing. The change of Y_n is most significant in the top 10%

span as shown in the inset of Figure 6-22. Overall, it can be seen that the grooved casing shows a higher Y_n for the top 10% span as compared to the smooth casing. M1 has the highest Y_n and followed by M2 as compared to the other single grooved casings. S0, S1, and S2 show comparable Y_n between each other. This may explain why M1 and M2 show a slight reduction in $\Delta\zeta$ as compared to the single grooved casings S0 and S1 although M1 and M2 show a larger overall blockage reduction as shown in Figure 6-19. The increase in Y_n with respect to the smooth casing is thought to be caused by the momentum transfer of flow between the groove and tip gap region. However, the increase of near casing losses with respect to the smooth casing show negligible effect on the η at operating point 8 as shown in Figure 6-16 and Figure 6-18.

6.5 Summary

The summary of this chapter is as the following.

1. Result of the optimised grooves: The optimised groove is found to increase the stall margin by about 0.6%. The efficiency change due to the introduction of the optimised groove is within $\pm 0.1\%$ with respect to the smooth casing. Through unsteady RANS simulations, it is found that the groove does not add any transient effects to the flow field. This shows that a steady RANS simulation is adequate to explain the effect of the groove on the near casing flow features.
2. Changes to the near casing flow region due to the grooves: As compared to the smooth casing, the optimised groove is found to affect the local blade tip loading which is explained to be due to the flow momentum transfer between the tip region and the groove. The radial transport of flow between the groove and tip region results in a reduction in the tip leakage flow momentum. This would mean that the groove weakens the tip leakage flow which is expected to have positive effects on the rotor performance. Furthermore, the optimised groove is shown to reduce the front part of the smooth peak blockage which can be linked to the radial transport of flow. However, an increase of blockage is seen aft of the smooth peak blockage which is possibly due to the mixing effect caused by the radial inward flow exiting from the groove into the blade passage.
3. Effect of the groove at part-speed: At part-speed conditions, the optimised groove do not show any detrimental effect to the stall margin and efficiency. Due to the absence of the passage shock at part-speed conditions, the blockage distribution

do not share the same characteristics as compared to at high-speed conditions. At part-speed conditions, the upstream movement of the peak blockage location as the compressor is throttled towards stall is not as pronounced as at high-speed conditions. Apart from that, the peak of the blockage at part-speed show a higher and broader peak which suggests that blockage is more distributed in the chord direction when the shock is not present. The blockage at near stall and part-speed conditions if shown to be about twice the blockage as compared to high speed case.

4. The axial location of the optimised groove, S1 is varied to obtain two more single grooves S0 and S2. From here, it is found that the configuration S0 that is located upstream of S1 has a relatively higher SMI than S1. This is possibly due to the fact that S0 is located within the shock-TLV interaction location which is the main source of the blockage. The singles grooves are combined to form two multiple grooved casing configurations M1 and M2. M1 and M2 do not show any significant increase in SMI as compared to the single grooves S0 and S1. This is associated with the additional losses generated by the multiple casing grooves as compared to the single grooves.

Chapter 7

Low-speed Axial Compressor Rotor Design and Single Groove Testing

7.1 Overview

This chapter presents the design procedure of a low-speed axial compressor rotor and testing of a single optimised groove design. The low-speed compressor rotor is an aerodynamically scaled version of Rotor 37 at part-speed condition. The low-speed compressor rotor is designed to mimic the tip-stalling behaviour of Rotor 37. An optimisation study for single casing groove is then performed with the intention to achieve stall margin.

7.2 Low speed modelling of Rotor 37

So far in this thesis, the optimisation method for obtaining a single casing groove design that results in an SMI has been shown to work for a high-speed compressor using numerical simulations. The purpose of this chapter is to verify the design optimisation method explained in Chapter 5 through testing on a real axial compressor rotor. The purpose of such an attempt is two-fold. Firstly, there is an intention to ascertain the usefulness of the 'physics-based' optimisation method as presented in Chapter 5 under low-speed conditions. In the low-speed environment the blockage development that leads to stall is still likely to be caused by tip leakage flow but without the presence of the shock. The advantage of the optimisation strategy, however, is that it only uses the alleviation of blockage as a means to achieve SMI whereas the cause of the blockage development itself is immaterial. The second purpose of the low-speed optimisation attempt is the intention to experimentally test the concept in cost-effective manner. High-speed transonic compressor rigs such as the Rotor 37 where the concept has been shown to work are extremely

complicated physically and expensive to construct, instrument, operate and maintain. There is an option, therefore, to model the high-speed compressor rotor as a low-speed compressor rotor based on the principles of aerodynamic similarity. Such scaling of compressors has been performed by other researches in the past such as Wisler (1985), Lyes and Ginder (1998), Chenkai et al. (2014) and Nan et al. (2018). The advantages of this high to low-speed transformation method is the low cost of the design, build and operation of the hardware required. One major limitation of this method is the inability to recreate the shock effects on the stalling of the high-speed compressors. This is a clear disadvantage to Rotor 37 since the stalling mechanism of Rotor 37 is due the shock-TLV interaction as discussed in Chapter 5. However, as a compromise to this problem the high to low-speed aerodynamic scaling can be done at a relatively lower speed than the design speed where the effect of the shock is weaker. This approach was performed by Nan et al., (2018) to compensate for the inability of recreating the shock effects at the design speed of a transonic compressor. Such a strategy can therefore be applied to Rotor 37 as well since the passage shock is absent when running at 60% speed as discussed in Chapter 7. In addition, the casing groove did not show any negative effects on the SMI when running at part-speed. This suggests that performing the high to low-speed transformation on Rotor 37 at 60% speed is a worthwhile exercise.

7.2.1 1D design

As mentioned earlier, the aim of the high to low-speed transformation is to obtain aerodynamically similar blades from the high-speed counterpart. This requires specific design targets obtained from the high-speed counterpart to be met with some compromises due to hardware restrictions. The design targets are determined from the numerical result of the part-speed Rotor 37 at operating point C as shown in Figure 6-12. Data for 7 spanwise positions across the blade are obtained at 50% of c_{ax} upstream and downstream of the rotor. The spanwise positions chosen are 5%, 15%, 30%, 50%, 70%, 85%, and 95% span.

A step-by-step method to obtain the design targets for the low-speed model is explained as the following:

1. **Finding the axial velocity of the model compressor, $V_{z,}$**. This is done by matching the flow coefficient, ϕ', between the low-speed model (LS) and the high-speed compressor rotor (HS) as shown in Equation 7-1. The blade speed, U, can be found from the radius, r, and the blade angular speed, Ω. The LS compressor blade speed, U_{LS}, is restricted by

the speed of the available motor and also the casing radius. In this case, the maximum available motor speed is 3000 rpm and the casing radius is 230 mm. The radius, r, for each spanwise position of the LS can be found by equating the hub-to-tip ratio of the design compressor with the model compressor. The hub to tip ratio of 0.7 results in a hub radius of 161 mm. The V_z of LS is designed to be constant across the span due to the usage of parallel annulus for simplifying the design process. This is not the case for the HS compressor the annulus area varies across the rotor. Therefore, some compromises are expected which are shown later as the velocity triangles are constructed.

$$\phi'_{LS} = \phi'_{HS} \; where \; \phi' = \frac{V_z}{U} \tag{7-1}$$

2. **Check the Reynolds number** The Reynolds number, Re, as defined in Equation 7-2, is controlled by the chord length, c, and $V_{z,}$. Quantities ρ and μ are calculated from the ideal gas law and Sutherland's law at standard atmospheric conditions, respectively. In order to achieve dynamic similarity, Re between LS and HS should ideally be the same. However, as mentioned earlier, the restrictions of the motor speed and casing diameter would not permit equal Re between the LS and HS compressor. Hence, the Re of the LS compressor is targeted to be as close as possible to the HS compressor. This requires some adjustment to chord length, c, and ϕ'. Scaling-up of c in return affects the pitch-to-chord ratio of the blade. This restricts the magnitude of the allowed change in c to obtain a comparable Re between the LS and HS compressor. As a result, the blade count of the LS compressor is slightly reduced in order to maintain the comparable pitch-to-chord ratio as of the HS compressor. The limitation of scaling up the c requires that the ϕ' is to be slightly increased as well. The increase in ϕ' is also restricted in order to have comparable velocity triangles as described in the next step.

$$Re = \frac{\rho V_z c}{\mu} \tag{7-2}$$

3. **Constructing the velocity triangles of the model compressor**. The velocity triangles as depicted in Figure 7-1 are required to obtain the inlet and outlet blade angles, β. Ideally, the normalised LS compressor velocity triangles are targeted to be equal of the high-speed counterpart. However, this is no longer possible due to the adjustments made to the ϕ' as explained earlier. The rotor blades in Figure 7-1 are for illustrative purpose only since at this stage, the blade shape is not yet known. For an isolated compressor case, the absolute inlet flow angle, β_1, is equal to zero. The relative blade inlet angle, $\beta_{1,rel}$, is fixed by the

pre-determined ϕ'. Hence the only unknown parameter to construct the velocity triangles is the outlet blade angles. The outlet blade angle can be found from the stage loading coefficient, Ψ'. As shown in Equation 7-3, the model compressor stage loading coefficient, Ψ'_{LS}, is fixed to the HS compressor, stage loading coefficient, Ψ'_{HS}. An equal Ψ' between the LS and HS compressor would mean that the non-dimensional work input on the flow by the rotor blade is the same. Hence, a similar blade loading distribution is expected. This is important especially at the tip region in order to mimic the tip-stalling criteria of the HS compressor. Δh_0 is the stagnation enthalpy change through the rotor and can be found from Euler's equation as shown in Equation 7-4. Since $\beta_1 = 0$, Ψ'_{model} can be written in terms of the ϕ' and $\beta_{2,rel}$ as shown in Equation 7-5.

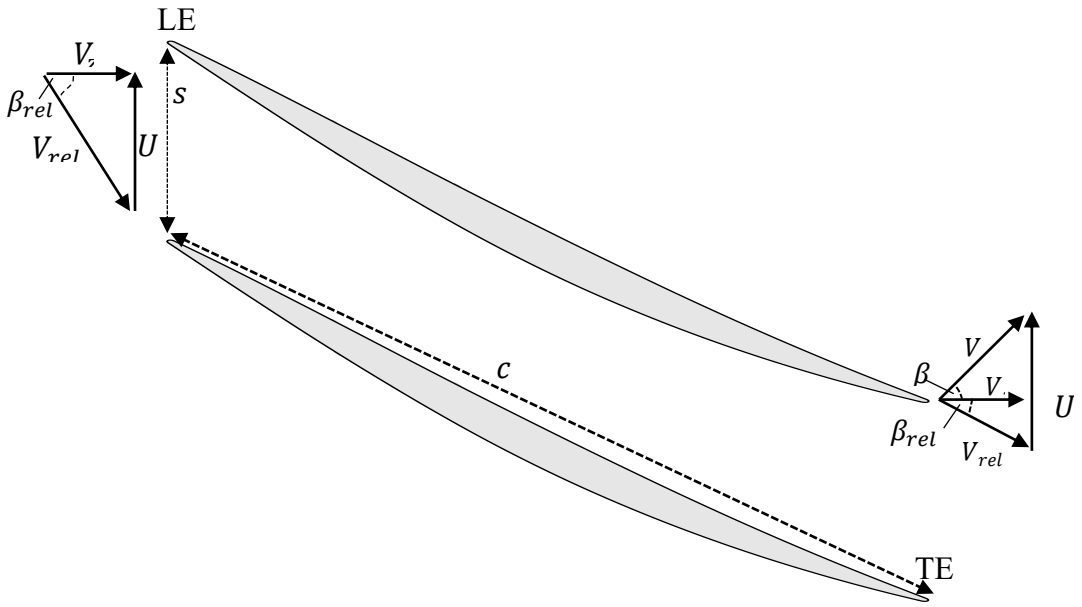

Figure 7-1 Generic isolated axial compressor velocity triangle (drawing not to scale).

$$\Psi'_{\text{LS}} = \Psi'_{\text{HS}} \; where \; \Psi' = \frac{\Delta h_0}{U^2} = \frac{\Delta P_0}{\rho U^2} \tag{7-3}$$

$$\Delta h_0 = UV(\tan\beta_2 - \tan\beta_1) \tag{7-4}$$

$$\Delta h_0 = U\left(\left(V_z \tan\beta_{2,rel} + U\right) - \tan\beta_1\right);\ \beta_1 = 0$$

$$\Psi'_{\text{LS}} = \frac{V_z}{U}\left(\tan\beta_{2,rel}\right) + 1$$

$$\Psi'_{\text{LS}} = \phi'\left(\tan\beta_{2,rel}\right) + 1 \tag{7-5}$$

4. **Further checks to blade diffusion factor, DF**. DF as shown in Equation 7-6 is the parameter that measures the tendency for separation of the suction side boundary layer (Lieblein et al., 1953). Data from a large amount of cascade testing suggest that the loss

increases as the DF exceeds a value of 0.6. At the tip, the loss increases as the DF exceeds a value of 0.45. The DF is normally chosen by the designer to find the pitch-to-chord ratio for a given change in velocity across the blade. From step 1, the pitch-to-chord ratio is already fixed to be same as the HS compressor. Hence the aim of this step is to only ensure that the DF of the LS compressor is within an acceptable value before proceeding with the blade design.

$$DF = \left(1 - \frac{\cos\beta_{1,rel}}{\cos\beta_{2,rel}}\right) + \cos\beta_{1,rel}\left(\frac{\tan\beta_{1,rel} - \tan\beta_{2,rel}}{2}\right)\frac{s}{c} \leq 0.6 \qquad (7\text{-}6)$$

The procedure of obtaining the design values of the LS compressor is repeated to obtain input design parameters for each of the seven radial heights positions as mentioned earlier in order to proceed with the blade design. Figure 7-2a) shows the comparison between the HS flow angles and the input design flow angles used for designing the LS blades. The DF at each radial height positions are calculated using the input design angles and are shown in Figure 7-2b). A summary of the blade design parameter of the LSAC and comparison with the HS compressor at mid-span is shown in Table 7-1.

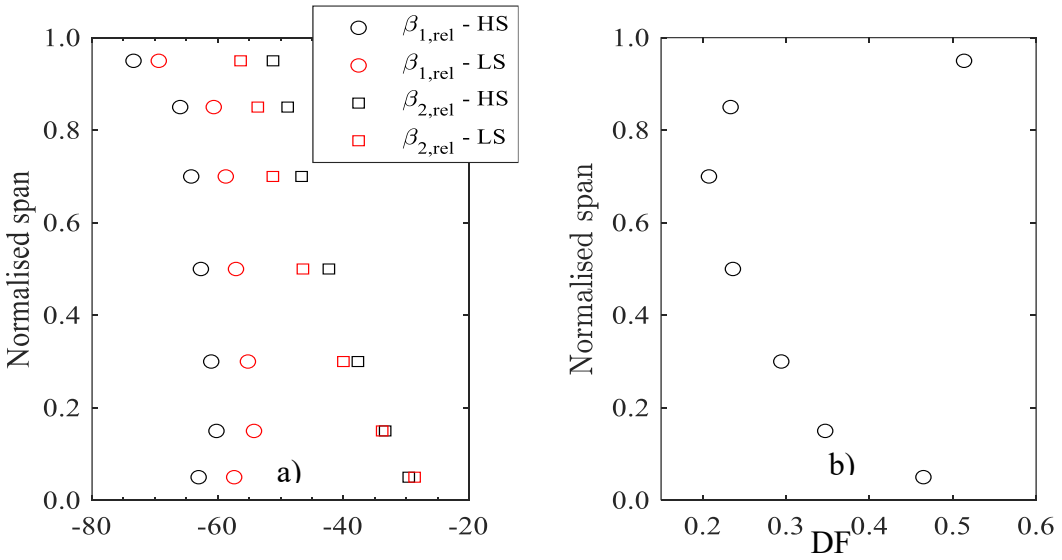

Figure 7-2 a) Comparison between the HS compressor inlet/outlet flow angles with respect to the LS target design inlet/outlet flow angles at several spanwise position. b) Calculated DF values for the LS compressor

Table 7-1 Summary of the LSAC aerodynamic design parameters with respect to the HS compressor

	HS	LS
Ψ'_{mid}	0.37	0.37
ϕ'_{mid}	0.51	0.64
Blade count	36	27
Re_{mid} (true chord)	4.4×10^5	1.8×10^5
RPM	10313	3000
Hub-to-tip ratio	0.7	0.7
True chord, c [mm]	56.23	68.553
Tip pitch-to-chord ratio	0.77	0.74
Tip gap height [mm]	0.356	1
Tip radius at LE [mm]	253.7	229

7.2.2 Blade design

The rotor blade shape is obtained using an inverse design approach (de Vito et al., (2003) and Dang et al. (2003)). The inverse design method is an iterative method where a blade shape is tailored until a desired blade loading distribution is obtained. This method is an advantage for design problems where the desired blade loading distribution is known. As mentioned previously, the aim of the low speed modelling is to mimic the flow conditions of the HS compressor. This is especially at the tip region in order to re-create the flow mechanism that is responsible for a tip-stalling compressor. This requires the LS compressor to have ideally the same c_p as the HS compressor. Hence, the HS compressor blade c_p is prescribed as the target c_p for obtaining the LS compressor blades using the inverse design method.

The computer code used for the inverse design method is MISES which is described in Youngren and Drela (2008) and Youngren (1991). MISES is a 2D cascade analysis and design code that uses a coupled viscous-inviscid interaction technique to obtain the flow solution. Here, the flow solution in the shear layer and inviscid region is solved separately and combined to form a complete solution. Once the 2D flow solution is obtained, mode-shapes are used to perturb the geometry of an initial blade shape in order to iterate towards

a final shape that satisfies the target c_p. This involves re-cambering the initial blade shape towards the final blade shape.

For each of the 7 spanwise locations as mentioned in the previous section, an initial 2D blade shape which is based on the HS compressor (Rotor 37) is generated first. The camber line is scaled-up to meet the Re requirement as explained previously. The LS blade profiles are required to be relatively thicker than Rotor 37 due to the structural properties of the selected LS blade material. The Rotor 37 LE and TE radii reduce from hub to tip as found in Reid and Moore (1980). For the LS compressor blade, the LE and TE radii are scaled-up so that the minimum tip LE and TE radii are 1.2 mm. In order to obtain the initial 2D shape, therefore, the thickness distribution of the corresponding Rotor 37 profile is increased based on the change in the LE and TE radii to form the new thickness distribution of the LS compressor blade. The procedure is repeated for each of the 7 spanwise positions. Figure 7-3a) shows an example of a scaled-up initial blade geometry of the LS compressor as compared to the Rotor 37 blade at 95% span. Once the initial blade shapes are generated, the flow solution of that 2D blade shape is obtained from MISES using the input design parameters as specified by the 1D design. The target c_p is then prescribed for the inverse design method. The blades may also require some turning to obtain the desired target c_p. Figure 7-3b) shows a comparison of an initial and final version of the blade profile subjected to the inverse design method at 95% span. An example of the inverse design method is detailed in Appendix I.

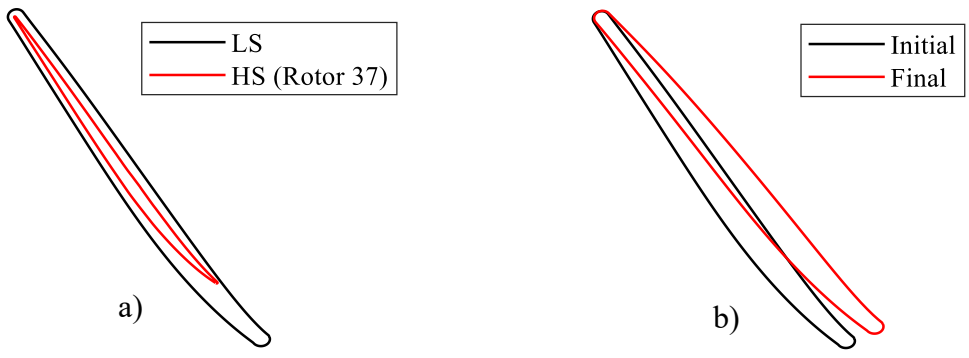

Figure 7-3 a) Scaled-up initial LS blade profile with respect to HS blade profile at 95% span. b) Transformation of the final blade profile through the inverse design method with respect to the initial blade profile at 95% span.

The final 2D blade profiles at all the seven spanwise positions are then radially stacked to obtain a 3D blade. The 2D blade profiles are stacked using a radial stacking line that

passes through the centroid of all the blade sections. This is similar to the stacking method adopted for the Rotor 37 blade (Reid and Moore, 1978). The outcome of the stacking procedure is shown in Figure 7-4.

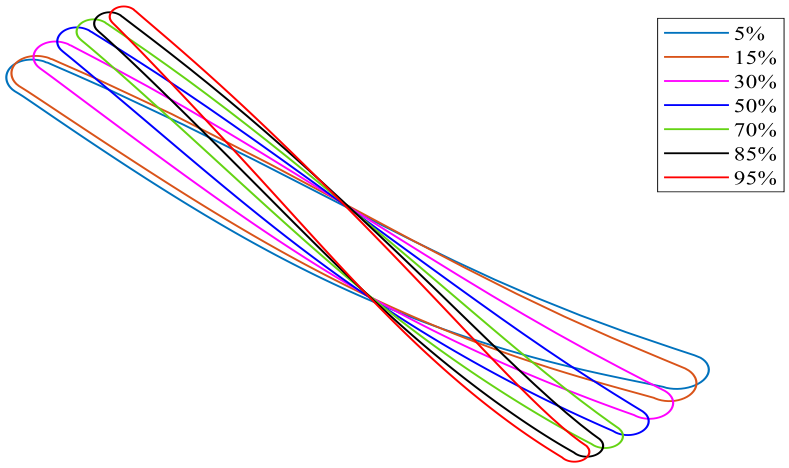

Figure 7-4 Radial stacking of the seven 2D blade profiles to obtain the 3D blade shape. (Not to scale)

7.2.3 3D RANS simulation

The 3D blade obtained is validated further using a steady RANS simulation. The computational setup, grid and numerical setup for this simulation are explained in Chapter 3. Figure 7-5 shows the performance characteristics of the LSAC. The abscissa of Figure 7-5 is the flow coefficient, ϕ, which is defined as the average axial velocity at the inlet, $V_{z,1}$, over the midspan blade speed, U_{mid}. The total-to-static pressure rise coefficient, ψ_{ts}, and isentropic efficiency, η, are calculated using Equation 7-7 and 7-8, respectively. The mass averaged fluid density, ρ, is calculated at the inlet. P and P_0 are the static and total pressures, respectively and T_0 is the total temperature. The static pressure is area averaged at inlet whereas the total pressure and total temperatures are mass averaged at the appropriate measuring planes. Operating point 4 and 8 represent the conditions at near design (ND) and near stall (NS) respectively. Operating point 10 is the last stable operating point found using the 'bisection method' type approach outlined earlier in Chapter 3.

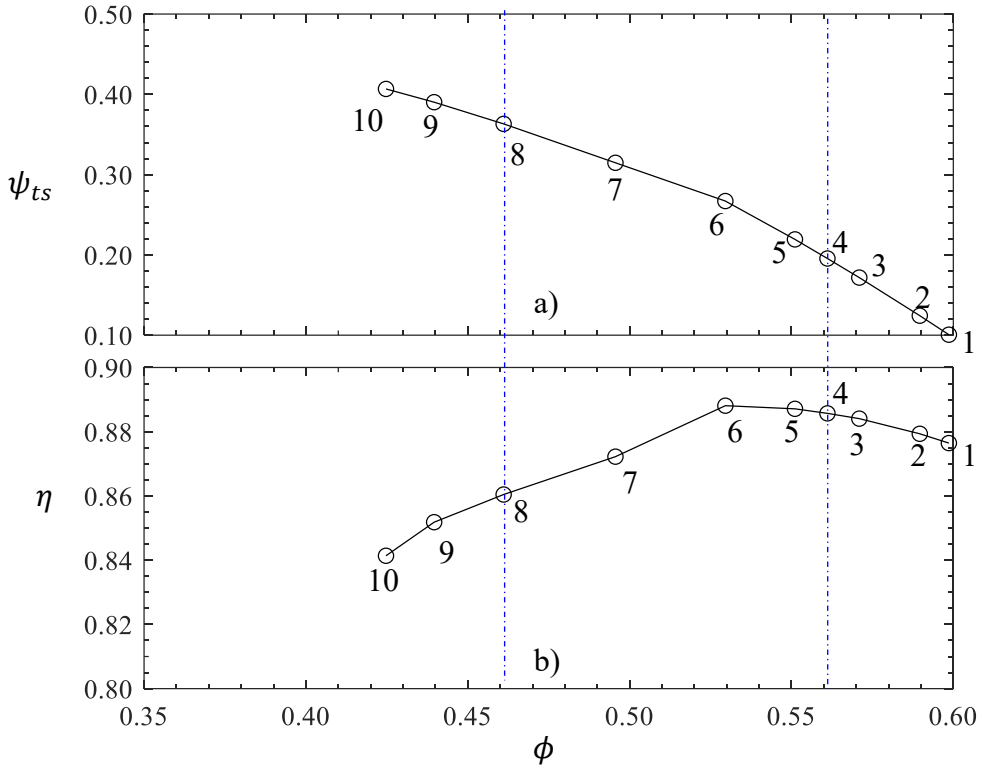

Figure 7-5 Performance characteristics of the LSAC a) Total to static pressure rise coefficient and b) isentropic efficiency

$$\psi_{ts} = \frac{\bar{\bar{P}}_{exit} - \bar{\bar{P}}_{01}}{0.5\,\rho U_{mid}^2} \tag{7-7}$$

$$\eta = \frac{\bar{\bar{P}}_{0,exit} - \bar{\bar{P}}_{01}}{\bar{\bar{\rho}} C_p (\bar{\bar{T}}_{0,exit} - \bar{\bar{T}}_{01})} \tag{7-8}$$

Figure 7-6 shows the comparison between the 3D RANS simulation results at operating point 4 and the design target values specified at the seven radial height positions. The aim of the plots here is to understand the 3-dimensional flow behaviour around the blade that is constructed from several discrete 2D profiles. Differences may occur due to the presence of 3D flow phenomena such as hub and casing endwall boundary layers, leakage flow at the blade tip and possible 3D separation over the blade surfaces, none of which are accounted for during the design process as described earlier. Figure 7-6 compares the design and the simulated radial distribution of the pitch-wise averaged values of Ψ' , ϕ', β_1, and β_2. The relevant upstream and downstream variable values required for these calculations are extracted from axial planes located 50% c_{ax} upstream of the blade LE and 50% c_{ax} downstream of the blade TE, respectively. Overall the radial distribution of

the Ψ' and ϕ' qualitatively agree with the design target values. The discrepancies can be attributed to 3D flow effects that was not predicted during the 1D and 2D design processes. For instance, in Figure 7-6d), the β_2 distribution near the tip and hub shows a mismatch with respect to the design target trend. This is due to the effect of tip leakage flow at the tip region and the hub wall boundary layer effect that is difficult to incorporate during the initial 1D and 2D design process. The near endwall trend mismatch are less intense for β_1 with respect to β_2 since β_1 is not affected by the aerodynamic effects of the flow in the blade passage. Nevertheless, the near endwall discrepancies of β_2 are within an acceptable range since the trend far from the endwalls (between 20% and 80% span) show a good qualitative agreement with the design target values.

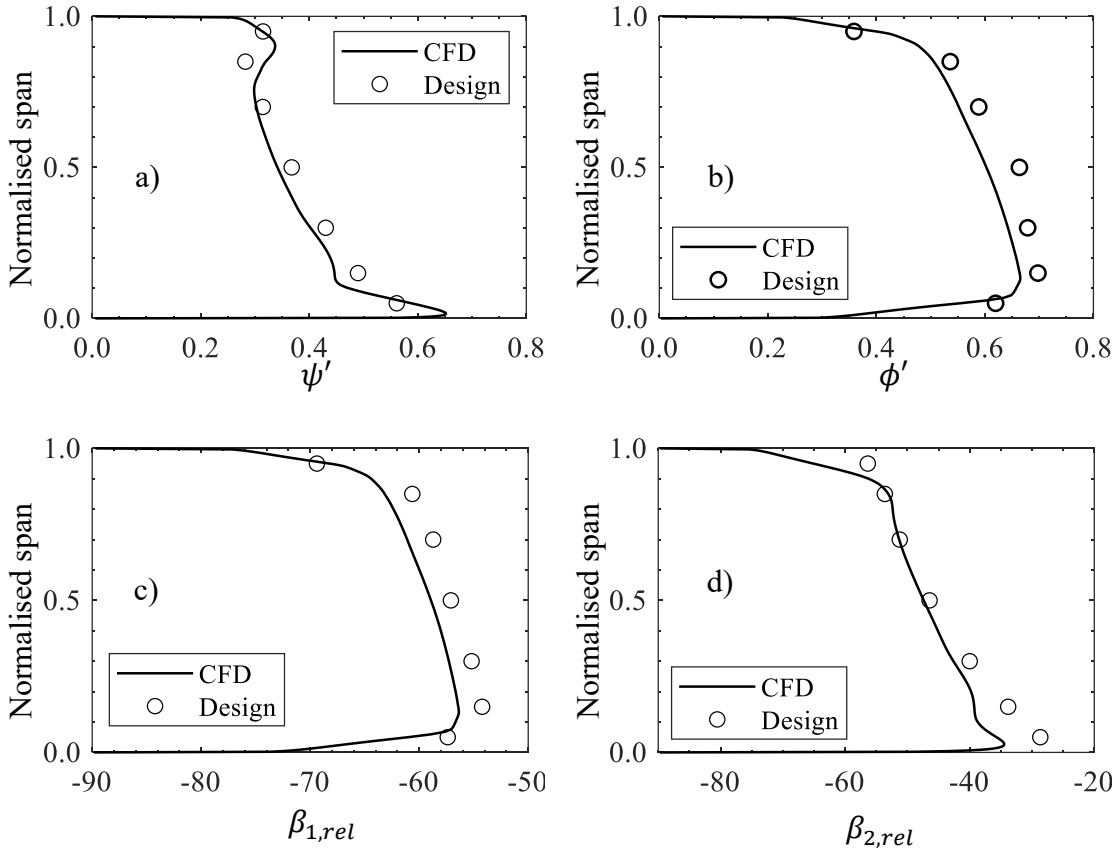

Figure 7-6 Comparison the 3D RANS simulation at near design conditions with respect to the design target values. a) Stage loading coefficient, b) Flow coefficient, c) Inlet relative angle and d) Exit relative angle.

Figure 7-7 shows the comparison between LSAC blade loading at ND conditions with respect to the prescribed blade loading obtained from the HS compressor. The blade loading distributions are compared at 10%, 50% and 90% span. The LSAC blade loading at

the respective span position show good qualitative agreement with respect to HS blade loading. A good match between the LSAC and HS blade loading is important especially at the tip in order to mimic the tip-stalling mechanism of the HS compressor. Matching the local diffusion levels at each of the spanwise station is also important to make sure that there is no unwanted flow deceleration with respect to the original blade that could lead to blade surface boundary layer separation.

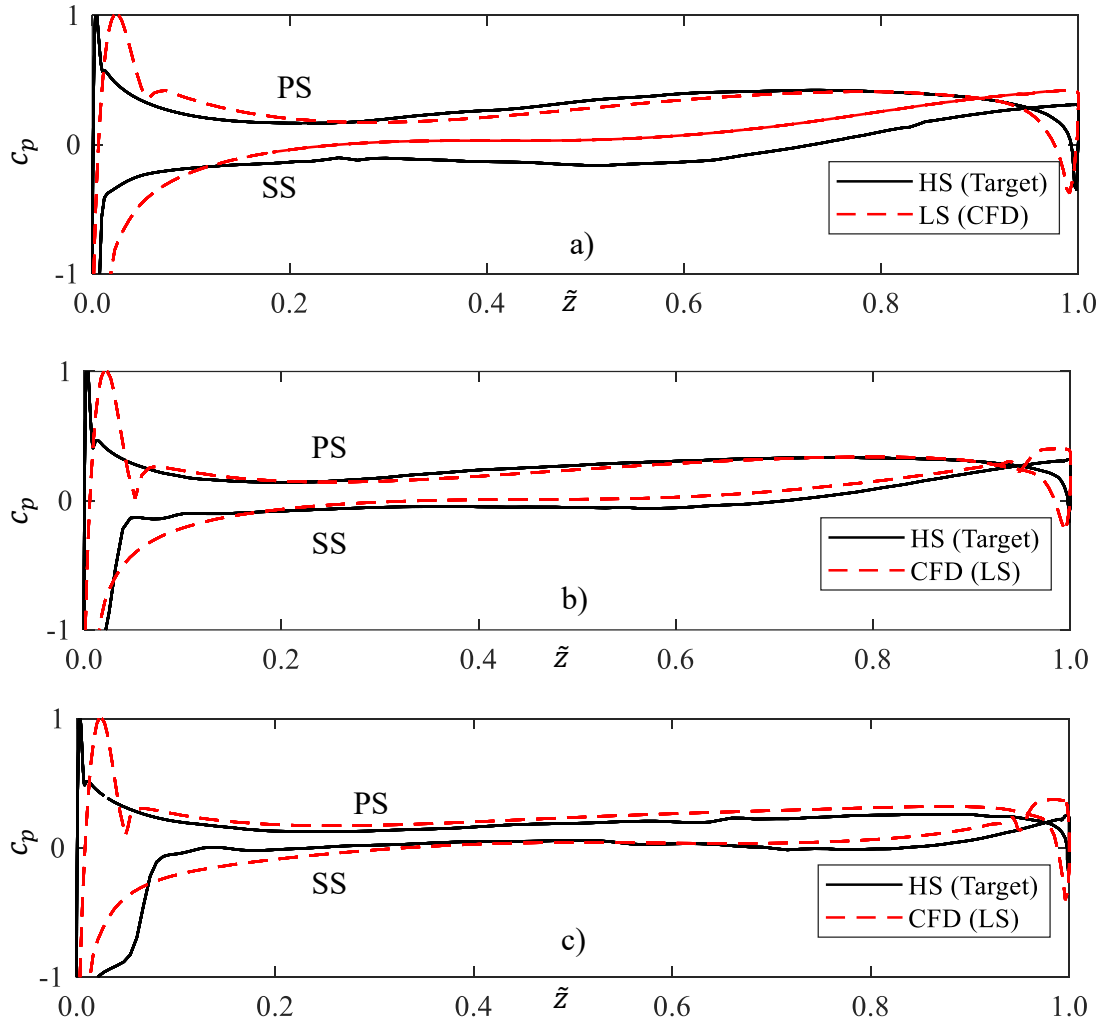

Figure 7-7 Comparison of the 3D blade loading at near-design conditions with respect to the prescribed HS blade loading distribution. a) 10% span, b) 50% span and c) 90% span

For each of blade loading presented, a ‘spike’ can be observed at the blade LE suction side. The ‘spike’ can be attributed to the profile of the blade LE as the flow navigates and accelerates around the curvature. The LSAC has a relatively thicker LE profile as compared to the HS blade to avoid structural integrity problems. If examined carefully, the HS blade loading also show a ‘spike’ at the LE. However, the ‘spike’ is not as pronounced

as in the LSAC loading distribution due to the relatively thin LE profile which causes the 'spike' to quickly disappear. The effect of the 'spike' is non-detrimental on the compressor performance for isolated rotor cases (Goodhand and Miller, 2010).

The suction surface streamlines of the LSAC and HS blade at near design conditions are compared in Figure 7-8. It can be seen that the LSAC suction surface streamline share the same pattern as the HS blade. This is especially so in relation to the features seen near the tip LE and hub TE. The streamline patter near the tip LE is likely due to the tip leakage flow near the origin of the leakage vortex whereas near the hub TE, the streamlines are moving radially upward due to the overturned hub endwall secondary flow. The similarity of the suction surface streamline features between the LSAC and HS blade further verifies the design process of the LSAC rotor.

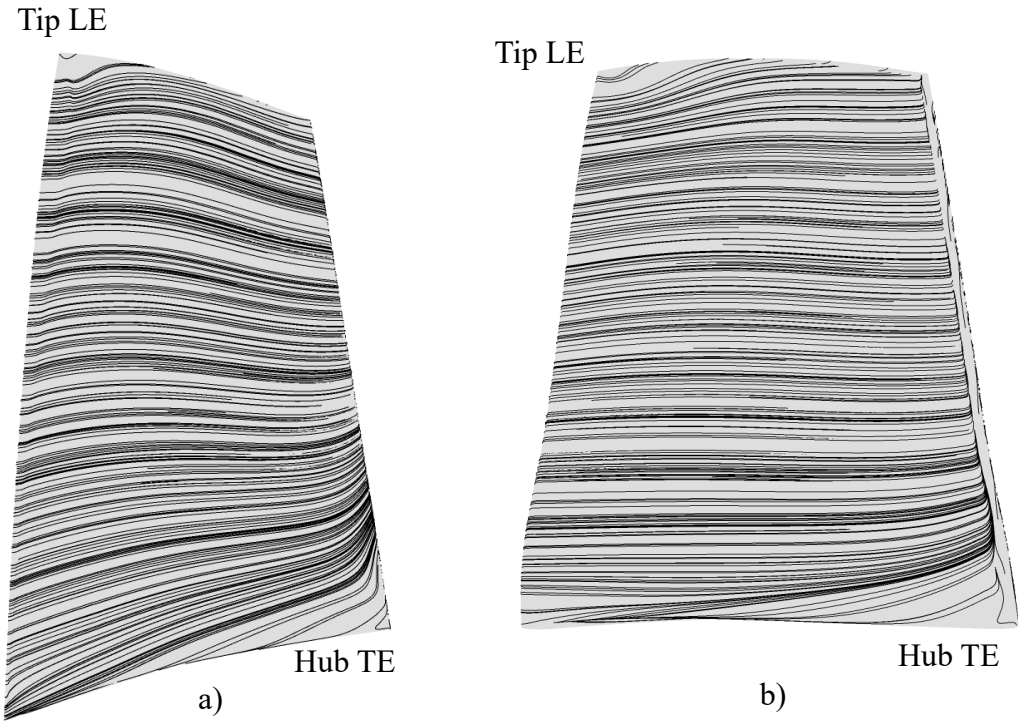

Figure 7-8 Similarity of the suction surface streamline pattern of a) HS and b) LSAC blade at near design conditions

7.3 LSAC tip region flow

As previously discussed in Chapter 2, casing treatments can only be effective for tip-critical compressors. Therefore, further checks are required to ensure that the designed LSAC is indeed a tip-critical compressor that is suitable for casing treatment. Tip-critical

compressors normally exhibit a spike-type stalling pattern (Camp and Day, 1998). According to Camp and Day (1998), the performance characteristic of a compressor can be used to infer the stalling pattern of a compressor. The stability limit of a compressor that exhibits a spike-type stalling pattern is found to occur before the performance (pressure rise) curve reaches the its peak hence on the negative slope of the curve. From Figure 7-5a), it can be seen that the numerical stability limit (operating point 10) occurs on the negative slope of the ψ_{ts} characteristic. From this, it can be inferred that the LSAC is indeed a tip-critical compressor that is suitable for casing treatment. For a tip-critical compressor, the stall is initiated at the tip-region due to the build-up of low axial momentum flow. This can be evaluated by plotting the normalized axial velocity contour at an axial plane located near the LE as shown in Figure 7-9a).

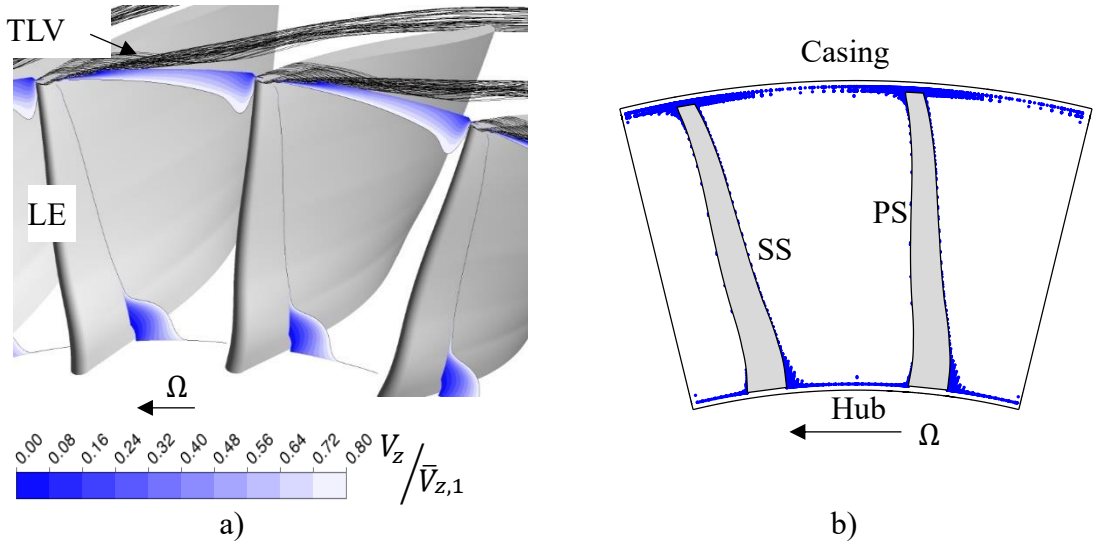

Figure 7-9 a) Normalised axial velocity contour and b) and location of the 'blocked' cells for the same axial location near the tip LE at NS conditions.

The normalized axial velocity contour is plotted at an axial plane located 4% of $c_{ax,t}$ aft of the LE at operating point 8 which represents the near-stall condition. The low axial velocity region which is represented by darker shades of blue are found near the hub and tip region. The blockage is found to be predominantly located near the rotor casing where the blockage region extends much further in the circumferential direction with respect to that near the hub. The blockage located in the hub region is caused by a separation on the suction side near leading edge and is largely confined radially and circumferentially to the LE suction side hub corner. Further analysis using the binary blockage index param-

eter, ψ, as shown in Figure 7-9b) also suggests that the blockage is found to be predominantly located near the rotor casing. The definition of the binary blockage index parameter, ψ, is identical to the one introduced in Chapter 4. The blockage analysis is done for the same axial location as in Figure 7-9a). This further suggests that the aerodynamics of the tip region flow is responsible for initiating the stalling process of the LSAC.

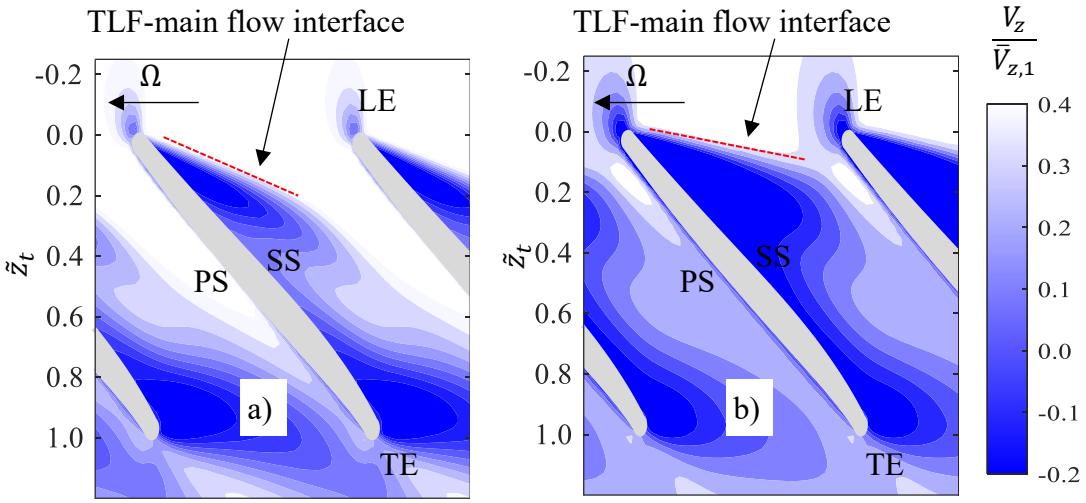

Figure 7-10 Normalised axial velocity contour inside the tip gap (50% of tip gap height, $\boldsymbol{\tau}$) at a) ND and b) NS conditions

The aerodynamics of the tip region flow is susceptible to the build-up of blockage near the casing as the compressor approaches stall. This can be investigated by plotting the normalised axial velocity contour inside the tip gap at ND and NS conditions as shown in Figure 7-10. The blockage region (dark shades of blue) is due to the tip leakage flow (TLF) and tip leakage vortex (TLV). The TLF and TLV are responsible for low axial velocity regions within the blade passage at two regions; one in the forward part of the blade in line with the TLV and the second region close to the blade trailing edge. In comparison to ND conditions, the blockage region due to the TLF at NS conditions occupies a relatively larger portion of tip gap region within the blade passage. This is expected since the TLF is pressure-driven such that at a lower ϕ, the blade loading increases (close to the blade tip LE) with increasing ψ_{ts}. This results in a stronger TLV and TLF with an increased pitch-wise velocity component which causes the TLF-main flow interface to be more aligned to the pitch-wise direction at NS as compared to ND conditions. The upstream movement of the TLF-main flow interface may be linked to the upstream movement of the TLV at conditions close to stall. As described by Hoying et al. (Hoying et al.,

1999), the upstream movement of the TLV at conditions close to stall eventually leads to a 'spill forward' effect that results in the incoming flow to be diverted to adjacent blade passages. The 'spill forward' effect is known as one of the criterion for a 'spike'-type stall to occur (Vo et al., 2008).

The upstream movement of the TLV as the compressor approaches stall can be further studied by determining the trajectory of the TLV. Here, the method used to calculate the TLV trajectory is identical to the method presented in Chapter 5 where the trough in the casing static pressure distribution is used as a marker. The casing static pressure presented in Figure 7-11a) is shown as the total to static pressure rise coefficient, ψ_{ts}, at ND conditions. The location of the minima of the static pressure across constant pitch lines are marked as open circles in Figure 7-11a). The TLV trajectory is then found through linear fitting across the circles. The TLV angle, ξ, is measured from the axial direction and is positive in the direction of rotation. The procedure to find ξ is repeated for the remaining operating points and are plotted as in Figure 7-11b). The variation of ξ in Figure 7-11b) is plotted against ψ_{ts} and is annotated by its respective operating point number as found in Figure 7-5. The change in ξ as the backpressure increases from ND conditions to operating point 10 (last stable operating point), is about 4°. The increase in ξ here is partly responsible for the upstream movement of the TLV-main flow interface as previously explained.

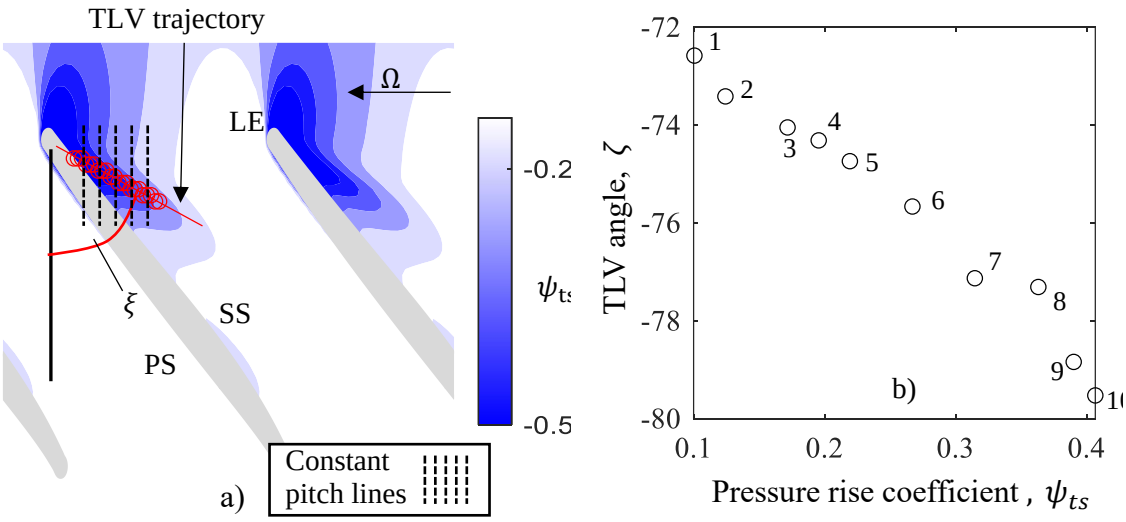

Figure 7-11 a) TLV trajectory (red line) extracted from the casing static pressure contour at ND conditions. **b)** TLV angles with respect to the axial direction for all operating points.

7.3.1 Tip loading and tip leakage momentum

Previously, it has been shown in Figure 7-10 that at conditions close to stall, the blockage region occupies a larger portion of the blade passage as compared to the near-design conditions. This can be attributed to the increased loading near the blade tip as compressor approaches stall as shown in Figure 7-12.

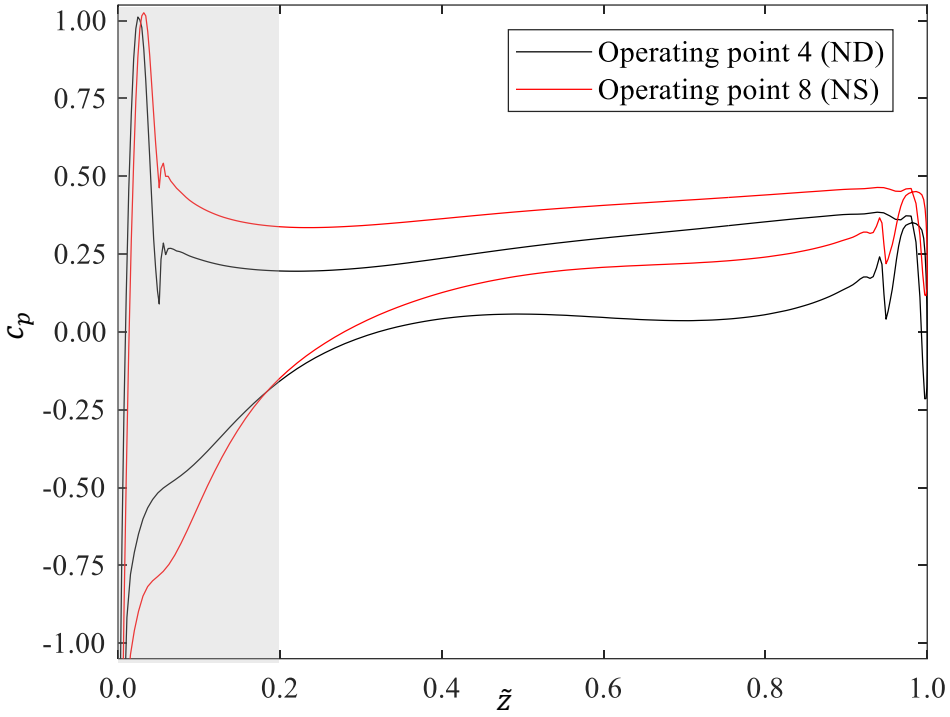

Figure 7-12 Comparison of the blade loading between ND and NS conditions at 97% span.

The c_p is plotted at 97% span which is near the blade tip. As shown in Figure 7-12, the loading near the blade tip LE (shaded region) at NS is higher as compared to at ND conditions. This is expected due to the increase of the ψ_{ts} as the compressor approaches stall. Here, the blade loading is calculated as the difference of the c_p between the suction and pressure surface. The increased loading near the blade tip contributes to the increase of the TLF pitch-wise velocity component which, in turn, appears as blockage due to the decrease in axial velocity component. In addition, it can be seen that towards the TE shows that blade loading decreases at near-stall conditions as compared to the near-design condition. This is in agreement with the contours shown in Figure 7-10. At near stall conditions, it is shown that the blockage region near the LE intensifies and moves upstream whereas that near the blade TE suction side becomes less intense as compared to the near design case. This is the effect of the reduced blade loading in the rear part of the

blade which is thought to be caused by the modification of the passage flow as the up-stream blockage increases.

The effect of the blade loading modification on the strength of the TLF between near design and near stall conditions can be understood by evaluating the TLF momentum, Φ. The TLF momentum, Φ, inside the tip gap region as shown in Equation 7-9.

$$\Phi = \frac{\rho V_{\perp}^2}{\bar{\bar{\rho}}_1 U_{tip}^2} = \frac{V_{\perp}^2}{U_{tip}^2} \because \rho \approx \bar{\bar{\rho}}_1 \tag{7-9}$$

Here, Φ is the TLF momentum normalised by the blade tip momentum. U_{tip} is the blade tip speed and $V_{\perp}$ is the local velocity normal to the blade camber at the tip. At low-speed conditions, the flow is thought be incompressible such that the density, ρ, can be omitted. The TLF momentum is calculated at ND and NS conditions as shown in Figure 7-13.

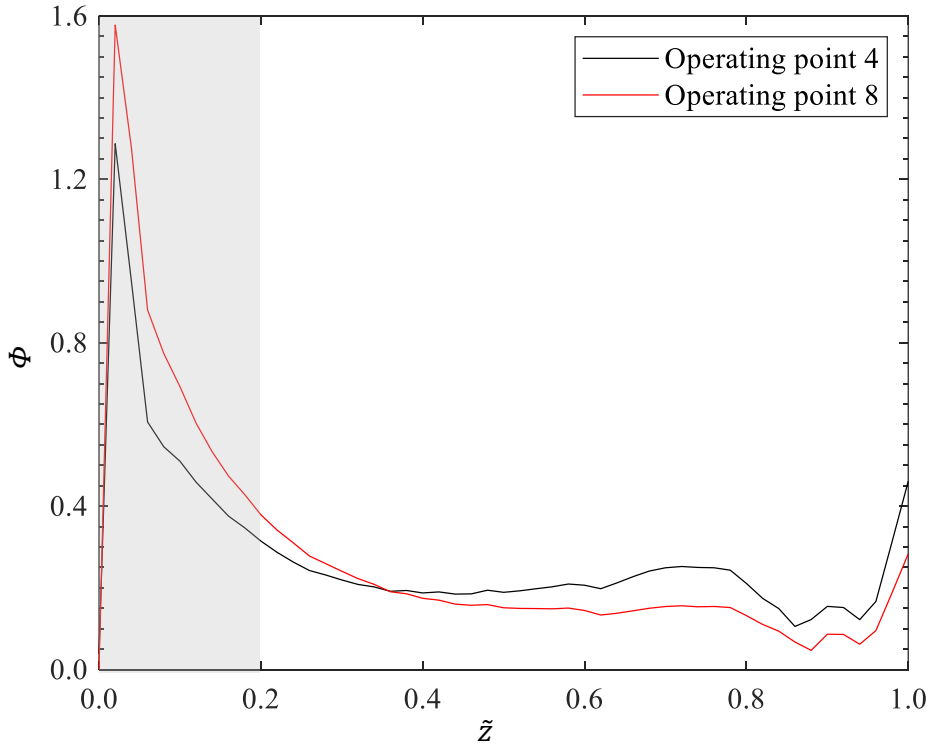

Figure 7-13 Comparison of the tip leakage flow momentum, Φ, between operating point 4 and operating point 8.

The shaded region (between the tip LE and 20% of $c_{ax,t}$ aft of tip LE) is the region where the increased blade tip loading is significant as in Figure 7-12. Within this region, it can be seen that Φ at NS conditions is about 30% higher with respect to ND conditions. The

increased leakage momentum (stronger TLF) which also affects the strength of the TLV contributes to reduced and even axial velocity in the vicinity of the tip LE. This coupled with the increase in back pressure at near stall conditions causes the upstream movement of the TLF-main flow interface as shown in Figure 7-10. At the rear part of the tip ($\tilde{z}_t > 0.5$), as the stall is approached, the tip leakage momentum is seen to decrease with respect to at ND conditions. This is consistent with the reduced blade loading as shown in Figure 7-12.

The effect of the increased strength of the TLF and TLV at near-stall conditions on the blockage development near the tip region can be evaluated by quantifying the blockage. The blockage quantification uses the same method explained in Chapter 4. Figure 7-14 shows the distribution of the normalised blockage mass flow rate, Ψ_m, across the rotor blade for all the operating points that are shown in the performance map in Figure 7-5. The distribution is obtained by extracting data for about 100 axial planes across the blade. The distribution of Ψ_m is only evaluated for the outer 20% span region as it was shown that for a tip-critical compressor, the blockage in the tip region is more significant than at the hub region. The ND (operating point 4) peak blockage located at approximately $0.15\tilde{z}_t$ grows rapidly as the compressor is throttled while gradually moving upstream. At the last numerically stable point (operating point 10) the peak blockage has grown almost eight times compared to that of ND conditions. In addition, the location of the peak has moved upstream, by approximately 3% of $c_{ax,t}$ between ND and operating point 10. The increase in the peak value of the blockage is consistent with the TLF momentum increase at conditions near stall as shown in Figure 7-13. However, the relatively small upstream movement of the location of the peak blockage does not agree with the upstream movement of the TLF-main flow interface as the compressor approaches stall. This seems to suggest that the peak is likely due to the build-up of blockage originating from the TLV rather than the TLF-main flow interface itself. The TLV trajectory approximation exercise presented in Figure 7-11 also showed only a moderate 4° change in TLV angle (ξ) from ND to operating point 10. Hence, the rise in the peak value of the blockage as the compressor approaches stall points to a stronger roll-up of the TLV that is a result of the increase in TLF momentum. This in turn causes an increase in the axial velocity deficit (blockage) near the LE region. The intensification and movement of the vortex along with

the increased TLF with a negative axial velocity at near stall conditions is thought to be responsible for the upstream movement of the TLF-main flow interface.

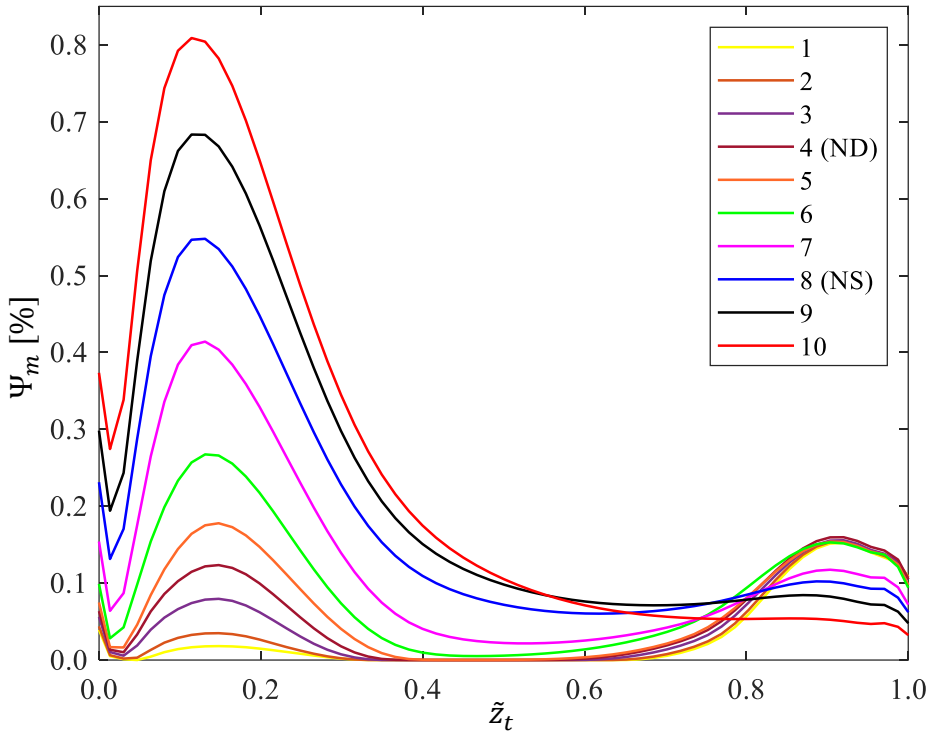

Figure 7-14 Distribution of Ψ_m across the blade for all operating points

7.4 Single circumferential groove design

A single circumferential groove design that improves stall margin is attempted using the same method discussed in Chapter 5. The peak blockage location to be used in the optimisation method is obtained from Figure 7-14 which is located at about 10% of $c_{ax,t}$ aft of tip LE. This is the peak blockage location at operating point 10 which is the last stable operating point. The optimisation routine is performed at a single operating condition corresponding to operating point 8 in Figure 7-5 which represents the near-stall condition. Figure 7-15a) shows the input parameters used to define the groove design. The parameters z', w', H and α are the normalised groove axial position, upper width, height and the upper internal angle, respectively of the groove. All parameters except α are normalised by the blade tip axial chord ($c_{ax,t}$) which is 40 mm.

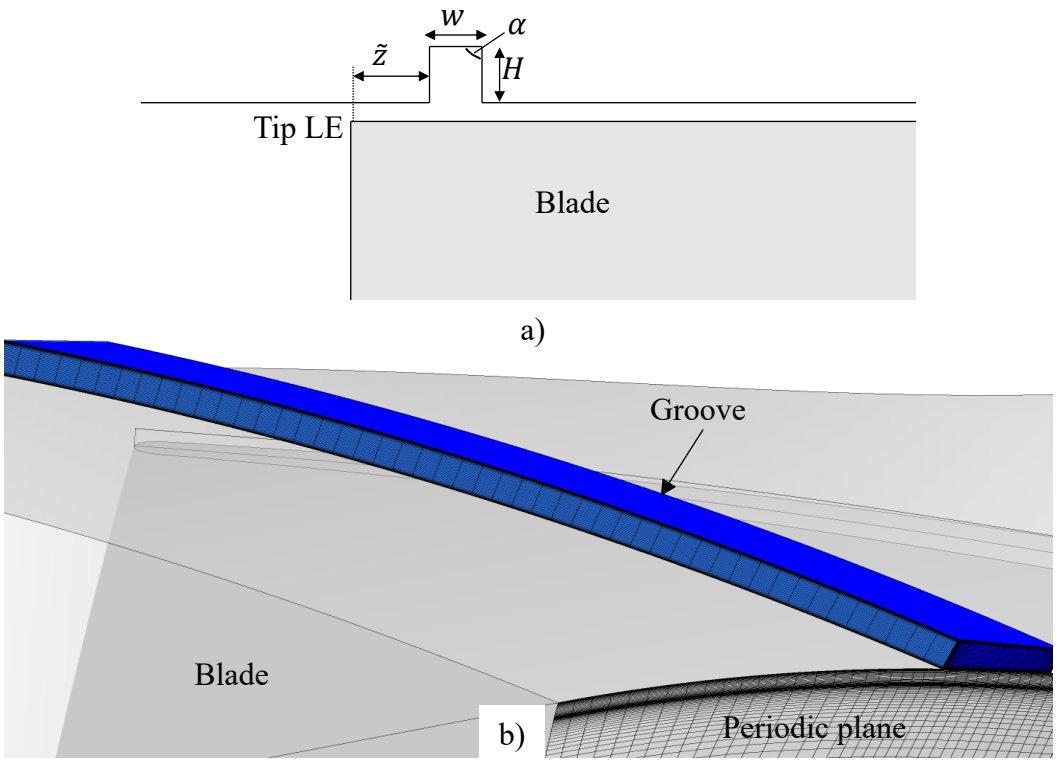

Figure 7-15 a) Groove parameters and b) optimised groove domain and mesh

The optimised values for z', w', H and α are 0.094, 0.094, 0.051 and 92°, respectively. The optimised values are obtained using the similar method outlined in Chapter 6. The values are chosen after running all design candidates in the Pareto optimal solution through 3D steady CFD simulations. The groove that stall with the least flow coefficient is determined to be the optimised groove design. The domain and the mesh for the optimised groove generated are shown in Figure 7-15b). The groove domain has about 0.2 million grid points and is connected to the blade domain via a GGI grid connection.

The performance characteristics of the optimised casing groove with respect to the smooth casing are compared in Figure 7-16. The SMI ($\Delta\zeta$) for the optimised grooved casing is calculated using Equation 7-10.

$$\Delta\zeta = \zeta_{GC} - \zeta_{SC}; \quad \zeta = \frac{(\phi_4 - \phi_{10})}{\phi_4} \tag{7-10}$$

Here, ϕ is the flow coefficient corresponding to the relevant operating conditions (4 & 10) of the smooth and grooved casing. The parameter ϕ is defined as the average axial velocity at the inlet, $V_{z,1}$, over the midspan blade speed. The SMI ($\Delta\zeta$) is calculated to be

5.4 %. The efficiency penalty is calculated to be negligible (±0.2%) for each of the operating points simulated as shown by the overlapping efficiency characteristics for the smooth and the grooved cases in Figure 7-16b). The increase in pressure rise and the dip in efficiency corresponding to the last converged operating point (operating point 10) for the grooved casing are consistent with the slopes of the overall trend of the corresponding characteristic curves.

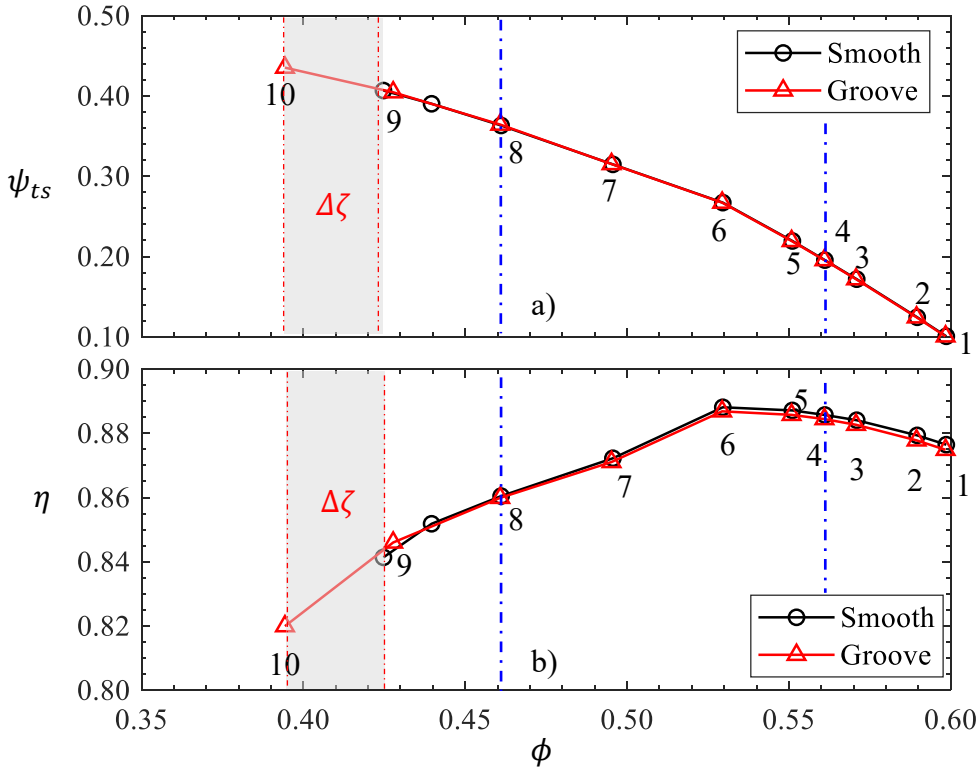

Figure 7-16 Performance characteristic comparison of the optimised groove and the smooth casing. a) Pressure rise coefficient and b) isentropic efficiency

7.5 Comparison of the tip region flow between smooth and grooved casing

Figure 7-17 compares the normalised axial velocity inside the tip gap at operating point 8 (NS) between the smooth and grooved casing. Here, it can be seen that the TLF-main flow interface (dashed red line) of the grooved casing is located closer towards the blade suction side in relation to that of the smooth casing. This suggests that the groove has shifted the TLF-main flow interface forward movement of which is known to be responsible for the 'spill-forward' effect. The delay in the 'spill-forward' effect results in an improved stall margin. Figure 7-18 shows the casing static pressure contour at NS conditions for the smooth and grooved casing. The TLV trajectory is overlaid on top of the

static pressure contour using the method explained previously as in Figure 7-11a). In Figure 7-18b), the TLV trajectory of the smooth and grooved casing are compared. The red line shows the TLV trajectory of the grooved casing while the black dashed line shows the smooth TLV trajectory. It can be seen here that the presence of the groove results in a reduced TLV angle, ξ, where the grooved casing TLV trajectory aligns much closer towards the blade suction side. The reduction of the ξ is estimated to be 2.7° which is significant given that the increase in ξ from operating point 4 to operating point 8 in Figure 7-11 is about 4°.

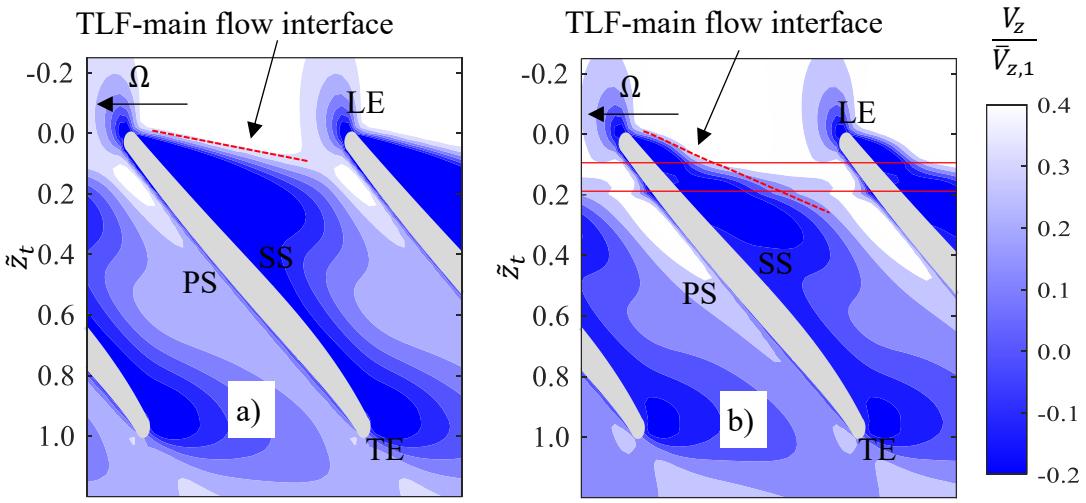

Figure 7-17 Normalised axial velocity contour inside tip gap (50% of the tip gap height, τ) for a) smooth and b) grooved casing at operating point 8

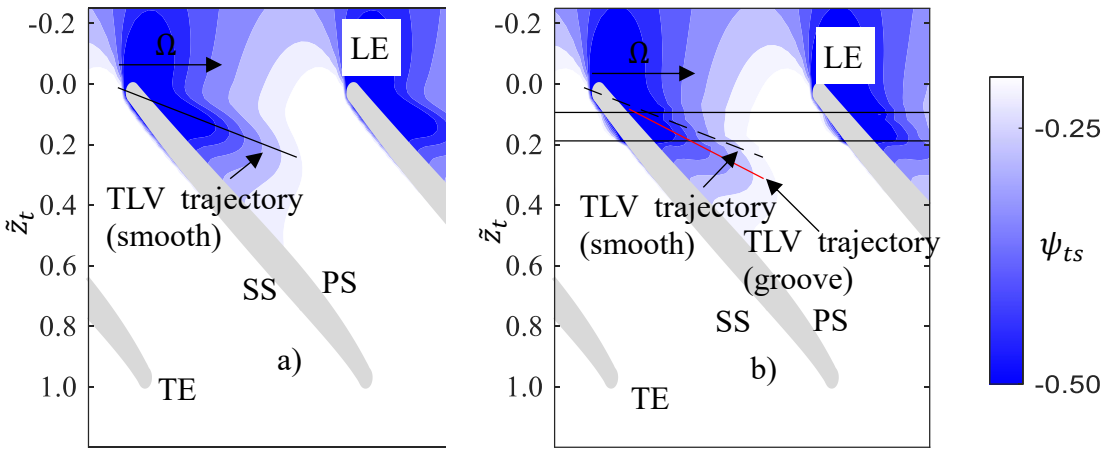

Figure 7-18 Normalised casing static pressure contour with the extracted TLV trajectory at for a) smooth 4 and b) grooved casing at operating point 8

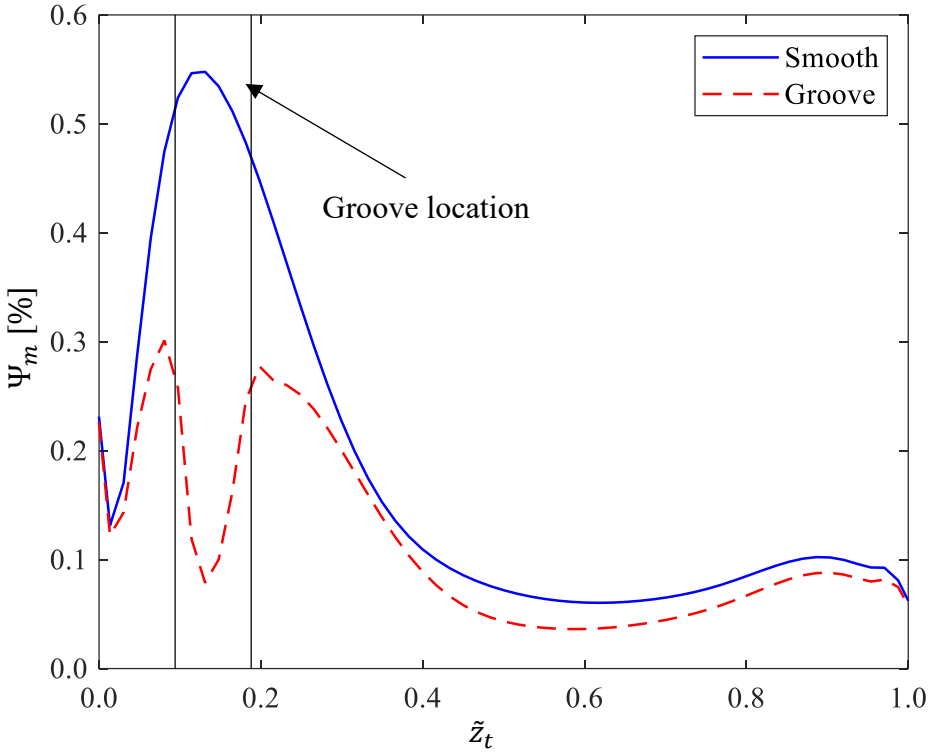

Figure 7-19 Comparison of the grooved casing blockage parameter, Ψ_m, at operating point 8 with respect to the smooth casing.

In a high-speed environment, the shift in TLV angle has been linked to the SMI (Sakuma et al., 2013). In a low-speed compressor , Houghton and Day (2011) explained that the TLV angle shift is not necessarily required for obtaining an SMI. However, the above authors do agree that positioning the groove downstream of the TLV origin but closer to the LE modifies the TLV trajectory. This further points to the fact that the positioning of the groove in relation to the peak blockage as implemented in the present study is key to achieving SMI. The effect of the groove on peak blockage is clearly shown in Figure 7-19. Here, the distribution of the non-dimensional blockage mass flow rate parameter, Ψ_m, at operating point 8 is compared between the smooth and grooved casing. The peak blockage is significantly reduced by the groove with respect to the smooth casing. The presence of the optimised groove therefore reduces the axial velocity deficit in the tip region. Reduction in axial velocity deficit means that the tip region can admit more throughflow and hence delays the upstream movement of the TLF interface at conditions near to stall. Therefore, this shows that, the reduction of the peak blockage that results in the delay of the upstream movement of the TLF interface is the primary factor for achieving an SMI. It is notable, however, that none of the SMI studies such as by Sakuma et al.

(2013) and Houghton and Day (2011) have quantified the blockage inside passage near the tip region and linked it to the improved stall margin that they have reported.

7.6 Low speed testing

It was mentioned at the beginning of the chapter that one of the motivations for undertaking the low-speed compressor design and groove optimisation study is to enable experimental validation of the SMI methodology as described in this thesis. The intention was to set up a low-speed rig incorporating the blade design as detailed in this chapter. Steady and transient structural analysis of the blade and the rotor assembly was carried out the details of which can be seen in Appendix II. Blades were manufactured using 3-D printing and the structural properties of the material was tested using a load test. This is also described in Appendix II. However, due to delays with manufacture and further delays with the COVID-19 pandemic related lock-down, the experimental campaign couldn't be completed in a manner that is useful to the present study. The PhD submission deadline as stipulated by the research sponsor was not favourable to this cause either. A basic rotor only compressor rig with limited instrumentation was put together relatively late after the lock-down restrictions were lifted. Some preliminary measurements were conducted. Some details of the rig and the preliminary results and its analysis is presented in Appendix III.

7.7 Summary

The summary of this chapter is as the following:

1. A tip-critical low-speed axial compressor (LSAC) rotor has been designed for numerically testing an optimised single circumferential casing groove. The LSAC is an aerodynamically scaled version of Rotor 37. An inverse design method has been performed to obtain the blade profiles. From 3D steady CFD simulations, the last stable operating point of the LSAC occurs on the negative slope of the pressure rise characteristic line. This infers that the LSAC designed is indeed a tip-critical compressor. Further checks are done by comparing the hub and tip region blockage at near stall conditions. It has been shown that the near casing blockage region covers a larger circumferential extent with respect to the hub blockage. This shows that the blockage is built-up near the casing is more significant with respect to the hub region at conditions near stall.

2. In a low-speed environment, the tip leakage flow (TLF) and tip leakage vortex (TLV) are predominantly responsible for the development of blockage in the near casing region. At near stall conditions, the blade loading near the LE increases due to the increased back pressure. This results in a stronger roll-up of the TLV and TLF momentum. The trajectory line of the TLV is approximated from the casing static pressure. The TLV angle increases by about 4° from near design to the near stall conditions. The increase in the TLV angle contributes to the up-stream shift of the TLF-main flow interface at conditions near stall.
3. The near casing blockage region is quantified using the mass flow-based blockage parameter (Ψ_m). It is shown that the location of the peak tip blockage moves up-stream about 5% of $c_{ax,t}$ from near design to the last stable operating point. This upstream movement is not as pronounced as in the high-speed cases presented in the previous chapters. The increase of the magnitude of the peak blockage is thought to be caused by the build-up of low axial momentum as the TLF rolls-up into the TLV.
4. The design optimisation to obtain a single circumferential groove that reduces the peak blockage with least efficiency penalty is implemented on the LSAC. The optimised single groove results in a SMI of about 5.4%. The SMI due to the opti-mised single groove is shown to be a result of the reduction of the peak blockage magnitude and a shift in the TLV angle. Both factors result in reducing the 'spill forward' effect that is primarily due to the upstream movement of the TLF-main flow interface.

Chapter 8

Conclusions and Recommendations

The potential use of passive casing treatment technology, circumferential casing grooves in particular, for stall margin improvement has been demonstrated since the 1970's through experiments and numerical simulations in both tip critical high and low-speed axial compressors. After nearly 50 years, the design of circumferential casing grooves remains a subject of active research. One of the challenges of designing circumferential grooves is that each compressor designed and built has distinctive blockage features that contribute to the stalling mechanism of the compressor. Hence, for optimum stall margin improvement, circumferential casing groove designs should be tailored according to the blockage characteristics of the compressor. This requires a thorough understanding of the near casing blockage and a method for quantifying it adequately. The main contribution of this study is to introduce a physics-based method that links the stall margin improvement of a single groove design to the blockage features of the compressor. The contribution is summarised into two parts. The first part mainly discusses the physics of the near casing flow region and its link to blockage development. Based on this, a method used to quantify the near casing blockage in a high-speed environment was presented. The second part presents the implementation of the physics-based approach on a high-speed transonic compressor and a low-speed axial compressor, respectively. Finally, recommendations for further works are presented.

8.1 Near casing flow of Rotor 37

Chapter 4 begins by validating the numerical results from the steady CFD simulations of Rotor 37 with a smooth casing by comparing it with available measured data. The calculated total pressure ratio (π) and adiabatic efficiency (η) for most of the operating points are within an error band of $\pm 2\%$ and $\pm 1\%$, respectively. Since Rotor 37 is an isolated rotor (absence of periodic unsteadiness caused by upstream and downstream blade row),

steady-state calculations were used to construct the performance characteristics. A convergence criterion was introduced to consistently determine the numerical stall point. This is very important since this thesis deals with evaluating the stall margin improvement due to casing groove design variations. Without a clear and consistent definition of the numerical stall point, the SMI of various casing groove designs cannot be directly compared. The measured outlet total pressure ratio radial distribution was compared against the result of the simulations using three commonly used turbulence models namely; $k-\epsilon$, $k-\omega$, and SST. From here, it was found that the $k-\epsilon$ model was superior than the other models in terms of predicting the trend of the total pressure ratio radial distribution. The outlet hub pressure deficit observed in the measurements was not captured by the simulations due to the absence of the leakage flow that was thought to be present in the real Rotor 37 test rig. However, this was successfully recreated by removing the inlet boundary layer skew.

In Rotor 37, Suder (1996) has demonstrated through measurements and numerical simulations that the shock-TLV interaction is primarily responsible for the development of the near casing blockage as the compressor approaches stall. This was revisited in this thesis, in order to draw a link between the shock-TLV interaction location and the development of the near casing blockage. From the casing static pressure contour, the shock and TLV trajectory lines were identified and their respective slopes across all operating points are calculated. The change of the TLV trajectory line slope across all operating points is relatively small as compared to the shock trajectory line slope. The slope of the shock trajectory line changes by about 20° away from the blade pressure side from near design conditions to the last stable operating point. The upstream movement of the shock, as it detaches from the blade, is calculated by finding the intersection point between the two trajectory lines. From the near design conditions to the last stable operating point, the shock moves upstream by about 10% of $c_{ax,t}$. By examining the structure of the TLV at near stall conditions, the shock-TLV interaction is thought to have caused a TLV breakdown despite not being able to visually capture the 'bubble' structure that is typically associated with a vortex breakdown. The change in normalised helicity, H_n, on the TLV streamlines due to the interaction with the shock further supports the claim of the TLV breakdown. The TLV breakdown can also be justified by a large blockage region close to where shock-TLV interaction occurs.

The near casing blockage is quantified using a newly defined non-dimensional mass flow blockage parameter, Ψ_m. The parameter Ψ_m, used to quantify blockage is adapted from a binary blockage identification method introduced by Sakuma et al. (2013). This quantification method allows for evaluating the blockage inside the passage which is expensive to perform in experiments. The evaluation of the change in the distribution of Ψ_m inside the passage across all operating points allows for understanding the build-up of blockage as the compressor approaches stall. The Ψ_m is evaluated for the outer 20% span only, because the blockage is found to be more significant with respect to bottom 80% of the span. From near design conditions to the last stable operating point, the location of the peak Ψ_m moves upstream by about 20% of $c_{ax,t}$. The upstream movement of the peak Ψ_m location is consistent with the upstream movement of the shock as previously mentioned. The change of shock trajectory and location causes a stronger interaction with the TLV. This results in an increase of the peak Ψ_m as the compressor approaches stall. The effect of the shock on the near casing blockage is further evaluated by simulating the compressor at part-speed (60%) as discussed in Chapter 6. Without the presence of passage shock, the upstream movement of the peak Ψ_m location is not pronounced as compared to the design speed case. Furthermore, the Ψ_m distribution at part-speed shows a higher and broader peak with respect to the design speed case. The absence of the passage shock causes the blockage to be more distributed along the chord direction. This clearly shows that at design (high)-speed, the near casing blockage is strongly dominated by the shock-TLV interaction. Therefore, the near casing blockage quantification exercise using Ψ_m has further established the role of the shock-TLV interaction and development of blockage that is mainly responsible for the onset of rotating stall in Rotor 37.

Tip critical compressors such as Rotor 37 are known to exhibit a ‘spike’-type stalling pattern in pressure and velocity traces near the casing region as the compressor approaches stall. This was not numerically shown in this thesis as this was not within the scope of this thesis and this also requires transient calculations with considerably high computing resources. However, an alternative way of proving a ‘spike’-type stalling pattern can be achieved through proving the existence of a radial separation vortex (RSV). The RSV which is linked to the ‘spike’ originates from the flow separation at the LE due to a highly loaded tip. The RSV is proven to exist by plotting the ‘lamda2’ isosurfaces together with the radial vorticity contour at the near casing region. The location of the

'tornado'-like structure is consistent with the location where there is positive radial vorticity on the contour. This suggests the existence of a radial vortex. To the author's best knowledge, the existence of the RSV has never been reported in the literature despite numerous numerical studies have been published in relation to the tip aerodynamics of Rotor 37.

8.2 Physics-based method for designing a single circumferential casing groove in a high-speed and low-speed environment

A physics-based approach for designing a single casing groove design is possible since the passage blockage characteristics can be evaluated from the Ψ_m distribution. The physics-based approach is a surrogate based optimisation approach that is first implemented on a high-speed environment with and without the presence of passage shock as discussed in Chapter 6. The physics-based approach that is explained in Chapter 5 reduces the computational cost of the design optimisation in two different ways. First, the surrogate model reduces computational cost of the optimiser algorithm for evaluating the objective functions. The outputs of the objective functions are obtained from a surrogate model that is constructed from high-fidelity CFD simulations. Secondly, the use of Ψ_m as one of the objective functions reduces the number of CFD simulations required for obtaining the output value of the objective function. If the SMI is selected as the objective function, one would have to run multiple simulations at various operating conditions to find the numerical stall point and to obtain the performance characteristics. This is because, the SMI can only be evaluated once the full performance characteristic is constructed. Instead, using Ψ_m as one of the objective functions only requires the simulation to be performed at only one operating point (near stall condition) since it is the build-up of blockage near stall that has shown to be responsible for stall.

The optimised casing groove design implemented on Rotor 37 produces an SMI of about 0.6% with negligible efficiency loss. Albeit the SMI being small, this finding is considerably realistic after comparing this result with a different multi-groove design optimisation approach conducted on Rotor 37. The study by Qin et al. (2013) reported a 0.7% SMI when a 5 groove with variable depth arrangement was applied on Rotor 37. The effect of the optimised casing groove design at part-speed conditions also show no deterioration where a 0.6% SMI is obtained. At design speed conditions, the sensitivity of the SMI on

axial location of the casing groove is investigated by varying the axial location of the optimised casing groove design, S1. Two more single groove design; S0 and S2 are obtained by axially moving the grooves upstream and downstream of S1. From this exercise, it was found that the SMI of S0 is the highest among the other single cases, S1 and S2. The SMI of S0 and S2 are about 1.3% and 0.13%, respectively. Comparison of the Ψ_m distribution of the single grooves shows that highest SMI achieved by S0 was due the reduction of the front part of the peak Ψ_m distribution. S0 is located upstream of the peak Ψ_m location where it might have affected the source of the blockage itself which is the shock-TLV interaction. The reduction of the front part of the peak Ψ_m allows the incoming flow through the passage with reduced resistance which results in SMI. Adding the single grooves together to form multiple-groove configurations did not contribute to a significant increase to SMI. It was found that the SMI of the multiple-groove configuration follow the same trend of the upstream groove in each configuration. From this, it can be stressed that the upstream groove plays a larger role by reducing the blockage that is providing resistance to the incoming through the passage. Additional downstream do not necessarily lead to a higher SMI but also may contribute to additional losses near the casing.

The physics-based approach for designing a single casing groove is further tested numerically on a low-speed axial compressor. For this purpose, a tip critical and isolated low-speed axial compressor (LSAC) rotor is designed using an inverse design approach. The design procedure of the LSAC has been presented in the first part of Chapter 7. In a low-speed environment, the source of the near casing blockage is primarily linked to the tip leakage flow (TLF) and the TLV. At the compressor approaches stall, the TLF-main flow interface advances away from the blade SS to become more aligned with the circumferential direction. This provides a resistance for the incoming flow through the passage. The advancement of the TLF-main flow interface is caused by the increased backpressure, tip leakage momentum and the axial velocity deficit due to the roll-up of the TLV at conditions near stall. With the absence of shock, the advancement of peak Ψ_m location is not pronounced as found in Rotor 37 at design speed. It is shown that the location of the peak Ψ_m moves upstream by about 5% of $c_{ax,t}$ from near design to the last stable operating point. At the last stable operating point, the peak Ψ_m is located about 10% of $c_{ax,t}$ aft of the tip LE. From this information, an optimised single casing groove design is

obtained using the same method used for the high-speed case presented in Chapter 6. The SMI obtained from the optimised casing groove design is about 5.4%. It was found that the reduction of the near casing blockage and the shift in TLV angle by the optimised groove delays the advancement of the TLF-main flow interface. This results in the delay of the onset of rotating stall.

8.3 Closure

This thesis provides a possible method for compressor designers to achieve SMI using an optimised single casing groove design. The introduction of a blockage-based parameter, Ψ_m further helps to understand and explain the missing link between SMI and various casing groove designs.

8.4 Recommendation for further work

The physics-based method has been successfully implemented numerically onto a high-speed and low-speed compressor to find an optimised single casing groove design for SMI. Up until now, this method has only been validated numerically and for rotor only configurations.

8.4.1 Experiments

The low speed design and analysis was partly aimed at making a cost-effective test rig experimental validation viable for the optimisation methodology presented in this thesis. Although there was an intention to do this as part of the current thesis work delay in manufacturing, pandemic related lock-down and the thesis submission deadline as stipulated all contributed to a lack of time to conduct any meaningful experimentation. It is therefore recommended that a complete and detailed experimental validation of the SMI improvement strategy be carried out. These could range from performance only tests to very detailed measurements to quantify the blockage.

8.4.2 Complete compressor stage configuration and multi-stage environment

In this thesis, the simulation has been performed on an isolated compressor rotor configuration. It would be interesting to numerically test the design optimisation method in a complete compressor stage and also in a multi-stage environment. This will take into account the effects of upstream and downstream blade rows on the development of blockage which is not present in this thesis.

8.4.3 Other casing treatment methods

The optimisation method developed in this thesis is based on the identification of blockage, whatever the source of it may be, and its minimisation by using it (i.e. the blockage parameter) as one of the objective function to be minimised. The choice of the SMI methodology could then be changed in theory from single circumferential groove to the employment of other concepts such as axial grooves, casing recirculation strategies or active injection methods. Optimisation of multiple circumferential grooves could also be a topic for future study.

Bibliography

Adamczyk, J. J., Celestina, M. L., & Greitzer, E. M. (1993). The Role of Tip Clearance in High-Speed Fan Stall. *Journal of Turbomachinery*, *115*(1), 28. https://doi.org/10.1115/1.2929212

Ahmad, M. W., Mourshed, M., & Rezgui, Y. (2017). Trees vs Neurons: Comparison between random forest and ANN for high-resolution prediction of building energy consumption. *Energy and Buildings*, *147*, 77–89. https://doi.org/https://doi.org/10.1016/j.enbuild.2017.04.038

Ameri, A. A. (2009). NASA ROTOR 37 CFD CODE validation Glenn-HT code. In *47th AIAA Aerospace Sciences Meeting including the New Horizons Forum and Aerospace Exposition*. https://doi.org/10.2514/6.2009-1060

ANSYS CFX 17.1 Documentation. (n.d.). ANSYS Inc.

Bailey, E. E. (1972). Effect of grooved casing treatment on the flow range capability of a single-stage axial-flow compressor. *NASA Technical Report*, (NASA-TM-X-2459, E-6560), 17. Retrieved from https://ntrs.nasa.gov/search.jsp?R=19720007335

Bishop, C. M. (2006). *Pattern Recognition and Machine Learning (Information Science and Statistics)*. Berlin, Heidelberg: Springer-Verlag.

Brandstetter, C., Jüngst, M., & Schiffer, H.-P. (2018). Measurements of Radial Vortices, Spill Forward, and Vortex Breakdown in a Transonic Compressor. *Journal of Turbomachinery*, *140*(6). https://doi.org/10.1115/1.4039053

Breiman, L. (1996). Bagging Predictors. *Machine Learning*, *24*(2), 123–140. https://doi.org/10.1023/A:1018054314350

Breiman, L. (2001). Random Forests. *Machine Learning*, *45*(1), 5–32. https://doi.org/10.1023/A:1010933404324

Bruna, D., & Turner, M. G. (2013). Isothermal Boundary Condition at Casing Applied to the Rotor 37 Transonic Axial Flow Compressor. *Journal of Turbomachinery*,

135(3). https://doi.org/10.1115/1.4007569

Camp, T. R., & Day, I. J. (1998). A study of spike and modal stall phenomena in a low-speed axial compressor. *Journal of Turbomachinery*, *120*(3), 393–401. https://doi.org/10.1115/1.2841730

Chen, H., Huang, X., Shi, K., Fu, S., Ross, M., Bennington, M. A., … Wadia, A. (2013). A Computational Fluid Dynamics Study of Circumferential Groove Casing Treatment in a Transonic Axial Compressor. *Journal of Turbomachinery*, *136*(3). https://doi.org/10.1115/1.4024651

Chenkai, Z., Jun, H., Zhiqiang, W., & Xiang, G. (2014). Design Work of a Compressor Stage Through High-To-Low Speed Compressor Transformation. *Journal of Engineering for Gas Turbines and Power*, *136*(6). https://doi.org/10.1115/1.4026520

Cornelius, C., Biesinger, T., Galpin, P., & Braune, A. (2013). Experimental and Computational Analysis of a Multistage Axial Compressor Including Stall Prediction by Steady and Transient CFD Methods. *Journal of Turbomachinery*, *136*(6), 61013. https://doi.org/10.1115/1.4025583

Cutler, A., Cutler, D., & Stevens, J. (2011). Random Forests. In *Machine Learning - ML* (Vol. 45, pp. 157–176). https://doi.org/10.1007/978-1-4419-9326-7_5

Dang, T. Q., van Rooij, M. P. C., & Larosiliere, L. M. (2003). *Design of Aspirated Compressor Blades Using Three-Dimensional Inverse Method*. *Volume 6:*, 479–488. https://doi.org/10.1115/GT2003-38492

Day, I. J. (1993a). Active Suppression of Rotating Stall and Surge in Axial Compressors. *Journal of Turbomachinery*, *115*(1), 40. https://doi.org/10.1115/1.2929216

Day, I. J. (1993b). Stall Inception in Axial Flow Compressors. *Journal of Turbomachinery*, *115*(1), 1. https://doi.org/10.1115/1.2929209

Day, I. J., Breuer, T., Escuret, J., Cherrett, M., & Wilson, A. (1999). Stall Inception and the Prospects for Active Control in Four High-Speed Compressors. *Journal of*

Turbomachinery, *121*(1), 18–27. Retrieved from http://dx.doi.org/10.1115/1.2841229

de Vito, L., den Braembussche R. A., V., & Deconinck, H. (2003). A Novel Two-Dimensional Viscous Inverse Design Method for Turbomachinery Blading . *Journal of Turbomachinery*, *125*(2), 310–316. https://doi.org/10.1115/1.1545765

Denton, J. D. (1997). Lessons from rotor 37. *Journal of Thermal Science*, *6*(1), 1–13. https://doi.org/10.1007/s11630-997-0010-9

Dunham, J. (1998). CFD Validation for Propulsion System. In *AGARD Advisory Report 355*. NEUILLY-SUR-SEINE, FRANCE.

Emmons, H. W., Pearson, C. E. and Grant, H. P. (1955). Compressor Surge and Stall Propagation. *Trans. ASME*, *77*, 455–467.

Fonseca, C. M., & Fleming, P. J. (1993). Genetic Algorithms for Multiobjective Optimization: FormulationDiscussion and Generalization. *Proceedings of the 5th International Conference on Genetic Algorithms*, 416–423. Retrieved from http://dl.acm.org/citation.cfm?id=645513.657757

Freeman, C., Wilson, A. G., Day, I. J., & Swinbanks, M. A. (1998). Experiments in Active Control of Stall on an Aeroengine Gas Turbine. *J. Turbomach.*, *120*(October 1998), 637–647. https://doi.org/http://dx.doi.org/10.1016/S0920-5489(99)92014-7

Fujita, H., & Takata, H. (1984). A Study on Configurations of Casing Treatment for Axial Flow Compressors. *Bulletin of JSME*, *27*(230), 1675–1681. https://doi.org/10.1299/jsme1958.27.1675

Furukawa, M., Inoue, M., Saiki, K., & Yamada, K. (1999). The role of tip leakage vortex breakdown in compressor rotor aerodynamics. *Journal of Turbomachinery*, *121*(3), 469–480. https://doi.org/10.1115/1.2841339

Goinis, G., Voß, C., & Aulich, M. (2013). Circumferential Grooves for a Modern Transonic Compressor: Aerodynamic Effects, Benefits and Limitations. *10th European Conference on Turbomachinery Fluid Dynamics and Thermodynamics*,

ETC 2013, 58–71.

Goldberg, D. E. (1989). *Genetic Algorithms in Search, Optimization and Machine Learning* (1st ed.). Boston, MA, USA: Addison-Wesley Longman Publishing Co., Inc.

Goodhand, M. N., & Miller, R. J. (2010). Compressor Leading Edge Spikes: A New Performance Criterion. *Journal of Turbomachinery*, *133*(2). https://doi.org/10.1115/1.4000567

Greitzer, E. M. (1976a). Surge and Rotating Stall in Axial Flow Compressors—Part I: Theoretical Compression System Model. *Journal of Engineering for Power*, *98*(2), 190–198. https://doi.org/10.1115/1.3446138

Greitzer, E. M. (1976b). Surge and Rotating Stall in Axial Flow Compressors—Part II: Experimental Results and Comparison With Theory. *Journal of Engineering for Power*, *98*(2), 199–211. https://doi.org/10.1115/1.3446139

Hah, C., & Loellbach, J. (1999). Development of Hub Corner Stall and Its Influence on the Performance of Axial Compressor Blade Rows. *Journal of Turbomachinery*, *121*(1), 67–77. https://doi.org/10.1115/1.2841235

Han, T., Jiang, D., Zhao, Q., Wang, L., & Yin, K. (2018). Comparison of random forest, artificial neural networks and support vector machine for intelligent diagnosis of rotating machinery. *Transactions of the Institute of Measurement and Control*, *40*(8), 2681–2693. https://doi.org/10.1177/0142331217708242

Hathaway, M. D. (2002). Self-Recirculating Casing Treatment Concept for Enhanced Compressor Performance. *ASME Turbo Expo 2002: Power for Land, Sea, and Air*, (July), GT2002-30368, 411–420. https://doi.org/GT-2002-30368

Hathaway, M. D. (2007). Passive Endwall Treatments for Enhancing Stability. *NASA Report No. TM-2007-214409*.

Houghton, T., & Day, I. (2011). Enhancing the stability of subsonic compressors using casing grooves. *Journal of Turbomachinery*, *133*(2). https://doi.org/10.1115/1.4000569

Houghton, T. O. (2010). *Axial Compressor Stability Enhancement* , PhD Thesis, University of Cambridge. Retrieved from https://www.repository.cam.ac.uk/handle/1810/252194

Hoying, D. A., Tan, C. S., Vo, H. D., & Greitzer, E. M. (1999). Role of Blade Passage Flow Structurs in Axial Compressor Rotating Stall Inception. *Journal of Turbomachinery*, *121*(4), 735. https://doi.org/10.1115/1.2836727

Huppert, M. C. (1952). Prelimanary Investigation of Flow Fluctuations During Surge and Blade Row Stall in Axial-Flow Compressors. *National Advisory Committee for Aeronautics Research Memorandum*, NACA RME5258.

Inoue, M., Kuroumaru, M., Tanino, T., & Furukawa, M. (1999). Propagation of Multiple Short-Length-Scale Stall Cells in an Axial Compressor Rotor. *Journal of Turbomachinery*, *122*(1), 45–54. Retrieved from http://dx.doi.org/10.1115/1.555426

Jeong, J., & Hussain, F. (1995). On the identification of a vortex. *J. Fluid Mech.*, *332*, 339–363.

Khaleghi, H. (2014). Effect of discrete endwall recirculation on the stability of a high-speed compressor rotor. *Aerospace Science and Technology*, *37*, 130–137. https://doi.org/10.1016/j.ast.2014.05.009

Kim, J.-H., Choi, K.-J., Husain, A., & Kim, K.-Y. (2011). Multiobjective Optimization of Circumferential Casing Grooves for a Transonic Axial Compressor. *Journal of Propulsion and Power*, *27*(3), 730–733. https://doi.org/10.2514/1.50563

Launder, B. E., & Spalding, D. B. (1974). The numerical computation of turbulent flows. *Computer Methods in Applied Mechanics and Engineering*, *3*(2), 269–289. https://doi.org/https://doi.org/10.1016/0045-7825(74)90029-2

Lei, V.-M., Spakovszky, Z. S., & Greitzer, E. M. (2008). A Criterion for Axial Compressor Hub-Corner Stall. *Journal of Turbomachinery*, *130*(3). https://doi.org/10.1115/1.2775492

Li, J., Lin, F., Wang, S., Du, J., Nie, C., & Chen, J. (2014). *Extensive Experimental*

Study of Circumferential Single Groove in an Axial Flow Compressor. *Volume 2D:* https://doi.org/10.1115/GT2014-26859

Li, Y.-L. (2014). *Numerical Simulations of Rotating Stall in Axial Flow Compressors*, Phd Thesis, University of Sussex.

Lieblein, S., Schwenk, F. C., & Broderick, R. L. (1953). Diffusion factor for estimating losses and limiting blade loadings in axial-flow-compressor blade elements. *NASA Research Memorandum*, NACA RM E53D01.

Losey, S. (2019). Compressor stall led to fatal T-38 crash. Retrieved August 15, 2020, from Air Force Times website: https://www.airforcetimes.com/news/your-air-force/2019/06/18/compressor-stall-led-to-fatal-t-38-crash/

Lyes, P. A., & Ginder, R. B. (1998). Experimental Evaluation of the High-to-Low Speed Transformation Process for a Highly Loaded Core Compressor Stage. *Journal of Turbomachinery, Volume 1:* https://doi.org/10.1115/98-GT-334

Mailach, R., Lehmann, I., & Vogeler, K. (2000). Rotating Instabilities in an Axial Compressor Originating From the Fluctuating Blade Tip Vortex. *Journal of Turbomachinery*, *123*(3), 453–460. https://doi.org/10.1115/1.1370160

McDougall, N. M., Cumpsty, N. A., & Hynes, T. P. (1990). Stall Inception in Axial Compressors. *Journal of Turbomachinery*, *112*(1), 116. https://doi.org/10.1115/1.2927406

Mckay, M., Beckman, R., & Conover, W. (1979). A Comparison of Three Methods for Selecting Vales of Input Variables in the Analysis of Output From a Computer Code. *Technometrics*, *21*, 239–245. https://doi.org/10.1080/00401706.1979.10489755

Mengistu, T., & Ghaly, W. (2008). Aerodynamic optimization of turbomachinery blades using evolutionary methods and ANN-based surrogate models. *Optimization and Engineering*, *9*, 239–255. https://doi.org/10.1007/s11081-007-9031-1

Montgomery, D. C. (2006). *Design and Analysis of Experiments*. Hoboken, NJ, USA:

John Wiley & Sons, Inc.

Moore, R., D., Kovich, G., & Blade, R., J. (1971). Effect of casing treatment on overall and blade element performance of a compressor rotor. *NASA Technical Report*, NASA-TN-D-6538.

Moukalled, F., Mangani, L., & Darwish, M. (2015). *The Finite Volume Method in Computational Fluid Dynamics: An Advanced Introduction with OpenFOAM and Matlab* (1st ed.). Springer Publishing Company, Incorporated.

Mu¨ller, M. W., Schiffer, H.-P., Voges, M., & Hah, C. (2011). Investigation of Passage Flow Features in a Transonic Compressor Rotor With Casing Treatments. *Proceedings of the ASME 2011 Turbo Expo: Turbine Technical Conference and Exposition. Volume 7: Turbomachinery, Parts A, B, and C.*, 65–75. https://doi.org/10.1115/GT2011-45364

Nan, X., Ma, N., Lin, F., Himeno, T., & Watanabe, T. (2018). A new approach of casing treatment design for high speed compressors running at partial speeds with low speed large scale test. *Aerospace Science and Technology*, *72*, 104–113. https://doi.org/https://doi.org/10.1016/j.ast.2017.10.032

Öksüz, Ö., & Akmandor, I. S. (2010). Multi-objective aerodynamic optimization of axial turbine blades using a NOVEL multilevel genetic algorithm. *Journal of Turbomachinery*, *132*(4), 1–14. https://doi.org/10.1115/1.3213558

Osborn, W. M., Lewis, G. W., J., & Heidelberg, L. J. (1971). Effect of several porous casing treatments on stall limit and on overall performance of an axial flow compressor rotor. *NASA Technical Report*, (NASA-TN-D-6537).

Paduano, J. D., Epstein, A. H., Valavani, L., Longley, J. P., Greitzer, E. M., & Guenette, G. R. (1993). Active Control of Rotating Stall in a Low-Speed Axial Compressor. *Journal of Turbomachinery*, *115*(1), 48. https://doi.org/10.1115/1.2929217

Pierret, S., Filomeno Coelho, R., & Kato, H. (2007). Multidisciplinary and multiple operating points shape optimization of three-dimensional compressor blades. *Structural and Multidisciplinary Optimization*, *33*(1), 61–70. https://doi.org/10.1007/s00158-006-0033-y

Pierret, Stephane, & Braembussche, R. (1999). Turbomachinery Blade Design Using a Navier–Stokes Solver and Artificial Neural Network. *Journal of Turbomachinery-Transactions of The Asme - J TURBOMACH-T ASME*, *121*. https://doi.org/10.1115/1.2841318

Prince D. C., J., Wisler, D. C., & Hilvers, D. E. (1975). A Study of Casing Treatment Stall Margin Improvement Phenomena. *Proceedings of the ASME 1975 International Gas Turbine Conference and Products Show*, Volume 1A: https://doi.org/10.1115/75-GT-60

Pullan, G., Young, A. M., Day, I. J., Greitzer, E. M., & Spakovszky, Z. S. (2015). Origins and structure of spike-type rotating stall. *Journal of Turbomachinery*, *137*(5). https://doi.org/10.1115/1.4028494

Qin, N., Carnie, G., Wang, Y., & Shahpar, S. (2013). Design Optimization of Casing Grooves Using Zipper Layer Meshing. *Journal of Turbomachinery*, *136*(3). https://doi.org/10.1115/1.4024650

Queipo, N. V., Haftka, R. T., Shyy, W., Goel, T., Vaidyanathan, R., & Kevin Tucker, P. (2005). Surrogate-based analysis and optimization. *Progress in Aerospace Sciences*, *41*(1), 1–28. https://doi.org/10.1016/j.paerosci.2005.02.001

Rabe, D. C., & Hah, C. (2002). *Application of Casing Circumferential Grooves for Improved Stall Margin in a Transonic Axial Compressor*. *Volume 5:*, 1141–1153. https://doi.org/10.1115/GT2002-30641

Reid, L., Moore, R. D. (1978). Design and Overall Performance of Four Highly Loaded, High-Speed Inlet Stages for an Advanced High-Pressure Ratio Core Compressor. *NASA Technical Paper*, *1337*. https://doi.org/NASA TP 1337

Reid, R. D. and Moore, L. (1980). Performance of Single-Stage Axial-Flow Transonic Compressor With Rotor and Stator Aspect Ratios of 1. 19 and 1. 26, Respectively, and With Design Pressure Ratio of 2. 05. *NASA Technical Paper*, (1659).

Ross, M. H., Cameron, J. D., Morris, S. C., Chen, H., & Shi, K. (2017). Axial Compressor Stall, Circumferential Groove Casing Treatment, and the Tip-Clearance Momentum Flux. *Journal of Propulsion and Power*, *34*(1), 146–152.

https://doi.org/10.2514/1.B36181

Sakuma, Y., Watanabe, T., Himeno, T., Kato, D., Murooka, T., & Shuto, Y. (2013). Numerical Analysis of Flow in a Transonic Compressor With a Single Circumferential Casing Groove: Influence of Groove Location and Depth on Flow Instability. *Journal of Turbomachinery*, *136*(3), 031017. https://doi.org/10.1115/1.4025575

Schlechtriem, S., & Lötzerich, M. (1997). Breakdown of Tip Leakage Vortices in Compressors at Flow Conditions Close to Stall. *Proceedings of the ASME 1997 International Gas Turbine and Aeroengine Congress and Exhibition*, Volume 1. https://doi.org/10.1115/97-GT-041

Seshadri, P., Parks, G. T., & Shahpar, S. (2014). Leakage Uncertainties in Compressors: The Case of Rotor 37. *Journal of Propulsion and Power*, *35*(1), 1–11. https://doi.org/10.2514/1.B35039

Shabbir, A, Celestina, M. L., Adamczyk, J. J., & Strazisar, A. J. (1997). The effect of hub leakage flow on two high speed axial flow compressor rotors. *ASME 1997 International Gas Turbine and Aeroengine Congress and Exhibition*, V001T03A053--V001T03A053.

Shabbir, Aamir, & Adamczyk, J. J. (2005). Flow Mechanism for Stall Margin Improvement due to Circumferential Casing Grooves on Axial Compressors. *Journal of Turbomachinery*, *127*(4), 708. https://doi.org/10.1115/1.2008970

Strazisar, A. J., Bright, M. M., Thorp, S., Culley, D. E., & Suder, K. L. (2004). Compressor Stall Control Through Endwall Recirculation, *Proceedings of the ASME Turbo Expo 2004: Power for Land, Sea, and Air, Volume 5:*, 655–667. https://doi.org/10.1115/GT2004-54295

Suder, K. L., & Celestina, M. L. (1996). Experimental and Computational Investigation of the Tip Clearance Flow in a Transonic Axial Compressor Rotor. *Journal of Turbomachinery*, *118*(2), 218. https://doi.org/10.1115/1.2836629

Suder, K L, Chima, R. V, Strazisar, A. J., & Roberts, W. B. (1995). The Effect of Adding Roughness and Thickness to a Transonic Axial Compressor Rotor. *Journal*

of Turbomachinery, *117*(4), 491–505. https://doi.org/10.1115/1.2836561

Suder, Kenneth L. (1996). Experimental Investigation of the Flow Field in a Transonic, Axial Flow Compressor with Respect to the Development of Blockage and Loss, Phd Thesis, Case Western Reserve University. https://doi.org/10.16953/deusbed.74839

Suder, Kenneth L. (1998). Blockage Development in a Transonic, Axial Compressor Rotor. *Journal of Turbomachinery*, *120*(3), 465–476. https://doi.org/10.1115/1.2841741

Tikkanen, A. (2020). US Airways flight 1549. Retrieved August 16, 2020, from Encyclopædia Britannica, inc. website: https://www.britannica.com/topic/US-Airways-Flight-1549-incident

Vekinis, A., & Longley, J. (2018). Convergence Criteria for Axial Compressor Flow Calculations. *Global Power and Propulsion Forum*.

Verikas, A., Gelzinis, A., & Bacauskiene, M. (2011). Mining data with random forests: A survey and results of new tests. *Pattern Recognition*, *44*(2), 330–349. https://doi.org/https://doi.org/10.1016/j.patcog.2010.08.011

Vo, H. D., Tan, C. S., & Greitzer, E. M. (2008). Criteria for Spike Initiated Rotating Stall. *Journal of Turbomachinery*, *130*(1), 011023. https://doi.org/10.1115/1.2750674

Williams, B. A., & Cremaschi, S. (2019). Surrogate Model Selection for Design Space Approximation And Surrogatebased Optimization. In S. G. Muñoz, C. D. Laird, & M. J. Realff (Eds.), *Proceedings of the 9th International Conference on Foundations of Computer-Aided Process Design* (pp. 353–358). https://doi.org/https://doi.org/10.1016/B978-0-12-818597-1.50056-4

Wisler, D. C. (1985). Loss Reduction in Axial-Flow Compressors Through Low-Speed Model Testing. *Journal of Engineering for Gas Turbines and Power*, *107*(2), 354–363. https://doi.org/10.1115/1.3239730

Yamada, K, Funazaki, K., & Furukawa, M. (2007). *The Behavior of Tip Clearance*

Flow at Near-stall Condition in a Transonic Axial Compressor Rotor.

Yamada, Kazutoyo, Kikuta, H., Iwakiri, K., Furukawa, M., & Gunjishima, S. (2012). An Explanation for Flow Features of Spike-Type Stall Inception in an Axial Compressor Rotor. *Journal of Turbomachinery*, *135*(2). https://doi.org/10.1115/1.4007570

Yang, X.-S. (2014). Chapter 14 - Multi-Objective Optimization. In X.-S. Yang (Ed.), *Nature-Inspired Optimization Algorithms* (pp. 197–211). https://doi.org/https://doi.org/10.1016/B978-0-12-416743-8.00014-2

Youngren, H. H., Drela, M. (2008). *A User's Guide to MISES 2.63*.

Youngren, H. H. (1991). *Analysis and design of transonic cascades with splitter vanes*. Massachusetts Institute of Technology.

Appendix I

Inverse blade design using MISES

Introduction

An example for obtaining a 2D blade shape through an inverse design method is shown in this appendix.

Pre-requisites

Seed geometry

The inverse design method is an iterative method where the blade shape is transformed towards a specified design target. Hence, a seed geometry is required to begin with. Using a simple MATLAB code, a blade shape is defined by specifying the camber profile, thickness distribution and leading and trailing edge profiles. Figure A1- 1 shows the parameters to define the initial blade shape.

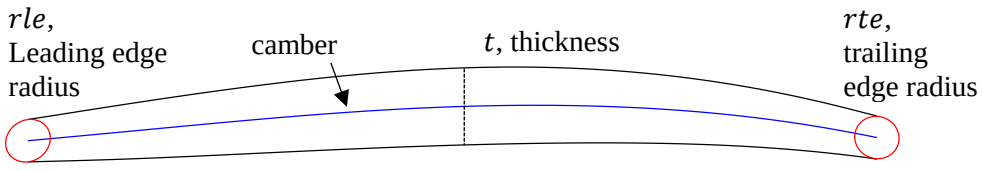

Figure A1- 1 Blade shape parameterisation

Target blade loading

The next pre-requisite is the specified design target which is the blade loading. The target blade loading is normally obtained from an existing blade shape. In this study, the target blade loading is obtained numerically from 3D RANS simulations. The blade loading is extracted at a specified radius.

MISES

The MISES is a collection of programs developed for 2D cascade design and analysis. The snapshot of the MISES menu is shown in Figure A1- 2. For the inverse design procedure, Option 1, 3 and 4 are used. Option 1 (ISES) is the program that solves the flow domain. The flow in the inviscid region is obtained by solving the Euler equations. In the boundary layer region, the integral boundary layer equation is solved. Option 3 (EDP) is the inverse design program. The target blade loading and inverse design setup are performed using this program. MISES uses mode shapes to transform the initial blade shape towards the final blade shape that satisfies the target blade loading. Option 4 is the geometry import and grid meshing program.

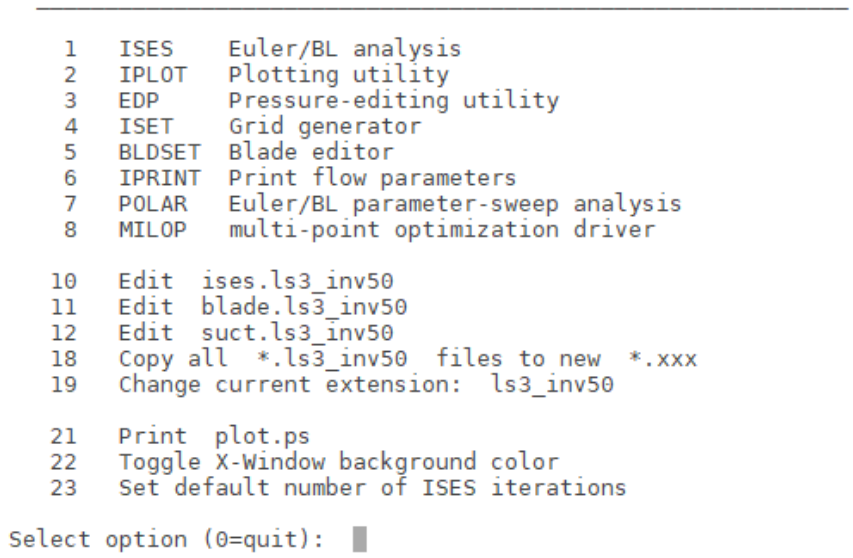

Figure A1- 2 MISES menu

Input geometry and grid generation

The blade shape is first input into MISES. The geometric input parameters required are blade coordinates, pitch and flow angles. Figure A1- 3 shows the seed geometry read into the program. The dashed line represents the location of the inlet and outlet of the numerical domain. Next, the grid is automatically generated by the program. Figure A1- 4 shows

the generated grid with default setup. The grid nodes are distributed along the blade surface and the streamwise nodes are obtained from simple linear interpolation. The grid undergoes several iterations of smoothing to improve the quality.

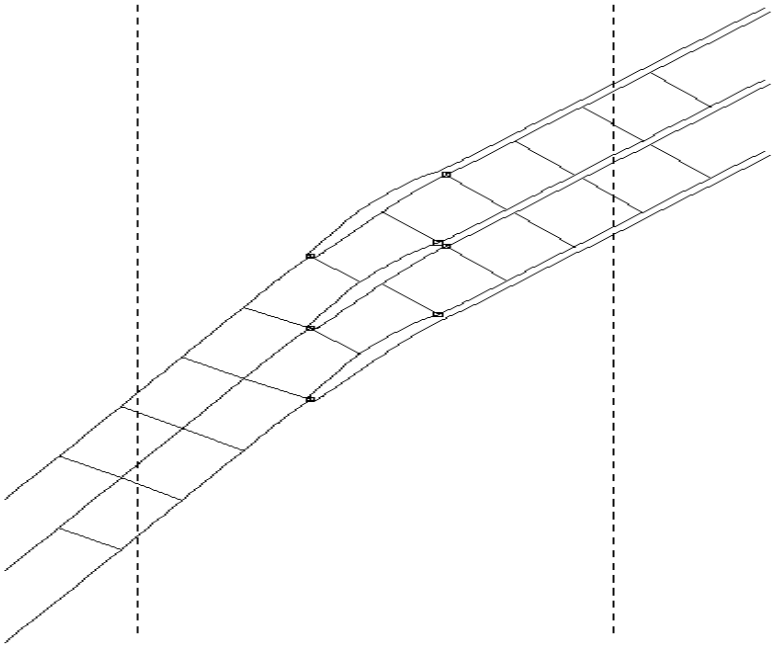

Figure A1- 3 Blade input into MISES

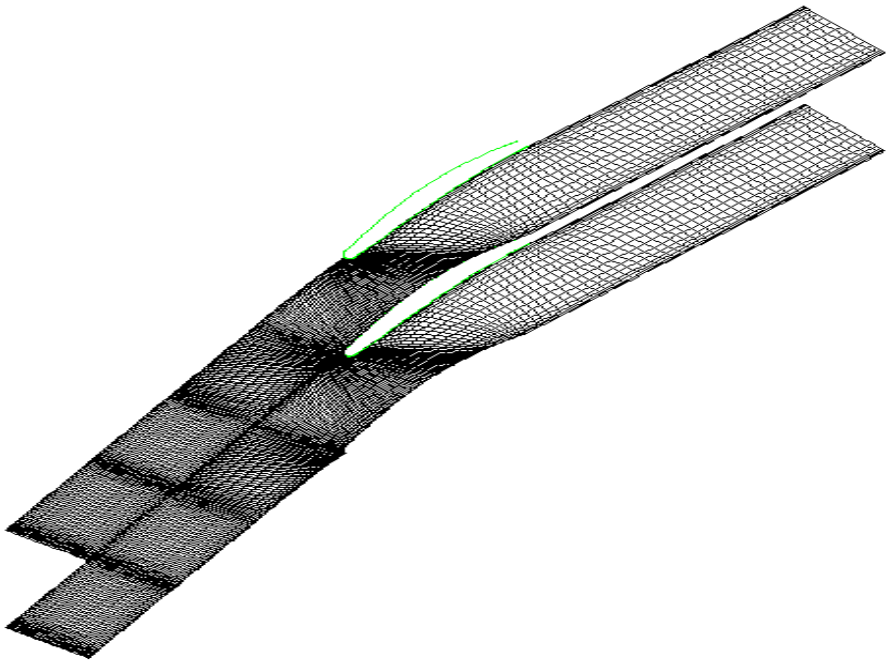

Figure A1- 4 Grid of the numerical domain

Setup and initial flow solution

The numerical setup is input using ISES program (option 1) from the main menu. Here, the numerical setup and boundary conditions are prescribed. The flow angle, Mach number and pressure are required at the inlet and outlet. These values are obtained from a 1D design analysis. The calculation is iterated until the flow converges. The convergence occurs when the changes of global variables fall below 1×10^{-5}. Figure A1- 5 shows the blade loading for a converged calculation. The aim now is to modify the blade shape until the blade loading shown in Figure A1- 5 matches the target blade loading.

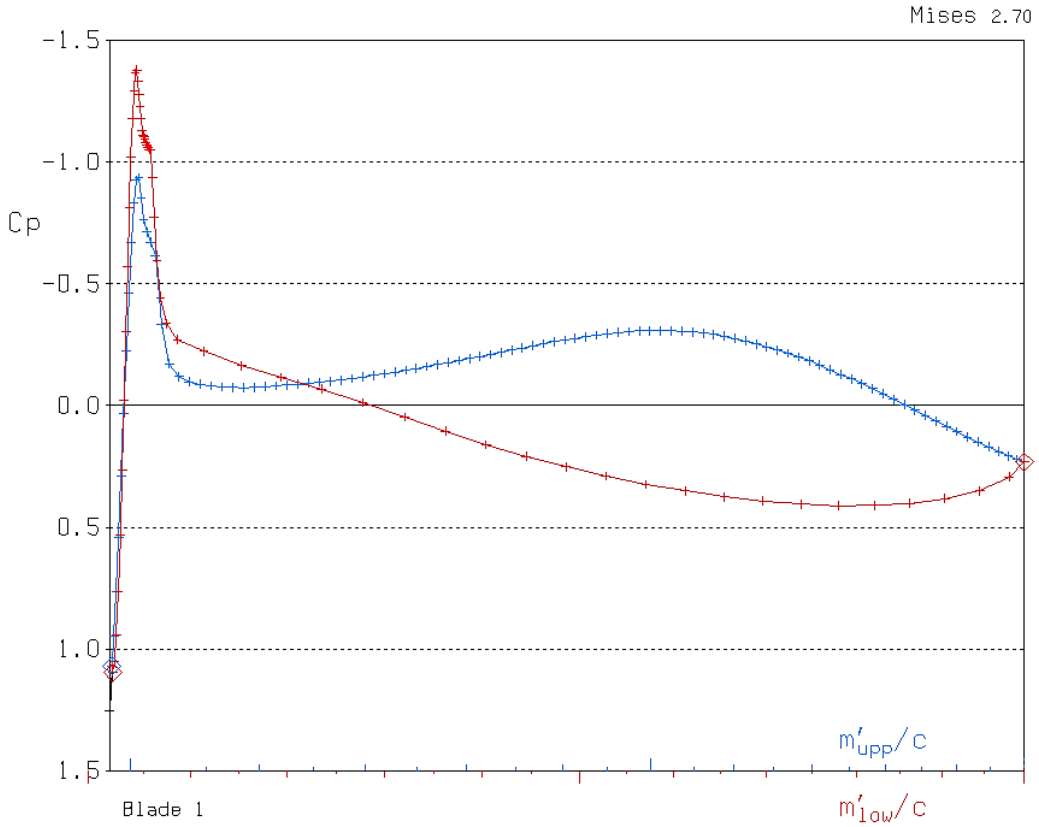

Figure A1- 5 Blade loading of the initial seed geometry

Inverse design

The input of the target blade loading and setting up for the inverse design are performed using the EDP program (Option 4) from the main menu. Figure A1- 6 shows the comparison of the initial blade loading (dotted line) with respect to the target blade loading (smooth line). The inverse design method uses a modal-inverse method. Here, the sum of mode shapes is used to deform the surface normal of the blade with respect to the initial

shape. The blade shape is perturbed iteratively until the target blade loading is matched using a method of least squares. The user also has an option to re-camber or vary the blade stagger angle to reduce the error between the target and the obtained blade loading. Figure A1- 7 to Figure A1- 9 shows the iterative procedure of matching the target blade loading. In the first iteration as shown in Figure A1- 7, there is a slight mismatch at the front part of the blade suction side (red line). This is improved in Figure A1- 8 where the blade has been rotated ever so slightly to reduce the blade incidence at the leading edge. The blade undergoes another round of perturbation where the result is shown in Figure A1- 9. The blade loading now is a relatively better match of the target blade loading. The comparison of the initial seed geometry with respect to the final blade shape is shown in Figure A1- 10.

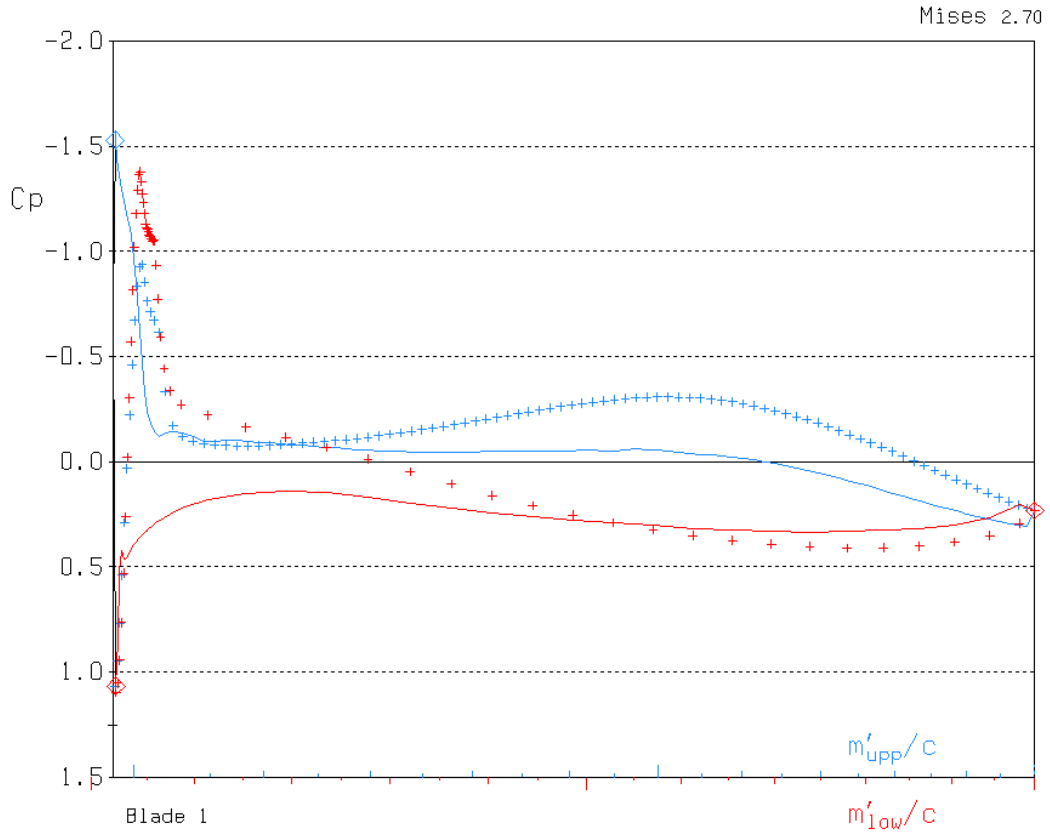

Figure A1- 6 Comparison between initial blade loading (dotted lines) and target blade loading (smooth lines)

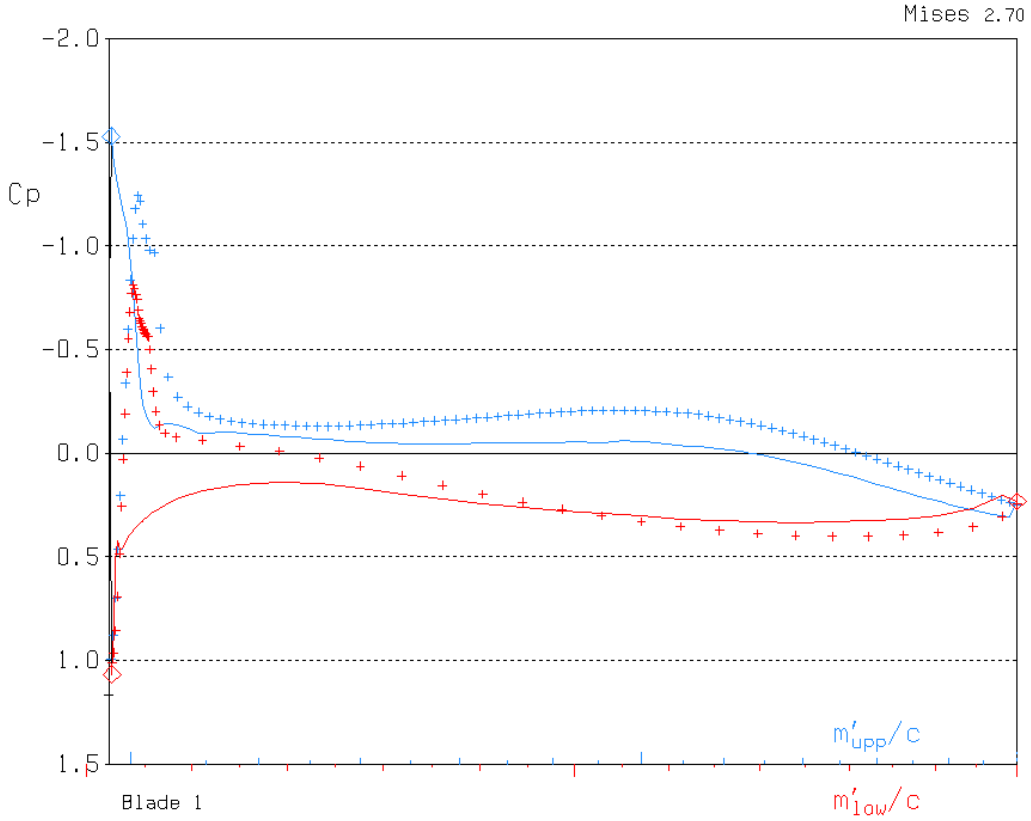

Figure A1- 7 First iteration of the modal inverse design.

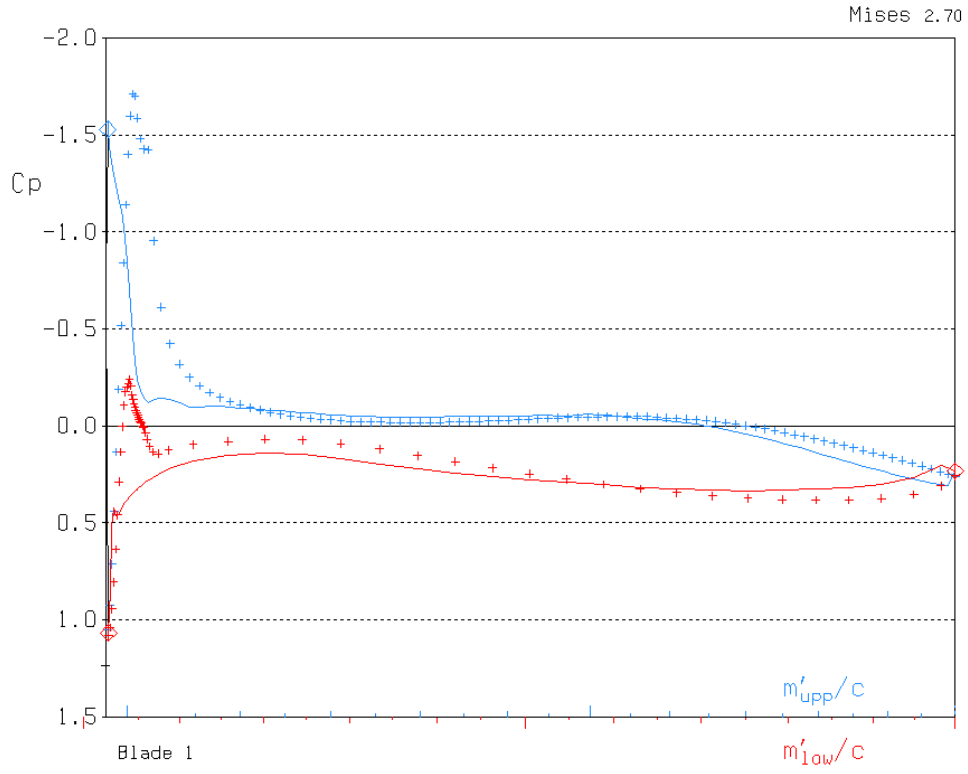

Figure A1- 8 Second iteration of the modal inverse design.

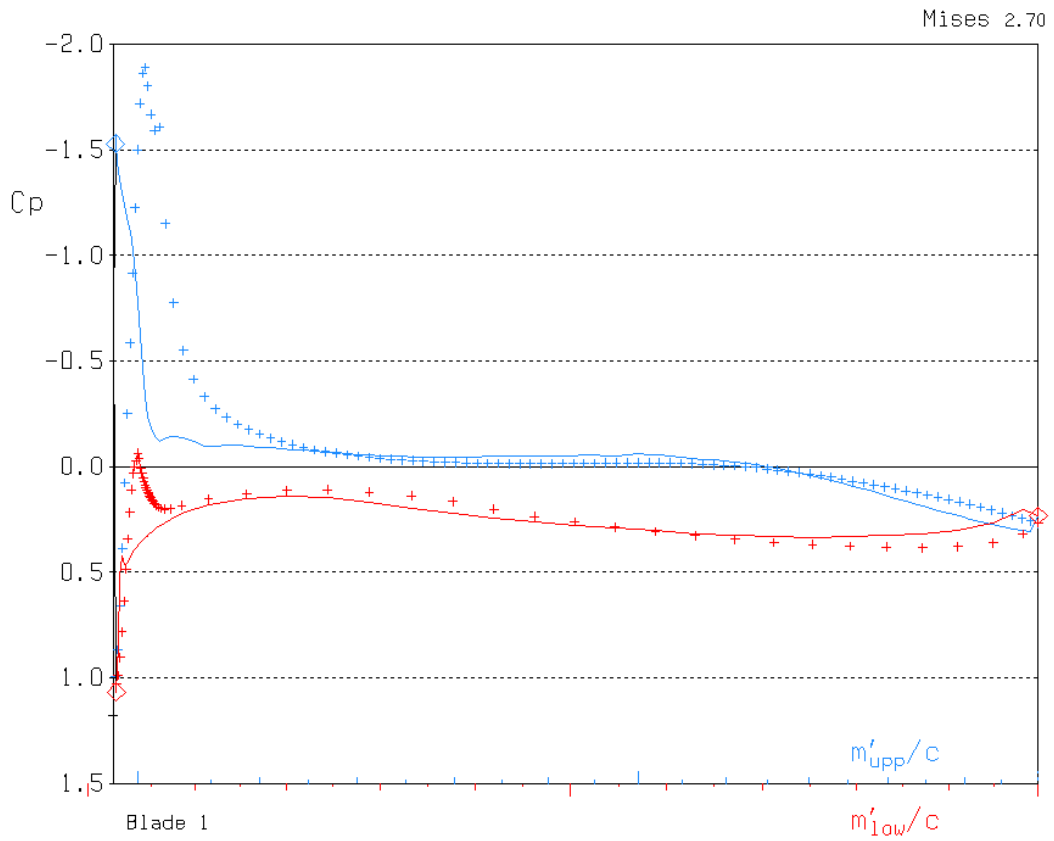

Figure A1- 9 Third iteration of the modal inverse design

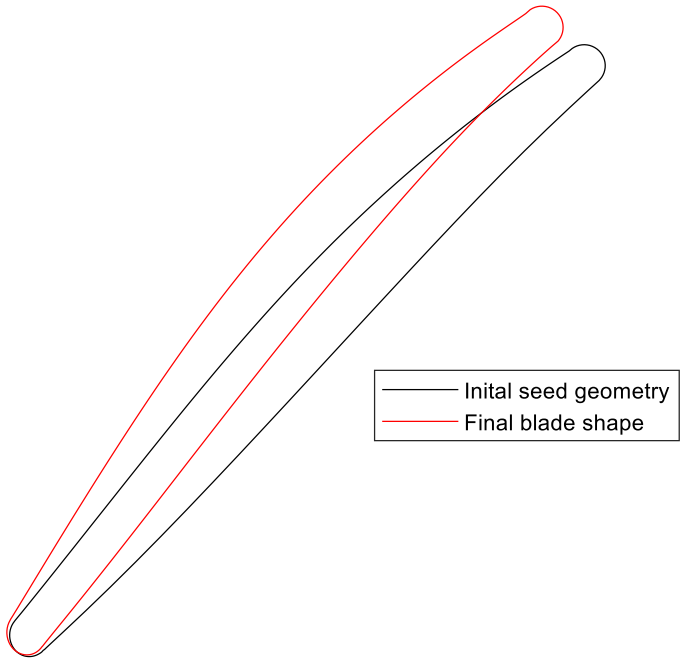

Figure A1- 10 Comparison of the final blade shape with respect to the initial seed geometry

Appendix II

Structural Analysis and Testing of a Low-speed Rotor

Among the downside of experimentation in the field of turbomachinery is the associated cost. However, with the advent of polymer additive manufacturing technology, the cost of manufacturing the blades can be significantly reduced. Polymer additive manufacturing allows for the blade to be rapidly manufactured at a lower cost than metallic blades. An FEA analysis is conducted to ensure that the 3D polymer printed blades can withstand the load during the experimentation. A simplified diagram for the low speed axial compressor (LSAC) structural analysis is shown in Figure A2- 1. Table A2-1 presents the material properties of the selected polymer material. The material properties are taken from the product information brochure. Later in this appendix, description of a tensile test conducted to validate the use of the selected blade material is presented.

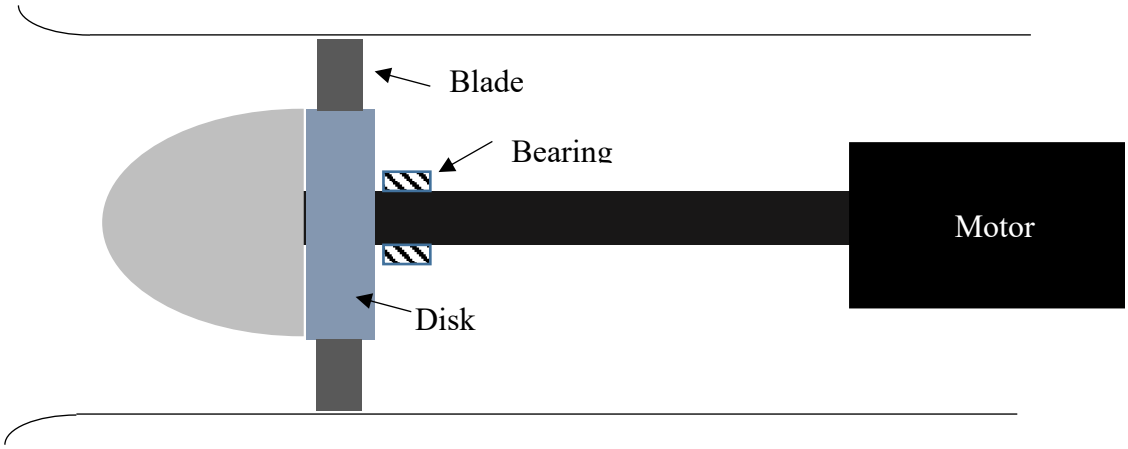

Figure A2-1 Schematic diagram of the test rig (not to scale).

Table A2-1 Vero Clear TM material properties as specified by the manufacturer

Material property	Testing standards	Value
Tensile Strength	D-638-03	50-65 MPa
Elongation at Break	D-638-05	10-15%
Modulus of Elasticity	D-638-04	2000-3000 MPa
Flexural Strength	D-790-03	75-110 MPa
Flexural Modulus	D-790-04	2200-3200 MPa
HDT °C @ 0.45MPa	D-648-06	45-50 °C
HDT °C @ 1.82MPa	D-648-07	45-50 °C
Izod Notched Impact	D-256-06	20-30 J/m
Glass transition temperature, Tg	DMA	52-54 °C
Shore Hardness (D)	Scale D	83-86
Rockwell Hardness	Scale M	73-76
Polymerized Density	ASTM D792	1.18-1.19 g/cm^3
Ash content	USP281	0.02-0.06%

Numerical Method

The rotor blades are designed to be printed individually and are mounted on an aluminium disk as shown in Figure A2- 2. The material specification for the rotor blades can be found in Table A2-1. The structural analysis contains two parts. The first part is a static analysis where the focus is to calculate the stresses and deflection of the rotor blades under load. Secondly, a modal analysis is performed to study the rotor-dynamics of the axial compressor. This is to investigate the critical speed of the compressor (rotating speed that excites the natural frequency of the compressor). Both analyses are done using ANSYS Mechanical software package. For the static analysis, the stress on the disk can be assumed to be circumferentially uniform. Hence a sector of the blade and disc assembly with periodic boundary conditions (on the disc) is modelled as shown in Figure A2- 2. The meshed model contains about 35000 grid points. For the modal analysis, a full bladed disk domain is used as shown in Figure A2- 3.

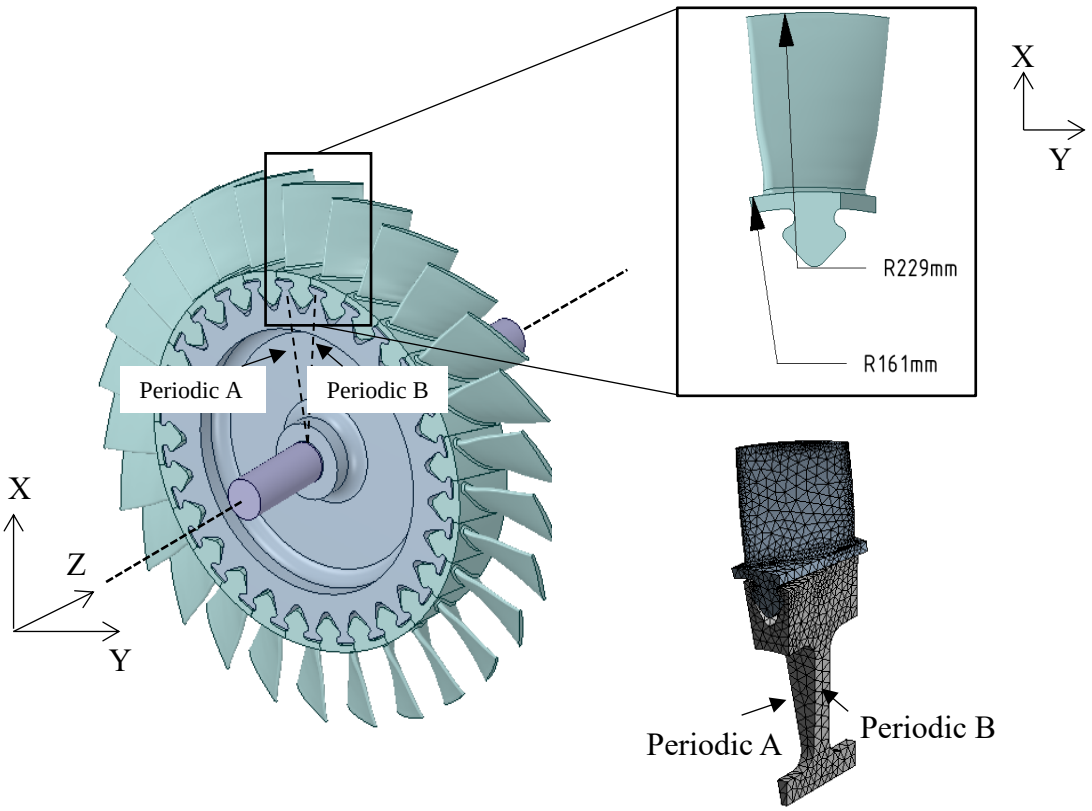

Figure A2-1 Isometric view of the rotor blades mounted on a shaft fitted disk. Inset: Grid of a single rotor blade used for the static analysis.

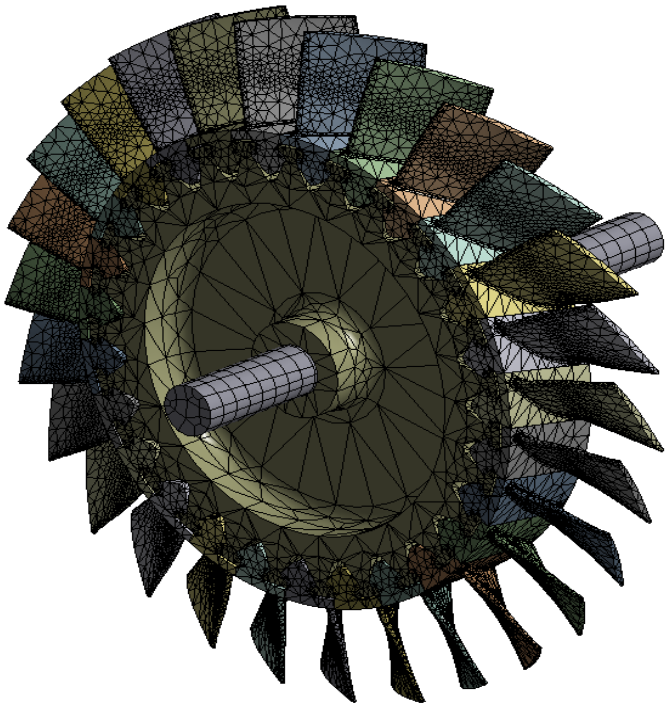

Figure A2-3 Mesh of a full sector blade assembly used for the Modal analysis

Figure A2-4 shows the load applied on the numerical domain for the static analysis. The effect of the centrifugal load on the blade is prescribed through the rotational velocity. The force of 2.85 N (obtained from CFD results) is imposed on the blade surface is equivalent to the reaction force due to the torque exerted on the air by the rotor blade at design conditions. The setup for the modal analysis is shown in Figure A2-5. Contact surfaces are modelled as bonded contact to simplify the analysis. The bearing is modelled as a simple support with a restricted degree of freedom.

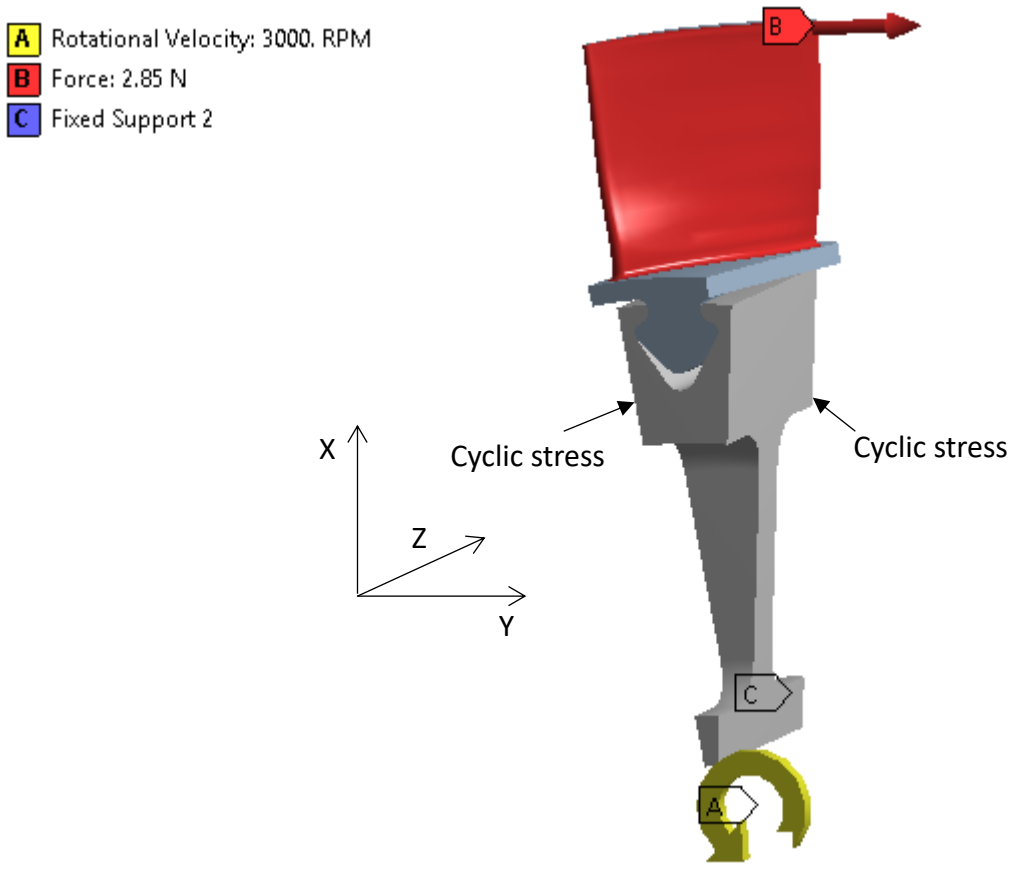

Figure A2-4 Boundary conditions of the static analysis.

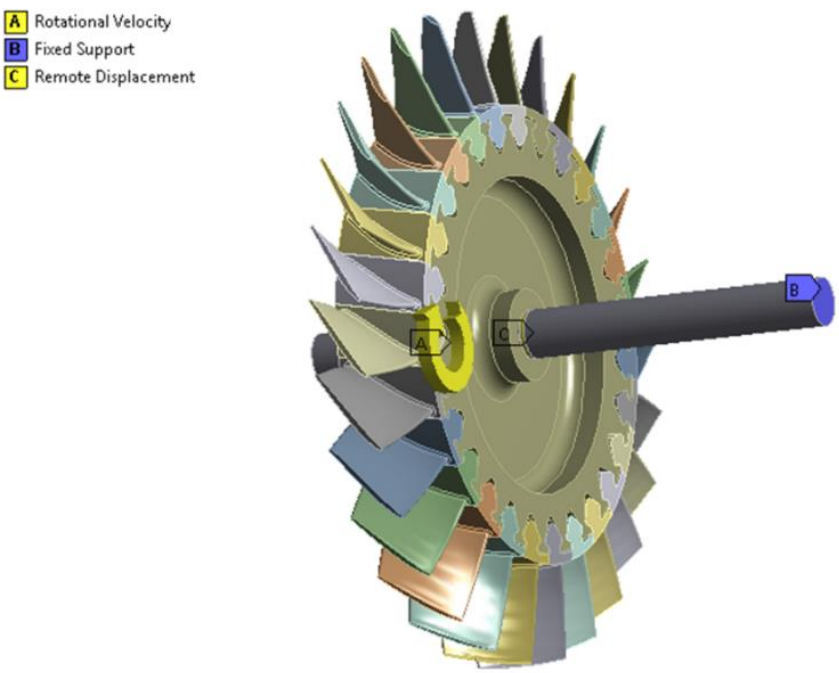

Figure A2-5 Boundary conditions of the Modal analysis.

Results of the Structural Analysis

Stress (Von-Mises)

Figure A2-6 and Figure A2-7 show the stress calculated on the disk and the blades. The maximum stress on the disk is about 18.2 MPa. For the blade, the maximum stress is about 4 MPa. This is less than 1/10th of the tensile strength of the polymer material.

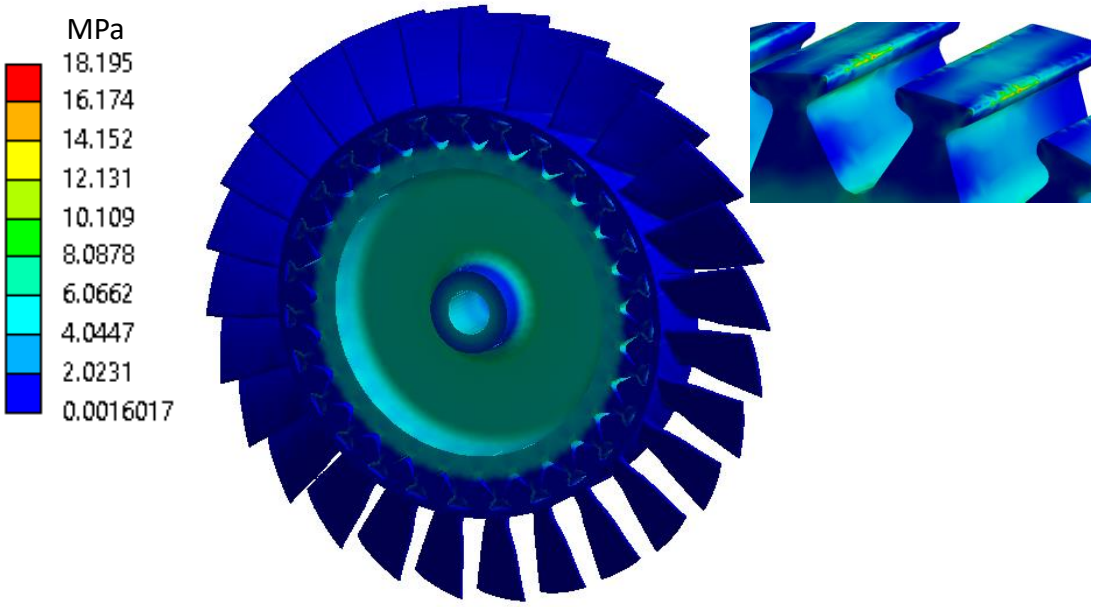

Figure A2-6 Stress contour calculated on the blade disk assembly. Inset: Stress on the disk.

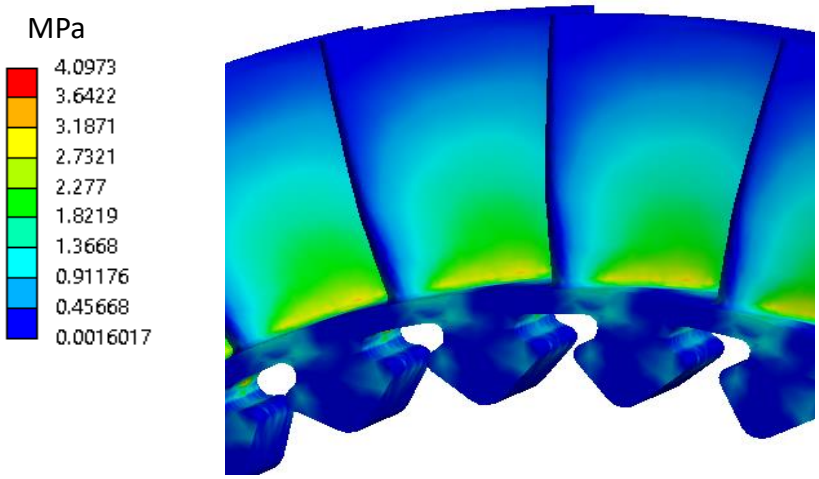

Figure A2-7 Stress calculated on the blade surface

Deformation

The deformation of the blade is shown in Figure A2-8 to Figure A2-11. Overall, the deflection is found to be within an acceptable range. The maximum overall deformation is 0.237 mm and direction wise; the deformation is small. The maximum radial deformation as shown in Figure A2-9 is found to be about 0.06 mm which is less than 1/10th of the nominal tip clearance of 1mm. A significant radial deformation is not permitted as the blade will 'rub' the casing. This will damage the blades and the test rig.

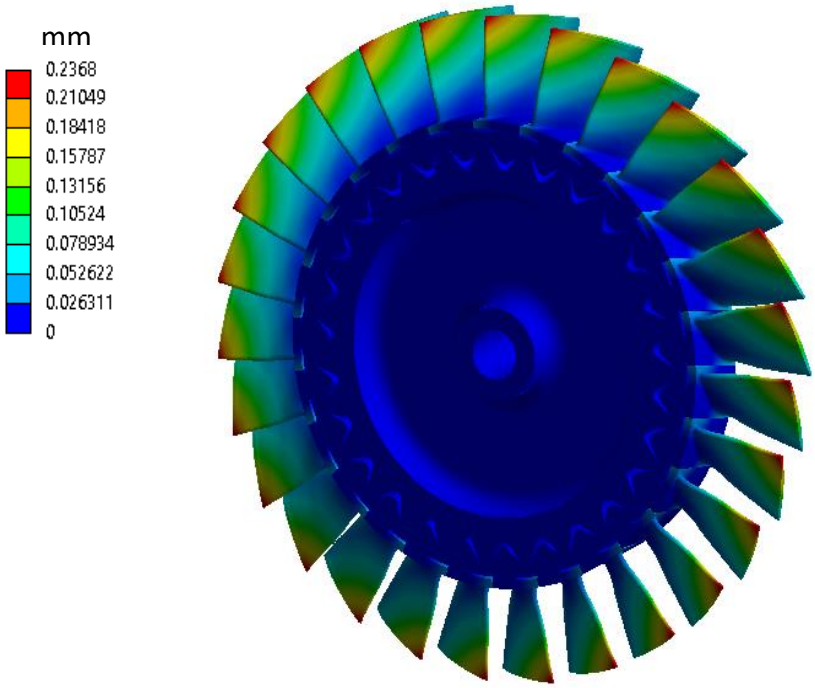

Figure A2-8 Total deformation calculated on the blades and disk

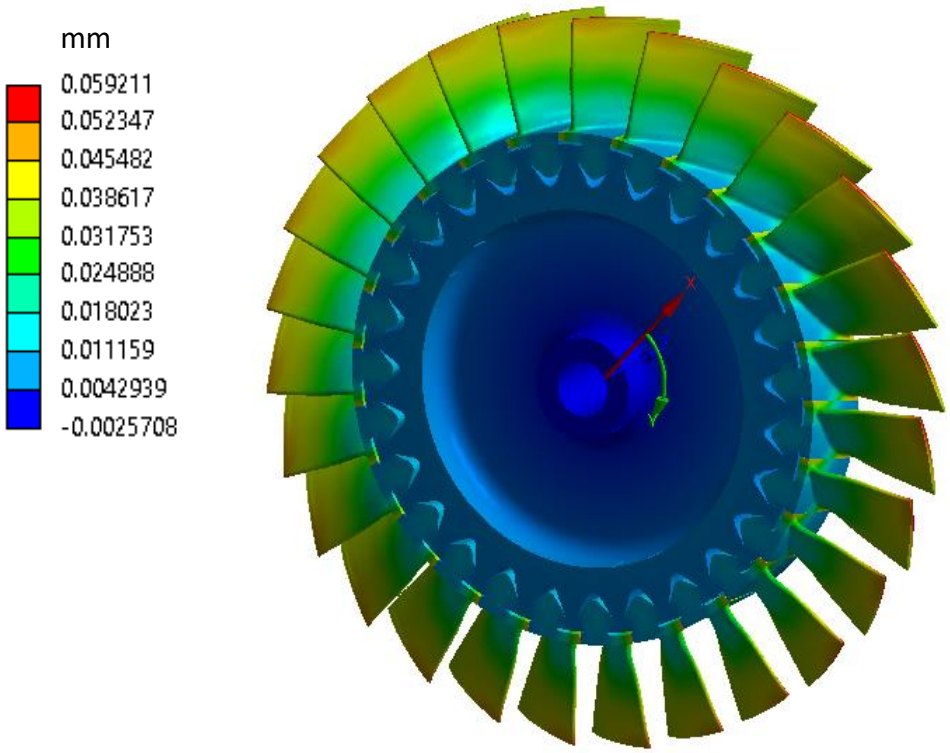

Figure A2-9 Deformation along the radial direction

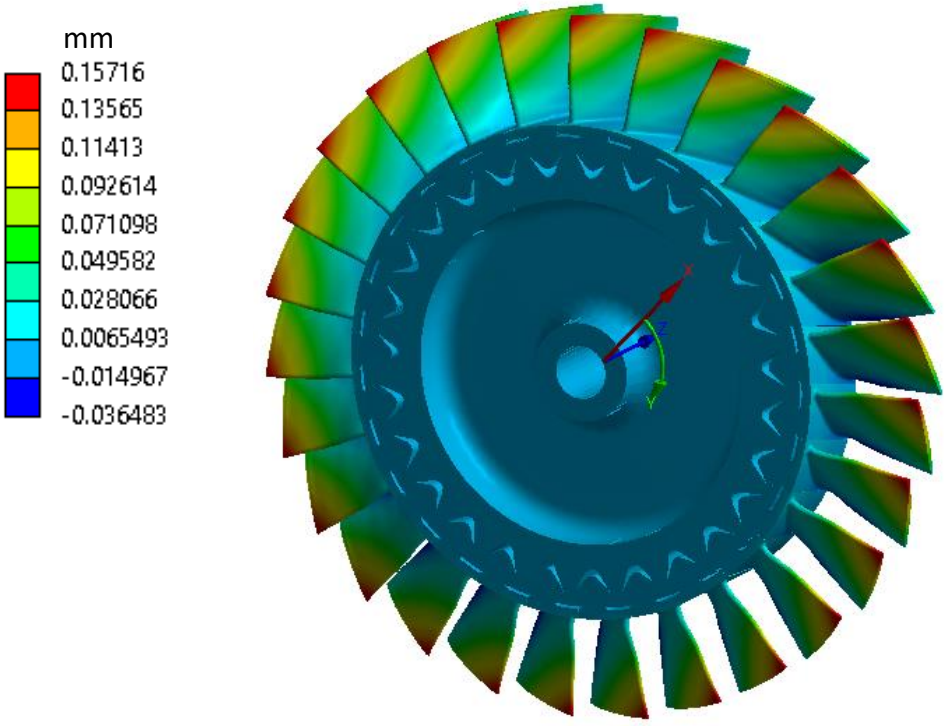

Figure A2-10 Deformation along the pitch direction

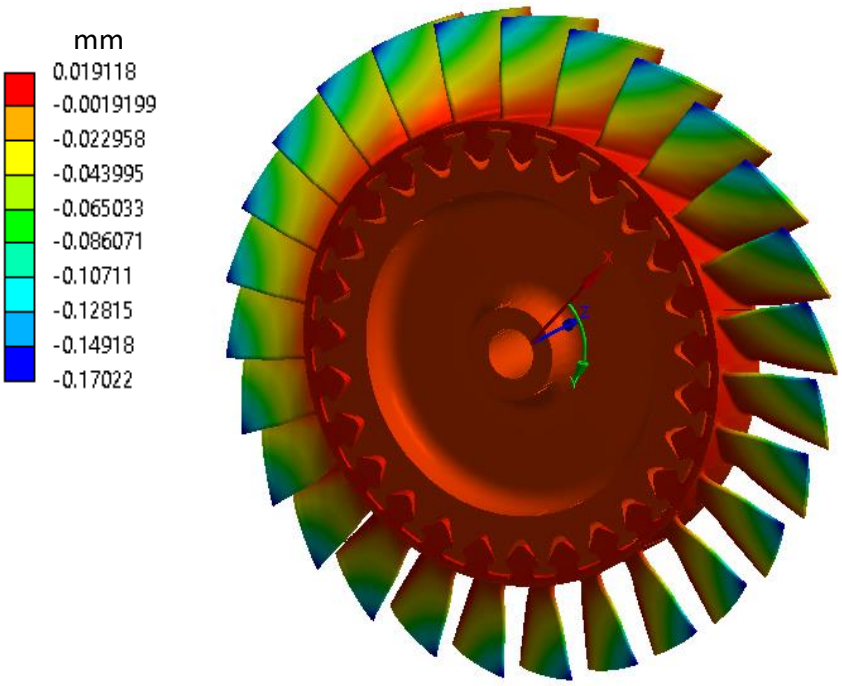

Figure A2-11 Deformation along the axial direction

Results of the modal analysis (Campbell diagram)

The Campbell diagram as shown in Figure A2-12 shows the mode frequencies at different rotating speed. From, the Campbell diagram it can be seen that the mode frequency does not cross the rotating frequency of the blade disk which suggest that the rotating body will not be subjected to resonance in the intended operational speed range of the LSAC.

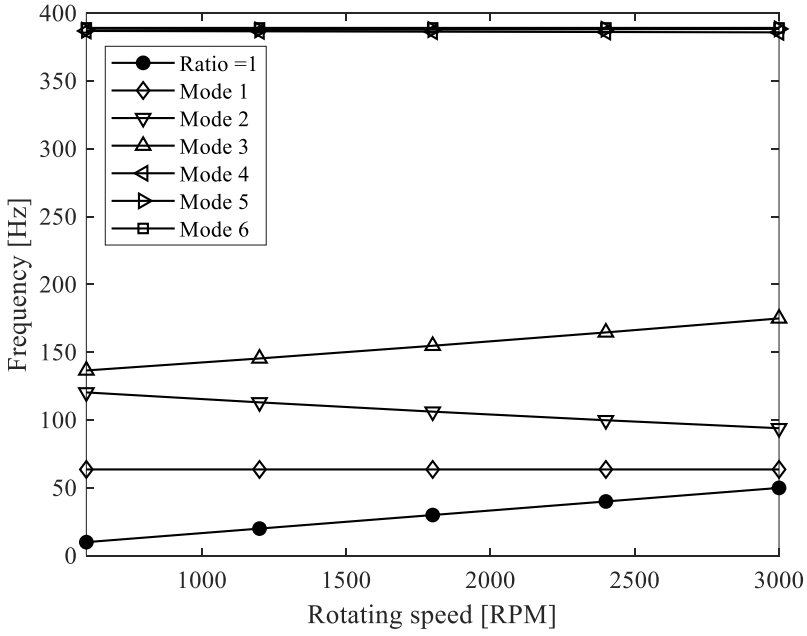

Figure A2-12 Campbell diagram of the rotor blades

Tensile test of the selected rotor blade material

Further to the structural analysis presented in the previous sections, a tensile test on the blade material is performed to find out the breaking strength of the material. This is to verify the tensile strength of the material quoted by the manufacturer as found in Table A2-1. The setup for the material tensile test is shown in Figure A2-13. The test specimen which has a radius of 3mm is mounted in-line to an S-type beam load cell. The tensile load is controlled using a threaded rod and nut. The tensile load is increased by gradually and uniformly tightening the nut. The tensile load as obtained as an output from the calibrated load cell is logged into a computer for monitoring after the acquisition of the signals from a bridge based signal conditioner. The result of the tensile test is shown in Figure A2-14. The ultimate tensile strength is about 65 MPa which falls within the value range provided by the manufacturer. Furthermore, the material is found to experience negligible necking before braking. This can be seen in the reduction of the stress past the ultimate tensile strength limit. The occurrence of necking has been captured using a portable microscopic camera as shown in Figure A2-15a). Figure A2-15b) shows the fractured surface of the test specimen. The clean fracture of the surface and relatively small percentage of necking suggest a brittle type failure.

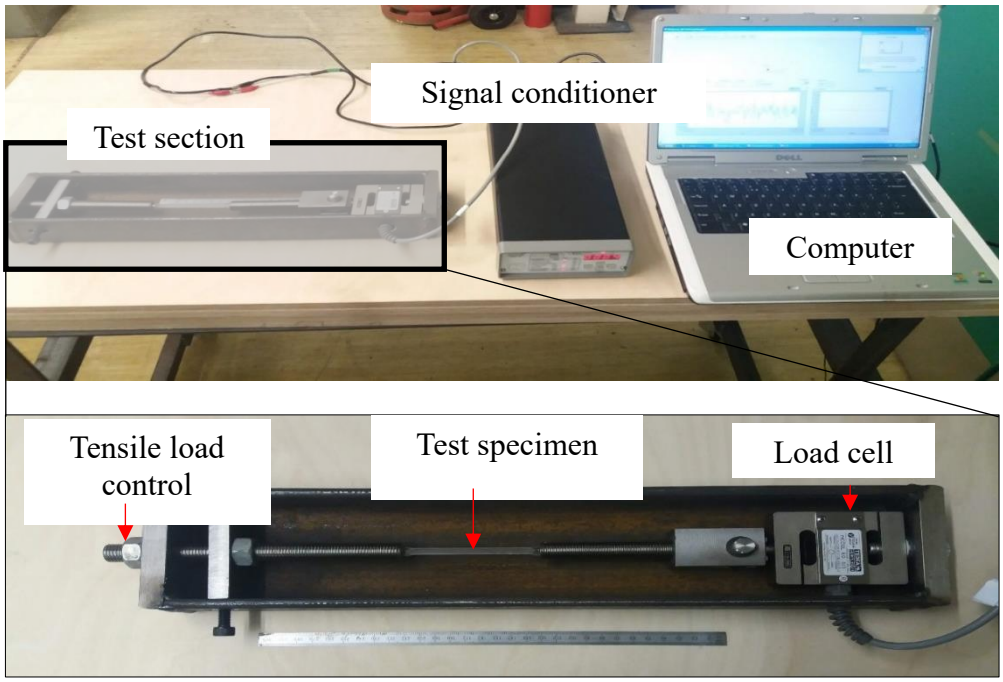

Figure A2-13 Blade material tensile test rig and setup

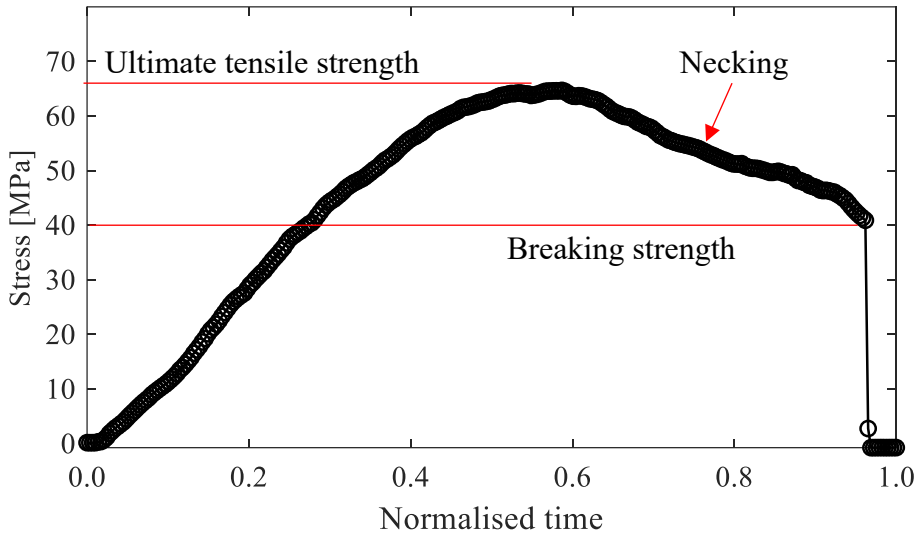

Figure A2-14 Blade material tensile stress curve

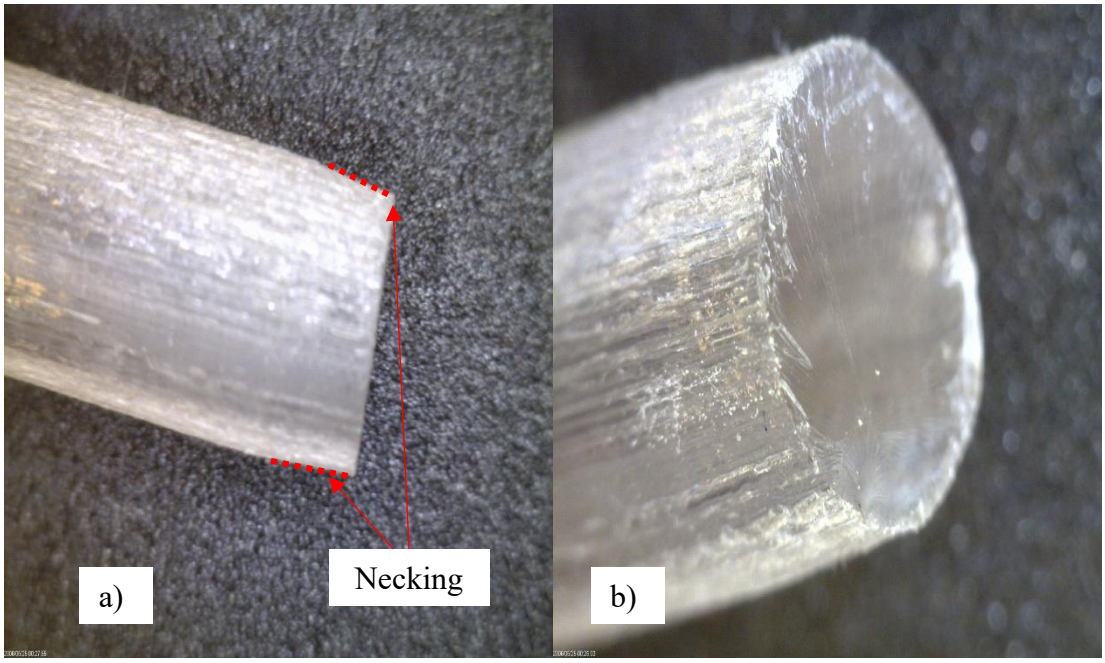

Figure A2-15 a) Necking on the test specimen and b) fracture surface of the test specimen

The printed rotor blades are weighed and labelled to ensure that the blades printed are within the allowable engineering tolerance. The standard deviation of the blades' mass is within 1% of the mean. A low standard deviation means that the blades are similar. This is important for balancing the rotor and avoiding catastrophic vibrations during operation.

Appendix III

Low Speed Compressor Rig: Preliminary Test Results and Analysis

Introduction

Continuing the discussion from Chapter 7, this appendix describes the assembly and instrumentation of a low-speed axial compressor test rig that was built for experimentally validating the SMI methodology explained in this thesis. However, as mentioned before, due to the unprecedented lockdown caused by the global pandemic (COVID-19) and the thesis submission deadline imposed by the financial sponsors, no extensive experimental studies were possible other than for a few days prior to the submission of this thesis. The first and second section of this appendix details the test rig setup and instrumentation, respectively. In the final section, the preliminary results from the rig are presented.

Compressor rig setup

The compressor used in this study is a low-speed axial compressor rotor test rig as shown in Figure A3- 1. The test rig is vertically designed to save space and to avoid the need for horizontal alignment of the sections that requires expensive support framework. The rig consists of a single rotor blade row with no inlet guide vanes and downstream stator blades. Exact details of test section are explained in Figure A3- 2 and Table A3-1. The motor speed is controlled by using a variable frequency drive controller. Rotatable motor-powered flaps are used as the compressor outlet throttle as shown in Figure A3- 3. The assembly of the rotor blades, disk, and shaft is shown in Figure A3- 4.

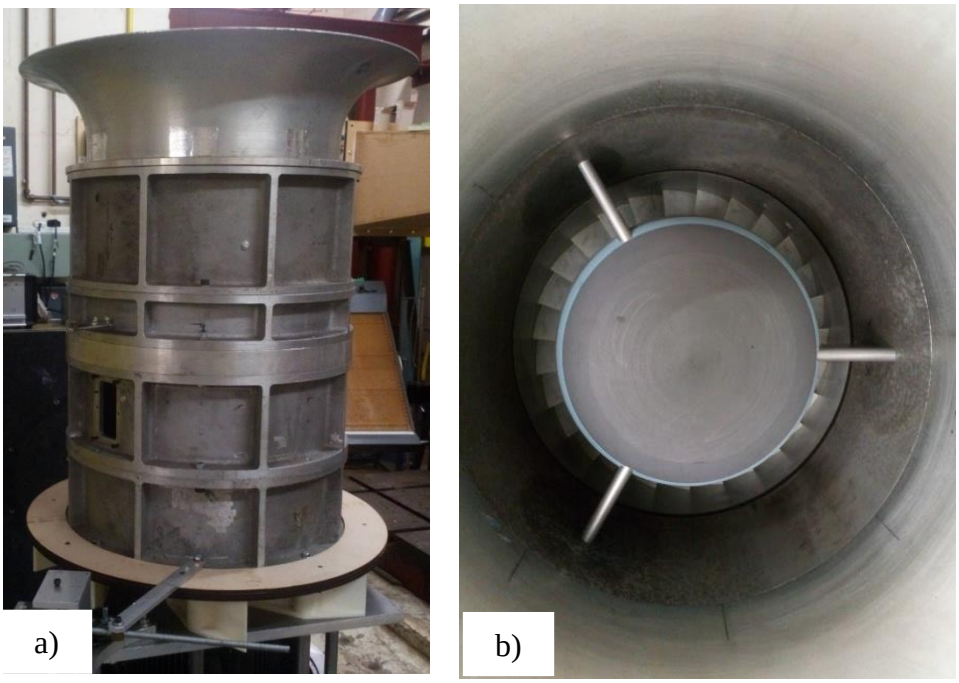

Figure A3- 1 a) The photo of the LSAC and b) the view inside of the LSAC looking into the inlet from the top.

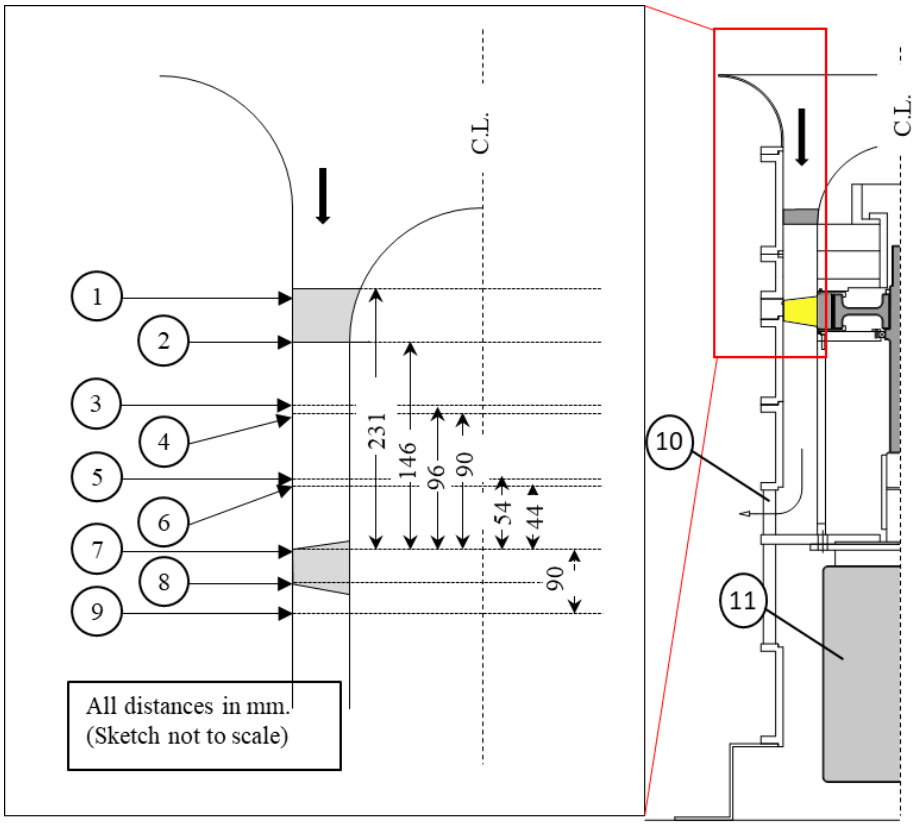

Figure A3- 2 GA drawing of the rig with exact measurements for instrumentation. Legends are supplied in Table A3-1.

Table A3-1 Legends explaining Figure A3- 2.

1	3 × support struts at 120º (15mm thick plates)
2	Beginning of parallel annulus
3	Provisions for boundary layer trip
4	Provisions for turbulence grid
5	Boundary layer traverse
6	3 × inlet pitot (mid-span) & casing wall static pressure tappings
7	Rotor blade tip LE
8	Rotor blade tip TE
9	3 × exit casing wall static pressure tappings
11	8 motor-powered rotatable flaps
12	3 phase AC motor with maximum speed of 3000 RPM

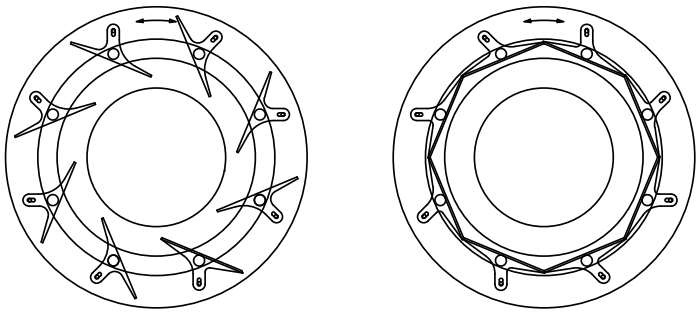

Figure A3- 3 Outlet throttle mechanism

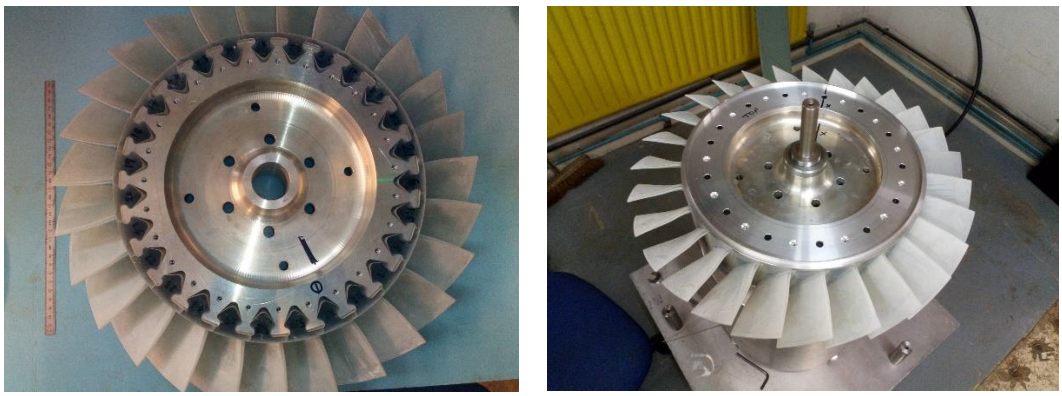

Figure A3- 4 Rotor blades mounted on the disk (left) and the rotor blades-disk-shaft assembly (right)

Instrumentation

Steady pressures were measured with a DSA 3017 pressure array, 9 of the 16 channels of which were used. The inlet pitot-tube and static wall tappings are positioned within the 120º sectors created by the inlet nose-cone support struts such that they avoided being in the wakes emanating from the struts. Flexible plastic tubings with 1.1 mm internal diameter (ID) were used for connecting the pressure tapping and pitot probe (hypodermic tubes) to the DSA. The only DSA available was of a higher pressure range ($0 - 35$ kPa). The accuracy of pressure measurements was only within $\pm$15 Pa. Since this is inadequate for determining the compressor operating points (especially the stall point) of the low speed compressor with reasonable accuracy. Two Furness Controls micromanometers (differential type) were used by doubling up on the respective channels of the DSA. The inlet dynamic head was measured using a $0 - 1$ kPa range micromanometer whereas the total to static pressure rise across the rotor was measured using a $0 - 1.5$ kPa range micromanometer. The transducer output was zeroed at the beginning of each measurement cycle. Once the manometers were warmed up, the zero-level drift was less than $\pm$1.5 Pa within a measurement cycle. The use of the lower range pressure transducers ensured that the flow coefficient and the pressure rise coefficient were measured to within $\pm$0.005. At the beginning of the measurement cycle, the ambient conditions are recorded using a digital thermometer and a digital manometer both located in the same test cell as the rig.

Preliminary results

Figure A3- 5 shows the total to static pressure rise, ψ_{ts}, characteristic lines obtained from the 5 test runs. The total to static pressure rise, ψ_{ts}, and flow coefficient, ϕ'_{mid}, are defined using Equation 1 and 2, respectively.

$$\psi_{ts} = \frac{P_{casing,exit} - P_{01}}{0.5\,\rho U_{mid}^2} \tag{1}$$

$$\phi'_{mid} = \frac{V_{z,mid}}{U_{mid}} \tag{2}$$

The numerator of Equation 1 is the difference between the outlet casing pressure, $P_{casing,exit}$, and the inlet total pressure, P_{01}. P_{01} is obtained from the inlet pitot tube at

mid-span. The quantities ρ, and U_{mid} are the air density and the mid-span blade speed, respectively. The abscissa of Figure A3- 5 is the mid-span flow coefficient, ϕ'_{mid}. The axial velocity, $V_{z,mid}$, is calculated from the inlet pitot tube and the wall static pressure tapping on the casing located at the same axial plane as the head of the pitot probe.

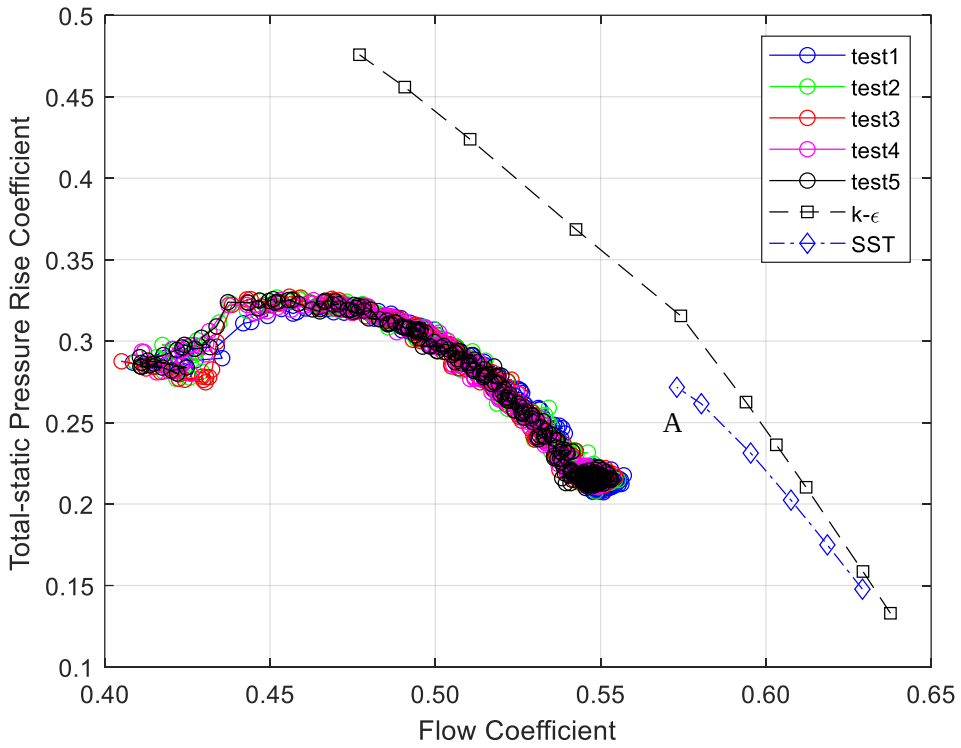

Figure A3- 5 Comparison of the total to static pressure lines between the test and CFD results.

Unfortunately, the LSAC did not produce the desired pressure rise as what it was designed for. The design pressure rise corresponds to the pressure rise predicted by the CFD ($k-\epsilon$ line). Instead, the pressure line of the LSAC indicates a roll-over before reaching the design pressure rise. This does not correspond to a 'spike'-type stall as what a tip-critical compressor would normally show as reported in the literature. Casing treatments would be less effective if the compressor does not stall at the near casing. Therefore, further test runs using a grooved casing would be inconclusive if the compressor is not tip-critical.

One of the reasons that might be causing this problem is a possible flow separation on the rotor blades. Since the $k-\epsilon$ turbulence model that was originally used in the design verification of the LSAC blade has some known limitations in predicting flow separation near the blade surface, additional CFD calculations were carried out using an SST turbulence model. Operating point A in Figure A3- 5 is the last stable operating point (based

on convergence criteria in Chapter 3) of the CFD run using an SST model. Initial investigations as shown in Figure A3- 6 suggest that there is a separation bubble on the suction side surface near the LE. This is plotted at 85% span for operating point A and operating point A' (un-converged case that has a slightly higher backpressure than operating point A).

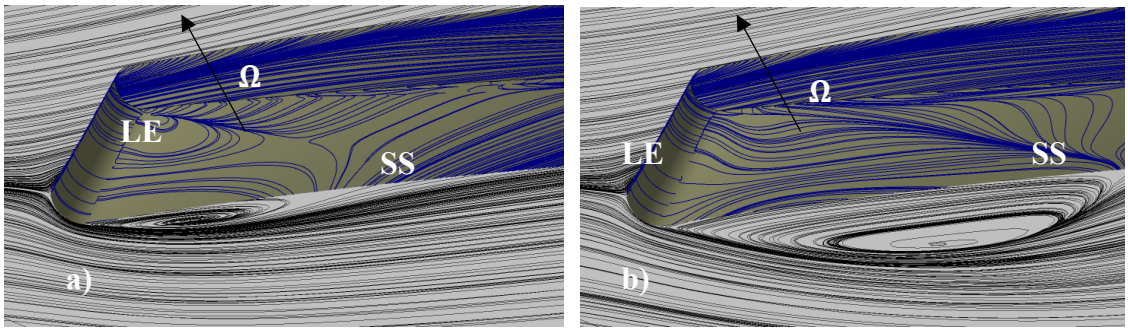

Figure A3- 6 Separation bubble on the blade LE suction side at 85% span for operating point A and A'

The flow separation can be caused by either a badly designed blade or due to the existence of a laminar boundary flow separation on the blade surface. The former might be possible since the design of the blade were based on steady CFD results using a $k-\epsilon$ model. The latter can be caused by the low turbulence intensity levels inside the rig. Note that the simulations used for the design verification assumed a fully turbulent boundary layer with a turbulent inlet prescription. If the flow entering the blade is laminar then transition to turbulence may occur through a separation process at high incidence angles. The turbulence model is unable to capture the laminar-turbulent boundary layer transition on the blades. Neither of these theories could be confirmed due to the lack of time to conduct further investigations. In addition, the current rig did not perform well on installing turbulence grid to induce artificial turbulence at the inlet. This is because the pressure loss through the gird resulted in the compressor operating at a low flow coefficient even at fully open throttle conditions.